Computational approaches and structural prediction of high pressure molecular solids

A Thesis Submitted to the College of

Graduate Studies and Research

In Partial Fulfillment of the Requirements

For the Degree of Doctor of Philosophy

In the Department of Physics and Engineering Physics

University of Saskatchewan

Saskatoon

By

Niloofar Zarifi

Permission to Use

In presenting this thesis in partial fulfilment of the requirements for a Postgraduate degree from the University of Saskatchewan, I agree that the Libraries of this University may make it freely available for inspection. I further agree that permission for copying of this thesis in any manner, in whole or in part, for scholarly purposes may be granted by the professor or professors who supervised my thesis work or, in their absence, by the Head of the Department or the Dean of the College in which my thesis work was done. It is understood that any copying or publication or use of this thesis or parts thereof for financial gain shall not be allowed without my written permission. It is also understood that due recognition shall be given to me and to the University of Saskatchewan in any scholarly use which may be made of any material in my thesis.

Requests for permission to copy or to make other use of material in this thesis in whole or part should be addressed to:

Head of the Department of Physics and Engineering Physics
116 Science Place
University of Saskatchewan
Saskatoon, Saskatchewan
Canada
S7N 5E2

ABSTRACT

The objective of this thesis is to study the crystal structures and electronic properties of solids at high pressure using state-of-the-art electronic structure computational methods. The thesis is divided into two main sections. The first part is to examine the performance and reliability of several current density functionals in the description of the electronic structures of small band gap materials and strongly correlated systems. The second part is to compare and evaluate two recently proposed first-principles methods for the prediction of stable structures of solids at high pressure.

To accomplish the first goal, first-principle electronic structure calculations employing density functional theory (DFT) and several "correlation corrected" functionals calculations were used to investigate the properties of solid AlH_3 and EuO at high pressure. The primary reason to study AlH_3 is to resolve a discrepancy between previously predicted superconductivity behavior at 110 GPa but was not observed in experimental resistance measurements. The key to resolve the discrepancy is an accurate calculation of the valence and conduction band energies. The results shows that the Fermi surface is modified by the "improved" functionals over the previous calculations using "standard" gradient corrected functional. These changes in the Fermi surface topology removed the possibility of nesting of the electronic bands, therefore, solid AlH_3 above 100 GPa is a poor metal instead of a superconductor. In the second system, we have studied EuO with highly localized electrons in the Eu 4*f* orbitals. A particular interest in this compound is the report of an anomalous isostructural phase transition with a significant volume reduction at 35-40 GPa and the relationship with the electronic state of Eu at high pressure. Using the Hubbard on-site repulsion model (LDA+U), we successfully predicted the insulator $\rightarrow$ metal transition of EuO at 12 GPa and the trend in the Mössbauer isomer shifts. However, the isostructural transition was not reproduced. The U on-site repulsion to localized Eu 4*f* orbtials helped to ameliorate some deficiencies of the PBE functional and improved the agreement with experimental observations but not all the properties were correctly reproduced.

The second objective of this investigation is to predict energetically stable crystalline structures at high pressure. The reliability and relative efficiency of two recently proposed structure prediction methods, *viz*, Particle Swarm Optimization (PSO) and the Genetic Algorithm (GA) were critically examined. We applied the techniques to two separate systems. The first system is solid CS_2. The motivation is that this compound was recently found to be a superconductor with a critical temperature of 6 K from 60 – 120 GPa. However, no crystalline

structure was found by experiment in this pressure range. Our calculations suggest the energetic favorable structures contain segregated regions of carbon and sulfur atoms. The sulfur atoms adopt a planar closed pack arrangement forming 2D square or hexagonal networks and the carbon atoms tend to form hexagonal rings. A global minimum crystalline structure with structural features observed in the amorphous structure was found and shown to be superconductive. In the second case, we studied the possibility on the existence of Xe-halides (XeH_n (H=Cl, Br and I, n = 1, 2 and 4)) compounds below 60 GPa. We reported the stability, crystal and electronic structures, vibrational and optical spectra of a number of stoichiometric crystalline polymorphs. We found that only XeCl and $XeCl_2$ form thermodynamically stable compounds at pressure exceeding 60 GPa. A stable cubic fcc structure of $XeBr_2$ was found to be a superconductor with critical temperature of 1.4 K. From these studies, we found both merits and shortcomings with the two structural prediction approaches. In the end, we proposed a hybrid approach to assure the same stable structure is predicted from both computational strategies.

ACKNOWLEDGMENTS

Many wonderful people have helped me during the five years of my study at the University of Saskatchewan. Firstly, I would like to thank my supervisor Dr. John Tse who gave me the chance to work as I felt with total support and encouragement. I was always challenged by Professor Tse to criticize the literature, raise questions, come up with new ideas, implement the ideas, and eventually complete my thesis. I am grateful for the continuous support in many aspects, whether it was providing excellent academic guidance, exposure to wide scientific interests, financial contributions, great patience, friendliness, or thoughtful career advice.

I owe a big thanks to all the fellow students and postdocs, past and present, from Professor Tse's group for the collaborations, to share their skills and interests with me. I enjoyed collaborating with Hanyu Liu on the CS_2 project. He was always so nice and patient in answering my questions and helped me to develop my knowledge. The names of all other group members also deserve a mention: Jianjun Yang, Xue Yong, Jianbao Zhao, Min Wu and Hui Wang. I enjoyed and benefited a lot from many scientific and non-scientific conversations with them. From my interactions over the last five years, I have to admit, I am now more than enthusiastic about visiting China.

It is important to acknowledge all of my thesis committee members: Professor Tom Steele, Gapsoo Chang, and Richard Bowles for their time, encouragement, valuable suggestions and insightful comments. Additionally, I wish to thank Brian Zulkoskey and Yannis Pahatouroglou for their support and guidance throughout my teaching experience. My appreciation goes to Fred Sage for his willingness to correct my written English. I would also like to thank my entire family and friends for the encouragement over the years.

TABLE OF CONTENTS

Permission to Use i

ABSTRACT ii

ACKNOWLEDGMENTS iv

TABLE OF CONTENTS v

LIST OF TABLES viii

LIST OF FIGURES ix

LIST OF ABBREVIATIONS xvi

1. Introduction and computational methodology 1

1.1 Electronic structure 4

1.1.1 Hartree-Fock approximation 4

1.1.2 Hohenberg-Kohn theorems 6

1.1.3 Kohn-Sham equations 6

1.1.4 Functional forms of exchange correlations 8

1.1.5 DFT+U 9

1.1.6 Calculation of the Hubbard U parameter 9

1.1.7 Hybrid functional 10

1.1.8 Semi-local mBJLDA functional 11

1.1.9 Periodic boundary conditions 12

1.1.10 Plane-wave basis sets 13

1.1.11 Pseudopotential approximations 14

1.1.12 Projected augmented wave potentials 15

1.1.13 Full potential linear augmented plane wave 16

1.1.14 Self-consistent solution 17

1.1.15 The GW approximation 18

1.1.16 Wannier function 20

1.1.17 Bethe-Salpeter equations 22

1.1.18 Electronic localization function 24

1.1.19 Structural stability of solids 24

1.2 Structural prediction 25

1.2.1 Crystal lattice and Gibbs free energy 26

1.2.2 Particle swarm optimization 27

1.2.3 Genetic algorithms 29

2. Study of the electronic structures in AlH_3 and EuO at high pressure 32
2.1 Electronic structure of the high pressure cubic phase of AlH_3 33
2.1.1 Introduction....33
2.1.2 Structure of AlH_3 34
2.1.3 Electronic properties using standard functional....34
2.1.4 Methodology....36
2.1.5 Results and discussions....37
2.1.6 Conclusions....42
2.2 Insulator-metal transition and valence instability in EuO....42
2.2.1 Introduction....42
2.2.2 Computational details 45
2.2.3 The electronic band structure of EuO 45
2.2.4 Isomer shift of EuO under pressure 47
2.2.5 Conclusions....50
2.3 Summary 51
3. Structures of the metallic and superconducting high pressure phases of solid CS_2 52
3.1 Computational details....53
3.2 Results and discussions at 2 GPa 54
3.3 Structures predicted at 60 and 100 GPa 58
3.4 Molecular dynamics simulations....62
3.5 Stability of the predicted structures....63
3.6 Radial distribution functions 64
3.7 Electronic and vibrational properties 66
3.8 Conclusions 70
4. Crystal structures and electronic properties of Xe and Cl compounds at high pressure 72
4.1 Computational details....73
4.2 Thermodynamic stability of $XeCl_n$ (n=1, 2 and 4)....74
4.3 Predicted high pressure structures of $XeCl_2$....75
4.3.1 Structural analysis at 10 GPa 80
4.3.2 Electronic and dynamical properties at 10 GPa 81
4.3.3 Energy corrections beyond PBE functional....84
4.3.4 Comparison with experiment....85
4.3.5 Electronic structures at 15 GPa....88
4.3.6 Structural analysis at 60 GPa 90

4.3.7 Dynamical stability at 60 GPa 93
4.3.8 Raman spectra and electronic structures at 60 GPa 94
4.4 Predicted high pressure structures of XeCl 97
4.4.1 Structural analysis at 10 GPa 99
4.4.2 Energy corrections and electronic properties 102
4.4.3 Comparison with experiment 103
4.4.4 Electronic structure at 15 GPa 105
4.4.5 Structural analysis at 40 and 60 GPa 106
4.4.6 Electronic properties at 40 and 60 GPa 108
4.4.7 Raman spectra and electronic structures at 40 and 60 GPa 109
4.5 Predicted high pressure structures of $XeCl_4$ 111
4.6 Conclusions 113
5. Crystal structures and electronic properties of xenon bromide and iodide at high pressure 115
5.1 Thermodynamics stability of $XeBr_n$ (n=1, 2 and 4) 116
5.2 Predicted high pressure structures of XeBr 116
5.2.1 Structural analysis at 10 GPa 118
5.2.2 Electronic and dynamical properties 120
5.2.3 The *Fmm*2 structure at 60 GPa 121
5.2.4 The *Cmcm* structure at 60 GPa 123
5.3 Predicted high pressure structures of $XeBr_2$ 125
5.3.1 The *P*1 structure at 10 GPa 126
5.3.2 Comparison of the *Pnma* and *Fd*3*m* structures 127
5.3.3 The *Fd*3*m* structure at 60 GPa 127
5.4 Predicted high pressure structures of $XeBr_4$ 129
5.5 Predicted structures of XeI_n (n=1, 2 and 4) 131
5.5.1 Predicted high pressure structures of XeI 132
5.5.2 Predicted high pressure structures of XeI_2 135
5.5.3 Predicted high pressure structures of XeI_4 137
5.6 Conclusions 139
6. Summary and conclusion 141
APPENDIX A 145
LIST OF REFERENCES 150

LIST OF TABLES

Table 3.1 The calculated lowest enthalpy structures with vdW corrections for CS_2 at 2 GPa. 57

Table 4.1 Comparison of the lowest enthalpy structures of $XeCl_2$ (4 formula units) predicted with the GA and PSO methods in the pressure range from 10 to 60 GPa. 78

Table 4.2 Numerical values of the calculated lowest enthalpy structures with ZPE and vdW corrections. 84

Table 4.3 Comparison of the lowest enthalpy structures of 8 formula units of XeCl, predicted with GA and PSO methods in pressure ranges of 20 to 60 GPa. 98

Table 4.4 Calculated lowest enthalpy structures with vdW corrections for XeCl compound at 10 GPa. 102

Table 4.5 Comparison of the lowest enthalpy structures of 4 formula units of $XeCl_4$ predicted by GA and PSO methods in pressure range of 20 to 60 GPa. 112

Table 5.1 The lowest enthalpy structures of XeBr with PSO method in pressure range of 10 to 60 GPa. 117

Table 5.2 The lowest enthalpy structures of $XeBr_2$ with PSO method in pressure ranges of 10 to 60 GPa. 125

Table 5.3 The lowest enthalpy structures of $XeBr_4$ with PSO method in pressure ranges of 10 to 60 GPa. 129

Table 5.4 Comparison of the lowest enthalpy structures of 8 formula units of XeI with GA and PSO methods in pressure ranges of 10 to 60 GPa. 133

Table 5.5 Comparison of the lowest enthalpy structures of 4 formula units of XeI_2 with GA and PSO methods in pressure ranges of 10 to 60 GPa. 135

Table 5.6 Comparison of the lowest enthalpy structures of 4 formula units of XeI_4 with GA and PSO methods in pressure ranges of 10 to 60 GPa. 138

LIST OF FIGURES

Figure 1.1 (a) All wave functions and (b) comparison of all and pseudo wave functions of valence electrons of aluminum..... 15

Figure 1.2 A depiction of reconstructed PAW wave function that contains contribution of the all-electron (inside core region) and pseudo (outsite of core region) wave function..... 15

Figure 1.3 The workflow chart describing the KS self-consistent calculation. 18

Figure 1.4 Schematic overview of the Wannier interpolation procedure from Ref [48]. The left panel shows a coarse q mesh in BZ, where the f(**q**) is explicitly calculated using first-principle methods. The F(**R**) is calculated in real space (middle panel) and the right panel shows f(k) obtained from interpolation of k points in the BZ. 22

Figure 1.5 The left panel shows ground state energy, the middle panel is QP energies using GW correction and the last panel shows exciton energy obtained from BSE. 23

Figure 1.6 Several particles in grey color move in different directions of free energy surface. Balck dot circle is the global minimum and blue dot circles is a local minimum. 27

Figure 1.7 (a) A schematic diagram [81] depicting how generated structures explore minima within the PSO algorithm in a 1D PES. (b) The workflow in the PSO technique as implemented in the CALYPSO code..... 28

Figure 1.8 The PSO search performed on XeI_2 at 10 GPa..... 29

Figure 1.9 The offspring structures generated via heredity and mutation. 30

Figure 1.10 The GA search performed on XeCl at 40 GPa. 31

Figure 2.1 The $Pm\bar{3}n$ structure of AlH_3 has been suggested at 100 GPa. 34

Figure 2.2 Electronic band structure of the cubic $Pm\bar{3}n$ phase of AlH_3 calculated with PBE functional at 100 GPa from Ref [100]. Two bands cross the Fermi level at M and R. The red arrow indicates the nesting vector connecting the two pieces of Fermi surfaces. 35

Figure 2.3 Electronic band structure of AlH_3 calculated from PBE (red) and TB-mBJLDA functionals using the WIEN2k code (black) from Ref [101]. The pressures are obtained from the equation of states calculated from the respective functionals..... 38

Figure 2.4 Comparison of calculated maximum energy at R and minimum energy at M relative to the Fermi energy using (a) PBE functional with VASP and Wien2k code and GW corrections; (b) TB-MBLJDA; (c) Comparison of HSE functional with VASP and GW corrections; (d). Pseudo-gap energy between the R and M using PBE (VASP and WIEN2k), TB-mBJLDA, HSE, G0W0 (PBE and HSE) and SCGW (PBE and HSE) [101] 40

Figure 2.5 Pressure-volume dependence of EuO up to 92 GPa obtained from Ref [136]. The inset panel shows a modest isostructural volume collapse at about 35 GPa. Two schematic figures show the local coordination in NaCl (B1) and CsCl (B2) phases. 44

Figure 2.6 Electronic band structures of EuO (a) Hybrid fuctional, (b) mBJLDA at ground state. Red (PBE+U) and black (mBJLDA+U) lines represents electronic band structures at (c) ground states and (d) 0.88V0. 46

Figure 2.7 Equation of state of EuO using PBE+U functional as a function of (a) volume and (b) pressure. Inset (a) illustrates the calculated small kink around the 0.88 V/V_0. 47

Figure 2.8 Electron densities ρ_0 of EuO at the nucleus under pressure with two different radial mesh points. 48

Figure 2.9 Electron densities at the nucleus and (b) calculated energy as a function of volume of EuO with different R0s. 49

Figure 2.10 Pressure-induced electron densities at the nucleus of EuO. The inset shows IS measured by Ref [136]. 50

Figure 3.1 Black and Red circles show the enthalpy of optimized structures by PSO and GA, respectively. The enthalpy of the $P2_1/c$ structure was 0.098 eV/atom lower than the Cmca structure and the $P1$ structure found by GA had the lowest energy at 2 GPa. 54

Figure 3.2 Ten lowest predicted enthalpy structures for solid CS_2 at 2 GPa from Ref [149]..... 55

Figure 3.3 Relative enthalpies (ΔH) *vs* pressure for several CS_2 structures, with respect to the *Cmca* structure..... 56

Figure 3.4 Enthalpy of the best structure versus generation for CS_2 at (a) 60 and (b) 100 GPa... 59

Figure 3.5 Comparison of the $P2_1/m$ and $P2_1/c$ structures at 60 GPa. 60

Figure 3.6 Ten lowest predicted enthalpy structures for solid CS_2 at 60 GPa from Ref [149]..... 60

Figure 3.7 The proposed structure of α-tridymite ($P2_12_12_1$, left) and α-chalcopyrite (I-42d, right) at 60 GPa. 61

Figure 3.8 Ten lowest predicted enthalpy structures for solid CS_2 at 100 GPa from Ref [149]... 61

Figure 3.9 Snapshot of molecular dynamics calculations on CS_2 from Ref [149]. (a) 10 GPa, (b) 20 GPa, (c) 80 GPa and (d) 120 GPa. The red circle highlights the formation of C-C "clusters" at 80 GPa. The occurrence of S square nets is clearly seen at 120 GPa. 62

Figure 3.10 The phonon-band structure for the $P2_1/c$ structure of CS_2 at 60 GPa. 63

Figure 3.11 Relavtie enthalpy of molecular CS_2 with respect to *Cmca* structure..... 64

Figure 3.12 (a) Structural factor and (b) radial distributional function of solid CS_2 at 55 GPa from Ref [149]. 65

Figure 3.14 Calculated electronic density of states for the $P2_1/m$ and MD structures at 60 and 80 GPa, respectively. 67

Figure 3.15 Calculated (left) phonon band structure and Eliashberg spectral function ($\alpha^2F(\omega)$) with DFPT, Ref [149], and (right) phonon band structure with FP method. 67

Figure 3.16 The nesting function $\xi(q)$ of $P2_1/m$ CS_2 at 60 GPa along selected high symmetry lines of the nesting vector, *q*. 69

Figure 3.17 Phonon and electronic band structures of the $P2_1/m$ structure, at 80 and 100 GPa. . 70

Figure 4.1 Predicted thermodynamic stabilities of $XeCl_n$ (n=1,2 and 4) compounds. 74

Figure 4.2 (a), (b), (c) and (d) represent the PSO and GA searches performed on $XeCl_2$ at 10, 20, 30 and 60 GPa. 77

Figure 4.3 Relative enthalpies (ΔH) vs pressure for several $XeCl_2$ configurations, with respect to the *Cmcm* structure. 79

Figure 4.4 The lowest predicted enthalpy structures, $P2_1/m$ (a, b and c), $P1$ (d, e and f) and *Cmcm* (g, h and i) for solid $XeCl_2$ at 10 GPa. To distinguish layers in (b) and (h), Xe (blue) and Cl (green) atoms are shown with two different dark and light color tones. 80

Figure 4.5 The ELF values for $P2_1/m$, $P1$ and *Cmcm* structures of $XeCl_2$ with cross sections of (010), (100) and (100) are shown at 10 GPa, respectively. The positions of Xe and Cl atoms are also shown for clarity. 82

Figure 4.6 Phonon dispersion curves for $P2_1/m$ (a), $P1$ (b) and *Cmcm* (c) of XCl_2 at 10 GPa. ... 83

Figure 4.7 Comparison of phonon densities of states for molecular Cl_2 and Xe solids with $XeCl_2$ structures at 10 GPa. 83

Figure 4.8 Comparison of calculated PBE and vdW-DF2 functionals for *Cmcm* and $P2_1/m$ structures of $XeCl_2$. (a) Relative enthalpy with respect to $P2_1/m$ structure. (b) and (c) the calculated equation of states of $P2_1/m$ and *Cmcm* structures, respectively. 85

Figure 4.9 (a) The microscopic picture of Xe-Cl at ~ 0.1 MPa. The clear spherical regions were xenon-rich and (b) Xe-Cl at ~8 GPa. The crystals agglomerated as seen in the upper left on further cooling from 440 K [189]. The sample chamber is approximately 120 μm in diameter. 86

Figure 4.10 Comparison of Raman spectra of our calculated $P2_1/m$ and $Cmcm$ structures of $XeCl_2$ at 4 and 20 GPa with the experimental result of that at 4 GPa [189]. 87

Figure 4.11 Comparison of the measured X-ray diffraction pattern of the Xe-Cl_2 sample [189] with $P2_1/m$ and $Cmcm$ structures at 4 GPa. 88

Figure 4.12 Band structures (top) and partial electronic DOSs (bottom) of the $Cmcm$ and $P2_1/m$ structures of $XeCl_2$ are shown at 15 GPa. The black and red solid lines in band structure plots show results of PBE and GW corrections. 89

Figure 4.13 Absorption and reflectivity of $Cmcm$ and $P2_1/m$ structures of $XeCl_2$ at 15 GPa are shown on the top, middle and bottom, respectively. The black and red solid lines in band structure plots show results of PBE and GW corrections. 90

Figure 4.14 (a) the lowest predicted enthalpy structure, $P4_12_12$, for solid $XeCl_2$ at 60 GPa. (b) and (c) present the sublattices of Xe and Cl, respectively. (d) and (e) show the coordination of Xe and Cl_2. 91

Figure 4.15 The coordination of Cl_2 and Xe for the $P4_32_12$ structure of solid $XeCl_2$ at 60 GPa. 92

Figure 4.16 The coordination of Cl_2 and Xe for the $P2_12_12_1$ structure of solid $XeCl_2$ at 60 GPa. 92

Figure 4.17 Phonon dispersion curves for $P4_12_12$, $P4_32_12$, and $P2_12_12_1$ structures of $XeCl_2$ at 60 GPa. 93

Figure 4.18 Three calculated equations of state of the $P4_32_12$ structure for $XeCl_2$ compound. ... 94

Figure 4.19 The calculated Raman spectra for the $P4_12_12$ and $P2_12_12_1$ structures of $XeCl_2$ at 60 GPa. 95

Figure 4.20 At 60 GPa, band structures (top) and partial electronic DOSs (bottom) of the $P4_12_12$ and $P2_12_12_1$ structures of $XeCl_2$ are shown. The black and red solid lines in band structure plots show results of PBE and GW corrections. 96

Figure 4.21 At 60 GPa, absorption and reflectivity of $P4_12_12$ (left) and $P2_12_12_1$(right) structures of $XeCl_2$. 97

Figure 4.22 Relative enthalpy *vs*. pressure plot of the predicted structures of XeCl relative to the $C2/m$ structure. 98

Figure 4.23 (a) The lowest enthalpy $C2/m$ structures of solid XeCl at 10 GPa. This structure is shown along the *c* axis with (b) shorter and (c) longer cutoff of Xe..Xe atomic bonding distance and (d) is the sublattice of Xe. 99

Figure 4.24 (a) The second lowest enthalpy *Cmca* structures of solid XeCl at 10 GPa. To preserve clarity, deep and light blue colors are used to illustrate the Xe atoms in the two planes. (b) shows the structure along a axis. (c) and (d) illustrate the Xe layers. 100

Figure 4.25 (a) The third lowest enthalpy $P2_1/m$ structures of solid XeCl at 10 GPa. (b), (c) and (d) show sublattices of Xe with different bond cutoffs. (e) shows Cl_2 molecules are located along Xe channels. 101

Figure 4.26 At 10 GPa, the ELF values for the $C2/m$, *Cmca* and $P2_1/m$ structures of XeCl with cross sections of (010), (100) and (010), respectively. The positions of Xe and Cl atoms are also shown for clarity. 103

Figure 4.27 Comparison of Raman spectra of our calculated $C2/m$, *Cmca* and $P2_1/m$ structures of XeCl at 4 GPa with the experimental result of that at 4.2 GPa in Figure 5.10. 104

Figure 4.28 Comparison of the measured X-ray diffraction pattern of the Xe-Cl_2 sample [189] with $C2/m$, *Cmca* and $P2_1/m$ structures of XeCl at 4 GPa. 105

Figure 4.29 Band structures, partial electronic densities of states, absorption and reflectivity of the XeCl $C2/m$ structure at 15 GPa. 106

Figure 4.30 The $Cmc2_1$ structure for solid XeCl at 40 GPa. To preserve clarity, the Xe atoms are shown with deep and light blue colors. Different Cl and Xe bond cutoffs, (a) and (b) shorter and (c) and (d) longer, are shown. 107

Figure 4.31 The *Cmcm* structure for solid XeCl at 60 GPa, shown in two perspectives. 108

Figure 4.32 The ELF values for the (a) $Cmc2_1$ (b) and (c) *Cmcm* structures of XeCl with cross sections of (100). The ELF values were computed for the $Cmc2_1$ and *Cmcm* structures at 40 and 60 GPa, respectively. The positions of Xe (light and dark blue color) and Cl atoms are also shown for clarity. 109

Figure 4.33 The calculated Raman spectra for $Cmc2_1$ and *Cmcm* structures of XeCl at 40 and 60 GPa, respectively. 110

Figure 4.34 Band structures of $Cmc2_1$ and *Cmcm* structures of XeCl shown by black and red lines for PBE and GW corrections at 40 and 60 GPa, respectively. Total and partial DOSs of both structures are shown as well. 111

Figure 4.35 The lowest enthalpy predicted structures for solid $XeCl_4$ at 60 GPa. 113

Figure 5.1 Predicted formation enthalpies of Xe–Br compounds below 60 GPa. 116

Figure 5.2 The formation per atom with respect to elemental Xe and molecular Br_2 for XeBr compounds. 118

Figure 5.3 (a) the lowest predicted enthalpy *Pccn* structure of XeBr at 10 GPa. Br sublattice in two different directions is shown in (b). (c), (d) and (e) show sublattice of Xe with bond cutoff < 3.6 Å and (f) the *Pccn* structure with Xe bond cutoff < 3.75 Å..... 119

Figure 5.4 The second lowest predicted enthalpy $P2_1/c$ structure of XeBr at 10 GPa. 119

Figure 5.5 The calculated equation of state of *Pccn* structure of XeBr compound. 120

Figure 5.6 The ELF values of zigzag chains of Br atoms in the *Pccn* and $P2_1/c$ structures. For clarity, the positions of Xe and Br atoms were shown. 121

Figure 5.7 The *Fmm*2 structure of XeBr at 60 GPa. For clarity sublattice of Xe and Br atoms were shown with deep and light colors..... 122

Figure 5.8 The band structure of the *Fmm*2 structure of XeBr at 60 GPa. 122

Figure 5.9 The *Cmcm* structures for solid XeBr at 60 GPa. 123

Figure 5.10 The ELF values for the *Cmcm* structure of XeBr with cross section of (100). 123

Figure 5.11 The band structures and phonon dispersion of the *Cmcm* structure of XeBr at 60 GPa. 124

Figure 5.12 The relative enthalpies of formation per atom with respect to elemental Xe and molecular Br_2 for $XeBr_2$ compounds. 126

Figure 5.13 The lowest enthalpy *P*1 structure found at 10 GPa for $XeBr_2$ compound..... 126

Figure 5.14 The top view along the [111] direction of the (a) *Pnma* and (b) *Fd*3*m* structures of $XeBr_2$ at 30 and 60 GPa, respectively. 127

Figure 5.15 The *Fd*3*m* structure for $XeBr_2$ compound at 60 GPa. 128

Figure 5.16 The ELF values of Br network in the *Fd*3*m* structure of $XeBr_2$ at 60 GPa..... 128

Figure 5.17 The band structures and phonon dispersion of the *Fd*3*m* structure of $XeBr_2$ at 60 GPa. 129

Figure 5.18 The relative enthalpies of formation per atom with respect to elemental Xe and molecular Br_2 for $XeBr_4$ compounds. 130

Figure 5.19 The group of the lowest predicted enthalpy structures for solid $XeBr_4$ at 60 GPa. 130

Figure 5.20 The convex hull plots of Xe–I systems at 10, 30 and 60 GPa. 132

Figure 5.21 The lowest predicted enthalpy structures for solid XeI at 10 GPa. 133

Figure 5.22 The relative enthalpies of formation per atom with respect to elemental Xe and molecular I_2 for XeI compounds. 134

Figure 5.23 The group of the lowest predicted enthalpy structures for solid XeI at 60 GPa. 134

Figure 5.24 The relative enthalpies of formation per atom with respect to elemental Xe and molecular I_2 for XeI_2 compounds. 136

Figure 5.25 Phonon dispersion curves for the *P*1 structure of XeI_2 found by, (left) PSO and (right) GA at 60 GPa. 136

Figure 5.26 The group of the lowest predicted enthalpy structures for solid XeI_2 at 60 GPa. ... 137

Figure 5.27 The relative enthalpies of formation per atom with respect to elemental Xe and molecular I_2 for XeI_4 compounds. 138

Figure 5.28 The group of the lowest predicted enthalpy structures for solid XeI_4 at 60 GPa. ... 139

Figure A.1 Electronic band structure of the *Cmcm* structure of $XeCl_2$ at 15 GPa using two different pseudopotentials (black and red lines including valence electron configuration of s^2p^6 and $d^{10}s^2p^6$, respectively. 145

Figure A.2 Optical properties of Cmcm structure of $XeCl_2$ at 15 GPa with convergence test of BSE calculations using different number of valence (S) and conducting (V) bands. 146

Figure A.3 Band structures, phonon dispersion, absorption and reflectivity of the $XeCl_2$ $P4_32_12$ structure at 60 GPa. 147

Figure A.4 Phonon dispersions of predicted XeCl structures in Table 4.3..... 148

Figure A.5 Phonon dispersions of predicted $XeCl_4$ structures in Table 4.4. 149

LIST OF ABBREVIATIONS

1D	One-dimensional
2D	Two-dimensional
3D	Three-dimensional
BCS	Bardeen-Cooper-Schrieffer
BLYP	Becke-Lee-Yang-Parr
BO	Bloch orbitals
BJ	Becke-Johnson
BSE	Bethe-Salpeter-equation
BZ	Brillouin zone
DFT	Density functional theory
DFPT	density functional perturbation theory
ELF	Electron localization function
EOS	Equation of state
fcc	Face-centered cubic
GA	Genetic Algorithm
GGA	Generalized gradient approximation
hcp	Hexagonal close pack
HF	Hartree Fock
H-K	Hohenberg-Kohn
HSE	Heyd-Scuseria-Erhzerhof
KS	Kohn and Sham
LAPW	Linear Augmented Plane Wave
LDA	Local density approximation
mBJ	modified Becke-Johnson
MD	Molecular dynamics
NFS	Nuclear forward scattering
NPT	Constant-pressure and constant-temperature
PW	Plane wave

PAW	Projector augmented wave
PBE	Perdew-Burke-Ernzerhof
PSO	Particle Swarm Optimization
QP	Quasi particle
RDF	Radial distribution function
U	Hubbard
vdW	Van der Waals
VASP	Vienna Ab-initio Simulation Package
XANES	X-ray absorption near-edge spectroscopy
XC	Exchange-correlation
ZPE	Zero point energy

CHAPTER 1

Introduction and computational methodology

To uncover the nature and properties of materials, scientists have to employ sophisticated experimental techniques to obtain accurate measurements on their chemical, physical and electronic properties. Although many properties of materials can be determined by experiments, sometimes it is difficult, or even infeasible to characterize systems, under extreme pressure and temperature conditions. To tackle this problem, first-principles or *ab initio* methods has been developed to study complex materials based on laws of quantum mechanics. These methods have been applied to the study of the electronic structure and prediction of the properties of a wide variety of materials. In this thesis, Density Function Theory method (DFT) [1]–[3], the most widely used electronic theory for theoretical calculations was employed. To find the solution to the many body Schrödinger equation without any adjustable parameter. Conceptually, DFT reduces the description of a system with N electrons from the $3N$-dimentional total electron wave function to just the density. Hohenberg and Kohn theorem [1] proved that this mapping is exact. Kohn and Sham [2] also derived a practical scheme to compute the approximate solution of the Schrödinger equation by replacing an artificial non-interacting system, in which all many body (complex) effects are included in the exchange-correlation (XC) functional. The remaining problem, however, is the form of a universal density functional which describes the exchange and correlation of electrons. It is very complicated and not known. To overcome this shortcoming, over the years, a variety of XC functionals have been developed to describe a real electronic system under different conditions. Despite the success of some of the functionals to describe the electronic structure on a wide range of materials, major drawbacks of these functionals still remain. For example, due to the separate treatments of the exchange and coulomb interactions, the functional resulted in the unphysical interaction of an electron with itself was not cancelled exactly and this error needs to be corrected. For this reason, a few properties such as the band gap of insulators, cannot be predicted reliably. Methods to remediate this shortcoming have been proposed. In this thesis, we examined several approaches with an emphasis to the properties of solids under high pressure.

The study of material properties under extreme pressure and temperature conditions is an important subject in geophysics, planetary physics, and applied materials science. It is known that

the physical and chemical properties of almost all condensed systems can be dramatically changed by compression. In this thesis, the electronic structure of two particularly problematic compounds, AlH_3 and EuO were studied and the results are reported in Chapter 2. Above 100 GPa, AlH_3 was predicted to be a metal and a superconductor by using the usual Generalized Gradient Approximation (GGA). Although the metallic character is confirmed by experiment, so far superconductivity has not been observed. This is a very important system as AlH_3 is one of the few solid hydrides in which the structure at very high pressure is known unambiguously. The failure to verify the predicted superconductivity is a critical issue to be resolved, as it directly challenges the computational methods currently used to predict the critical temperature from the Bardeen-Cooper-Schreiffer (BCS) theory of superconductivity. We have examined several functionals to improve the description of the electronic structure of AlH_3 in the pressure range from 90 to 160 GPa. All calculations suggest that AlH_3 is a poor metal at 100 GPa with decreasing metallicity at high pressures. Significantly, it is found that the Fermi surface topology is dependent on the functional used. We also performed perturbative GW calculations to correct for the eigenvalues obtained from the GGA functional. Another system of interest is EuO. EuO has strongly localized 4*f* electrons with complex electron-election interactions. Experimental measurements show this compound is a semiconductor under ambient conditions and transformed to a metal by compression. A small volume change associated with no change in the crystal structure (isostructural phase transition) was found to occur near 35 GPa. This observation has not been explained in a satisfactory manner. We investigate several other methods, such as the local-density-approximation + Hubbard parameter (LDA+U), hybrid functional and modified Becke-Johnson (mBJLDA) to examine the electronic structure of EuO and the phase transitions under pressure. All the methods employed failed to predict isostructural phase transition due to difficulties to describe strongly localized energy states but, LDA+U successfully predicts the pressure-induced semiconductor to metal transition.

The conventional way to characterize the crystal structure of a material is based on diffraction experiments [4]. There are obstacles preventing direct experimental characterization of crystal structures under high pressure. An example, is that even under most favorable conditions it is difficult to define accurately the positions of light elements such as hydrogen or lithium at high pressure and theoretical electronic calculation becomes an indispensable tool to understand the electronic and crystal structure. Nowadays, in principle, it is possible to predict the structure

of any material from first-principle that is only from the information of the chemical composition, *i.e*. the type and number of constituent atoms.

In the past decade, new computational strategies have been developed to predict crystal structures. Here, we examine in detail the performance and reliability of two recently proposed methods, revolutionary algorithm and particle swarm optimization. In spite of the claims that these methods are almost infallible, we found it is not always to be the case. We have found different "global minimum" on a number of systems predicted using the two methods. The result led us to suggest a hybrid approach to assure the most stable structure is found. In Chapter 3, we investigated structures of solid CS_2 at the pressure range from 2 to 120 GPa. We found substantial energy barrier is required to break the molecular C=S bond. At high compression, CS_2 decomposed and segregated into C and S regions. A crystalline structure with the $P2_1/m$ space group was found to be most stable from 60 to 100 GPa. Consistent with experiment, the predicted structure is metallic and superconductive in this pressure range. In Chapter 4, we report a systematic and detailed structural search for the low energy structures in $XeCl_n$ (n=1,2 and 4) below 60 GPa. We have computed the optical absorption spectra from the solution of the Bethe-Salpeter-equation (BSE) based on the GW corrected quasi-particle energies. The results suggest that most XeCl and $XeCl_2$ compounds are semiconductors and thermodynamically unstable with respect to solid Xe and halogens lower than 60 GPa. We have also explored possible stable structures of Xe-Br and Xe-I in Chapter 5. A stable cubic structure of $XeBr_2$ is found at 60 GPa. This structure is metallic and superconductive with a critical temperature of 1.4 K. For XeI_n, the theoretical results suggest that no thermodynamically stable compound can be formed.

A material is simply a collection of atoms composed of electrons and nuclei and their behaviors are governed by the laws of physics. Therefore, any property of a solid, whether electronic, mechanical or optical, can in principle, be calculated by solving the many-body Schrödinger equation. Over the years, very accurate solutions of the Schrödinger equation have been feasible only for the simplest systems such as isolated atoms or simple molecules. As a result, approximate numerical solutions have been developed to study the behaviors of larger systems. First-principles methods are very powerful tools in physics and chemistry since they are based on the laws of quantum mechanics. These methods do not require experimental input beyond the general information on the composition of the system. However, a full quantum mechanical

treatment of a many-body system is still intractable. The many-particle Hamiltonian for a solid system in SI unit can be written as

$$H = -\frac{\hbar^2}{2}\sum_i \frac{\nabla_{\boldsymbol{R}_i}^2}{M_n} - \frac{\hbar^2}{2}\sum_i \frac{\nabla_{\boldsymbol{r}_i}^2}{m_e} + \frac{1}{4\pi\epsilon_0}\sum_{i<j}\frac{e^2 Z_i Z_j}{|\boldsymbol{R}_i - \boldsymbol{R}_j|} - \frac{1}{4\pi\epsilon_0}\sum_{i,j}\frac{e^2 Z_i}{|\boldsymbol{R}_i - \boldsymbol{r}_i|} + \frac{1}{4\pi\epsilon_0}\sum_{i<j}\frac{e^2}{|\boldsymbol{r}_i - \boldsymbol{r}_j|}, \tag{1.1}$$

where M_n and m_e are the masses of the nucleus and electrons, respectively. The first and second term are kinetic energies and the last three terms describe nucleus-nucleus, electron-nucleus and electron-electron Coulomb interactions.

Many approximations have been developed to reduce the burden of solving the many-body problems. For example, the Born-Oppenheimer approximation [5] separates the motion of electrons from the nuclei by assuming that the velocity of the nuclei are much slower compared to that of the electrons. In this way, the positions of nuclei can be regarded as fixed and only contribute as an external potential. This approximation has proven to be sufficiently accurate for a large number of systems. Many first-principles methods such as Hartree-Fock method (HF) [6] and DFT have been developed within the Born-Oppenheimer assumption. The HF approximation is a mean field theory assuming individual electron motion does not depend explicitly on the instantaneous motions of the other electrons. Each electron is assumed to be described by its own spin orbitals. The DFT [1]–[3] assumes that electron density is the fundamental property and in principle, requires no orbital approximation. However, all these approximations have been developed to solve many-body problems. In the following, we described the theory behind the electronic structure calculations employed in this research.

1.1 Electronic structure

1.1.1 Hartree-Fock approximation

Hartree-Fock theory is the first method employed to solve the many-body problem. The starting point is the construction of a total wave function for the system expressed as a product of one-electron wave functions. This approximation assumes that electrons are independent of each other and the total wave function of the system is a superposition of the one-electron wave

functions. To satisfy the Pauli Exclusion Principle, the total HF wave function can be expressed as a Slater determinant [7]

$$\psi_{HF} = \frac{1}{\sqrt{N!}} \begin{vmatrix} \psi_1(\boldsymbol{r}_1) & \psi_2(\boldsymbol{r}_1) & \dots & \psi_N(\boldsymbol{r}_1) \\ \psi_1(\boldsymbol{r}_2) & \psi_2(\boldsymbol{r}_2) & \dots & \psi_N(\boldsymbol{r}_2) \\ \vdots & \vdots & & \vdots \\ \psi_1(\boldsymbol{r}_N) & \psi_2(\boldsymbol{r}_N) & \dots & \psi_N(\boldsymbol{r}_N) \end{vmatrix}, \tag{1.2}$$

the ground state wave function ψ_{HF} is an antisymmetrized product of *N* orthonormal spin orbitals $\psi_i(\boldsymbol{r}_i)$ which is a product of a spatial orbital and spin function. The optimal wave function ψ_{HF} should minimize the total energy

$$E_{HF} = min_{(\psi_{HF} \to N)} E[\psi_{HF}]. \tag{1.3}$$

As a result, the full HF energy of a solid in atomic unit can be written as

$$E_{HF} = \int \psi_i^*(\boldsymbol{r}) \left[-\frac{\nabla^2}{2} + V_{ext}(\boldsymbol{r}) \right] \psi_i(\boldsymbol{r}) d^3r + \frac{1}{2} \sum_{i,j=1} \left(J_{ij} - K_{ij} \right), \tag{1.4}$$

the first and second terms are the kinetic energy and the electron-nucleus attractive (external) potential. The last term, so-called HF potential (V_{HF}), is consisted of Coulomb integrals (J_{ij}) and exchange (K_{ij}) integrals. The two electrons integrals are expressed as

$$J_{ij} = \iint \psi_i^*(\boldsymbol{r}_1) \psi_i(\boldsymbol{r}_1) \frac{1}{r_{12}} \psi_j^*(\boldsymbol{r}_2) \psi_j(\boldsymbol{r}_2) d^3r_1 d^3r_2, \tag{1.5}$$

$$K_{ij} = \iint \psi_i^*(\boldsymbol{r}_1) \psi_j(\boldsymbol{r}_1) \frac{1}{r_{12}} \psi_i(\boldsymbol{r}_2) \psi_j^*(\boldsymbol{r}_2) d^3r_1 d^3r_2, \tag{1.6}$$

J_{ij} is the electrostatic potential arising from the charge distribution of electron 1 and 2. This term includes a 'self-interaction' of the electron ($i = j$) which has no physical meaning and should be removed from the total energy. In the case of HF method, this self-interaction is exactly cancelled by the corresponding $K_{i=j}$ exchange integrals.

Although the HF approximation treats the electron self-interaction correctly, it is a mean field theory and neglects electron correlation effects since the one-electron wave function depends only on the coordinate of a single electron and is independent from the others. To overcome this shortcoming, explicit consideration of electron correlation must be exploited. This includes the construction of many-electron wave functions and this makes the calculation of a solid almost intractable.

1.1.2 Hohenberg-Kohn theorems

DFT is a method that in principle does not need the assumption of a wave function. Historically, the first density functional was developed by Thomas [8] and Fermi [9] to describe the kinetic energy of a free electron gas in 1927. Not until 1964, DFT was formally established by two theorems due to Hohenberg and Kohn [1]

Theorem I For any system of interacting particles in an external potential $V_{ext}(\boldsymbol{r})$, the total energy is determined uniquely, except for a constant, by the ground-state particle density $n_0(\boldsymbol{r})$

Theorem II A universal functional for the energy $E[n]$ in terms of the density $n(\boldsymbol{r})$ can be defined, valid for any external potential $V_{ext}(\boldsymbol{r})$. For any particular $V_{ext}(\boldsymbol{r})$ the exact ground-state energy of the system is the global minimum value of this functional, and the density $n(\boldsymbol{r})$ that minimizes the functional is the exact ground-state density $n_0(\boldsymbol{r})$.

The first Hohenberg-Kohn (H-K) theorem implies that if the density of the system is known, everything about the system can be determined since the density of a system corresponds uniquely to the external potential. To solve the problem, we only need to find the ground state density. The second H-K theorem provides a recipe to construct the ground state energy functional. So far the exact energy functional of an interacting many-body system is not known. In 1965, Kohn and Sham (KS) [2] proposed a practical scheme for DFT calculation as will be described in the next section.

1.1.3 Kohn-Sham equations

The KS approach states that a system of 'non-interacting' particles corresponds to a system of 'interacting' particles yielding the same ground state electron density. This means that instead of solving a system of interacting particles in an external potential, one can reproduce a solution with the assumption of non-interacting particles in an effective potential. In this way, the local electron densities obtained in these two systems are identical. All many-body interactions are defined by an effective potential and independent electrons will only interact through the effective potential.

Following the KS approach, each electron in the interacting electron system is described by a set of single particle Schrödinger equations in SI unit

$$\left(-\frac{\hbar^2}{2m_e}\nabla^2 + V_{eff}(\boldsymbol{r})\right)\varphi_i(\boldsymbol{r}) = \epsilon_i\varphi_i(\boldsymbol{r}). \tag{1.7}$$

Note that φ is the single particle wave function in the interacting system often referred to as the KS orbital. The effective potential is defined as

$$V_{eff}(\boldsymbol{r}) = V_{ext}(\boldsymbol{r}) + \int \frac{n(\boldsymbol{r}')}{|\boldsymbol{r}-\boldsymbol{r}'|} d^3r' + \frac{\delta E_{xc}[n(\boldsymbol{r})]}{\delta n(\boldsymbol{r})}, \tag{1.8}$$

where V_{ext}, the external potential, includes electrons-nuclei interactions. The second term is the electron-density interaction and the exchange-correlation is represented by the last term. The electron density is simply a sum over squares of the KS orbitals

$$n(\boldsymbol{r}) = \sum_i |\varphi_i(\boldsymbol{r})|^2. \tag{1.9}$$

As a result, the ground state total energy of a solid can be written in terms of a functional of the electron density $n(\boldsymbol{r})$ and energy of nuclei

$$E_{total}[n] = E_{electron}[n] + E_{ion}. \tag{1.10}$$

Note that based on Born-Oppenheimer approximation, E_{ion} is only the energy of Coulomb interaction between nuclei and is explicitly determined by the atomic configurations. The complex term is $E_{electron}$ which is

$$E_{electron}[n(\boldsymbol{r})] = T_0[n(\boldsymbol{r})] + \frac{1}{2}\iint \frac{n(\boldsymbol{r})n(\boldsymbol{r}')}{|\boldsymbol{r}-\boldsymbol{r}'|} d^3r d^3r' + \int V_{ext} n(\boldsymbol{r}) d^3r + E_{xc}[n(\boldsymbol{r})], \tag{1.11}$$

$$T_0[n(\boldsymbol{r})] = \sum_i \int d^3r \varphi_i^*(\boldsymbol{r}) \left(-\frac{\hbar^2}{2m_e}\nabla^2\right) \varphi_i(\boldsymbol{r}). \tag{1.12}$$

As seen in Eq.(1.12), kinetic energy functional T_0 consists of the independent motions of electrons. The second term of Eq.(1.11), the Hartree Coulomb energy, is obtained from electron-electron Coulomb interactions and the third term is comprised of the external potential describing the Coulomb interaction between the electrons for a given arrangement of the nuclei. Eventually the last term of Eq.(1.11) is the exchange-correlation energy functional E_{xc}.

The correct ground state total energy can be expressed by $\frac{\partial E_{electron}}{\partial n(\boldsymbol{r})}$ which means minimizing the Eq.(1.11) in terms of the ground state electron density $n(\boldsymbol{r})$. Note that the electron number is conserved in a solid system

$$\int n(\boldsymbol{r}) d^3r = N. \tag{1.13}$$

Unfortunately, the exact form of E_{xc} is unknown. Different methods (functionals) have been developed to approximate this quantity.

1.1.4 Functional forms of exchange correlations

Although the DFT approach simplified the solution of the many-body problem, a shortcoming is that the exact form of the exchange-correlation functional is not known. The easiest approximation assumed a homogeneous electron gas and is known as the local density approximation (LDA) [2]. It assumes the electron density of the system is constant in a small region of space. This earliest approximation treated a general inhomogeneous electronic system as locally homogenous. The exchange-correlation energy per electron is approximated using the electron density of a uniform electron gas

$$E_{xc}^{LDA}[n] = \int d^3r n(\boldsymbol{r})\, \varepsilon_{xc}[n], \tag{1.14}$$

$$\varepsilon_{xc}[n] = \varepsilon_{xc}^{uniform}[n]. \tag{1.15}$$

The numerical values of $\varepsilon_{xc}^{uniform}$ were calculated using quantum Monte Carlo techniques [10] for a uniform electron gas at a variety of electron densities. This approximation was highly successful but failed in situations where the electron density undergoes rapid changes, such as in transition metals and highly correlated systems. For non-uniform charge densities, LDA can significantly deviate from an accurate solution. Subsequently, the LDA approximation can be improved by Generalized Gradient Approximation (GGA) [11]–[14] where the gradient of the charge density is applied. The GGA functional can be written as

$$E_{xc}^{GGA}[n] = \int d^3r n(\boldsymbol{r}) \varepsilon_{xc}^{GGA}[n, \nabla n], \tag{1.16}$$

E_{xc}^{GGA} is expressed in terms of the gradient and higher spatial derivatives of the $n(\mathbf{r})$. Furthermore, E_{xc}^{GGA} is separated into the sum of the exchange E_x and the correlation E_c functionals

$$E_{xc}^{GGA}[n] = \int d^3r \varepsilon_x^{uniform}[n] F_{xc}[n, \nabla n] n(\boldsymbol{r}), \tag{1.17}$$

where $\varepsilon_x^{uniform} = (-3\,\boldsymbol{k}_f/4\pi)$ is defined as the Slater exchange energy density for homogenous electronic system [15] and $\boldsymbol{k}_f = [3\pi^2 n(\boldsymbol{r})]^{1/3}$ is a local Fermi wave vector. An analytic function, $F_{xc}[n, \nabla n]$, known as the enhancement factor, modifies the energy density by including two exchange (F_x) and correlation (E_c) terms. The exchange enhancement factor F_x is a function of an important dimensionless reduced density gradient which is defined as

$$s = \frac{|\nabla n(\boldsymbol{r})|}{2\boldsymbol{k}_f n(\boldsymbol{r})}. \tag{1.18}$$

The correlation term is given by

$$E_c = \int d^3r n(\boldsymbol{r})\{\varepsilon_c[n] + H(r_s, t, \xi)\}. \tag{1.19}$$

Here, $\varepsilon_c[n]$ is the homogeneous electron gas correlation energy and r_s is the Seitz radius. Note that in the correlation term $H(r_s, t, \xi)$, r_s is independent of F_x because the exchange energy scales linearly with uniform density [16]. Therefore, F_x does not change with different r_s values. Another dimensionless gradient term is t defined as

$$t = \frac{|\nabla n(\boldsymbol{r})|}{2g\boldsymbol{k}_s n(\boldsymbol{r})}, \tag{1.20}$$

$$g = \frac{[(1+\xi)^{2/3}+(1-\xi)^{2/3}]}{2}, \tag{1.21}$$

where $\boldsymbol{k}_s$ is a function of $\boldsymbol{k}_f$ and ξ is the degree of spin polarization.

Beyond LDA and GGA, several functionals have been proposed, such as the meta-GGA [17], [18], Becke [11], the Becke-Lee-Yang-Parr (BLYP) [12]. Each approximation was developed to improve results for certain chosen properties. Among this class of functionals, Perdew, Burke and Ernzerhof (PBE)[14] is most successful and commonly used in the calculations.

1.1.5 DFT+U

Most DFT calculations on solids have been performed with either the LDA or GGA functionals. Although these approximations are able to describe the electronic properties of many materials, they are not sufficient for strongly correlated electronic systems with localized 3*d* or 4*f* electrons. Furthermore, LDA and GGA calculations often underestimate the band gaps and magnetic moments. The main reason for the failure is that electrons in *d* and *f* orbitals are localized with strong inter-electron interactions which cannot be treated as homogeneous electron gas and, moreover, the self-interaction term does not get cancelled explicitly. A remedy is an *ad hoc* approximation to overcome this problem. In 1991 V.I.Anisimov, *et al* [19] suggested the LDA+U method. The one electron Hamiltonian is augmented by a Hubbard like term to account for strong local electron correlation. The on-site U parameter describes the effective electron-electron interaction (Coulomb interaction) in a solid state environment. If the U parameter is chosen properly, LDA+U can provide a reasonable description of the electronic structure.

1.1.6 Calculation of the Hubbard U parameter

The U parameter is dependent on the atom and the electron configuration. It is known that with an increasing number of *d* electrons, the spatial expansion of the *d* wave function also changes

[20]. U is rigorously defined as the sum of the energy differences between two excited configurations, d^{n+1}, d^{n-1} and the ground state d^n. The energy cost for this reaction is

$$U = E(n_d + 1) + E(n_d - 1) - 2E(n_d), \tag{1.22}$$

E is the Coulomb energy of *d* orbitals. The strong Coulomb repulsion between *d* electrons can be taken into account by adding a term, $E^U = \frac{1}{2}U\sum_{i\neq j} n_i n_j$, in the Hamiltonian. Here, $n_i n_j$ (*n*=0 or 1) are the occupancies of the *i*th and *j*th localized *d* orbital. The total energy of a system can be written as

$$E^{DFT+U} = E^{DFT} + E^U - E^{dc}. \tag{1.23}$$

Since E^{DFT} already is contained in part of E^U, the energy contribution of these orbitals should be removed in order to not double count their contributions. The subtracted term is called 'double counting' which is equal to the on-site LDA contribution to the total energy. E^{dc} is approximated as the mean-field value of the Hubbard term U. Therefore, the mean value of E^{dc} and neglected orbital polarization effects is simply given by

$$E^{dc}(n_d) = \frac{1}{2}UN_d(N_d - 1) - \frac{1}{2}JN_d(N_d - 1), \tag{1.24}$$

where $N_d = \sum_i n_i$ is the total number of *d* electrons. The on-site exchange parameter J can be determined by fitting the expression (1.24) for the electron-electron interaction to the result of constrained LSDA calculations [20]. Several methods have been proposed to calculate the U value such as the linear response method [21] or most often U is empirically determined by fitting to experimental data [22]. In most cases, this simple approach permits a reasonable description of electronic structures of insulator/semiconductors with localized electrons which is underestimated by standard DFT functionals.

1.1.7 Hybrid functional

A hybrid functional is an approximation to improve the Hartree exchange and to correct for the self-interaction. The methodology is simple involving mixing of DFT exchange-correlation functional with a prescribed amount of non-local HF exchange. This simple approach has been shown to overcome some poor results given by GGA and LDA approximations for localized states [23]. A popular hybrid functional is the PBE0 [24], [25] functional where the exchange-correlation energy is given by

$$E_{xc} = \alpha E_x^{exact} + (1 - \alpha)E_x^{local} + E_c^{local}. \tag{1.25}$$

The value of α in Eq.(1.25) is set to 0.25 (*i.e.* 25% Fock-exchange). To reduce computational cost the exact exchange is only needed for a subset of the orbitals. For example, for the 3*d* electrons in a transition metal, often PBE0 preserves the popular density functional and is defined as

$$E_{xc}^{PBE0}[\rho] = E_{xc}^{PBE}[\rho] + \frac{1}{4}(E_x^{HF}[\psi_{sel}] - E_x^{PBE}[\rho_{sel}]), \tag{1.26}$$

where ψ_{sel} and ρ_{sel} represent the wave function and electron density of the relevant electrons. This approximation has been successfully applied to study a number of solids [26], [27]. However, it has not been well tested on transition metal compounds, in particular the metal oxides. A significant point missing in this discussion but central to this study is that all the previous studies were focused on systems at ambient pressure and the efficiency of hybrid functional methods under extreme conditions has not been critically examined.

1.1.8 Semi-local mBJLDA functional

Another method to improve the standard DFT calculation is to construct a functional that reproduces the exact exchange of the atom. As mentioned in Eq.(1.7), the Kohn-Sham density functional method is to solve the Schrödinger equation with the effective potential ($V_{ext} + V_H + V_{xc,\sigma}$) which is the sum of the external, Hartree and exchange-correlation terms. As we know, the last term is obtained as a functional derivative of the energy E_{xc} with respect to the electron density $\left(V_{xc,\sigma} = \delta E_{xc}/\delta\rho_\sigma\right)$. This multiplicative potential was first suggested by Becke-Johnson (BJ) and is given by

$$v_{x,\sigma}^{BJ}(\boldsymbol{r}) = v_{x,\sigma}^{BR}(\boldsymbol{r}) + \frac{1}{\pi}\sqrt{\frac{5}{6}}\sqrt{\frac{t_\sigma(\boldsymbol{r})}{\rho_\sigma(\boldsymbol{r})}}, \tag{1.27}$$

where $\rho_{N\sigma} = \sum_{i=1}^{N\sigma}\left|\psi_{i,\sigma}\right|^2$ is the electron density.

$$t_\sigma(\boldsymbol{r}) = \frac{1}{2}\sum_{i=1}^{N_\sigma}\nabla\psi_{i,\sigma}^*(\boldsymbol{r}).\nabla\psi_{i,\sigma}(\boldsymbol{r}), \tag{1.28}$$

is the kinetic energy density and

$$v_{x,\sigma}^{BR}(\boldsymbol{r}) = -\frac{1}{b_\sigma(\boldsymbol{r})}\left(1 - e^{-x_\sigma(\boldsymbol{r})} - \frac{1}{2}x_\sigma(\boldsymbol{r})e^{-x_\sigma(r)}\right). \tag{1.29}$$

Becke and Roussel [18] proposed to model the Coulomb potential by the exchange hole. In Eq (1.29) x_σ is determined from a nonlinear equation involving $\rho_\sigma, \nabla\rho_\sigma, \nabla^2\rho_\sigma$ and then b_σ is calculated with $b_\sigma = (x_\sigma^3 e^{-x_\sigma}/(8\pi\rho_\sigma))^{1/3}$ note that there is no exchange energy functional E_x whose functional derivatives $\delta E_x/\delta\rho_\sigma$ satisfies Eq.(1.27) so there is no unique choice of

functional for the evaluation of the exchange energy if the BJ potential is used [28]. A modification of the BJ potential+LDA-correlation (TB-mBJ) was proposed recently by changing the relative weights of the two terms in the BJ potential on the exchange term [29], [30]

$$v_{x,\sigma}^{TB-mBJ}(\boldsymbol{r}) = cv_{x,\sigma}^{BR}(\boldsymbol{r}) + (3c-2)\frac{1}{\pi}\sqrt{\frac{5}{6}}\sqrt{\frac{t_\sigma(\boldsymbol{r})}{\rho_\sigma(\boldsymbol{r})}}. \quad (1.30)$$

In the TB-mBJ method, *c* was chosen to depend linearly on the square root of the average of $|\nabla\rho|/\rho$

$$c = \alpha + \beta\left(\frac{1}{V_{cell}}\int_{cell}\frac{|\nabla\rho(\boldsymbol{r}\prime)|}{\rho(\boldsymbol{r}\prime)}d^3r'\right)^{1/2}, \quad (1.31)$$

where α and β are free parameters and V_{cell} is the unit cell volume. Based on a series of calculations the values of α and β were determined to be -0.012 (dimensionless) and 1.023 $bohr^{1/2}$, respectively. For *c*=1 the original BJ potential is recovered. In general, the band gap increases monotonically with respect to *c* using Eq.(1.31). A larger value for *c* leads to better agreement with experiment for small band gap semiconductors. However, for larger band gap the optimized *c* value should also be larger. Thus, the goal is to find an optimal value for *c* that can be applied to different solids. Several groups have used this potential for the calculation of electronic properties and the results show general improvement on the predicted band gap for a variety of materials. For some systems, the results of mBJLDA is similar to the very expensive GW calculations. In the WIEN2K code [31] used in this study, the kinetic energy density t_σ is calculated with Eq.(1.32) instead of Eq.(1.28) and correlation effects are implemented by adding LDA the correlation potential to $v_{x,\sigma}^{MBJ}(MBJLDA)$ [32]

$$t_\sigma(\boldsymbol{r}) = \sum_{i=1}^{N_\sigma}\varepsilon_{i,\sigma}\left|\psi_{i,\sigma}(\boldsymbol{r})\right|^2 - v_{eff,\sigma}^{KS}(\boldsymbol{r})\rho_\sigma(\boldsymbol{r}) + \frac{1}{4}\nabla^2\rho_\sigma(\boldsymbol{r}). \quad (1.32)$$

1.1.9 Periodic boundary conditions

The total number of particles in a solid, including nuclei and electrons, is on the scale of Avogadro's number (6.022 x 10^{23}). Numerical solution of the KS equations are usually found by expanding the one-electron orbitals in a basis set. For example, since the one-electron wave function of a metal is expected to extend throughout the entire system, the basis set required to expand the KS orbitals is infinite. Fortunately, an ideal crystal is defined by repeated unit cells and each consists of a finite number of electrons and nuclei. The existence of periodic unit cells leads to the periodic boundary conditions (PBC) and the use of the Bloch theorem. The starting point is

that the potential is periodic and the solution of the single particle Schrödinger equation in the presence of this potential taking the form of Bloch wave functions

$$\psi_n(\boldsymbol{k},\boldsymbol{r}) = e^{ik.r}u_n(\boldsymbol{k},\boldsymbol{r}). \tag{1.33}$$

Since $u_n(\boldsymbol{k},\boldsymbol{r}) = u_n(\boldsymbol{k},\boldsymbol{r}+\boldsymbol{R})$ is a periodic function for any lattice vector $\boldsymbol{R}$, equation above can be rewritten as

$$\psi_n(\boldsymbol{k},\boldsymbol{r}+\boldsymbol{R}) = e^{ik.\boldsymbol{R}}\psi_n(\boldsymbol{k},\boldsymbol{r}). \tag{1.34}$$

Here *n* represents the band, *k* is the wave vector of the electron in the first BZ. Substituting $\psi_j(\boldsymbol{k},\boldsymbol{r}+\boldsymbol{R})$ into the KS equation, a new set of eigen-equations are found for a given $\boldsymbol{k}$. The Bloch wave functions simplify the calculation of a large system with ~ 10^{23} electrons into a single unit cell with a finite number of electrons. The complete solution is given by simply multiplying a wave vector $\boldsymbol{k}$ to the phase factor of the solutions in a single reciprocal unit cell. Solving the KS equations for infinite number of *k* points, however, does not make the solution simpler. It should be noted that electronic wave functions at *k* points close to each other have similar results. Therefore, only a finite number of *k* points in a small region of the reciprocal lattice are required to determine the total energy of a solid.

1.1.10 Plane-wave basis sets

To solve the KS equation for a periodic system, the functional form of KS orbitals should be represented by well-defined basis sets. The plane wave (PW) basis set with simple mathematical functions is commonly used in periodic solids. The convergence of the basis set is easily adjustable, essentially through a single parameter, *i.e.*, the kinetic energy cutoff (E_{cut}). The KS orbital $\psi_n(\boldsymbol{k},\boldsymbol{r})$, can be expanded using the PW basis set as

$$\psi_n(\boldsymbol{k},\boldsymbol{r}) = e^{ik.r}u_n(\boldsymbol{k},\boldsymbol{r}) = \frac{1}{\sqrt{V}}\sum_G c_{i,\boldsymbol{k}+\boldsymbol{G}}.\, e^{i\boldsymbol{G}.\boldsymbol{r}}.\, e^{i\boldsymbol{k}.\boldsymbol{r}}, \tag{1.35}$$

where *V* is the volume of the unit cell and *G* is the reciprocal lattice vector. In principle, an infinite basis set of *G* should be used to expand the KS orbital $u_n(\boldsymbol{k},\boldsymbol{r})$. In practice, it is possible to truncate the infinite basis set to include only PW's that have kinetic energies less than a defined cutoff energy

$$\frac{1}{2}|\boldsymbol{k}+\boldsymbol{G}|^2 < E_{cut}. \tag{1.36}$$

Clearly, the truncation of the PW basis set will cause an error in the calculated total energy. However, to verify the accuracy of the computed total energy, a given tolerance should converge by gradually increasing the kinetic energy cutoff.

1.1.11 Pseudopotential approximations

One of the main problems with the use of plane waves as a basis set is the difficulty in describing the core wave functions. Since the Coulomb potential is proportional to (~ 1/$\boldsymbol{r}$), it is very steep in the nuclear core region. Thus, it results in rapid oscillations of orbital wave functions in the core region which requires a large number of PW components. For example, all orbital wave functions of aluminum are shown in Figure 1.1a. The core wave functions (1*s*, 2*s* and 2*p*) are sharply peaked near the nucleus. Valence wave functions (3*s* and 3*p*) are peaked far away from the nucleus but the oscillatory nature of the wave functions near the nucleus will require a large number of PW components to describe them properly.

To resolve this problem, a potential to mimic the effect of the core to the valence electrons, known as a 'pseudopotential', can be employed [33]. Since the core region of the atom has little influence to the electronic structure, the core electrons and ionic potential are removed and replaced by a smooth part, leading to a more effective PW expansion. In this approximation, only the valence electrons are explicitly considered. All-electron and pseudo wave functions of aluminum valence electrons are shown in Figure 1.1b. As can be seen, the constructed pseudo wave function is generally identical to the all-electron wave function in the valence region $\boldsymbol{r} > \boldsymbol{r}_c$ and for the core region is nodeless. The proper cutoff radius should avoid overlapping of core regions with neighbor atoms.

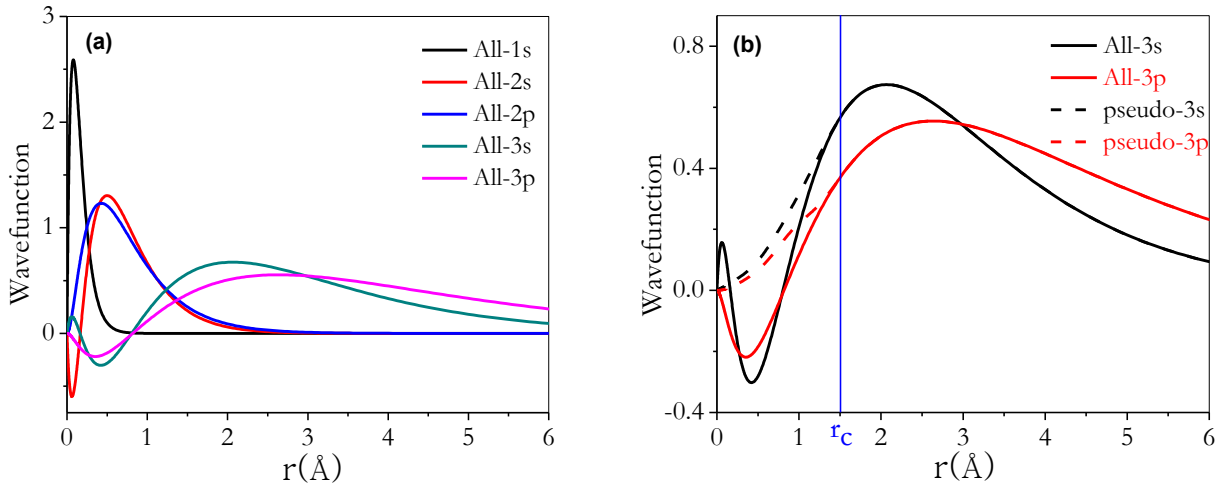

Figure 1.1 (a) All wave functions and (b) comparison of all and pseudo wave functions of valence electrons of aluminum.

1.1.12 Projected augmented wave potentials

The projector augmented-wave (PAW) method developed by Blöchl [34] is an extension to the pseudopotential method. In principle, PAW is an all-electron potential that accurately and efficiently calculate the electronic structure of materials. A PAW potential possesses numerical advantages of pseudopotential by reconstructing correct nodal behavior of the valence electrons in the core region [35]. The general scheme of PAW is the composition of the three wave functions as illustrated below (Figure 1.2).

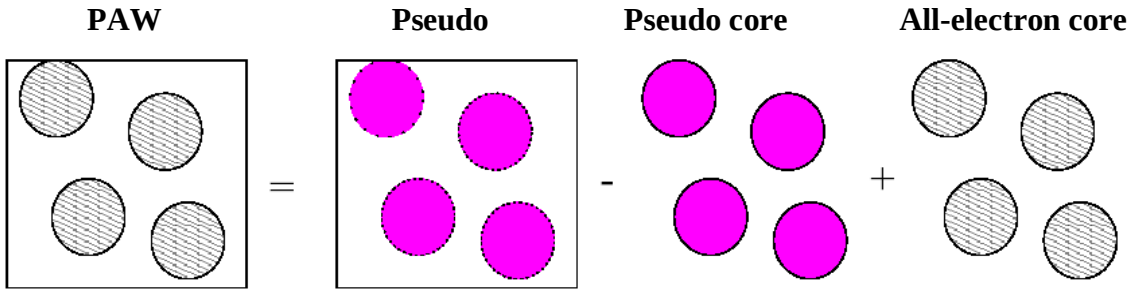

Figure 1.2 A depiction of reconstructed PAW wave function that contains contribution of the all-electron (inside core region) and pseudo (outsite of core region) wave function.

Note that when the all-electron partial waves $\sum_a \psi_n^a(\boldsymbol{r})$ are added to the total wave function, the corresponding pseudo partial waves $\sum_a \tilde{\psi}_n^a(\boldsymbol{r})$ must be subtracted. Therefore, the total wave function is a combination of the pseudo wave function outside the core region and the

all-electron wave function inside the core region. The all-electron single particle KS wave function can be written as

$$\psi_n(\boldsymbol{r}) = \tilde{\psi}_n(\boldsymbol{r}) - \sum_a \tilde{\psi}_n^a(\boldsymbol{r}) + \sum_a \psi_n^a(\boldsymbol{r}), \tag{1.37}$$

the first term in Eq. (1.37) is a pseudo wave function that is smooth everywhere. The second term is the smooth part within the spheres *a*, and the last term, a steep function defined only within each augmentation sphere. In this thesis, the PAW potentials were used with the "Vienna Ab-initio Simulation Package" (VASP) [36], [37].

1.1.13 Full potential linear augmented plane wave

An alternative strategy to describe the core wave functions is the use of Linear Augmented Plane Waves (LAPW's). This basis set is extremely efficient as modeling the properties related to core electrons such as the hyperfine fields or core level excitations. In the region far from the nuclei, the electrons which are more or less 'free' to move are described by plane waves. Close to the nuclei, the electrons are more accurately described by their atomic functions. A sphere with muffin tin radius ($\boldsymbol{R}_{mt}$) is defined to divide the valence electrons from the core electrons. Such an atomic sphere is called a muffin tin sphere and the remaining space outside the spheres is the interstitial region. Any eigenfunction $\psi_{\boldsymbol{k}}^n$ of a periodic Hamiltonian can be express exactly by a basis set with a finite set of coefficients $c_K^{n,\boldsymbol{k}}$. Therefore the wave function of band index *n* at $\boldsymbol{k}$ point is defined as $\psi_k^n(\boldsymbol{r}) = \sum_G c_G^{n,k} \phi_G^k(\boldsymbol{r})$. Note that for eigenstates with another $\boldsymbol{k}$, a new basis set using that other $\boldsymbol{k}$ has to be used. As mentioned above, it is infeasible to work with an infinite basis set, hence in practice, the plane wave expansion is limited to all $\boldsymbol{G}$ with $\boldsymbol{G} \leq \boldsymbol{G}_{\max}$ .In the BZ, a sphere with radius $\boldsymbol{G}_{max}$ is centered at the origin of reciprocal space. LAPW used in the expansion of ψ_k^n is defined as

$$\phi_G^k(\boldsymbol{r}) = \begin{cases} \frac{1}{\sqrt{V}} e^{i(\boldsymbol{k}+\boldsymbol{G}).\boldsymbol{r}} & \boldsymbol{r} > \boldsymbol{R}_{mt}\,, \\ \sum_{l,m} \left(A_{lm}^{\boldsymbol{k}+\boldsymbol{G}} u_l(\boldsymbol{r}', E_0) + B_{lm}^{\boldsymbol{k}+\boldsymbol{G}} \dot{u_l}(\boldsymbol{r}', E_0) \right) Y_m^l(\boldsymbol{r}') & \boldsymbol{r} < \boldsymbol{R}_{mt}\,. \end{cases} \tag{1.38}$$

The symbols $\boldsymbol{k}$, $\boldsymbol{G}$, *V* and $\boldsymbol{r}$ were defined in Eq.(1.35). The position inside the spheres is given with respect to the center of each sphere, $\boldsymbol{r}'$. The $A_{lm}^{\boldsymbol{k}+\boldsymbol{G}}$ and $B_{lm}^{\boldsymbol{k}+\boldsymbol{G}}$ are uniquely determined by expansion of the plane waves in spherical harmonics and must be continuous at the sphere boundary. The

muffin tin sphere u_l and its derivative ($u_l^{\cdot}$) are only parts of a basis function and are used to find how the actual eigenfunction looks like in that region of the crystal. It has to be constructed at the unknown eigenenergy E. The Y_m^l are spherical harmonics.

Up to this point we have defined LAPW as a basis set. To accurately describe the non-uniform potential in the interstitial region, a full-potential treatment is essential. In this scheme, the potential between the muffin tin spheres is expanded into plane waves and calculated self-consistently from the interstitial charge density [38]. Since the method includes non-spherical components, the choice of sphere radii is not very critical. The optimum choice for different radii depends on the potential or charge density, maximum between two adjacent atoms.

$$V(\boldsymbol{r}) = \begin{cases} \sum_{LM} V_{LM}(\boldsymbol{r}) Y_{LM}(\boldsymbol{r}) & \boldsymbol{r} < \boldsymbol{R}_{mt}\,, \\ \sum_{K} V_K e^{i\vec{\boldsymbol{K}}.\vec{\boldsymbol{r}}} & \boldsymbol{r} > \boldsymbol{R}_{mt}\,. \end{cases} \tag{1.39}$$

This is the general scheme of full potential calculation. In order to have a small number of *LM* in the lattice harmonics expansion, a local coordinate system is used for each atomic sphere according to the point group symmetry of the corresponding atom [38]. In this thesis, all FP-LAPW calculations were performed with the WIEN2K package [31].

1.1.14 Self-consistent solution

The ingredients needed to solve the KS equations have now been described. The ground-state electron density and ground-state total energy can be solved self-consistently using the pseudopotential, PAW and LAPW method [39], [40]. The general procedure is illustrated in the flow chart in Figure 1.3.

A self-consistent calculation starts with an initial guess of electron density ***n(r)*** that can be simply constructed from superposition of the electron densities of non-interacting atoms in the system. From this initial electron density, a set of KS equations including kinetic energy and V_{eff} can be constructed. The KS equations are then solved at each *k* point employing wave functions described by a finite set of plane waves and truncated at the kinetic energy cutoff E_{cut}. A new electron density and potential are then constructed. Convergence is achieved when variations of the charge density and potential are smaller than a pre-set tolerance. Otherwise, initial density will

be replaced by a new one and this procedure will be repeated. The following work flow illustrates the basic steps in the Kohn-Sham self-consistency solution.

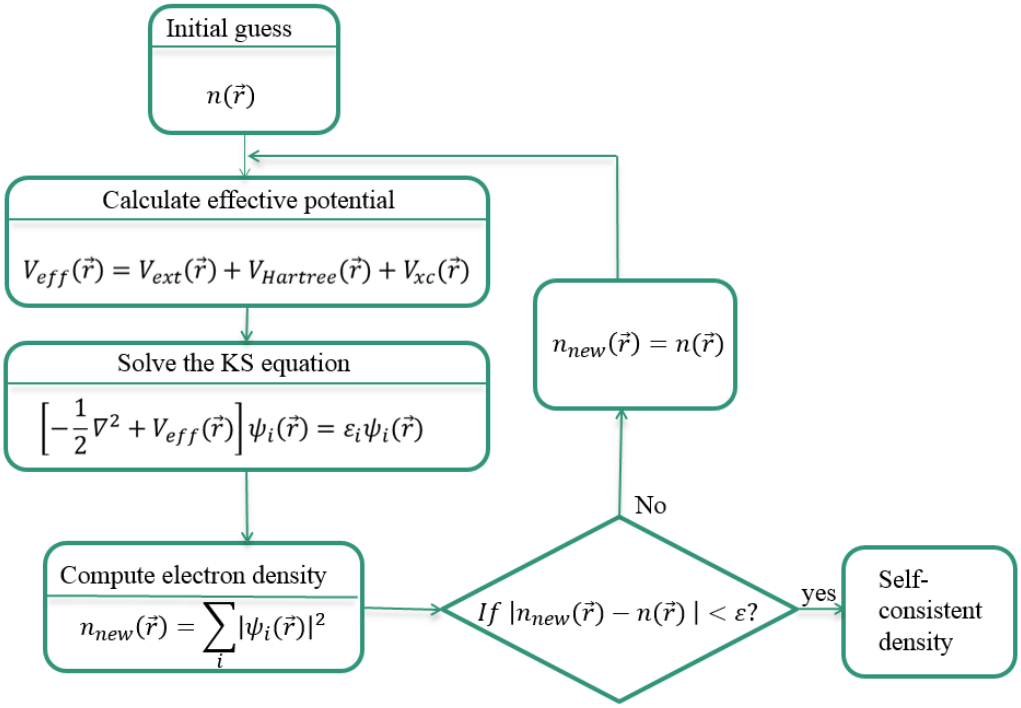

Figure 1.3 The workflow chart describing the KS self-consistent calculation.

1.1.15 The GW approximation

For a system of interacting electrons, due to the deficiency of the exchange correlation functional, DFT often fails to predict accurate band gaps and electronic excitation energies [41]. In 1965, Lars Hedin [42] suggested a method based on the GW approximation to compute the self-energy using perturbative treatment on the XC potential of the KS equation. The quasi particle (QP) energies computed with the many body perturbation theory employed the "GW" approximation, $\sum = iGW$, [43], [44] where G is the electron Green's function and W = ϵ^{-1} ν, the screened Coulomb interaction can be written as a product of the Coulomb kernel (ν) with the inverse dielectric matrix ϵ^{-1}.

Since the perturbed potential screens the interacting electrons, GW correctly describes the required energies to add/remove an electron from a system. The QP equations for a periodic crystal can be written as

$$\left(T + V_{ext}(\boldsymbol{r}) + V_H(\boldsymbol{r})\right)\psi_{n\boldsymbol{k}}(\boldsymbol{r}) + \int \sum(\boldsymbol{r}, \boldsymbol{r}', E_{n\boldsymbol{k}})\psi_{n\boldsymbol{k}}(\boldsymbol{r}')d^3r' = E_{nk}\psi_{n\boldsymbol{k}}(\boldsymbol{r}), \quad (1.40)$$

where T is the kinetic energy operator, $V_{ext}(\boldsymbol{r})$ the electrons-nuclei potential, $V_H(\boldsymbol{r})$ the Hartree potential, and the self-energy operator Σ includes the many-body effects due to exchange and correlation. The quasi-particle (QP) energies are complex quantities describing the positions (ReE_{nk}) and widths (ImE_{nk}) of the QP peaks.

Several steps are required to systematically improve the QP energies. The first step called G0W0, evaluates only the self-energy of the system while the wave functions of KS calculation are not updated. The dielectric function (ϵ) which is needed for the evaluation of the screened Coulomb interaction (W), is calculated using the DFT eigenvalues. In the second step, GW0, often leads to the better results. It is obtained by iterating only the G (partial self-consistency) term with the wave functions of KS fixed to the initial DFT calculations. Finally, in the self-consistent SCGW scheme, GW calculations were updated self-consistently with the eigenvalues in both G and W [45] being updated at each iteration.

If the QP wave functions are not updated (GW0 step), this corresponds to the neglect of non-diagonal matrix elements of the self-energy. The quasi particle energies can be written as [46]–[48]

$$E_{n\boldsymbol{k}} = Re[\langle\psi_{n\boldsymbol{k}}|T + V_{ext}(\boldsymbol{r}) + V_H(\boldsymbol{r}) + \sum(E_{n\boldsymbol{k}})|\psi_{n\boldsymbol{k}}\rangle]. \quad (1.41)$$

The eigenvalues of the QP excitation energy can be solved by iteration

$$\begin{aligned} E_{n\boldsymbol{k}}^{N+1} &= Re\left[\langle\psi_{n\boldsymbol{k}}\middle|T + V_{ext}(\boldsymbol{r}) + V_H(\boldsymbol{r}) + \sum\left(E_{n\boldsymbol{k}}^{N+1}\right)\middle|\psi_{n\boldsymbol{k}}\rangle\right] \quad (1.42)\\ &= Re\left[\langle\psi_{n\boldsymbol{k}}\middle|T + V_{ext}(\boldsymbol{r}) + V_H(\boldsymbol{r}) + \sum\left(E_{n\boldsymbol{k}}^{N}\right)\middle|\psi_{n\boldsymbol{k}}\rangle\right] + \\ &\quad \left(E_{n\boldsymbol{k}}^{N+1} - E_{n\boldsymbol{k}}^{N}\right)Re\left[\langle\psi_{n\boldsymbol{k}}|\left|\frac{\partial\sum(w)}{\partial w}\right|_{w=E_{n\boldsymbol{k}}^{N}}|\psi_{n\boldsymbol{k}}\rangle\right]. \end{aligned}$$

The N+1th iteration is related to the N^{th} iteration through the linearized equation and Z is the normalization factor. The QP energies can then be approximated as

$$E_{n\boldsymbol{k}}^{N+1} = E_{n\boldsymbol{k}}^{N} + Z_{n\boldsymbol{k}}^{N} Re\left[\langle\psi_{n\boldsymbol{k}}|T + V_{ext}(\boldsymbol{r}) + V_H(\boldsymbol{r}) + \sum(E_{n\boldsymbol{k}}^{N})|\psi_{n\boldsymbol{k}}\rangle - E_{n\boldsymbol{k}}^{N}\right]. \quad (1.43)$$

In summary, GW approximation can be used with wave functions generated from a variety of XC functionals such as LDA, HSE03, PBE0, and HF [46]. However, since it is a perturbative theory, the more accurate the initial wave function, the better the results.

1.1.16 Wannier function

The crystalline solids consist of spatially repeated unit cells and led to periodic boundary conditions in which the crystal wave functions can be expressed in terms of the Bloch orbitals (BOs) ($\psi_{n\boldsymbol{k}}$). The BOs are labelled with $\boldsymbol{k}$ and the band index n in reciprocal space. For a periodic system the translation operator T_R and Hamiltonian H commutes. So, the composition operators HT_R and T_RH acting on Bloch orbitals both give the same eigenstates.

$$[H, T_R] = 0 \qquad \Longrightarrow \quad \psi_{n\boldsymbol{k}}(\boldsymbol{r}) = u_{n\boldsymbol{k}}(\boldsymbol{r}) e^{i\boldsymbol{k}.\boldsymbol{r}}\,, \quad (1.44)$$

$u_{n\boldsymbol{k}}(\boldsymbol{r})$ has the same periodicity as the electric potential and $\boldsymbol{r}$ is the position in real space. $e^{i\boldsymbol{k}.\boldsymbol{r}}$ is called the envelope function [49] and constructs a different wave function for every $\boldsymbol{k}$. The construction of a wave function by the superposition of two or even more Bloch functions in $\boldsymbol{k}$ space is now feasible. A set of Wannier functions (WF's) in real space can be written as

$$w_0(\boldsymbol{r}) = \frac{V}{(2\pi)^3}\int_{BZ} \psi_{nk}(\boldsymbol{r}) d^3k, \quad (1.45)$$

where V is the volume of the real space primitive cell and integral is carried over the BZ. More generally, by inserting a phase factor $e^{-i\boldsymbol{k}.\boldsymbol{R}}$ into the integrand of Eq.(1.45), more WF's can be constructed.

$$|w_{n\boldsymbol{R}}> = \frac{V}{(2\pi)^3}\int_{BZ} |\psi_{nk}> e^{-i\boldsymbol{k}.\boldsymbol{R}} d^3k, \quad (1.46)$$

$|w_{n\boldsymbol{R}}>$ is in Drirac bra-ket notation for every value of n at real space lattice vector $\boldsymbol{R}$. Since the Bloch functions are normalized to one BZ and form an orthogonal set, WF's should also form an orthogonal set in real space. In practice, two WFs $|w_{n\boldsymbol{R}}>$ and $|w_{n\boldsymbol{R}'}>$ transform into each other under translation by the lattice vector $\boldsymbol{R}$-$\boldsymbol{R}$'. The inverse transform of Eq.(1.46) leads to the Bloch functions. Therefore, any set of Bloch functions can be built up by linearly superposing the WFs, if the appropriate $e^{-i\boldsymbol{k}.\boldsymbol{R}}$ are used.

Since the transformation of $|w_{n\boldsymbol{R}}>$ and $|\psi_{n\boldsymbol{k}}>$ constitute a unitary transformation between Bloch and Wannier states, both sets of states lead to same physical properties. Even

though WFs are not necessarily eigenstates of the Hamiltonian, both provide a valid and equal description of the band substance or charge density as the summation on the squares of $|w_{n\boldsymbol{R}}>$ or $|\psi_{n\boldsymbol{k}}>$.

WF's are non-unique and have an indeterminacy regarding the overall phase and the choice of gauge [49]. Therefore, Bloch functions can be defined without changing the physical description of the system

$$|\tilde{\psi}_{n\boldsymbol{k}}>= e^{i\varphi_n(\boldsymbol{k})}|\psi_{n\boldsymbol{k}}>, \tag{1.47}$$

or

$$\left|\tilde{u}_{n\boldsymbol{k}}>= e^{i\varphi_n(\boldsymbol{k})}\right|u_{n\boldsymbol{k}}>, \tag{1.48}$$

$\varphi(\boldsymbol{r})$ in Eqs.(1.47) and (1.48) is a real function that has the same periodicity as the Hamiltonian. However, the choice of a convenient gauge is important in the construction of maximally localized WF. Ref's [50], [51] present a method to show it is possible to interpolate WF in a dense *k* mesh to calculate band structure plots. Wannier interpolation is particularly useful to fine sampling of the BZ required to converge the parameter of interest. A schematic illustration of the Wannier interpolation procedure is shown in Figure 1.4. In the left panel, from first-principles calculation in reciprocal space (left panel), f($\boldsymbol{q}$) parameters are obtained for the Bloch eigenstates in coarse *q* points. Then, for selected bands the eigenstates and f($\boldsymbol{q}$) are transformed into WFs and F(**R**) in real space (middle panel). Note that Wannier-transformed F(**R**) should be strongly localized in the equivalent supercell. The f($\boldsymbol{q}$) parameters can be interpolated onto an arbitrary *k* point (e.g., *k* points along high symmetry paths) in reciprocal space by carrying out an inverse transformation (right panel). This procedure is mostly used in accurate Fermi surface energy and band structure calculations.

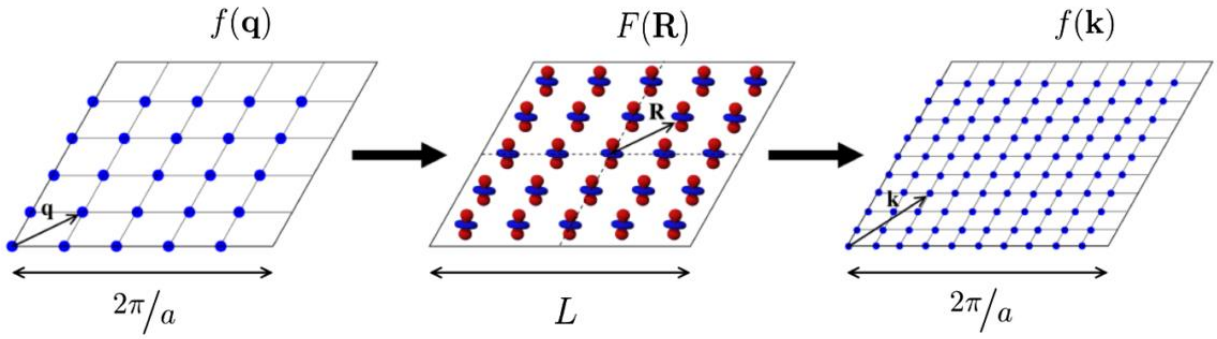

Figure 1.4 Schematic overview of the Wannier interpolation procedure from Ref [48]. The left panel shows a coarse q mesh in BZ, where the f(**q**) is explicitly calculated using first-principle methods. The F(**R**) is calculated in real space (middle panel) and the right panel shows f(k) obtained from interpolation of k points in the BZ.

In this thesis, accurate band structures of $XeCl_n$ were constructed from the interpolation of the GW corrected eigenvalues at selected *k* points using the wannier90 code developed by Ref [49], [52].

1.1.17 Bethe-Salpeter equations

Many-Body Perturbation theory has been successfully applied to describe one-particle and two-particle excitations. Within a similar theoretical framework of the GW approximation, the Bethe-Salpeter Equation (BSE) [53] takes into account electron-hole interactions in the calculation of the optical spectra. The first absorption spectrum using the BSE has been calculated by Hanke and Sham [54]. However, *ab initio* BSE approaches have only been used to compute the dielectric function of a large variety of materials, including semiconductors/insulators [55], [56].

Three steps are needed to compute an optical spectrum (Figure 1.5). In the first step, eigenvalues and KS orbitals are determined from DFT calculations. The second step, QP eigenvalues of energies are obtained from GW calculations. In the last step, electron-hole interactions are included, and solving the BSE provides an accurate solution of the absorption spectrum [57], [58].

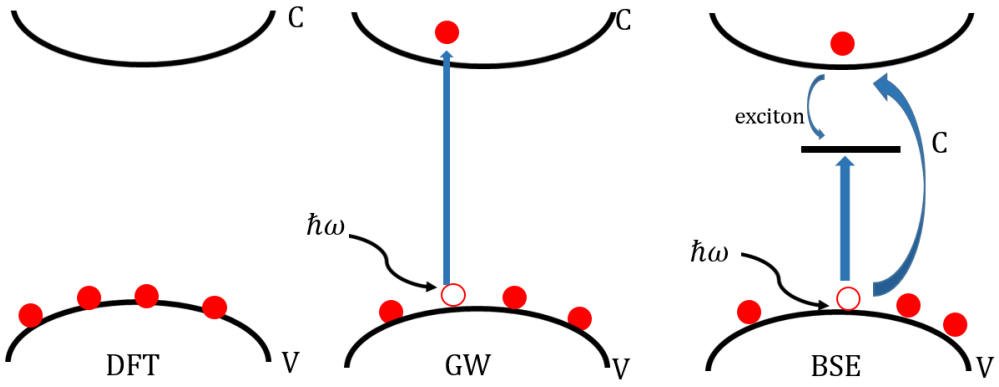

Figure 1.5 The left panel shows ground state energy, the middle panel is QP energies using GW correction and the last panel shows exciton energy obtained from BSE.

The excited states relevant to the optical processes involving the simultaneous creation of QP coupled electron-hole is [59]

$$|S>=\sum_v^e \sum_c^h A_{vc}^S a_v^\dagger b_c^\dagger |0>, \tag{1.49}$$

$|0>$ is the ground state of the many-electron system, $a_v^\dagger$ and $b_c^\dagger$ creates quasi-electrons and holes, respectively. The coupling coefficient A_{vc}^S, is determined for each k point. The effective two-particle Hamiltonian associated with the BSE can be written as

$$\left(\varepsilon_c^{QP} - \varepsilon_v^{QP}\right)A_{vc}^S + \sum_{v'c'} < vc|K^{eh}|v'c' > A_{v'c'}^S = \Omega^S A_{vc}^S. \tag{1.50}$$

The Hamiltonian in Eq.(1.50) is composed by the construction of a large matrix including all the valence and a sufficient number of conduction bands at different k points. The single particle valence (ε_c^{QP}) and conduction (ε_v^{QP}) band state energies are the GW QP energies and Ω^S is the excitation energy. The first term in Eq.(1.50) is the diagonal part containing the QP energies. The second term, K^{eh}, includes the electron-hole interaction kernel. For quasi-particle wave functions ψ_v and ψ_c the second term of Eq.(1.50) can be written as

$$< vc|K^{eh}|v'c' >= \int d^3r d^3r' \psi_c^*(\boldsymbol{r})\psi_v(\boldsymbol{r})v(\boldsymbol{r},\boldsymbol{r}')\,\psi_{c'}(\boldsymbol{r}')\psi_{v'}^*(\boldsymbol{r}') -$$
$$\int d^3r d^3r' \psi_c^*(\boldsymbol{r})\psi_{c'}(\boldsymbol{r})W(\boldsymbol{r},\boldsymbol{r}')\psi_v(\boldsymbol{r}')\psi_{v'}^*(\boldsymbol{r}'), \tag{1.51}$$

the first term contains the Coulomb kernel v which represents repulsive electron-hole exchange and the second term, W is the attractive screened electron-hole interaction for the single-particle. The dielectric function is obtained in terms of the eigenvectors and eigenvalues. In this thesis we used the G0W0-BSE method to obtain optical spectra of $XeCl_n$ structures at different pressures. Details of the implementation can be found in Refs [60], [61].

1.1.18 Electronic localization function

In quantum chemistry, the localized electrons help to determine covalent bond and lone pairs. In 1975, Bader *et al.* [62] realized that electron localization is related to same-spin pair probability and its associated Fermi hole function, which satisfies the Pauli exchange repulsion principle. Indeed, the probability of finding an electron close to a same-spin reference electron indicate the mapping of electron pair in multi-electrons systems. Becke and Edgecombe in 1990 introduced a method [63] to calculate electron localization function (ELF). The assumption is that when the probability of finding the same spin electron near the reference point is small, the reference electron is highly localized. Hence, electron localization is associated with the smallness of the following expression

$$D_\sigma = \tau_\sigma - \frac{1}{4}\frac{(\nabla\rho_\sigma)^2}{\rho_\sigma}, \tag{1.52}$$

where τ_σ is kinetic energy density with σ-spin and ρ_σ is electron density. The ELF is defined as follows

$$\mathrm{ELF} = \frac{1}{[1+\left(D_\sigma/D_\sigma^0\right)^2]}, \tag{1.53}$$

here, D_σ^0 corresponds to a uniform electron gas with spin density equal to the local value of ρ_σ. Note that ELF value is dimensionless and the possible values are between 0 and 1. An ELF value of 1 indicates perfect localization and an ELF value of 0.5 indicates free electron gas behavior. Therefore, ELF provides a convenient scheme for the classification of chemical bonding.

1.1.19 Structural stability of solids

One of the major conditions to confirm the existence of a stable phase is that when the structure is dynamically stable. Indeed, structural stability of a crystal structure is verified when its phonon band structure does not possess imaginary frequency. To obtain phonon band structure, the vibrational frequencies which are the eigenvalues of the dynamical matrix, $\widetilde{D}_{i,j}(q)$, should be calculated.

$$\widetilde{D}_{i,j}(q) = \frac{1}{\sqrt{M_i M_j}}\sum_{R_L} C_{i,j}(\boldsymbol{R}_L, \boldsymbol{R}_{L'}).\, e^{-i\boldsymbol{q}.\boldsymbol{R}_L}, \tag{1.54}$$

where M is the mass of atom with index i and j, $\boldsymbol{R}_L$ and $\boldsymbol{R}_{L'}$ are displacement of the atomic coordinates on the equilibrium positions, and $C_{i,j}$ coefficient is the inter-atomic force constant. Phonon frequencies can be obtained as the square root of the eigenvalues of the dynamical matrix.

Force constants can be computed from the second derivatives of the total potential energy with respect to atomic displacements. There are two strategies to obtain this quantity. First method is the supercell approach [64] which is a direct method to obtain phonon dispersion curves. The force constants are determined from the Hellmann-Feynman forces [65], [66] directly induced by the displacement of all atoms in the supercell. In this method, arbitrary $\boldsymbol{q}$ wave vectors in the first BZ are calculated through interpolation of the force constants. In the second method, vibrational frequencies are obtained within the framework of density functional perturbation theory (DFPT) [67], [68], also known as the linear response method. The main idea in DFPT, is to show that the first derivatives can usually be calculated directly through the Hellmann-Feynman theorem, which states that a linear order variation of the electronic charge density is calculated using the value of the first derivative of the Hamiltonian from unperturbed wave functions. The calculation of the second derivatives is more complicated. It includes the linear response of the ground state electronic charge density to the perturbation. An advantage of the second method is that the frequencies at any arbitrary $\boldsymbol{q}$ wave vector can be computed, contrary to the supercell.

1.2 Structural prediction

A main part of the thesis research is to predict the structure of materials at high pressure. Structure prediction is a global optimization problem. Many geometry search methods such as metadynamics [69],[70], minima hopping [71], simulated annealing [72], [73], particle swarm optimization [74], random sampling method [75] and evolutionary algorithms [76], [77] have been proposed and tested. In a sense, all these methods are conceptually related as they attempt to find the global minimum by overcoming energy barriers of the complicated potential energy surface. However, most optimization methods suffer from a common problem of being trapped in a local minimum. The strength of an optimization method relies on the ability to escape from these local minima. The ease of finding the global minimum is also a key in an optimization search. Random sampling method is a simple method and has been applied to many applications [78]–[80]. The evolutionary algorithm using self-improving algorithm has correctly predicted many structures [81]–[83]. Metadynamics is highly successful to yield reliable results if long simulation time was

employed [84], [85]. It is important to consider all the methods starting the search with randomly generated structures. It is almost impossible to benchmark the various methods in order to determine which ones work best for a given set of problems. In this thesis, two popular techniques, Particle Swarm Optimization (PSO) and Genetic Algorithm (GA) were investigated. We wish to compare the reliability and explore the strength of these two methods.

1.2.1 Crystal lattice and Gibbs free energy

A crystal lattice is composed of a unit cell repeated infinitely in three dimensions. Six parameters are needed to define a unit cell. Three lattice vectors (***a***,***b***,***c***) and the angles between them (α,β,γ). Positions of the atoms are defined by the Cartesian coordinates. Therefore, there are 3*N*-3 degrees of freedom associated with atomic positions with 3*N*+3 degrees of freedom in total to describe a crystal. Any crystal structure prediction technique must therefore optimize 3*N*+3 variables collectively known as particles. The grey circles in Figure 1.6 illustrate these "particles" in the search space. The task is to locate the global minimum in an efficient manner. In practice, for all the methods each particle samples the energy surface at specific points dictated by the structure prediction algorithm. A set of "particles" found at each move is called a generation. Note that the number of particles and generations play significant roles in the structure search. The probability of finding the global minimum increases with increasing number of particles and generations. The most stable structure is the one having the lowest Gibbs free energy, *G*

$$G = E + PV - TS \equiv H - TS, \tag{1.55}$$

where *E* is the internal energy at pressure *P* with volume *V*. *T* and *S* are the temperature and entropy of the system, respectively. Crystal structure searches were often performed at a selected pressure. Zero point energy (ZPE) is not included in the energy as temperature is ignored. Therefore, only the enthalpy *H=E+PV* is the relevant property to optimize. At high pressure, the *PV* term is the most important term of the free energy.

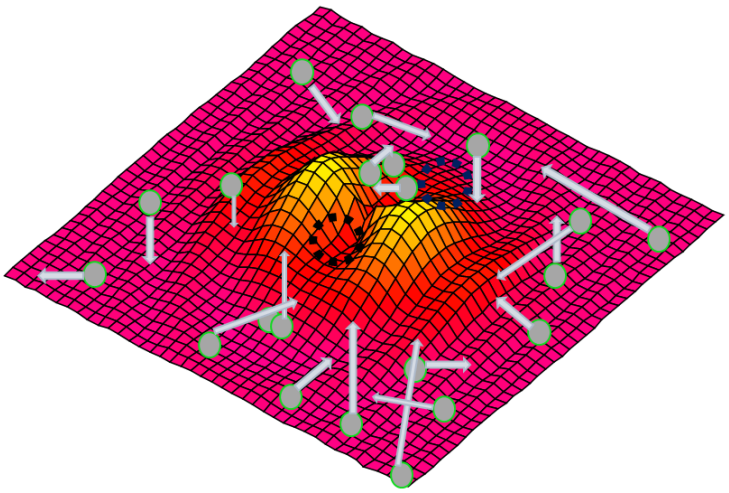

Figure 1.6 Several particles in grey color move in different directions of free energy surface. Balck dot circle is the global minimum and blue dot circles is a local minimum.

1.2.2 Particle swarm optimization

PSO is a technique originally introduced by J. Kennedy and R. C. Eberhart in 1995 [86]. PSO method was adopted for structural prediction by Mao *et.al,* [87]. This method was implemented in the CALYPSO code. The structural search starts with randomly generated structures but constrained by the crystallography space groups [88]. The trial structures can be constrained by the bond lengths information.

The position of each particle x_i(t) is randomly chosen in the free energy surface. Each particle then moves within the multidimensional PES with an initial velocity, V_i(t), which is randomly generated. In the PSO scheme, position of each individual particle in the subsequent step, x_i(t+1), is dependent upon its prior location, as well as the velocity, V_i(t+1), by

$$x_i[t+1] = x_i[t] + V_i[t+1], \tag{1.56}$$

$$V_i[t+1] = wV_i[t] + C_1r_1\{x_{ibest}[t] - x_i[t]\} + C_2r_2\{x_{gbest} - x_i[t]\}, \tag{1.57}$$

where, $i \in \{X, Y, Z\}$, w an inertia weight, $w = w_{max} - \frac{w_{max}-w_{min}}{iter_{max}} \times iter$ is modified during the calculations ranging between 0.4 to 0.9 [87]. Note that w is dynamically varied and decreases linearly during the iterations. The coefficients C_1 and C_2 are the self-confidence and swarm

confidence factors, respectively. These factors reflect how much the particle trusts its own experience more than the swarm. In this study, the default values of $C_1 = C_2 = 2$, determined from previous tests of the PSO method were used [87],[89]. r_1 and r_2 are random numbers generated within the range of [0,1]. x_i(t) after optimization moves into the nearest local minimum and the position is denoted as $x_{ibest}[t]$. $x_{gbest}[t]$ is the position of the global minimum with the best fitness value for a given population. The workflow of the CALYPSO program in a hypothetical 1D energy surface (Figure 1.7) shows how $x_i(t)$ propagate to the x_i(t+1) positions. At each generation, duplicate structures are identified and removed and new structures are generated *via* the PSO algorithm. Following the recommendation from previous studies, a certain percentage (often 60%) of the lowest energy structures employed from the previous generation are used to construct the new structures of the ensuing generation. The remaining 40% of the structures are then generated randomly to maintain diversity during the search. A PSO search is terminated if no new lowest enthalpy was found after 20 successive generations.

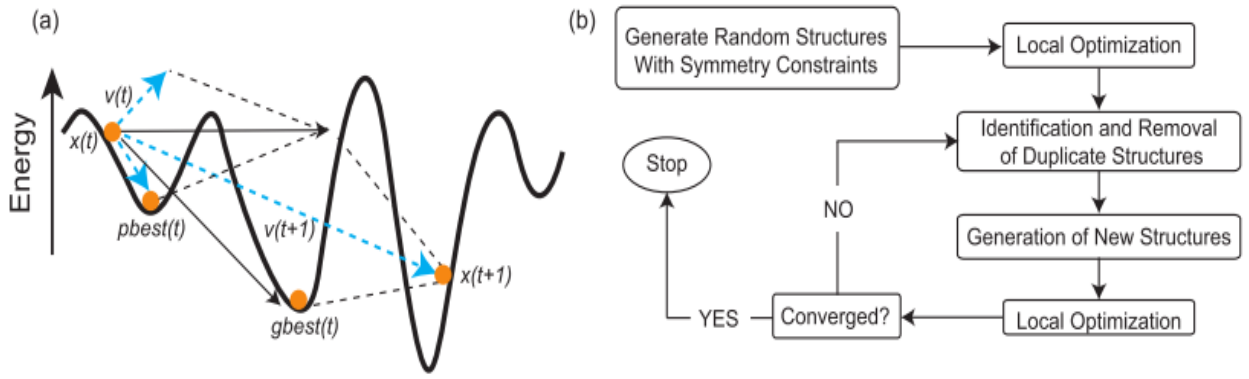

Figure 1.7 (a) A schematic diagram [81] depicting how generated structures explore minima within the PSO algorithm in a 1D PES. (b) The workflow in the PSO technique as implemented in the CALYPSO code.

Since, the "movement" of particles in the search space is dynamically influenced by $x_{gbest}[t]$, the particle position was not kept in succeeding generations. That means the best structure found in a particular generation is not necessary the same $x_{gbest}[t]$ for succeeding generations. For instance, the history of the search on the most stable structure of XeI_2 at 10 GPa is shown in Figure 1.8. The black line represents the lowest enthalpy structure found at each

generation. For example, a low energy structure $x_{gbest}[t]$ was found in the third generation. However, in the 15th generation an even lower enthalpy structure was found. Then, no better structure was found for succeeding generations and the search was terminated at the 41st generation.

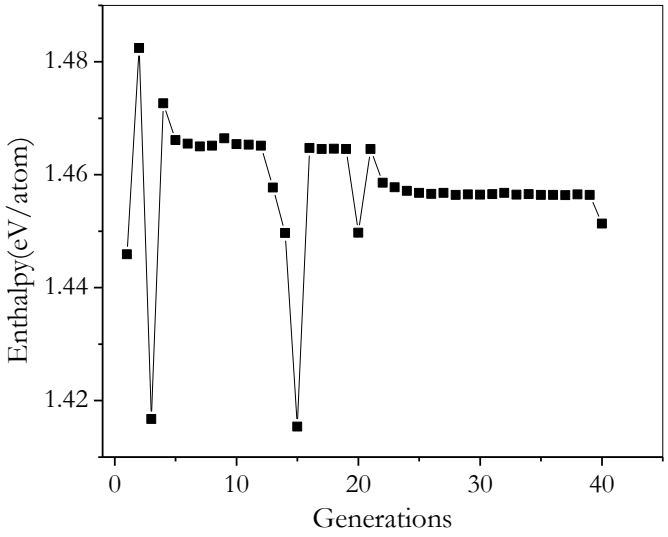

Figure 1.8 The PSO search performed on XeI_2 at 10 GPa.

1.2.3 Genetic algorithms

Another structure search method employed in this research is based on the evolutionary algorithm. The genetic algorithms (GAs) attempt to find the local minima and global minimum from evolutionary principles such as mutation and heredity. The best structure is the one with the lowest enthalpy. The two main genetic operations, heredity and mutation, are shown in a schematic Figure 1.9. An offspring structure is generated through mutation operation by distortion of the parent structure. The heredity operation is to combine two parents to produce a single offspring.

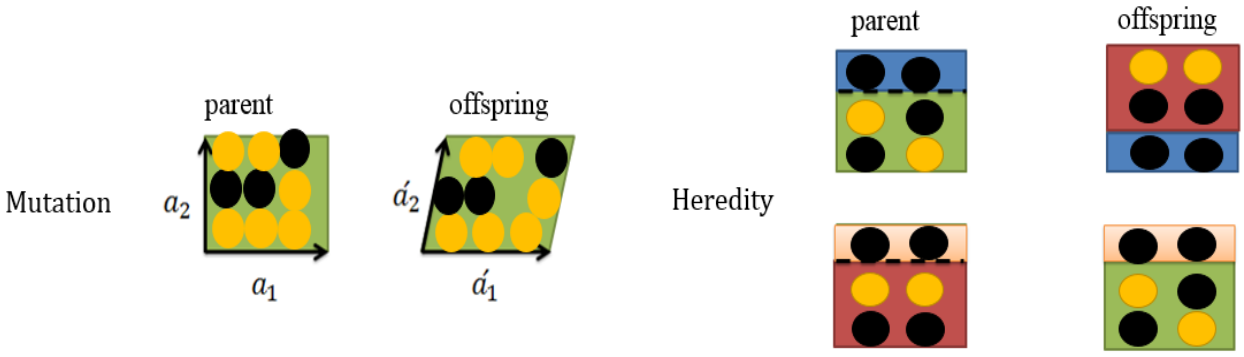

Figure 1.9 The offspring structures generated via heredity and mutation.

The GA software's have been implemented by several groups [90]–[93] including ourselves and many different heredity and mutation operators are used to propagate offsprings. In this work, the GA method was mainly performed with our ASAP code [94].

The only required input to the structural search is the chemical composition, such as the type and number of different atoms and bond length constrains. According to this information, random initial structures were generated. The mutation operation in ASAP code is performed in two steps. The first step, small distortions of the unit cell vectors are chosen randomly [95]–[98]. In practice, a symmetric strain matrix is applied

$$V_{new} = \begin{bmatrix} 1+\varepsilon_{11} & \varepsilon_{12}/2 & \varepsilon_{13}/2 \\ \varepsilon_{12}/2 & 1+\varepsilon_{22} & \varepsilon_{23}/2 \\ \varepsilon_{13}/2 & \varepsilon_{23}/2 & 1+\varepsilon_{33} \end{bmatrix} . V, \tag{1.58}$$

where the ε_{ij} are zero-mean Gaussian random numbers taken from a specified standard deviation. The new cell vectors are re-scaled to generate a reasonable volume. In the second step, to displace atomic positions, ASAP applies small random shifts on *x*, *y* and *z* directions. At the end, the neighbour's distances are calculated to ensure that the atomic distances are reasonable.

Using the 'cutting-shifting-splicing' procedure [95]–[98] employed in the ASAP, the heredity operator combines the preferable properties of the parent structures to the offspring. The 'cutting-shifting-splicing' procedure uses a spatially coherent fractional slab from each parent to assemble them together in order to produce the offspring. However, the generated offspring may not contain the correct number of atoms in the model cell. To overcome this problem, the parent structures are translated or shifted to generate the integer number of atoms in the offspring. After

the atomic coordinates are generated, the unit cell parameter of the offspring is determined from a weighted linear combination of the lattice vectors of the two parents.

The percentage of new structures created *via* mutation and heredity operators is different for different GA codes. In the default setting of the ASAP code used in this study, 10% of structures are kept from the prior generation, 30% and 60% are generated from mutation and heredity, respectively. The choices of these default values have been evaluated previously [94] and were adopted here. The workflow employed in ASAP is similar to PSO (Figure 1.7b). A set of initial structures is randomly created. This is followed by local optimization and removal of duplicate structures. Then the GA generates new structures. Since in our ASAP code the lowest enthalpy structures are always kept and pass on to the succeeding generations, the best local minimum (structure) is included into the next generation. For instance, the lowest enthalpy structure vs generations for XeCl at 40 GPa is shown in Figure 1.10. The lowest enthalpy structure is kept in the succeeding generation.

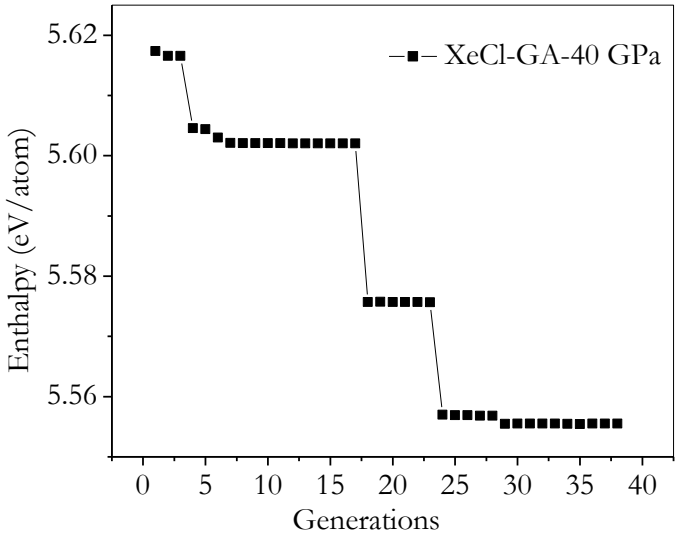

Figure 1.10 The GA search performed on XeCl at 40 GPa.

CHAPTER 2

Study of the electronic structures in AlH_3 and EuO at high pressure

As mentioned in the chapter on the theoretical background, in some systems very accurate descriptions of the band gap for insulators or semiconductors with localized *d* and *f* electrons are challenging with standard DFT functionals. In this chapter, we examine existing and recently developed density functionals that claimed to provide a satisfactory solution to this problem. If an efficient computational scheme could be found, it would be beneficial for routine studies of high pressure systems. For this reason, we tested several functionals and their performance in the description of the electronic band structures of AlH_3 and EuO.

AlH_3 is a solid with a high hydrogen content (10% by weight) [99]. At low pressure it is an insulator. Due to the high ionicity at high pressure electrons are being transferred from Al to H atoms. Aluminum hydride is very compressible and the volume can be reduced by almost 70% at 100 GPa. The strong compression results in broadening of the valence band leading to metallic character. Metallic AlH_3 has been predicted to be a superconductor with a critical temperature of 24 K [100]. The origin of superconductivity was attributed to the nesting of two parallel Fermi surfaces. However, the superconductivity has not been confirmed by experiment. One of the possible reasons is that the nesting of the valence bands at the Fermi level that give rise to the superconductivity behavior, may critically depend on the accuracy of the electronic band structure. To examine this possibility, we wish to compute more accurate electronic band structure for AlH_3 above 100 GPa using several functionals that have demonstrated success on a number of systems.

An accurate description of electronic structure of compounds containing *f* electrons is the most challenging problem. The strongly localized 4*f* orbitals of lanthanide are known to be difficult to describe correctly using the standard density functional. EuO is a protypical example of a highly correlated system. It is known to exhibit an anomalous isostructural transition at 35GPa. The origin of this transition has not been well established and often a $4f \rightarrow 5d$ (transition) hybridization is suggested to occur at high pressure. This conjecture is generally accepted by the community but has never been proven by rigorous theoretical calculations. The research to be performed here is to evaluate several theoretical approximations on their ability to describe the phase transition and the metallic state of EuO at high pressure. The intention is to examine whether these methods can provide reasonable results and reproduce the isostructural phase transition and isomer shifts

measured by Mössbauer spectroscopy. In this chapter, the results on the study of AlH_3 will be presented first then followed by EuO.

A portion of the research described in this chapter, namely the studies of solid AlH_3 has been published at Ref [101]

H. Shi, N. Zarifi, W. Yim, J. S. Tse, "Electron band structure of the high pressure cubic phase of AlH_3," J. Phys. Conf. Ser., vol. 377, p. 012093, Jul. 2012.

The author contributed as follow: Dr. Hongliang Shi performed screened hybrid density functionals and GW calculations in this paper.

2.1 Electronic structure of the high pressure cubic phase of AlH_3

2.1.1 Introduction

Dense solid hydrogen was expected to exhibit unusual physical properties, such as metallic conductivity and high temperature superconductivity [102]. So far, solid hydrogen in a metallic state has not been found. In view of the very high pressure required, it was suggested that superconductors with high critical temperature may also exist by compressing hydrogen-rich alloys [102]. This is a very tempting proposal and has stimulated many experimental and theoretical efforts to investigate the structural and electronic properties on a wide variety of hydride compounds. Experimentally, superconductivity has been reported in SiH_4 at high pressure [103]. However, the nature of SiH_4 and the origin of the superconductive behavior is still a topic of debate [104]–[106]. On the other hand, theoretical calculations have reported very optimistic predictions of T_c (> 80 K) in simple molecular hydrides at high pressure [107], [108]. Without exception, all theoretical studies employed "standard" density functionals with the ground state electronic structures and vibrational spectra obtained from semi-local (generalized gradient corrected GGA) density functionals with the pseudopotential plane wave method [109]. The electronic and vibrational information were then used in subsequent electron-phonon calculations in which T_c can be estimated [110]. It should be noted that an accurate band structure (Fermi surface) is critical to the prediction of the superconductivity. As will be shown later, it is particularly important in AlH_3.

2.1.2 Structure of AlH_3

Unlike most simple main group hydrides, e.g. SiH_4, there is no dispute on the crystal structure of the predicted superconductive phase of AlH_3 stable beyond 100 GPa. Both experimental x-ray diffraction and theoretical studies found a cubic structure to be stable at > 100 GPa [100]. The structure of the cubic phase $Pm\bar{3}n$ is remarkably simple and different from complex structures found in most high pressure hydrides. It is consisted of a bcc arrangement of Al at the corners and the center of the cube and pairs of H atoms (H_2 molecule) on the faces. The structure at 110 GPa (shown in Figure 2.1) has the H-H distances (1.54 Å) which are shorter than Al-H distances (1.72 Å).

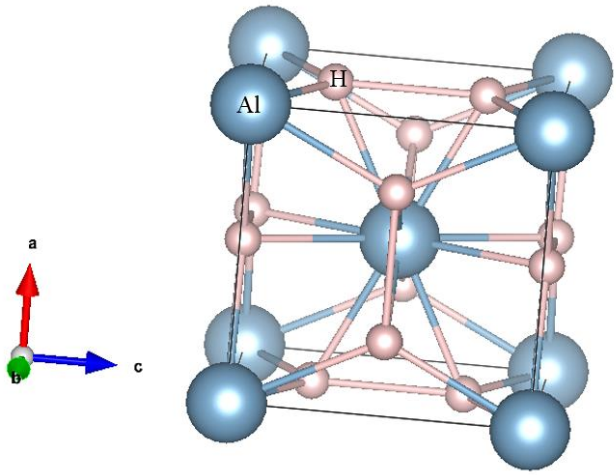

Figure 2.1 The $Pm\bar{3}n$ structure of AlH_3 has been suggested at 100 GPa.

2.1.3 Electronic properties using standard functional

The electronic band structure obtained from DFT calculations using the Perdew-Burke-Ernzerhof (PBE) functional revealed two electronic bands cross the Fermi level forming an electron pocket at R and an electron hole at M symmetry points (Figure 2.2). The theoretical results show the band dispersion of two bands along M → R are almost parallel at Fermi level and these two pieces of Fermi surfaces can be nested in the M → R direction. This feature has led to the predicted superconductive behavior of AlH_3.

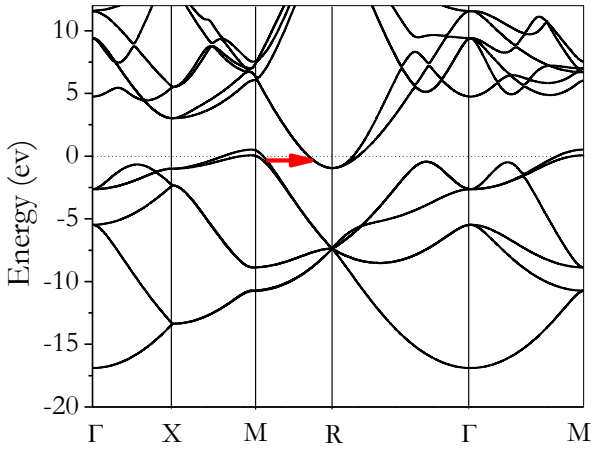

Figure 2.2 Electronic band structure of the cubic $Pm\bar{3}n$ phase of AlH_3 calculated with PBE functional at 100 GPa from Ref [100]. Two bands cross the Fermi level at M and R. The red arrow indicates the nesting vector connecting the two pieces of Fermi surfaces.

As the result of the nesting, a large mass enhancement parameter, λ =0.74, was obtained from electron-phonon calculations for the cubic AlH_3 phase. Using the extended McMillan equation, a fairly high T_c of 24 K was predicted at 110 GPa [100]. To test the theoretical prediction, resistance measurements have been performed down to 4 K and up to 164 GPa. Although the results show AlH_3 is a metal, no superconductivity was found [100]. The experimental result is somehow surprising with a judicial choice of a nominal Coulomb repulsion parameter (μ *, *ca*. 0.1 – 0.15). Since the calculated T_c's are often in reasonable agreement with experiment, the discrepancy between the theory and experiment in AlH_3 is perplexing and has motivated several theoretical investigations [111]. In one study, it was shown that the lattice vibrations in AlH_3 are highly anharmonic [112]. If the renormalized frequencies were used in the calculations of the phonon line-widths, a smaller mass-enhancement parameter was obtained. However, theoretically, anharmonicity should enhance the electron-phonon couplings as this is one of the basic assumptions of the Garland-Benneman-Mueller theory on the superconductivity of disordered solids [113]. More recently, calculations on the optical spectrum of cubic AlH_3 predicted a highly damped low energy transition below 1 eV that induced an abrupt edge in the reflectivity [111]. This observation is significant as the electronic excitation energy is very close to the H-H vibration frequencies, thus raising the possibility of strong coupling between them. In this study, we took a different viewpoint. Since the large electron-phonon coupling in AlH_3 was attributed to the nesting of the Fermi surfaces predicted from semi-local PBE calculations, it is relevant to investigate

possible changes in the band structure calculated with improved DFT methods proposed recently. These changes may help to explain the lack of superconductivity.

2.1.4 Methodology

The Kohn-Sham (KS)-DFT method is computationally efficient and can be used on a wide variety of complex materials. The calculated structural and chemical properties are often in good agreement with experiments. However, there are several known shortcomings with this approach using the existing GGA functional. Pertinent to the discussion here, is that these functionals often underestimate the energy gap between the occupied valence and unoccupied conduction band, and in some cases, even the profile of the band structure was incorrect. This deficiency can be traced back to the failure of DFT in describing the electron self-interaction and/or exchange interaction correctly. Several remedies to this problem have been proposed. Within the local density approximation (LDA) framework, an approximate functional designed to mimic the gap structure in the exact exchange of an atom was introduced by Becke and Johnson (BJLDA) [114] and later extended to solids by Tran and Blaha (TB-mBJLDA) [29], [30]. An alternative is to add a small amount of non-local Hartree-Fock (HF) exchange to the semi-local density functional. The PBE0 hybrid functional is a combination of the popular PBE functional with a 25% Hartree-exchange [24]. Taking advantage of the fast spatial decay of the short range HF exchange, a screened Coulomb hybrid functional separating the short-range and long range HF exchange was introduced by Heyd-Scuseria-Erhzerhof (HSE) [115]. The HSE functional offers an efficient computational scheme for extended periodic systems. On the other hand, a different approach based on many-body perturbation theory (GW) can be used to correct for the band gap problem. The GW method [57],[116] goes beyond the local exchange mean field approximation and includes many-body electron-electron interactions through the screening of the exchange term. Comparisons of the different methods have been made in several recent publications [46], [47], [117], [118] Therefore, a discussion on their strength and weakness will not be repeated here. In general, all the above mentioned methods have succeeded to ameliorate the underestimated band gap energies, albeit each has its own limitations and problems.

In this study, electronic band structures of AlH_3 in the pressure range from 90 to 160 GPa calculated from first-principles methods PBE [14], TB-mBJLDA [29], HSE [26], single shot G0W0 and self-consistent GW(SCGW) [46], [47] were investigated. The pressure was obtained

from the calculated equation of state (EOS, *i.e.* energy *vs* volume) from the respective methods. The exception is that the pressure for G0W0 and SCGW were taken from the PBE and HSE calculations. Full-potential linearized augmented plane wave (FLAPW) WIEN2k program [29] were used for the PBE calculations. The WIEN2k code was also used for TB-mBJLDA calculations using the PBE optimized wave functions as initial estimates. Converged FPLAPW results can be achieved with an RK_{max} value of 5 and a plane wave cutoff, G_{max}, of 20 Ry. HSE, G0W0 and SCGW calculations were performed with the VASP code. Projected augmented wave (PAW) potentials [37] for Al and H were used in the PAW planewave calculations. The energy for the planewave cutoff was 710 eV. A 12×12×12 Monkhorst-Pack *k* point mesh [119] was used for Brillouin integration. For G0W0 and SCGW, calculations were performed with both PBE and HSE optimized zeroth-order wave functions.

2.1.5 Results and discussions

High pressure cubic AlH_3 has been shown to be a metal from DFT calculations. However, DFT calculations using the common functional is expected to introduce large errors in the proper description of H atom due to incomplete cancellation of the Hartree and exchange-correlation self-interaction energies [117]. The PBE and TB-mBJLDA band structures for AlH_3 computed using WIEN2k at selected pressures are compared in Figure 2.3. The band structure profiles are similar to previous PBE results (Figure 2.2) [100].

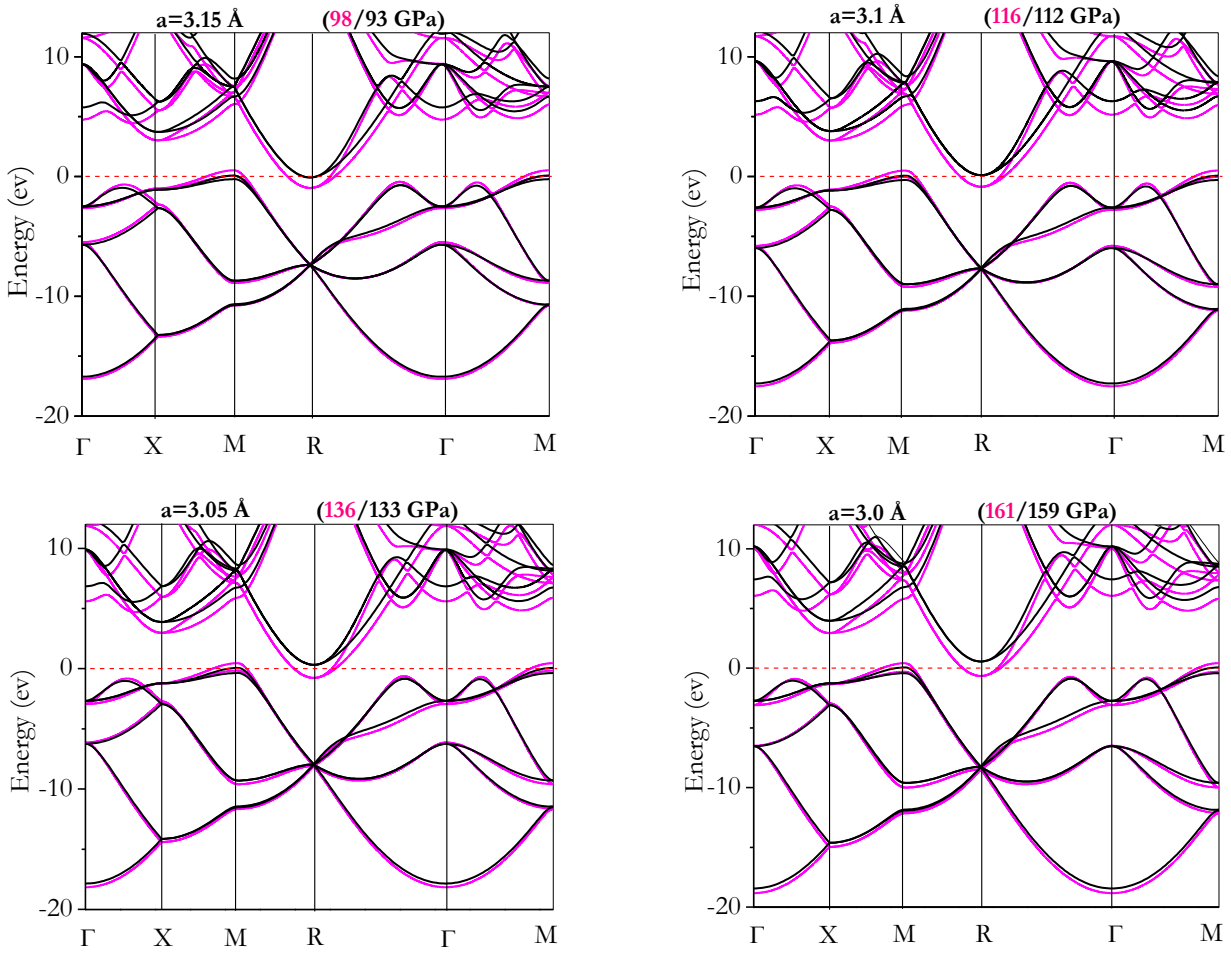

Figure 2.3 Electronic band structure of AlH_3 calculated from PBE (red) and TB-mBJLDA functionals using the WIEN2k code (black) from Ref [101]. The pressures are obtained from the equation of states calculated from the respective functionals.

Ensuing discussions will focus on the profile of the two energy bands crossing the Fermi level at the M and R symmetry point. At M, the electronic band has the shape of an inverted parabola while the band dispersion at R resembles a parabolic free-electron band. At first glance, there is little difference in the band structure of the occupied bands obtained from the two methods. In detail, the vacant TB-mBJLDA conduction bands were found to shift to higher energies. This observation is consistent with previous reports in which TB-mBJLDA exhibits a similar trend on the band shift. At 93 GPa with lattice constant of a=3.15 Å, the maximum at R and the minimum at M cross the Fermi level forming electron-hole and pocket, respectively. As the pressure increases, the energy minimum at R near the Fermi level also increases. Although the energy

maximum at M stays very close to the Fermi level using TB-mBJLDA method, the "pseudo-gap" between M and R increases with pressure.

Variation of the energy with pressure at R and M symmetry points relative to the Fermi level from PBE, TB-mBJLDA, HSE, G0W0 and SCGW calculations are compared in detail and the results are presented in Figure 2.4. If the energy at M is positive, the electronic band crosses the Fermi level. If the energy at R is positive, the band does not cross the Fermi level. The corollary is, if the energy at M is negative and the energy at R is positive then the system is a semiconductor or insulator. As long as the energy at M remains positive, the system is metallic. First we examine the consistency between the pseudopotential and all electron calculations using the PBE functional. As shown in Figure 2.4a, the results are almost identical. This observation confirms the choice of the various computational parameters. The PBE results show a steady decrease in the maximum energy at the M point with increasing pressure but still does not touch the Fermi level at pressure above 160 GPa. The minimum energy at R shows exactly the opposite trend. Since M is positive and R is negative within this pressure range, AlH_3 is metallic and the nesting of two pieces of Fermi surfaces at R and M is still possible.

The same conclusion is reached in a previous study using the PBE functional [100]. Although the trends on the variation of the band energy at M and R are similar to the PBE results, the TB-mBJLDA band structure in Figure 2.4b shows a significantly different profile. At 93 GPa, the band structure is broadly similar to that of the PBE functional. The maximum energy of the band at M is not very sensitive to pressure and remains above the Fermi level showing that the system is metallic up to the highest pressure studied here. The energy minimum at R, however, moves to higher energy at high pressure and no longer crosses the Fermi level. Therefore, nesting of the two Fermi surfaces is no longer possible.

The HSE results show a similar pattern as PBE (Figure 2.4c). The only difference is that the energy at R and M relative to the Fermi level are substantially smaller. For example, at 98 GPa, the PBE maximum energy at M of 0.53 eV and minimum energy at R -0.99 eV differ quite significantly from the corresponding HSE values of 0.18 eV and -0.44 eV. AlH_3 is still metallic within the pressure range studied, however, since the HSE conduction bands were shifted to higher energies, the curvatures of the two Fermi surfaces will no longer be same as predicted by PBE and nesting of the Fermi surfaces may not be feasible.

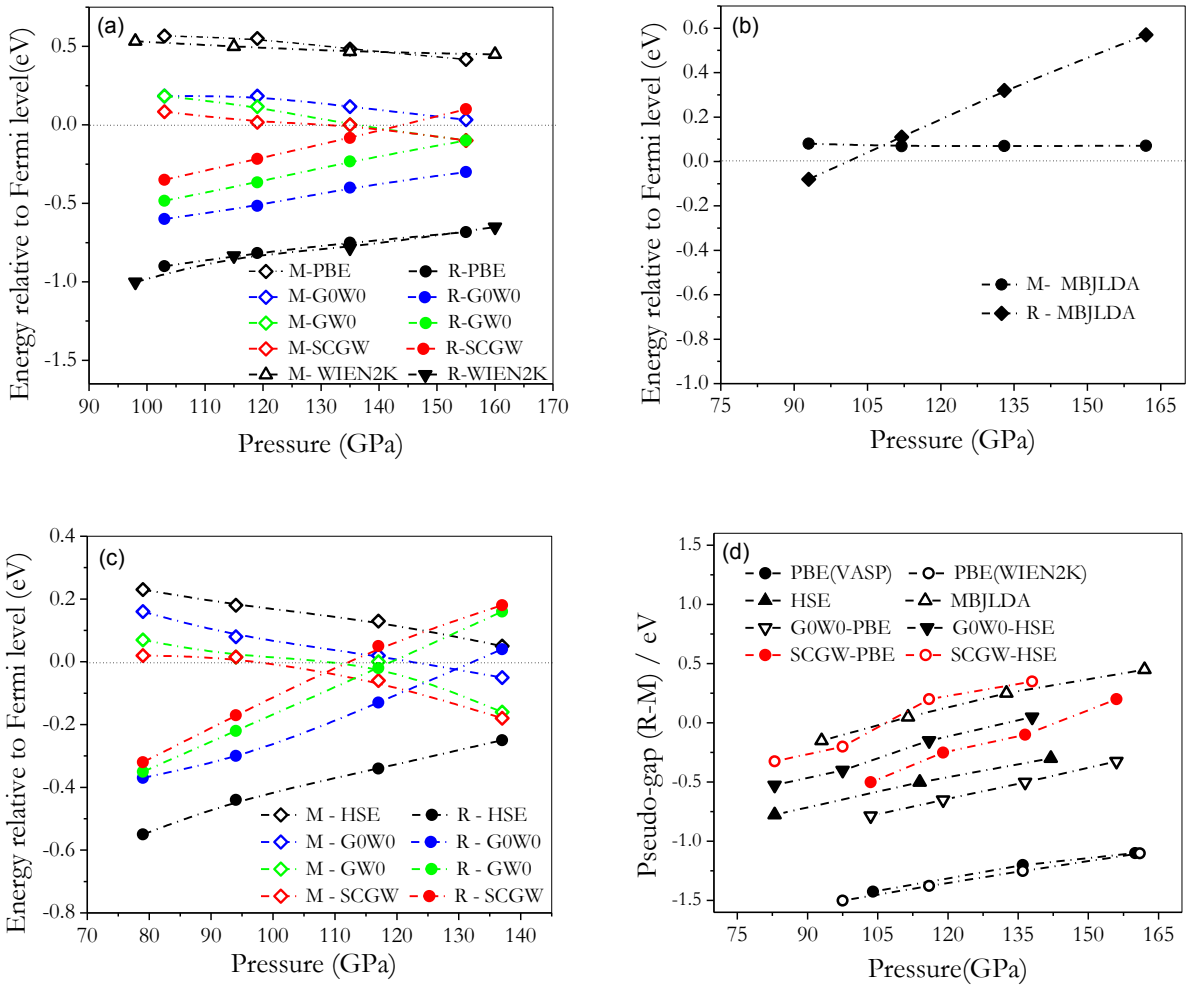

Figure 2.4 Comparison of calculated maximum energy at R and minimum energy at M relative to the Fermi energy using (a) PBE functional with VASP and Wien2k code and GW corrections; (b) TB-MBLJDA; (c) Comparison of HSE functional with VASP and GW corrections; (d). Pseudo-gap energy between the R and M using PBE (VASP and WIEN2k), TB-mBJLDA, HSE, G0W0 (PBE and HSE) and SCGW (PBE and HSE) [101] .

One shot G0W0 corrections were made using ground state wave functions computed from PBE and HSE functionals and are reported in Figure 2.4a, 4c and 4d. The variation of the energy at M and R with pressure follows a similar trend observed in the corresponding PBE and HSE calculations. G0W0 corrections to the quasi-particle energy are noticeably larger with the PBE wave function. Relative to the PBE, G0W0 (PBE) calculations show an almost uniform shift of +0.3 eV of the energy at R and -0.4 eV for the energy at M over the entire pressure range. In comparison, the G0W0 (HSE) corrected quasi-particle energies at R are much smaller. The quasi-

particle corrections, however, are more significant at M where the G0W0 (HSE) energies are *ca*. 0.2 eV lower than the corresponding HSE values. There is one important difference between the PBE and HSE G0W0 results. At pressures higher than 135 GPa, G0W0 (HSE) energy of M becomes lower than the Fermi energy and is higher than the Fermi level at R. Results of G0W0, GW0, and SCGW corrections on the PBE and HSE ground state wave functions are compared in Figure 2.4a and 4c, respectively. Both the PBE and HSE quasi-particle energy differences relative to the Fermi energy at M and R are reduced with increasing level of correlation treatment. For example, for the HSE corrections at 100 GPa, the energies at M relative to the Fermi level decrease from 0.18 eV (G0W0), to 0.12 eV (GW0) and then to 0.02 eV (SCGW). Similarly, the energies at R relative to the Fermi level increases steadily from -0.26 eV (G0W0), to -0.16 eV (GW0) and finally to -0.09 eV (SCGW). The GW0 corrections to the quasi-particle energies are close to of the SCGW values but the absolute differences are still fairly significant (< 0.1 eV). Shifts in the band energies lowered the possible "metal → insulator" transition pressure from the G0W0 (HSE) predicted value of 135 GPa to 120 GPa for SCGW. A similar trend in the energy shift is also observed on the quasi-particle GW corrections to the PBE eigenvalues at different level of approximations. The SCGW energies of the M and R points, like the pseudo R-M gaps calculated from the PBE wave functions are still noticeably different from the corresponding results using the HSE wave functions as references.

Since the original proposal of possible superconductivity in AlH_3 was attributed to the nesting of two pieces of Fermi surfaces cutting the Fermi level at M and R [100], the critical parameter to be examined is the pseudo-gap between the M and R point. The main results obtained from the present investigation are summarized in Figure 2.4d. All the methods studied here display the same general trend. Within the pressure range studied, all methods show AlH_3 is metallic and there is gradual opening of the gap between M and R. In comparison, GW calculations show the gap opening much faster with pressure and AlH_3 may become an insulator at higher pressure. It is interesting to note that even though the TB-mBJLDA calculations predicted that the energy change at M was not very sensitive to pressure, the predicted R-M pseudo-gap energies are very close to the SCGW (HSE) results.

2.1.6 Conclusions

Owing to a lack of experimental data, it is not possible to ascertain the accuracy of the band structures computed from the different methods. Experimental resistance measurements [100] show that the resistivity increased from 100 to 160 GPa and the temperature profiles resembled that of a bad metal. Present results obtained from more refined density functionals suggest there is an increase in the pseudo-gap between M and R with pressure. This band shift will affect curvatures of the bands at the Fermi level and the possibility of extensive nesting might diminish. The prediction from PBE calculations that the two electronic bands crossing the Fermi level near M and R led to nesting of Fermi surfaces may not be realized in reality. It can be concluded that AlH_3 will be a poor metal or even a low band gap semiconductor under pressure up to 160 GPa, not a superconductor. In passing, it is noteworthy that in spite of many successful applications of standard DFT calculations in reproducing structures and structural transitions for solids at high pressure, in some systems, accurate band structures are critical for the determination of the phase transitions. An example is that DFT calculations underestimate the insulator to metal transition in ε-O_2 transition pressure by almost 50 GPa [120], [121]. The discrepancy with experiment is removed once the quasi-particle corrections are made with G0W0 calculations [122]. In a recent calculation of the electron-phonon coupling in C60 molecules [123], the hybrid functional although did not alter the structure and vibrational properties significantly, it increased the contribution of the exchange energy to the total electron-phonon coupling by almost 40% bringing the theoretical prediction in better agreement with experiment.

2.2 Insulator-metal transition and valence instability in EuO

2.2.1 Introduction

Eu is a rare-earth lanthanide element and its magnetism arises from the open half-filled $4f$ shell with an electron configuration of $4f^7 5d^0 6s^2$. With perfect spin polarization and a large local moment of $7\mu_B$, EuO is an ideal spintronic material under ambient conditions [124], [125]. The first experimental study of the electronic structure of EuO was made in 1970 [126]. At 300 K, optical absorption spectra established that the indirect energy gap between the localized $4f$ state and the conduction band edge is about 1.12 eV [127]. The $4f$ electrons are highly localized near

the Fermi level forming almost flat bands. On the other hand, the $5d6s$ conduction bands are highly dispersive and separate from the filled states by a small energy gap. Unlike the majority of the lanthanide elements with trivalent electronic states, owing to the very stable heavy filled $4f^7$ configuration, Eu is a divalent metal under ordinary conditions [128]. A recent study reported that Eu metal, similar to EuO, remains nearly divalent to the highest pressures (87 GPa) with magnetic order persisting to at least 50 GPa [129]. The characteristics feature of valence electrons and magnetic instabilities of EuO and Eu_2O_3 have been the subject of many experimental and theoretical investigations [130]–[133].

The first pressure-induced semiconductor to metal transition of EuO at high pressure was reported in 1972 [134]. Recently, the experiment was repeated with Eu $L_{2,3}$ edges x-ray absorption and Eu Mössbauer spectroscopy using synchrotron radiation [135]. The experimental EOS in Figure 2.5 clearly shows two phase transitions at 35 and 45 GPa. Under ambient conditions, EuO has a simple NaCl (B1) crystal structure. A small volume change associated with an isostructural phase transition from B1 to B1' was found near 35 GPa. This transition with a modest volume collapse (~ 0.5%) was first noticed by Jayaraman [134]. The precise nature of this phase transition is still not known but it is often referred to as an electronic instability [135]. A first-order structural phase transition to a denser simple cubic CsCl (B2) structure occurs with a large coexistence region of both phases from 44 to 59 GPa [135], [136]. The B2 structure is stable up to at least 92 GPa. For lanthanides, pressure-induced electronic collapse has often been assumed to be due to the promotion of a 4*f* electron to the iterant 5*d* orbitals leading to mixed valence states. So far, no theoretical calculation has been able to reproduce all the experimental features. Here, we computed and compared EOS and electronic structures of EuO using PBE+U, mBJLDA and Hybrid PBE0 functionals.

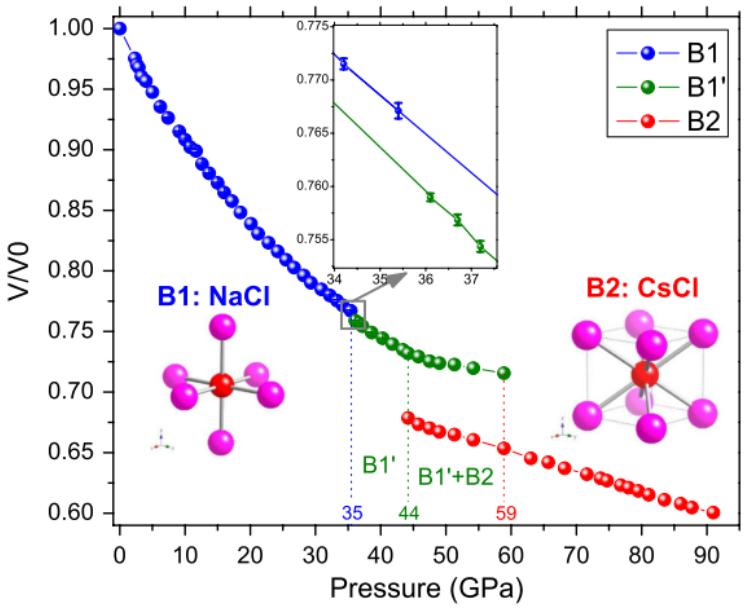

Figure 2.5 Pressure-volume dependence of EuO up to 92 GPa obtained from Ref [135]. The inset panel shows a modest isostructural volume collapse at about 35 GPa. Two schematic figures show the local coordination in NaCl (B1) and CsCl (B2) phases.

Nuclear forward scattering (NFS) and x-ray absorption near-edge spectroscopy (XANES) experiments have also been performed [135], [137]. From the comparison with the XANES Eu^{2+} and Eu^{3+} oxides, fractional occupation of 4*f* orbitals with a mixed valence (Eu^{2+} and Eu^{3+}) states between 14 and 40 GPa was suggested [138]–[140]. A surprise reentrant valence behavior (*i.e.* disappearance of the Eu^{+3} features and return that of Eu^{+2}) between 45 to 80 GPa was observed from the B1' to B2 phase transition. To provide support for a change of electronic transition, Mössbauer isomer shift (IS) were determined from the NFS experiments. In the hope that the change in the Eu IS can provide additional information on the valence states [141], [142]. The experimental Mössbauer spectra show a single resonance indicating that the compound is spatially homogeneous in the B1 phase below 40 GPa and B2 phase above 60GPa. Between 44 and 59 GPa where B1' and B2 phases coexist the Mössbauer spectra show two resonances indicating Eu is in a spatially inhomogeneous valence state. A second objective of this study is to investigate how nucleus charge density that affects the IS, changes as a function of pressure.

2.2.2 Computational details

Ab initio calculations were performed using the Full-potential linearized augmented plane-wave with WIEN2K program [31]. In the LDA+U calculations, an effective on-site Coulomb repulsion correction $U_{eff} = (U - J) = 6.9$ eV is applied to the Eu 4*f* orbitals [132]. The plane wave cutoff $R_{MT}K_{max}$ was set to 9. The charge density in the Fourier expansion was truncated at $G_{max} = 12 bohr^{-1}$ .The convergence in the charge density was better than $10^{-4}e$. A 21×21×21 *k* point mesh to sample the first Brillouin zone was used in all calculations. Only spin-polarized ferromagnetic states were considered and the contribution of the spin-orbit coupling was found to be negligible.

2.2.3 The electronic band structure of EuO

In the ground state, EuO is a semiconductor. Hybrid functional PBE0 and semi-local mBJLDA method, however predicted erroneously that EuO is a metal. The over-emphasis of the hybridization between Eu 4*f* and 5*d* orbtials is the cause for the closing of the indirect band gap for PBE0 at Γ and X (Figure 2.6a). Unlike AlH_3, mBjLDA did not improve the band structure and also failed to correctly describe the electronic structure of EuO even at an ambient pressure (Figure 2.6b).

As already discussed in Chapter 1, the Hubbard U correction was designed to model the on-site electron repulsion correction. Electronic band structure of EuO obtained from PBE+U calculations at the experimental structure is shown in Figure 2.6c. The occupied and unoccupied bands are separated with an indirect band gap of ~0.6 eV between Γ and X. The direct band gap at the X is significantly smaller than the direct gap at the Γ point. In the present study, only the correction for the *f* electrons was found to be necessary to provide a qualitatively correct band structure. In comparison to the Eu 4*f* bands, the dispersion of the unoccupied 5*d* conduction bands are much more significant. This may be the reason that it is not essential to take U_d into account in the 5*d* shell [134]. The indirect band gap was found to close at $0.88V_0$ with the equilibrium volume, V_0=238 $bohr^3$, obtained from EOS (Figure 2.6d). The PBE+U predicted the volume is 4% larger than experimental volume corresponding to $0.88V_0$ at 12 GPa. Adding the Hubbard model in the mBJLDA+U functional also gave the expected electronic band structures with a larger gap (Figure 2.6c). The inclusion of an on-site repulsion U_f shifted the occupied 4*f* bands down closer

to the O 2*p* bands. The Eu 5*d* states are still located at the bottom of the conduction band at *X* and at *Γ*. However, the gap between the Eu 4*f* and 5*d* bands closes much faster than the O 2*p* and Eu 4*f* band gap. The results obtained here show adding U one-site repulsion to the *f* orbitals with PBE and mBJLDA functionals helps to reproduce the expected band structures and the magnetic semiconductor ground state of EuO. However, from the band structure, mBJPBE+U wrongly predicted that EuO maintains a semiconductor for B1 phase at higher pressure.

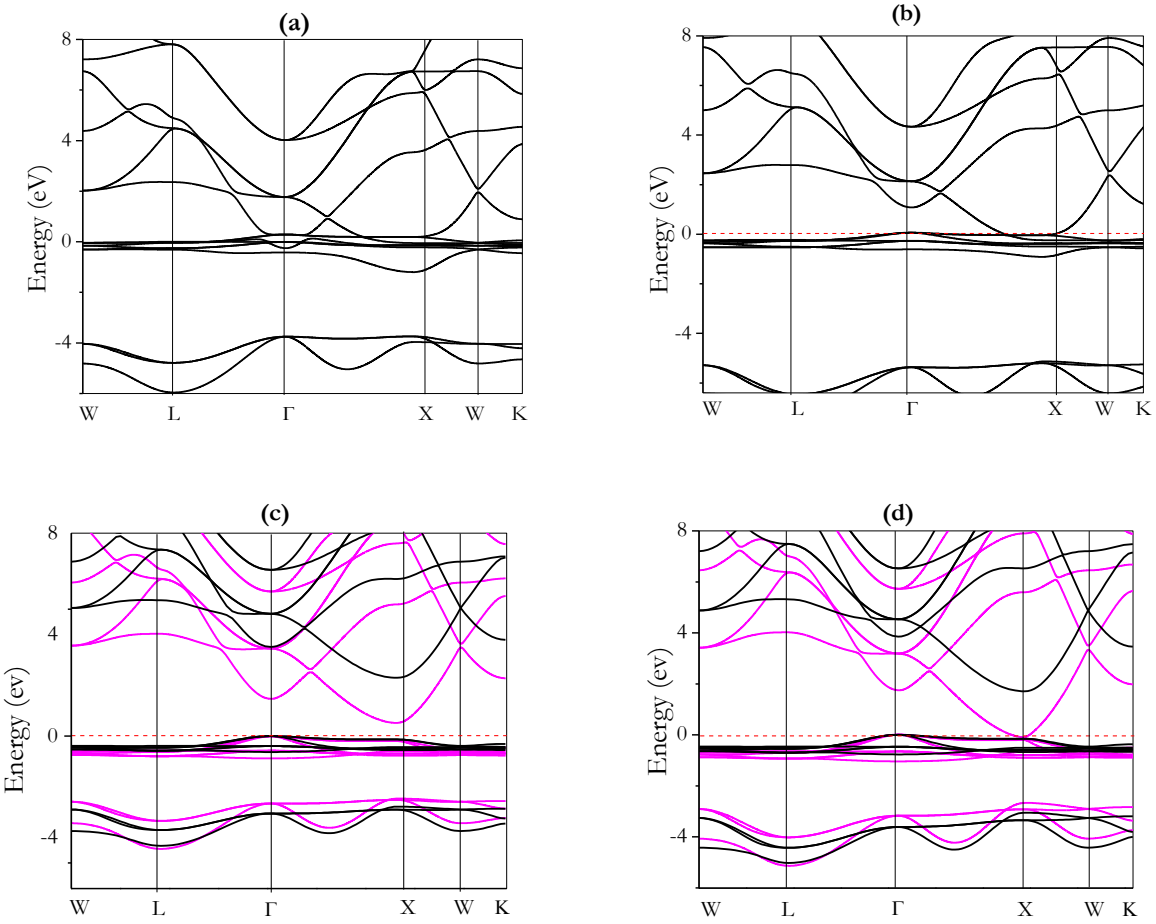

Figure 2.6 Electronic band structures of EuO (a) Hybrid fuctional, (b) mBJLDA at ground state. Red (PBE+U) and black (mBJLDA+U) lines represents electronic band structures at (c) ground states and (d) 0.88V0.

The EOS obtained from spin polarized PBE+U calculations are shown in Figure 2.7a. The energies and volumes were fitted to the Birch and Murnaghan equations of state [143], [144]. A very small volume discontinuity near $0.88V_0$ was found. This result is consistent with recent more

precise diffraction study which indeed shows a small volume change at 12 GPa pressure (see Figure 2.5). The reason for the discontinuity is that at 12 GPa, the *d* band touches the localized *f* bands at *X* closing the indirect gap, and EuO becomes a metal. When the system is compressed beyond 12 GPa, the EOS remains continuous and shows no sign of the observed B1 → B1' transition. Despite the failure to predict the isostructural phase transition at ~ 35 GPa, the EOS clearly shows the B1 to B2 phase transition occurs at $0.72V_0$ or 55 GPa. In agreement with experiment, Eu was found to maintain the high spin state in the calculated pressure range. It should be noted that mBJLDA and PBE0 calculations also failed to predict the isostructural B1→ B1' transition.

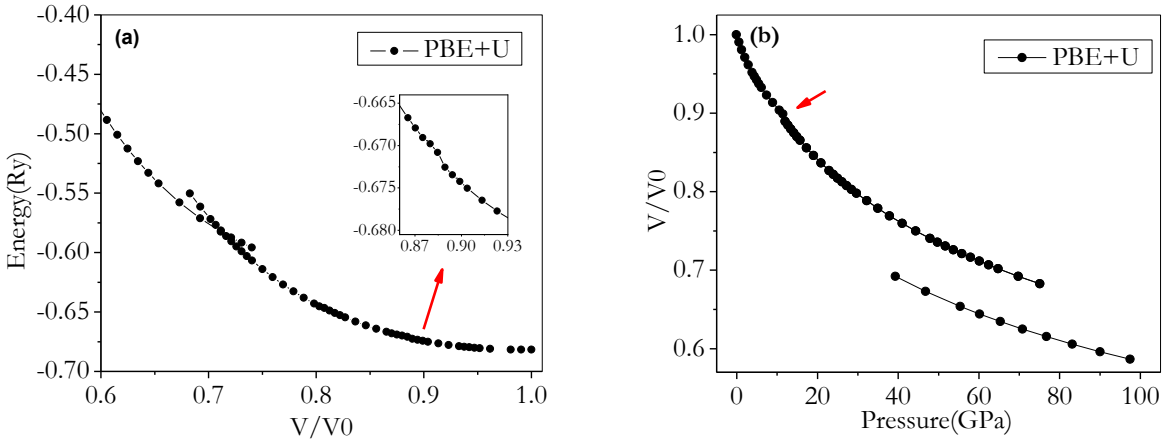

Figure 2.7 Equation of state of EuO using PBE+U functional as a function of (a) volume and (b) pressure. Inset (a) illustrates the calculated small kink around the 0.88 V/V_0.

2.2.4 Isomer shift of EuO under pressure

The Eu Mössbauer spectra of EuO obtained from NFS technique have been measured up to 80 GPa at ambient temperature. The results suggested that Eu remains in the divalent state at this pressure [135]. Mössbauer isomer shift is related to the *s*-electron density at the nucleus. However due to shielding by other atomic orbitals, the IS can be influenced by the valence state. We have calculated the *s*-electron density at the nucleus (ρ_0) using all electron PBE+U functional with WIEN2K in the B1 and B2 phases.

The electron densities were calculated using two different integration meshes and the results were compared in Figure 2.8. We found that the size of the integrating mesh plays a significant role in determining the absolute magnitude of the electron density. In the WIEN2K

code, the first radial mesh point (R_0) determines the logarithm mesh difference for the integration scheme. For heavier elements such as Eu, a smaller R_0 is recommended. We first examined the core (1*s*, 2*s*, 3*s* and 4*s*) and the valence (5*s* and 6*s*) contributions to the total sum of the *s*-electron densities using R_0=0.00001 and R_0=0.0001. Then, the calculations were repeated using R_0 with 0.00005 and 0.00008.

Several conclusions can be drawn by the analysis on the results obtained with choice of different radial mesh points. The core nucleus density computed with R_0=0.00001 (Figure 2.8a) shows significant fluctuations close to equilibrium volume at low pressure. This fluctuation suggested a serious numerical error. Even increasing the value of R_0 (Figure 2.8b) could not totally diminish the numerical error of the core orbitals. In comparison, the valence orbital contribution is less noisy for both R_0s, particularly for the larger R_0.

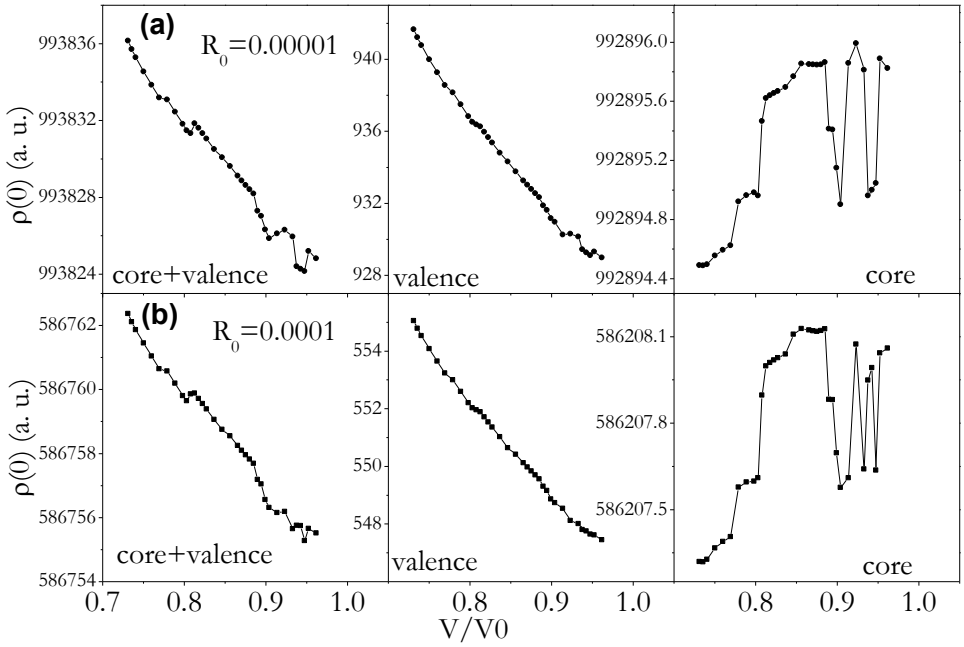

Figure 2.8 Electron densities ρ_0 of EuO at the nucleus under pressure with two different radial mesh points.

The absolute values of ρ_0 were found to be sensitive to the integration mesh. For instance, decreasing R_0 from $1x10^{-4}$ to $1x10^{-5}$ caused an increase in the *s*-electron density at the nucleus from 556755 to 993825 au^{-3}! In contrast, the ratio ρ_0/ρ_{max} shows very similar feature for the B1 phase and are identical from 0 to 70 GPa (Figure 2.9a). The errors are negligible at pressures greater than 10 GPa. Interestingly, a small discontinuity (red circle) was observed around ~12 GPa.

The discontinuity is directly related to the closing of the gap at *X* symmetry point leading to metal transition. In addition, two "kinks" were predicted around ~29 GPa and a smaller one at 35 GPa. We tentatively associate these features to the B1 to B1' transition.

In comparison, the calculated EOS (energy *vs*. volume) are identical regardless of the different radial mesh points (Figure 2.9b) Therefore, the total energy of EuO is not seriously affected by the choice of the integration mesh.

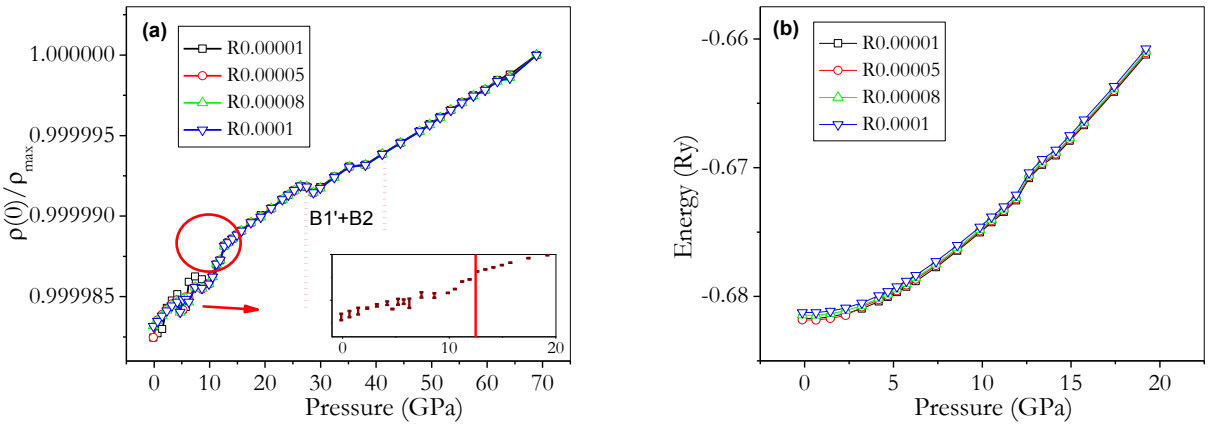

Figure 2.9 Electron densities at the nucleus and (b) calculated energy as a function of volume of EuO with different R0s.

The isomer shift is related to the density at the nucleus by a linear equation [145],

$$IS = A.\Delta\rho_0 + C, \tag{2.1}$$

where A is a calibration constant [146], [147]. $\Delta\rho_0$, is the relative density with respect to ρ_0 at zero pressure [129] and *C* is a numerical constant. The experimental isomer shifts and the calculated *s*-electron density ($\Delta\rho_0$) of Eu with R_0=0.00001 in the pressure range from 0 to 83 GPa are compared in Figure 2.10. The experimental isomer shift observed a small "kink" around 30 GPa (see inset) and the absolute values of IS decrease from -11.28 mm/s at low pressure to -3.97 mm/s at 60 GPa in B1 phase. The calculated nucleus *s*-density reproduces the experimental trend qualitatively, where a discontinuity predicted around ~30 GPa is consistent with the experiments. Furthermore, the calculated ρ_0 also decreased abruptly in the B2 phase.

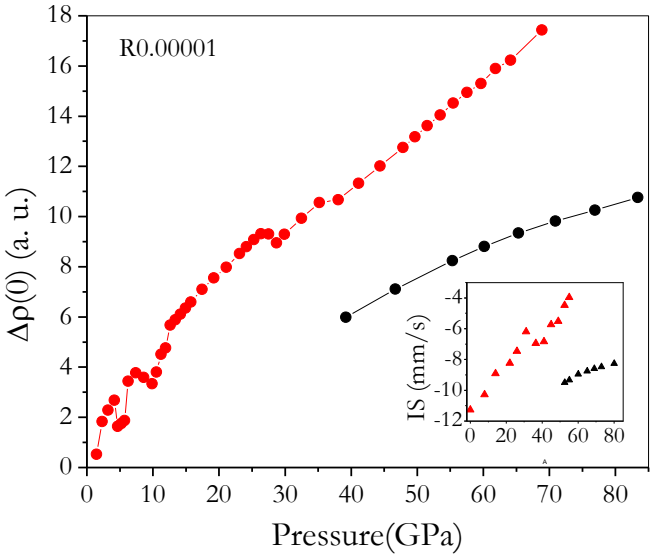

Figure 2.10 Pressure-induced electron densities at the nucleus of EuO. The inset shows IS measured by Ref [135].

2.2.5 Conclusions

In summary, although PBE+U functional was not able to reproduce the isostructural B1 → B1' phase transition, the semiconductor to metal transition with a very small volume change at 12 GPa was correctly described. The mBJPBE+U method also predicted an indirect band gap at ambient conditions but it failed to reproduce the metallic phase of B1 and B2 structures at high pressures. The Hubbard U is generally an empirical parameter and may be obtained by fitting to experimental results or using linear response. In this study we employed a constant U parameter at the pressure range studied. Isostructural phase transitions observed in the experiments were not predicted by the calculations. An accurate modeling of the electronic structure of this highly correlated system (EuO) at high pressure remains a challenge and may require a mixed-valence state multi-configurations composed of both Eu^{2+} and Eu^{3+} states.

Finally, we showed the numerical integration scheme plays an important role in computing the *s*-electron density near the nucleus. Although the choice of radial mesh for integration changes the absolute value of ρ_0, it does not affect the pressure trend. Our results indicate large numerical error in the nucleus electron density calculations below 10 GPa. At higher pressure a discontinuity related to the B1 to B1' transition was correctly predicted around ~30 GPa. The increase of ρ_0 in Eu^{2+} can be rationalized by the following reasons. A compression of *s*-like electron shells can

increase exchange interactions between 4*f* electrons and unoccupied *d* orbitals. In our case, 4*f* electrons decrease with increasing pressure but real valence change towards Eu^{3+} was not solved due to isostructural phase transition. Eventually, further compression reduces ρ_0 at B2 phase and increases valence electrons of *f* orbitals above 50 GPa.

2.3 Summary

In this chapter, the electronic band structures and properties of AlH_3 and EuO were examined using different functionals within the framework of DFT theory. For AlH_3, since the nesting feature is removed by all the methods employed in this study, this compound is a poor metal not a superconductor at high pressure. However, the profiles of the valance and conduction bands near the Fermi level can be quite different with these methods. For example, the GW calculations show the gap opens much faster with pressure and AlH_3 may become an insulator at higher pressure. The choice of the zeroth order wave functions from PBE and HSE calculations also affect the GW results. The GW predicted semiconductor behavior at 145 and 115 GPa starting from the PBE and HSE wave functions, respectively. The TB-mBJLDA predicted that the energy change at the M symmetry point is relatively insensitive to pressure as compare to other methods which showed the energy of M decreases. The results highlight the importance of the correction to the exchange and correlation energy to the band structures of metal hydrides at high pressure.

For EuO, no mean-field approximation (*i.e*. PBE+U or mBJLDA) can consistently reproduce all the experimental observation. The mBJLDA including the U parameter predicted an incorrect semiconductor with indirect gap. The volume reduction and Mössbauer IS associated with the insulator to metal transition in the B1 phase are correctly predicted by PBE+U calculations. However, the isostructural B1 to B1' is not evident. EuO as a highly correlated system may not be described by a single determinant wave function near the B1 to B1' phase transition. Sophisticated methods such as Quantum Mont Carlo (QMC) or Dynamical mean-field theory (DMFT) are needed in order to describe the mixed valence states of EuO.

CHAPTER 3

Structures of the metallic and superconducting high pressure phases of solid CS_2

The part of work presented in this chapter is in the following paper [148]

N. Zarifi, H. Liu and J. S. Tse. Structures of the metallic and superconducting high pressure phases of solid CS_2, Sci. Rep., vol. 5, no. April, p. 10458, 2015.

The co-author contributed as follow: Dr. Hanyu Liu performed the MD calculations in the CS_2 paper.

Pressure can induce structural changes as a result of the breaking or forming of chemical bonds. For example, simple molecular solids possessing strong covalent bonds are expected to undergo phase transition into non-molecular or disordered structures. Instability of molecular bonds or polymeric compounds has been found in O_2[120], [121], [149], [150], N_2[151]–[153], CO [154]–[156], and CO_2[157]–[159]. Previous studies on solid CO_2 demonstrate the successive structural transformations and eventual conversion into extended 3D non-molecular structures at 60 GPa [157]. On further comparison, the extended structure of CO_2 transformed into an amorphous solid at ambient temperature or an ionic solid at high temperature [159]. Compared to the molecular form, in an extended structure the electrons become more mobile and it is feasible that the system may transform from an insulator to a metal. However, the strong covalent C-O bonds are quite resistive to transformation into a metallic phase. Theoretical studies predict six coordinated CO_2 solids only exist at pressure close to 1 TPa but remain as insulators [160]. In comparison, although molecular CS_2 is similar to CO_2 it has weaker C-S bonds and it may offer an opportunity for metallization. CS_2 is a transparent liquid under ambient conditions [161]. It transformed into a molecular solid with the *Cmca* structure at 1 GPa [161], [162]. This phase is stable up to 9 GPa [163]. Further compression resulted in a highly reflecting, extended non-molecular solid above 40-50 GPa [164]. Within this pressure range, the electrical resistance decreased continuously and an insulator-metal transition was found at ~50 GPa [164]. A recent report further established that the metallic CS_2 phase is a superconductor with a critical temperature (T_c) of 6 K, which remains almost constant from 60 GPa to 170 GPa [165]. The latest study also reveals some interesting findings. For example, it is suggested magnetism exists in the normal state above 100 GPa and the structure is composed of six-fold coordinated carbon atoms. There is little

information on the structure of the high pressure phases. Above 9 GPa, x-ray diffraction [164] measurements show the intensity of the Bragg diffraction peaks weakened and the line-widths broadened indicating a gradual transformation into an amorphous form. Up to 120 GPa, no features characteristic of elemental carbon and sulfur were observed. Thus, CS_2 had not segregated into the elements. Due to a lack of structural information, first-principle calculation is an effective tool to explore the high pressure structure.

The objectives of this study are (i) exploration of the candidate structures responsible for the superconducting behavior; (ii) examination of the possible magnetic electronic states and (iii) investigation of the existence of unprecedented hypervalent six coordinated carbon atoms in the structures. For these purposes, first-principles molecular dynamics (MD) and structure prediction calculations using GA and PSO methods were performed. As is demonstrated in the ensuing discussion, both methods showed that structures with distinct carbon and sulfur domains are favored at high pressure. Moreover, a crystalline structure with a 2D sulfur network linked to carbon chains was found to be most stable between 60 and 120 GPa. This structure was metallic and superconductive. Within the experimental pressure range, no evidence of six coordinated carbon atoms or magnetism was found in any of the predicted structures.

3.1 Computational details

All electronic calculations were performed using the VASP, [36], [37] a plane wave code employing the projected-augmented wave (PAW) potentials [34] based on the density functional theory with the Perdew-Burke-Ernzerhof (PBE) [14] parameterization of the generalized gradient approximation (GGA). During the structural search, Monkhorst-Pack *k* point grids [119] were generated at a predefined mesh by scaling the reciprocal lattice vectors of each individual structure. The convergence criterion was that the forces acting on the atoms were all less than 10^{-3} eV/ Å using the highest *k* point mesh. A plane wave basis set cutoff of 500 eV was chosen to ensure that the enthalpy calculations converged with an accuracy better than 1 meV/atom. Both the supercell approach [64], [166] and the linear response method [67], [68] were used for phonon band structure calculations.

Structural searches were performed with the PSO method implemented in the CALYPSO suite [87] and GA method was performed with XtalOpt [90] and our ASAP code [94]. For these calculations, the only input was the chemical composition (*i.e*. the type and number of different

atoms and the size of the populations). For practical purposes, it was essential to impose chemically sensible constraints to guide the generation of the initial candidate structures. For CS_2, only structures with carbon-carbon, carbon-sulfur and sulfur-sulfur bonds longer than 1.1 Å, 1.7 Å and 1.9 Å, respectively, were accepted. Searches were performed at 2, 60 and 100 GPa with up to 24 atoms per cell. The population for investigation was 40 structures for CALYPSO and XtalOpt codes and 50 for ASAP. The structural search was terminated if a minimum enthalpy structure persisted over 20 generations. In this work, a total of 30 or 40 generations were needed for each set of structural searches and eventually over 10,000 structures were created and optimized in the procedure.

3.2 Results and discussions at 2 GPa

First we tested the performance of the two structural prediction methods on the known molecular CS_2 crystal structure observed at 2 GPa. To evaluate the efficiency of the computational methods, PSO and GA calculations consisting of 4 CS_2 formula units were performed and the results are summarized in Figure 3.1.

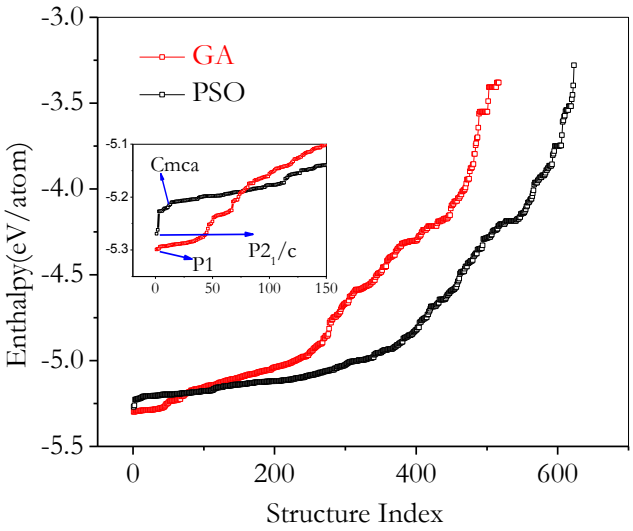

Figure 3.1 Black and Red circles show the enthalpy of optimized structures by PSO and GA, respectively. The enthalpy of the $P2_1/c$ structure was 0.098 eV/atom lower than the *Cmca* structure and the $P1$ structure found by GA had the lowest energy at 2 GPa.

Surprisingly, we found it was not straightforward to find the most stable molecular structure. Over 600 and 500 structures were examined by the PSO and GA methods, respectively. Although the observed *Cmca* structure was found, several structures with lower enthalpies were

predicted. For GA, over 90 structures were found to be energetically more favorable than the molecular structure. Furthermore, GA calculations failed to produce the experimental structure. Although several molecular structures were found, the CS_2 packing of these structures was slightly different from the *Cmca* structure. The results highlight the difficulty in theoretical prediction of the correct crystal structures of weakly interacting molecular solids. It is also significant to know that PSO and GA calculations do not produce exactly the same crystal structures with the same energetic order.

The low enthalpy structures found by PSO and GA are summarized in Figure 3.2. To distinguish different structures of *P*1 space group symmetry, they are labelled alphabetically *P*1-n (n=a,b,c …to g). These structures were characterized by the existence of molecular fragments composed of C-C, S-S, C-S bonds and C-S cyclic rings. The lowest enthalpy *P*1-a structure found by GA was ~0.1 eV/atom lower than the molecular *Cmca* structure. It was composed of ring-like four carbon and one sulfur atoms with separated S_2 molecules. On the other hand, a crystalline $P2_1/c$ structure was predicted to be most stable by the PSO method. This structure is consisted of C-C chains linked to S layers and molecular S_2. This is followed by three ring-like structures composed of 3 C and 2 S atoms in the ring and eventually at higher energies, several molecular structures with different CS_2 packings were found.

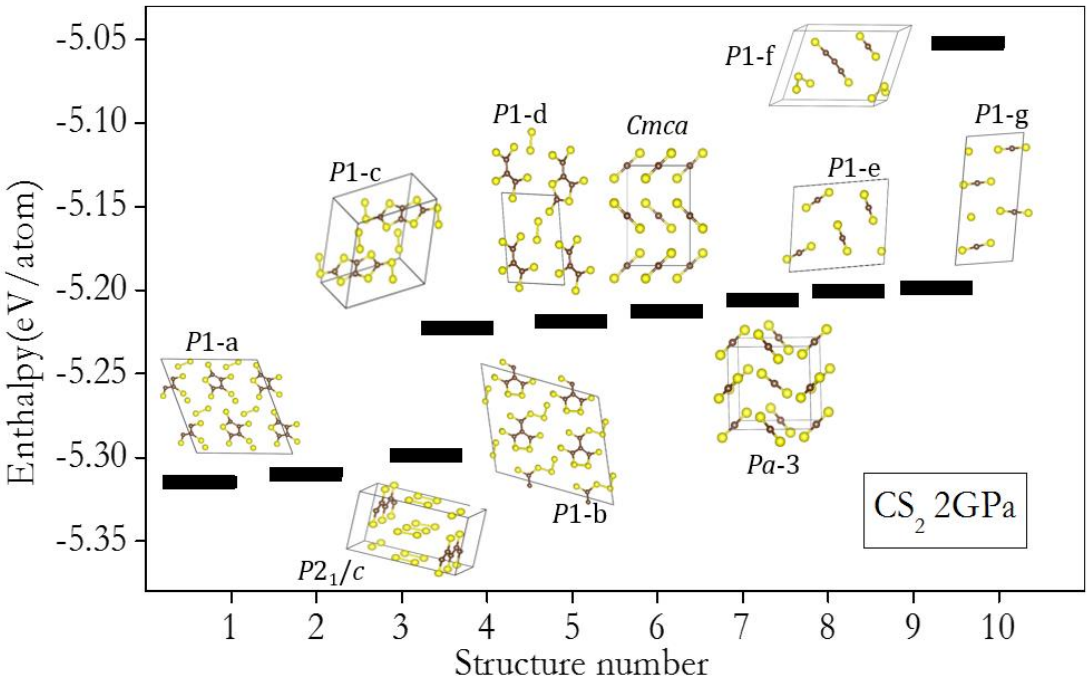

Figure 3.2 Ten lowest predicted enthalpy structures for solid CS_2 at 2 GPa from Ref [148].

To examine the stability of the structures at different pressures, the calculated enthalpies relative to the *Cmca* structure as a function of pressure were compared in Figure 3.3. The results confirm that the *Cmca* structure was indeed not the most stable C-S compound in the pressure range from 0 to 10 GPa. At 0 GPa, the energy of the molecular CS_2 was about 0.03 eV/atom higher than the predicted lowest enthalpy structure.

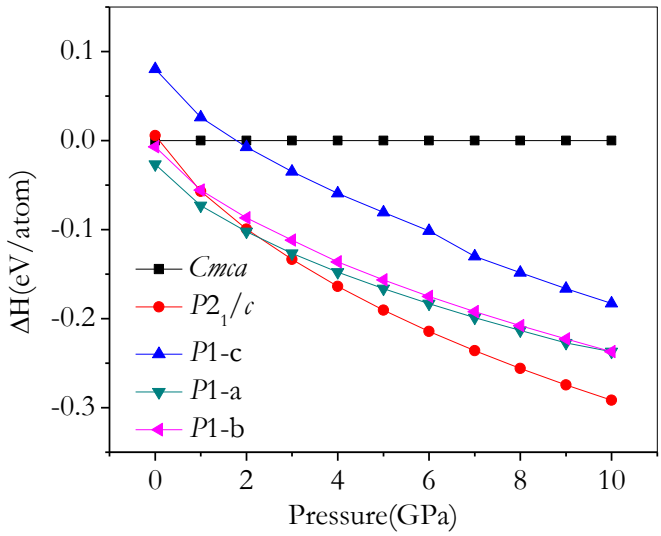

Figure 3.3 Relative enthalpies (ΔH) *vs* pressure for several CS_2 structures, with respect to the *Cmca* structure.

The fact that molecular CS_2 was not the lowest enthalpy structure can be explained by considering the bond energies. Empirical bond energy consideration shows structures with C-C chains and C and S ring units were energetically more favorable than those composed solely of molecular CS_2. Moreover, since a large number of predicted structures had low space group symmetries (e.g. *P*1) it indicates that these structures were probably disordered. Experimentally, crystalline CS_2 was obtained from the condensation of CS_2 molecules. A large energy barrier is expected to break the C=S bonds into molecular fragments of the extended structures and this explains the metastability of the molecular crystal structure. The preference towards the formation of connected extended structures has also been found in a recent theoretical study on solid carbon monoxide (CO). The molecular structure was only found to be stable at ambient pressure. At higher

pressures, polymeric C-O structures were preferred since the C-O triple bond is not energetically competitive with the formation of C-O chains [155].

It is known that van der Waals (vdW) interaction, which was neglected in the PBE functional, may be important in molecular crystals. To examine this effect, geometry optimizations and total energy calculations were performed using the vdW-DF2 functional [167] on several selected structures at 2 GPa. The results reported in Table 3.1 show the vdW functional gave lower total energies for all the structures. However, except for the *P*1-c structure, the relative stability sequence obtained from the PBE calculations remains the same. Therefore, we expected results obtained without inclusion of the vdW functional will not substantially change.

Table 3.1 The calculated lowest enthalpy structures with vdW corrections for CS_2 at 2 GPa.

Space Group	*P*1-a	$P2_1/c$	*P*1-b	*P*1-c	*Cmca*
PBE(eV/atom)	-5.31467	-5.31195	-5.18168	-5.21965	-5.21242
PBE+vdW-DF2(eV/atom)	-5.33501	-5.33366	-5.32610	-5.24672	-5.28835

Several conclusions can be drawn from the structural search for the low pressure structure of CS_2. Although both methods found similar extended structures with C-S cyclic rings, GA found the lowest enthalpy structure and only PSO found the molecular *Cmca* structure. The discrepancy between the results from these two structural search methods may be due to the following reasons: first, the initial crystal structures generated by GA were random with no space group symmetry imposed. This is in contrast to PSO in which the starting structures were generated randomly but subjected to conform to one of the 230 space groups. Therefore, PSO has a tendency to favor crystal structures with high space group symmetry. This explains the structures of PSO in finding the molecular but higher energy *Cmca* structure. Second, the number of structures in a population is very significant. The chance of finding the global minimum increases with the number of trial structures. The smaller number of candidate structures considered in the PSO calculations may explain the failure to find the lower energy ring-like structures. For a reasonable assessment of the performance of the three codes (CALYPSO, XtalOpt and ASAP), the number of structures in the population must be equal. Although both GA and PSO methods succeeded in finding metastable molecular CS_2 structures, the different low pressure crystalline structures predicted by PSO and

GA methods were problematic and prompted us to adopt an alternative protocol for the structural search in the ensuing calculations. First, structural searches were performed using the PSO and GA methods independently in the normal manner. If the two methods produced different energetically most stable structures, these structures were then introduced into both populations and the search was repeated. In this way we could increase the probability that the predicted structure was the global minimum.

3.3 Structures predicted at 60 and 100 GPa

Adopting the strategy described above, two sets of structural searches using PSO and GA were performed. If the global minimum structures predicted by the two methods were different in the first trial, then these structures were included in both populations and the searches were repeated. We then summarized the results obtained at 60 and 100 GPa.

The first structure searches are labelled PSO-I and GA-I and the second searches are labelled PSO-II and GA-II at 60 GPa as illustrated in Figure 3.4a. The first search, PSO-I, found a lowest enthalpy structure ($P2_1/c$) in the 13th generation but GA-I failed to find the same structure. As described above, the $P2_1/c$ structure was then included into the population of the second search (GA-II). Interestingly, a new $P2_1/m$ structure with lower energy was found at the 22nd generation. To ensure that the global minimum was achieved, the search was repeated with PSO-II by including the $P2_1/m$ structure in the population. We found this structure remained as the lowest enthalpy structure after 21 consecutive generations. At 100 GPa, once again the first searches are labelled PSO-I and GA-I. In PSO-I, the lowest enthalpy $P1$ structure (Figure 3.8, #4) was found in the 8th generation. Again, GA-I did not predict the same structure. On comparing the PSO-I and GA-I results, we found that a majority of the low energy structures predicted by PSO-I had one very long crystal axis and possessed no space group symmetry (*i.e.* $P1$). Since an axis in the GA-I search was constrained to be at most twice the length of the other two axes, we relaxed this constraint in the second search (GA-II). This resulted in a significant change in the predicted structures. The lowest enthalpy structure predicted by GA-II is shown in Figure 3.8, #3. Surprisingly, the $P2_1/c$ structure found at 60 GPa did not appear in the PSO and GA searches at 100 GPa. Additional calculations found the enthalpy of the $P2_1/c$ structure was lower than all the optimized structures at 100 GPa. Therefore, this structure was included in the population in the third round of structure searches (GA-III) and the $P2_1/m$ structure was again found in the 13th

generation. Eventually $P2_1/m$ was included into the population of the PSO-II search and its structure remained the most stable after 21 generations.

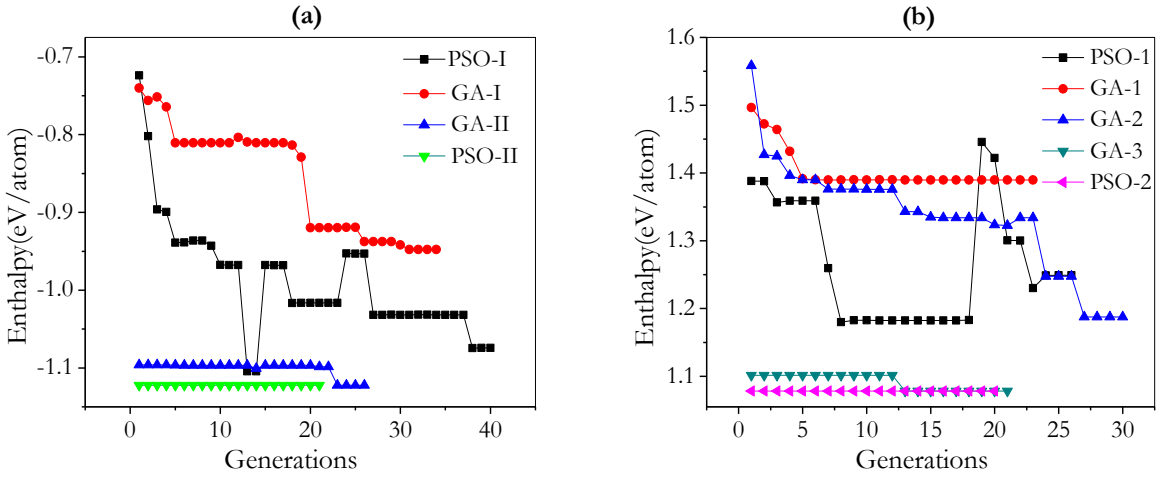

Figure 3.4 Enthalpy of the best structure versus generation for CS_2 at (a) 60 and (b) 100 GPa.

We can conclude that despite the often-claimed reliability of both GA and PSO methods, comparative tests are definitely required in order to ensure the lowest enthalpy structure. Now we return to the discussion of the crystalline $P2_1/m$ and $P2_1/c$ structures obtained from PSO and GA calculations. As shown in Figure 3.5, $P2_1/m$ was constructed from a C-C layer sandwiched between two S layers linked in the third dimension by C-S bonds. The C-C layer consisted of hexagonal rings in a chair conformation. Remarkably, a $P2_1/c$ structure with a very similar bonding pattern as the $P2_1/m$ was also found. To accommodate chemical bonding with the C layer arranged in the chair form in the $P2_1/c$ structure, the square net in the S layer was distorted. In comparison, the square nets in the $P2_1/m$ structure fit well to bond with C atoms in the chair conformation. The fact that a small difference in the 2D packing of S layers can affect the energy of the crystals illustrates that C-S bonding is important to the stability of the high pressure phases.

Several structures within an energy window of ~0.2 eV/atom at 60 GPa are shown in Figure 3.6. Predicted structures within a small energy interval often clustered into groups with similar local bonding patterns. For example, we found two structures within < 0.05 eV/atom ($C2/m$ and $C2/c$) of the $P2_1/m$ structure having similar carbon packing patterns. The major difference of these structures from $P2_1/m$ was their increasingly closed pack from squares to rhombuses ($C2/m$) and hexagons ($C2/c$) in the S layers. At higher energy, the chemical bonding in the solids changed

to a group of structures with disconnected mixed C-S regions and finally molecular fragments with C-C bonds starting to emerge. At this pressure, CS_2 molecules decomposed into segregated C and S regions.

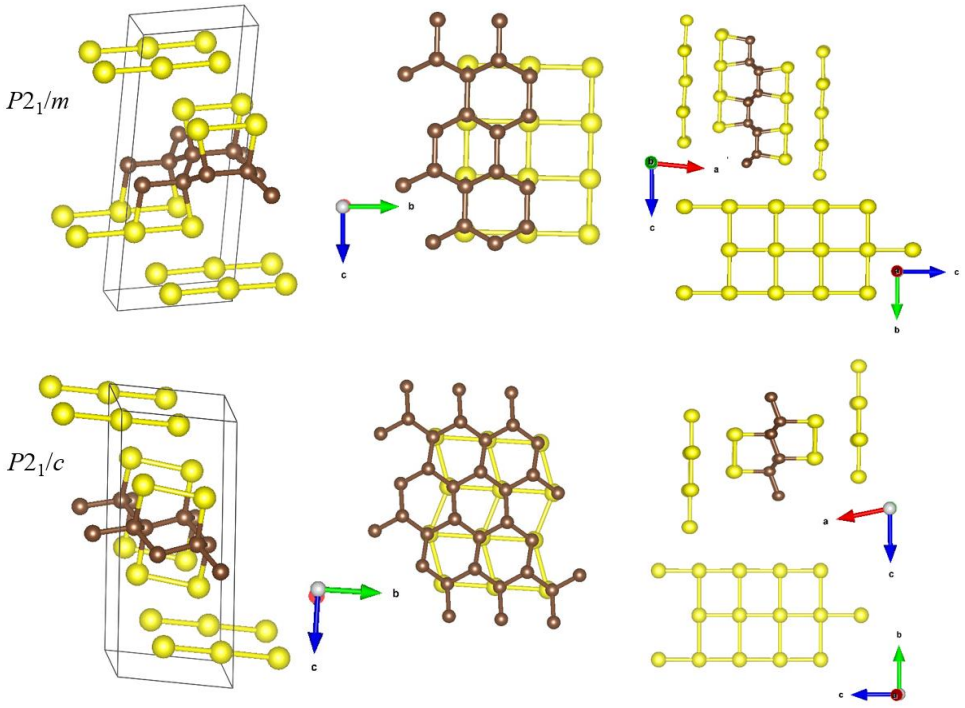

Figure 3.5 Comparison of the $P2_1/m$ and $P2_1/c$ structures at 60 GPa.

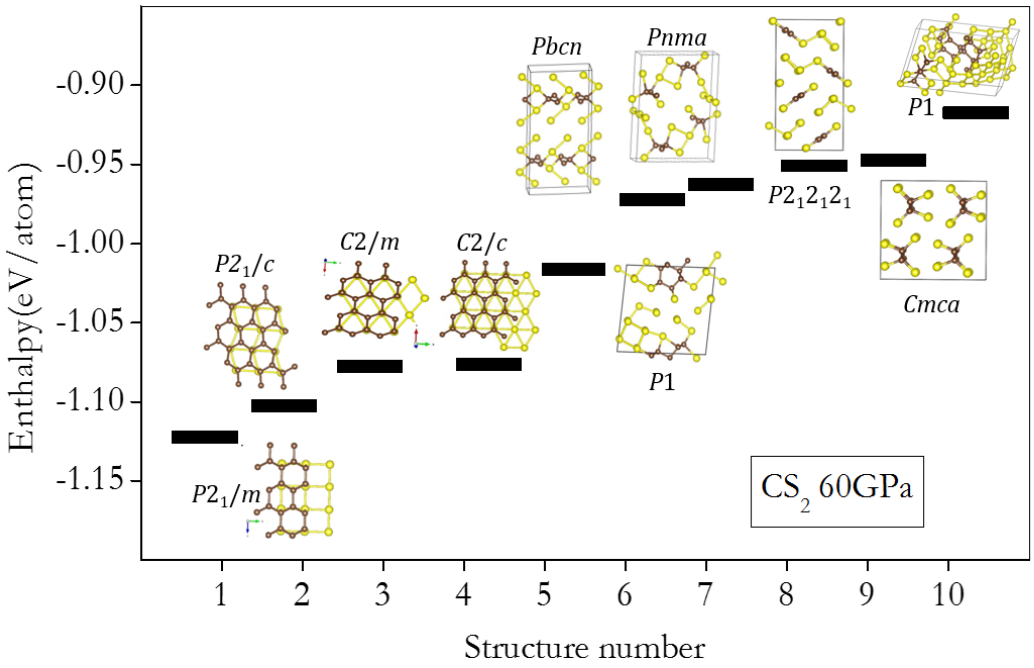

Figure 3.6 Ten lowest predicted enthalpy structures for solid CS_2 at 60 GPa from Ref [148].

There is limited experimental information on the structure of the high pressure metallic phase of CS_2. X-ray powder diffraction experiments performed at 55 GPa show that two broad peaks centered at 2.8 and 4.8 $Å^{-1}$ is typical of a disordered solid [164]. In the previous study, following the high pressure transformation sequence observed in the analogous solid CO_2, it is proposed that the disordered phase (Figure 3.7) had distorted tridymite $P2_12_12_1$ or chalcopyrite (I-42d) structures [158], [168]. These structures were not found in the search. Separate calculations show it had a substantially higher enthalpy of 0.2 eV/atom than the $P2_1/m$ structure. Indeed, four C-S bonds were not found in the low enthalpy structures.

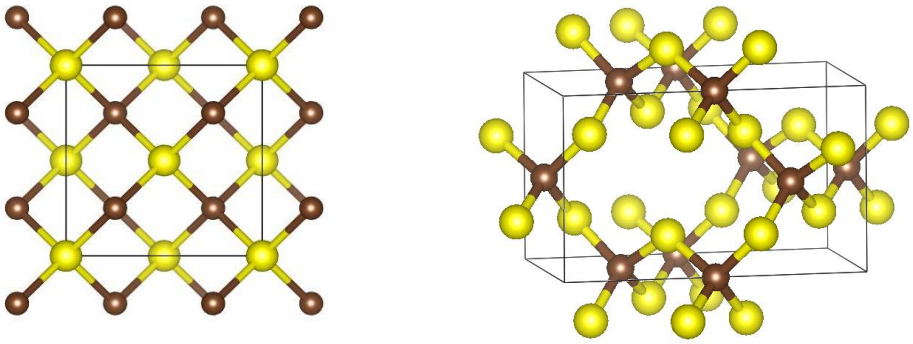

Figure 3.7 The proposed structure of α-tridymite ($P2_12_12_1$, left) and α-chalcopyrite (I-42d, right) at 60 GPa.

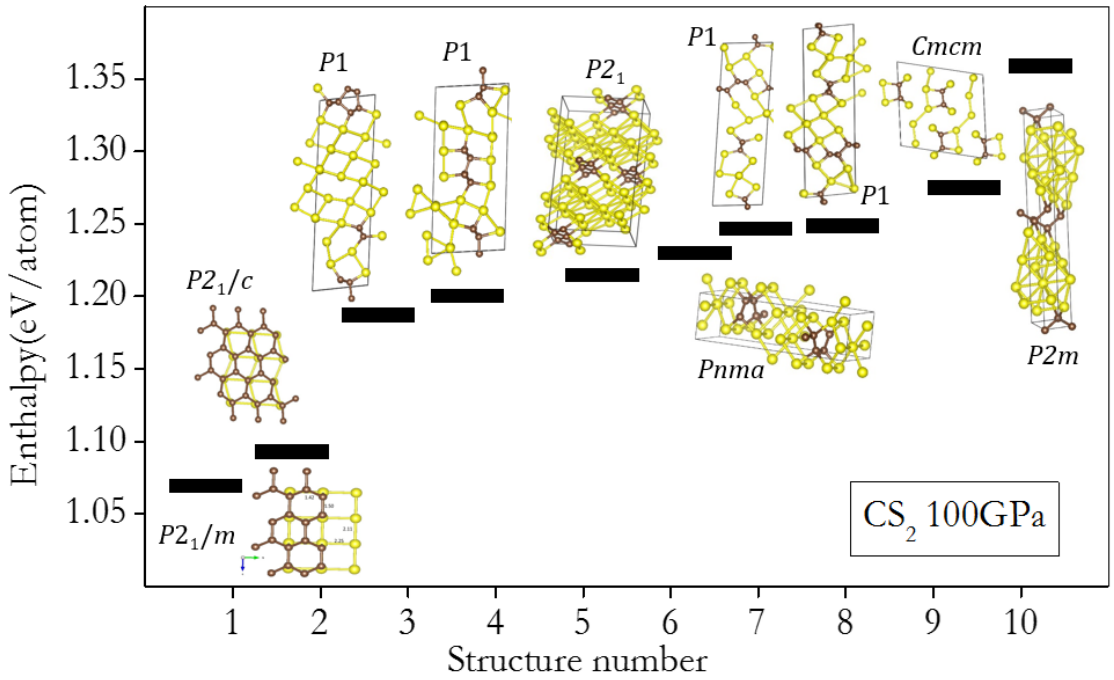

Figure 3.8 Ten lowest predicted enthalpy structures for solid CS_2 at 100 GPa from Ref [148].

To investigate the suggestion of unusual hypervalent carbon atoms in the structure above 100 GPa [165], structural searches were performed following a similar procedure described above. It was found that the $P2_1/m$ crystalline structure remained as the most stable. This was followed by the $P2_1/c$ structure. In the next group of structures with much higher enthalpy (< 0.12 eV/atom), instead of separate C and S layers, we found they consisted of C clusters embedded in the 2D plane composed of S atoms (Figure 3.8), while the second group of $P1$ structures tended to form ring-like C-C with a sulfur sub-network. The higher energy structures like $P2_1$ and *Pnma* were not composed of ring-like C atoms.

3.4 Molecular dynamics simulations

To complement the structural prediction calculations, we compressed the molecular CS_2 structure to high pressure with constant-pressure (*NPT*) molecular dynamics (MD) at 300 *K*. The motivation for the additional calculations was that under the experimental conditions the phase transition may follow a low energy path. Therefore, the observed structures determined by the kinetics and the energy landscape might likely be the precursor and product. In some cases, the predicted lowest enthalpy structure from the search techniques (*i.e*. PSO and GA) might not be realized.

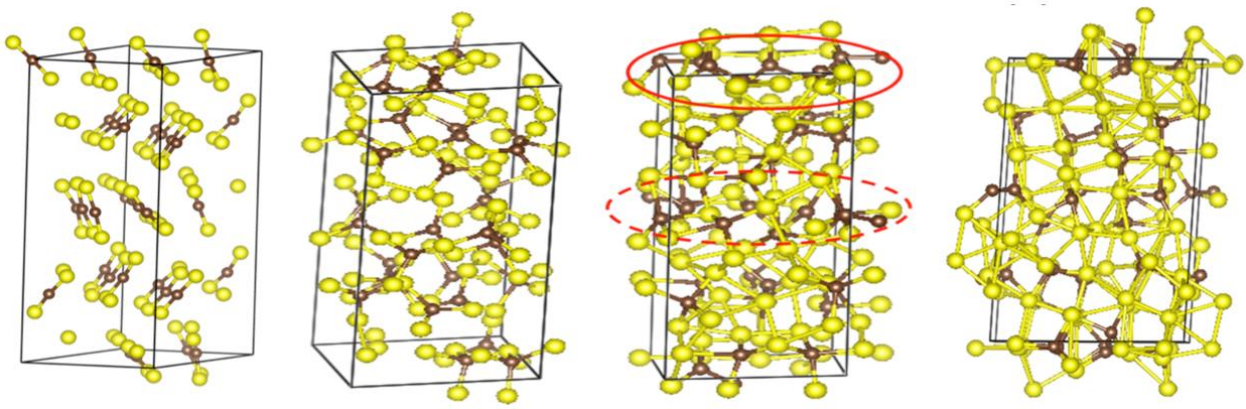

(a) 10GPa (b) 20GPa (c) 80GPa (d) 120GPa

Figure 3.9 Snapshot of molecular dynamics calculations on CS_2 from Ref [148]. (a) 10 GPa, (b) 20 GPa, (c) 80 GPa and (d) 120 GPa. The red circle highlights the formation of C-C "clusters" at 80 GPa. The occurrence of S square nets is clearly seen at 120 GPa.

Upon compression, the molecular *Cmca* structure was found to transform into a disordered 3D solid connected by C-C, C-S and S-S bonds (Figure 3.9b) at 20 GPa. Upon further

pressurization to 80 GPa, MD calculations revealed the existence of segregated C and S regions (Figure 3.9c). A layer of C-C was arranged between two S layers. This structural feature was similar to the $P2_1/m$, which was constructed from a C-C layer sandwiched between two S layers. At 120 GPa, planar square networks formed by S atoms were almost fully developed (Figure 3.9d).

3.5 Stability of the predicted structures

As discussed above, the $P2_1/m$ structure 2D planar square network of S layers was distorted to rhombus in the $P2_1/c$ structure. This feature affected the stability of the $P2_1/c$ structure making it unstable. The phonon-band structure of the $P2_1/c$ (Figure 3.10) shows imaginary modes along the A→ B and B→ D symmetry directions. Therefore, the structure is not stable and we do not further examine the properties of the $P2_1/c$ structure.

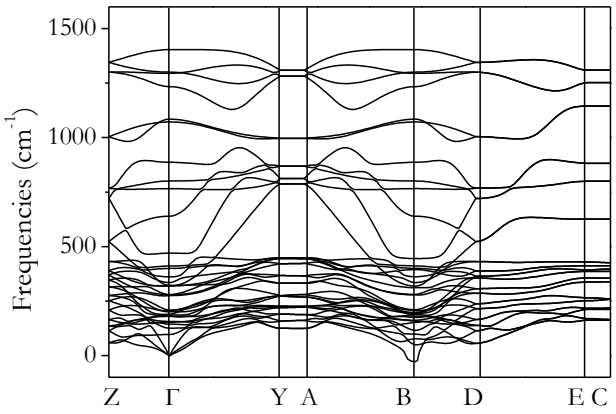

Figure 3.10 The phonon-band structure for the $P2_1/c$ structure of CS_2 at 60 GPa.

We now compared the molecular *Cmca* structure with the crystalline $P2_1/m$ structure. This structure becomes more stable than the crystalline molecular *Cmca* phase at pressures higher than 10 GPa (Figure 3.11). This result is consistent with the experimental findings [164] and the MD calculations shown in Figure 3.9a indicate that the molecular CS_2 is still stable at 10 GPa.

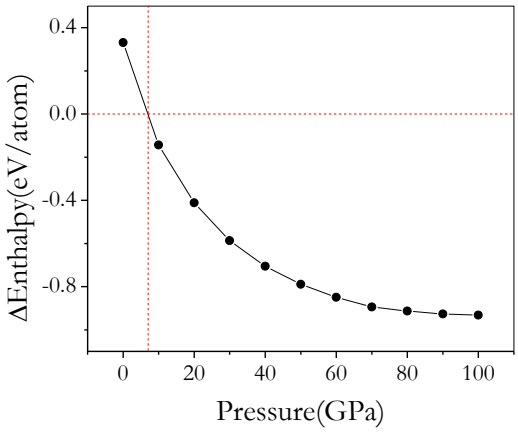

Figure 3.11 Relative enthalpy of molecular CS_2 with respect to *Cmca* structure.

3.6 Radial distribution functions

To compare the predicted structures with the experiment at 60 GPa, the calculated static structure factor, $S(q)$, for the crystalline $P2_1/m$ (broadened by a linewidth of 0.5 $Å^{-1}$ to mimic the disorder) and several low enthalpy structures were calculated (Figure 3.12a). Similar to the experiment, all the calculated diffraction patterns show two bands at ~ 2.8 and 4.8 $Å^{-1}$. The $P2_1/m$ structure shows an additional weak feature at ~ 4 $Å^{-1}$. The calculated pair distribution functions (PDF) and $G(r)$, are in agreement with the experimental assignment (Figure 3.12b). Previously, [164] the first peak in the radial distribution function (RDF) was assigned to the nearest C-S distance at ~1.7 Å and the second peak to neighbouring S-S distances at around 2.77 Å. These two features can be related to the calculated peaks at 1.5 and 2.6 Å. Inspection of the lowest energy structures can be attributed the first peak in the PDF to C-C bonds where the S-S distances are between 2.13-2.89 Å and the second-nearest neighbour C-C and C-S bonds distributed between 2.33-2.81 and 2.56-2.95 Å, respectively. The $S(q)$ and $G(r)$ obtained from the MD structure and the structural assignments are also consistent with the predicted structures and experiment. Unfortunately, the rather limited information from experiment precludes an unambiguous determination of the structure. Although, the observed high pressure disordered phase at 60 GPa is likely to be segregated into C- and S-rich domains linked by C-S bonds as predicted.

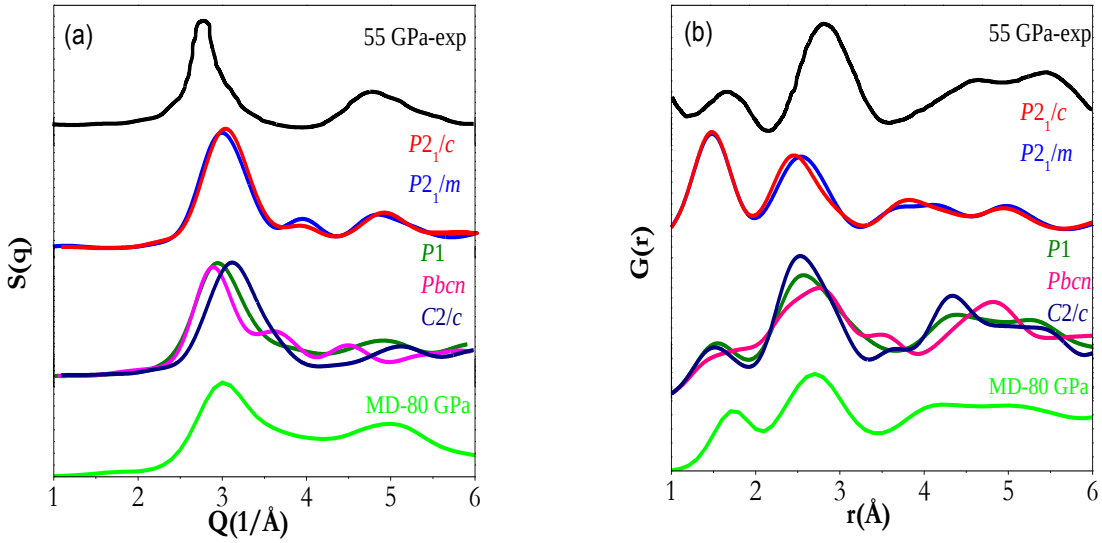

Figure 3.12 (a) Structural factor and (b) radial distributional function of solid CS_2 at 55 GPa from Ref [148].

In the experimental pair distribution function ($G(r)$) derived at 103GPa [165], the peaks at 1.9 and 2.7Å were assigned to the first nearest neighbour C-C, C-S distances and the second nearest neighbour C-C at 3.84 Å and C-S at 4.7 Å. Based on the assignments, an octahedral local configuration with six coordinated C atoms (Figure 3.13) was hypothesized. The theoretical $G(r)$ of several low enthalpy structures were compared with results obtained from experimental diffraction patterns at 103 GPa (Figure 3.13). The calculated $G(r)$ reproduced all the main features of the observed distribution function. The structure obtained from MD calculations also supported these assignments. Analysis shows the first observed peak can be attributed to the C-C distances. However, the second broad peak contains contributions from both second nearest neighbours of C-S and C-C and the first nearest neighbour S-S distances. Although the second nearest neighbour C-C was located at 3.84 Å in the crystalline $P2_1/m$ structure, the dominant peak in the experimental $G(r)$ also contained overlapping C-C, C-S and S-S bond distances. The peak at 4.7 Å was assigned to the next nearest C-S separation. We also examined predicted structures with much higher enthalpy. All features in the $G(r)$ derived from the experimental diffraction pattern can be explained adequately with a structure consisting solely of tetrahedrally coordinated C atoms. No evidence of the existence of six coordinated carbon atoms was found. Moreover, the proposed structural pattern, constructed from alternate C and S atoms at the corners (Figure 3.13) of a square net, was not found in any of the predicted structures.

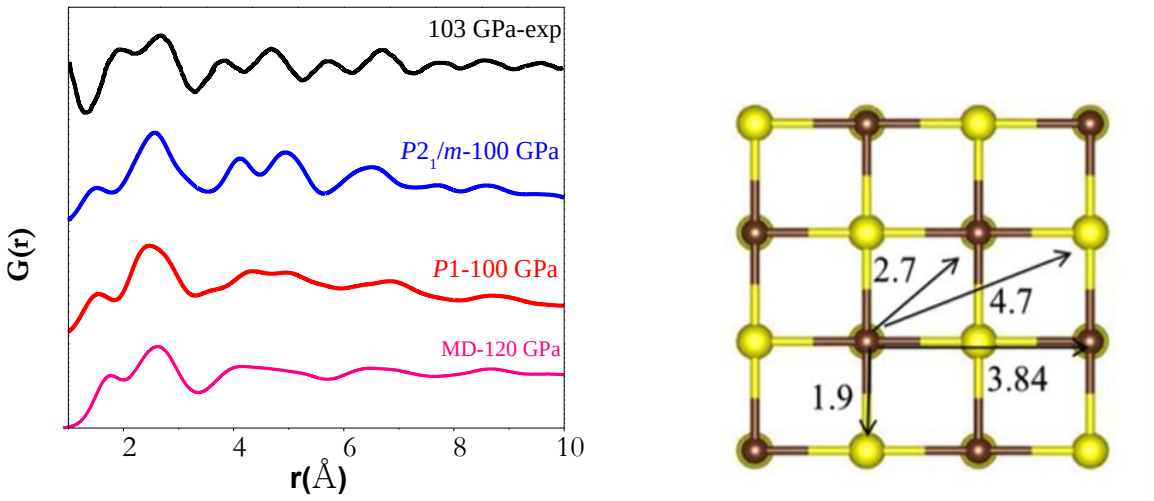

Figure 3.13 (Left) Radial distributional function of solid CS_2 compared with experimental data from Ref [148]. (Right) Six coordinated C structure of CS_2 proposed in Ref [165].

The $G(r)$ based on the diffraction pattern provides information on atom arrangement in the short and intermediate order. Undoubtedly, the experimental high pressure structure was non-crystalline. However, in view of the gross agreement between the experimental and calculated $G(r)$ of the predicted crystalline $P2_1/m$ and several energetically competitive structures, and with the disordered structure obtained from MD calculations, it is probable that the observed structure was composed of segregated C-C and S-S regions linked by C-S bonds with the latter forming 2D square nets or even micro-crystalline domains of the $P2_1/m$ phase.

3.7 Electronic and vibrational properties

We now examined the electronic structures of the high pressure phases. Apart from the structural similarities, the calculated electronic density of states (DOS) of both the crystalline $P2_1/m$ and the disordered MD structure show the electronic DOS near the Fermi level was also dominated by the S valence 3*p* and 3*d* orbitals (Figure 3.14).

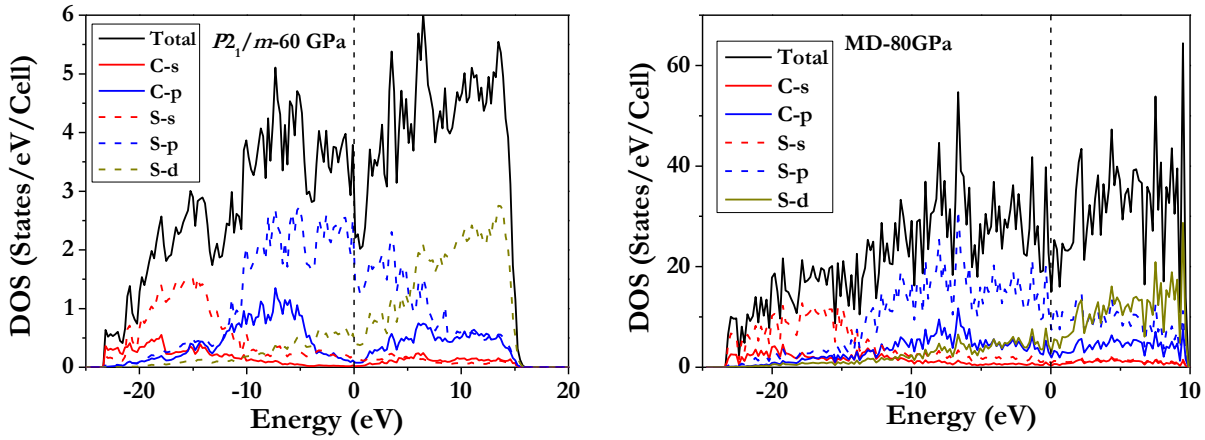

Figure 3.14 Calculated electronic density of states for the $P2_1/m$ and MD structures at 60 and 80 GPa, respectively.

Since electron-phonon coupling is determined by electronic states lying within a thin shell near the Fermi surface, it is not unreasonable to explore the origin of the superconducting behavior in the experimental disordered phase using the crystalline $P2_1/m$ structure as a model. Density functional perturbation theory and frozen phonon calculations were performed to establish the stability of the $P2_1/m$ structure (Figure 3.15). At 60 GPa, no imaginary frequency was found with either methods, indicating that the structure is dynamically stable.

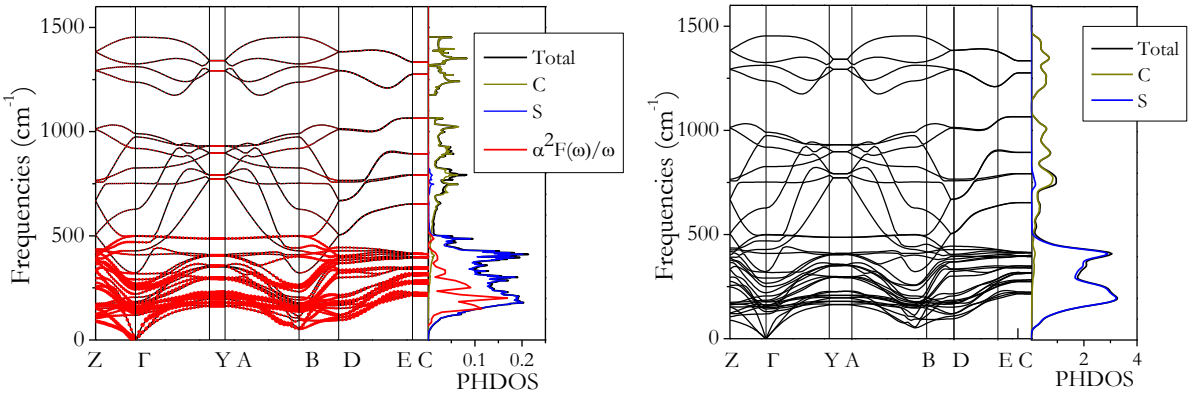

Figure 3.15 Calculated (left) phonon band structure and Eliashberg spectral function ($\alpha^2F(\omega)$) with DFPT, Ref [148], and (right) phonon band structure with FP method.

Inspection of the phonon dispersion curves shows that soft phonon modes, reminiscent of Kohn-anomalies, are found at the B and D symmetry points (Figure 3.15). The projected

vibrational density of states onto C and S atoms for the $P2_1/m$ phase are also presented. As expected, the low frequency modes were dominated by S-S vibrations due to the heavier atomic mass. The DOS of the $P2_1/m$ structure, depicted in Figure 3.14, shows unequivocally that it is metallic. The DOS near the Fermi energy was dominated by low-lying S-3*p* states. This is a consequence of the S-rich regions in the structure, a distinctive feature shared by all the predicted low energy structures. For this purpose, the electron-phonon coupling parameter (λ) and the logarithmic average phonon frequency (ω_{ln}) at 60 GPa were calculated using the linear response theory. The individual interatomic force-constant matrix and electron-phonon coupling matrix were calculated employing the linear response method at a 1×3×2 *q* point mesh with a 4×12×8 *k* point mesh for the first Brillouin zone integrations, and the plane wave cutoff was chosen as 60 Ry. At 60 GPa, the calculated coupling parameter λ is 1.04 with an average phonon frequency ω_{ln} of 341 K. Using the strong-coupling Allen-Dynes equation, an extension of the McMillan theory [169], and nominal Coulomb pseudopotential parameter (μ^*) with values of 0.1, 0.12 and 0.15, the estimated superconducting critical temperatures T_c are 25 K, 22.8 K and 19.5 K, respectively. These values are slightly higher than the observed 5.6 K. The origin of the superconductivity is revealed from the calculated Eliashberg spectral function: $\alpha^2F(\omega)/\omega$ [170]. As shown in Figure 3.15, nearly 100% of the electron-phonon coupling was contributed by S-S vibrations in the frequency region from 0–500 cm^{-1}. The strong interactions have led to a pronounced peak in the spectral function at 200 cm^{-1}. In addition, we also computed the phonon line widths and nesting functions $\xi(q)$ (Figure 3.16). The *k* points were sampled uniformly on the Fermi surface and a broadening of 0.05 was used in the Gaussian function to represent the δ function. The calculation employed 200 *k* points and 134 *q* points, which resulted in the evaluation of energy, ε_{k+q}, at 26,800 points. In the square planar S-S layers, strong nesting was found approximately midway from $\Gamma \rightarrow Y$, $D \rightarrow E$ and at the B symmetry point.

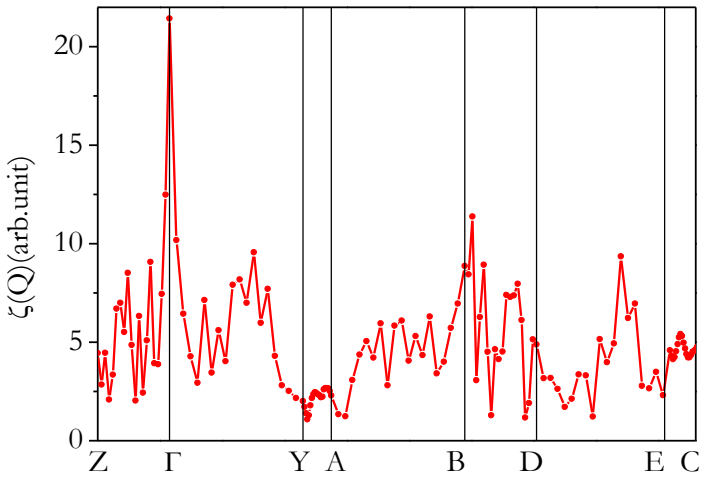

Figure 3.16 The nesting function ξ(q) of $P2_1/m$ CS_2 at 60 GPa along selected high symmetry lines of the nesting vector, *q*.

The superconductivity in high pressure CS_2 is a consequence of the S-S bands dominating the Fermi level. Further electronic and superconductivity calculations on the $P2_1/m$ structure were also performed at 80 and 100 GPa. The electron and phonon band structures are very similar to those at 60 GPa (Figure 3.17). It is remarkable that using a μ* of 0.12, the predicted T_c at both pressures is 13 K. This result is in accord with the almost constant T_c of 6 K reported from 60 – 172 GPa [165]. In passing, we also performed spin-unrestricted calculations on several low enthalpy structures and no stable magnetic state was found. However, since the electronic calculations were performed at 0 K, the results do not preclude possible magnetism at finite temperature.

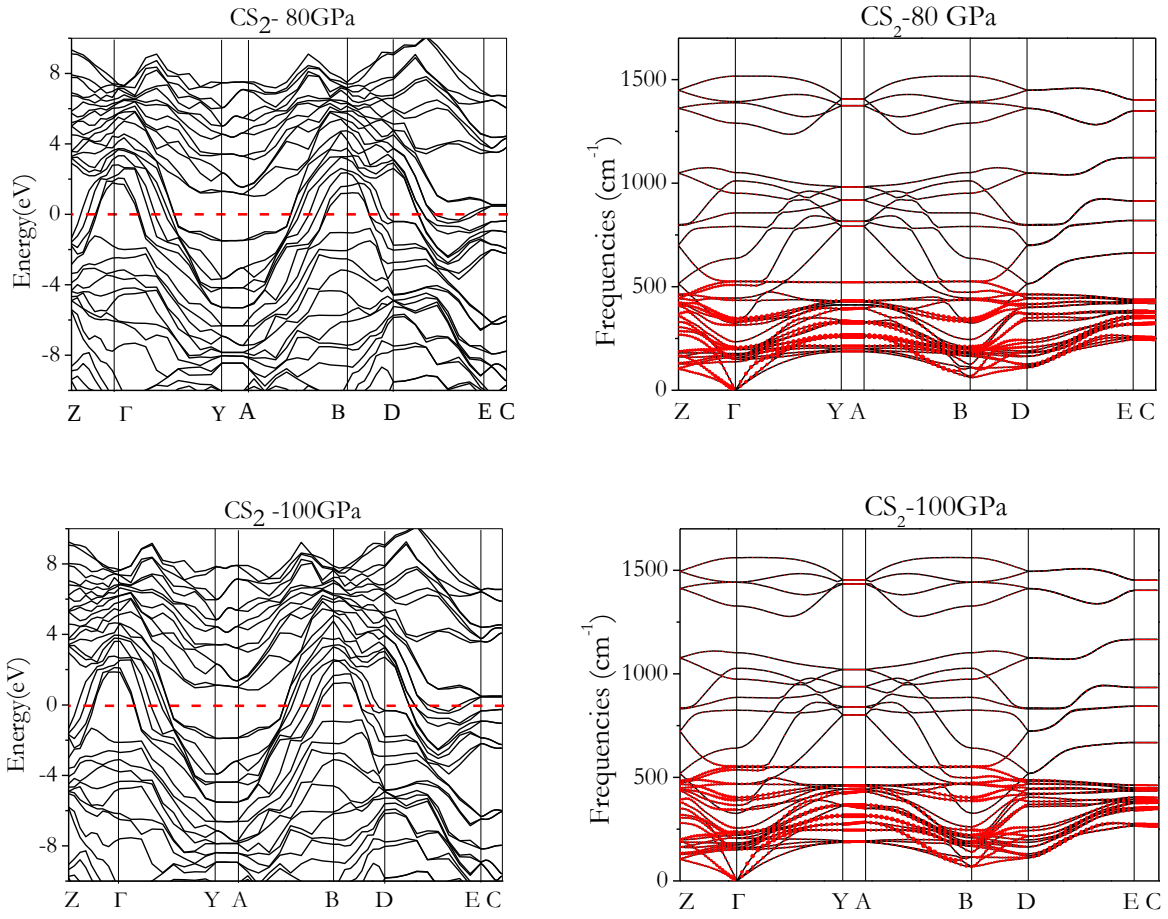

Figure 3.17 Phonon and electronic band structures of the $P2_1/m$ structure, at 80 and 100 GPa.

3.8 Conclusions

Structural search calculations indicate that molecular CS_2 will decomposes and segregates into C and S regions in the solid state at high pressure. The carbon atoms tend to form fused hexagonal rings either in the boat or chair conformation, akin to hexagonal and cubic diamonds, respectively. On the other hand, the sulfur atoms adopt a planar closed pack arrangement forming 2D square or hexagonal networks. Intuitively, it is logical to expect it is energetically favourable to form regions with diamond-like and sulfur-like sub-structures at high pressure. A crystalline structure with the $P2_1/m$ space group was found to be most stable between 60-120 GPa. This structure is metallic and superconductive with a T_c of 20-13 K from 60-120 GPa. The superconductivity is mainly due to electron-phonon coupling in the S layers. The measured diffraction pattern ($S(q)$) and the derived pair distribution functions ($G(\underline{r})$) at 55 GPa and 103 GPa can be reproduced from the predicted low enthalpy structures with 2D S-layers. The theoretical

results show the low enthalpy structure is non-magnetic and no evidence of six coordinated carbon atoms above 100 GPa was found.

It is pertinent to comment on the structural similarity in disordered CS_2 with the superconductive [171] phase-V of elemental sulfur [172]. Under compression, S undergoes a series of structural transformations. Between 83 – 253 GPa, a metallic state with superconductivity in an incommensurate structure was observed. The existence of closed pack S atom layers is a feature common to the predicted disorder high pressure structure of CS_2 presented here and S-V. In the former case, the S atoms are arranged in a hexagonal closed pack but cubic pack in the latter. It is evident that delocalization of electrons in planar S-layers is the essential ingredient for the superconducting behaviour. Recently, a very high T_c (*ca*. 190 K) has been found in hydrogen sulphide (H_2S) compressed to 200 GPa [173]. It is suggested that the high pressure phase is composed of decomposed H_2S. From the results obtained here, we speculate that similar S-layers are formed and strong electron-phonon coupling in these layers and with the hydrogen atoms may be the reason for the very high T_c.

CHAPTER 4

Crystal structures and electronic properties of Xe and Cl compounds at high pressure

Until the early 1960s, it was believed that only electrons in the partially filled outer shell (valence electrons) could participate in the formation of chemical bonds. Since the discovery of argon in 1894, noble gases with completely filled valence shells were thought to be unreactive and only exist as monoatomic elements. The stability and unreactive nature of octet valence configurations of these elements imposed a new law in science in 1916: "Nothing can force a noble gas (Ng) atom into a chemical bonding" [174], [175]. About half a century later, one of the most important discoveries in chemistry was made by Bartlett in 1962 [176]. It was found that Xe could form chemical compounds with oxygen and fluorine, which are two electronegative elements. These findings attracted great interest in the possibility of synthesizing a variety of compounds from Xe. Recent studies propose that less than 10% of the expected amount of Xe exists in the Earth's atmosphere while the missing Xe is probably found in the interior of the planet [177], [178]. Since chemical reactions in the Earth's core occur under extreme pressures and temperatures, they may lead to the formation of unusual or unexpected Xe compounds [179]. The objective of this project is to investigate the possible existence of Xe-halide compounds under high pressure.

The most studied Xe-halide is xenon fluorine. Recently, it was reported that the linear insulating XeF_2 solid transforms to a graphite-like semiconducting hexagonal layered structure at 22 GPa; above 67 GPa a metallic phase of Xe-F was observed [180]. In a theoretical study, D. Kurzydzowski *et al,* [181] found a structure maintaining the linear XeF_2 molecules have much lower enthalpy than the reported experimental phase below 100 GPa. The stability of XeF_n compounds with respect to decomposition into Xe and F_2 has been established up to 200 GPa from both theoretical and experimental studies. In comparison to XeF_n, the high pressure chemistry of other Xe-halides such as Cl, I and Br remains largely unexplored. A brief report on the synthesis of Xe-halide compounds with pressure up to 60 GPa and high temperature was published in 2012 at HPCAT workshop [182]. However, the structure of the Xe-halide has not yet been confirmed. The purpose of this study is to search for new promising structures of Xe-halide compounds at high pressure using first principle electronic structure calculations. In this chapter, we report the phase stabilities of stoichiometric $XeCl_n$ (n=1,2,4) up to 60 GPa. For each system, this is followed

by a discussion of the electronic, optical and vibrational properties of stable structures. Since experimental and theoretical results for high pressure XeF_2 are already available, we focused of the $XeCl_2$ calculations in the initial study.

4.1 Computational details

Structural searches were performed using two methods: the PSO method implemented in the CALYPSO code [87] and the genetic algorithms (GA) within the ASAP code [94]. As described in Chapter 1, to reduce the search space, minimum inter-atomic distance constraints were applied to generate the initial structures and were maintained during the structural searches. In all XeH_n calculations (H= Cl, Br and I), the minimum distances between xenon-xenon, xenon-halogen and halogen-halogen atoms were set to 2.9 Å, 1.9 Å and 1.2 Å, respectively. Structural optimizations, optical spectra and electronic structure calculations were performed with the VASP code [36], [37]. During the initial structural search, coarse *k* point meshes were chosen. The potentials of atoms were described using PAW within the PBE exchange-correlation as implemented in the VASP code [34]. The valence electron configurations s^2p^5 for halogens and s^2p^6 for xenon were used. The reliability of the PAW potentials have been checked against all electron calculations to ensure that the results are valid within the pressure range (10 to 60 GPa) studied (Figure 4.18). To achieve better geometry and energy convergence, much higher *k* point meshes with a tighter force criterion less than 1 meV/Å were used in further calculations on promising candidate structures. The plane wave basis energy cutoff was set to be 500 eV. Phonon band structures were calculated using the supercell approach [64], [166] and/or DFT perturbation theory [183]. In the supercell method, Hellmann-Feynman forces were calculated from a supercell constructed from replicating the optimized structure. Dynamical matrices were computed using the PHONPY code [184]. In selected cases, convergence of phonon band structures with the supercell sizes were examined and compared with the DFT linear response method. In the DFPT approach, the phonon spectra were calculated using VASP and QUANTUM ESPRESSO codes [185]. Accurate electronic band structures of Xe-halides were calculated with the GW method and the results were compared with the PBE approximation. Optical absorption spectra of structures were calculated by solving the Bethe-Salpeter equation (BSE) using the GW eigenvalues.

4.2 Thermodynamic stability of $XeCl_n$ (n=1, 2 and 4)

We first investigated the phase stabilities of $XeCl_n$ in the Cl-rich region by computing the formation enthalpy from 10 to 60 GPa. The enthalpies of formation of candidate structures at given pressures were calculated using the following formula:

$$\Delta H(XeCl_n) = [H(XeCl_n) - H(Xe) - nH(Cl)]/n \quad (4.1)$$

Where ΔH is the enthalpy of formation per atom and H is the calculated enthalpy per formula unit of $XeCl_n$ with respect to the decomposition into Xe and molecular Cl_2 solids at the same pressure. Previous studies report that the fcc structure of Xe is stable at room temperature up to at least at pressure of 55 GPa [186], [187] and the molecular structure of Cl_2 with the *Cmca* space group is stable up to 142 GPa [188]. To compute the enthalpy differences, the *Cmca* phase of Cl_2 and fcc phase of Xe atoms were optimized in the pressure range studied. The stability of the predicted lowest enthalpy structures at different Xe-Cl stoicheometries is compared with the convex hull plot shown in Figure 4.1. The results show that below 50 GPa all the predicted compounds are thermodynamically unstable with respect to solid Xe and Cl_2 since the predicted structures have positive formation enthalpies (ΔH). In apparent contradiction to the theoretical prediction, experimentalists have found that a solid solution of Xe and Cl_2 can be formed above 15 GPa at high temperature [189]. As will be shown below, the calculations show when the pressure is increased above 50 GPa, XeCl and $XeCl_2$ structures can be formed. In the following section we discuss in detail the structures and properties of the lowest enthalpy phases of $XeCl_n$ (n=1,2 and 4) obtained from this structural search.

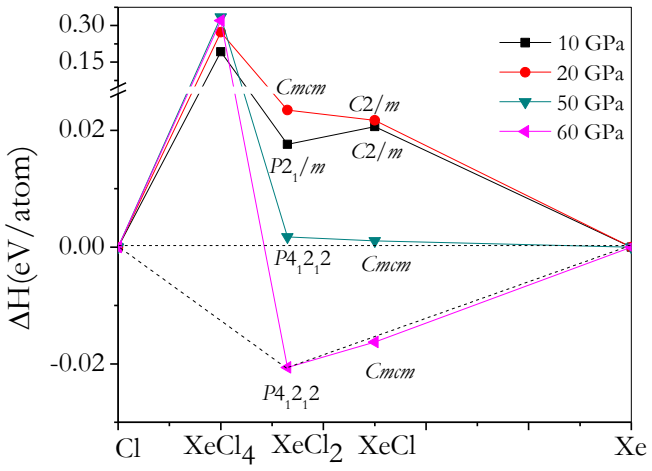

Figure 4.1 Predicted thermodynamic stabilities of $XeCl_n$ (n=1,2 and 4) compounds.

4.3 Predicted high pressure structures of $XeCl_2$

In this section, results of the structures, energetics, electronics and phonon properties of $XeCl_2$ in the pressures range from 10-60 GPa are reported and discussed. One of the objectives of the study is to explore and compare the efficiency and reliability of the PSO and GA methods. For this purpose, several tests were performed with $XeCl_2$ as a model to ensure that the global minimum is found in the structural search. As mentioned in Chapter 1, the structural search was terminated after a minimum energy structure was found and no new lower enthalpy structure appeared for at least 20 successive generations. For the PSO method, we also examined the effect of the population size with models consisting of 40 and 50 structures with 4 $XeCl_2$ formula units. To monitor the progress of the search, enthalpy of the most stable structure found in each generation was plotted for both GA and PSO calculations. The structural searches are labelled PSO-p(x)-n and GA-p(x)-n, where "x" is defined by the population size (40 and 50 structures) and "n" denotes the number of the trial (I, II or III). The results, illustrated in Figure 4.2, show that except in 30 GPa calculations, the larger population (50 structures) reached the most stable structure with fewer generations. This observation suggests that the PSO procedure is more efficient in finding the global minimum with a large population. The reason may be that a richer variety of random structures are generated by the method and helps to sample broader regions of the potential energy landscape. In addition, structural diversity is also desirable to avoid trapping during the structural search at local minima in a large population. However the obvious shortcoming is that since more structures must be optimized in a larger population, the calculations become lengthier. As will be shown below, in this case, it appears that populations of 40 and 50 structures are adequate.

Increasing the number of atoms (formula units) in the model will increase the number of degrees of freedom. To test the efficiency, we considered two different models consisting of 4 and 8 formula units per unit cell with the same population size (40 structures) at 20 GPa. In Figure 4.2b, the PSO-p40-III results indicate that the 24 atom calculations failed to predict the lowest energy structure even after 35 generations. In comparison, the PSO-p40-I calculations were repeated with 12 atoms and found the most stable structure in the 8^{th} generation. As expected, increasing the system size demands more generations to fully explore the energy landscape. Therefore, a "global" minimum structure is easier to find in a smaller model with fewer degrees of freedom. However,

very small structural models with a few atoms may lead to false results. From the limited test, we may conclude that 4 formula units in this case are adequate for this system.

At 30 GPa, the GA method with a population of 50 structures (GA-p50-I) failed to find the minimum energy structure found by PSO. The GA search was trapped at a local minimum even after 40 generations. The GA-p50-I run in Figure 4.2c shows that the structure found in the 10^{th} generation has high enthalpy. In this case, we attribute the failure to the inefficiency of the GA evolution operators (*i.e*. heredity, permutation and mutation). These operators were not able to successfully explore different regions of the energy landscape. This observation is similar to our prior experience on the CS_2 study when GA did not find the lowest enthalpy structure at the first trial. The most favorable structure predicted by the PSO search was included in GA and the search was repeated. In Figure 4.2c, GA-p50-II, the structure was maintained to be the lowest enthalpy after 21 generations. This test helped to ascertain that the candidate structure is indeed the global minimum.

At 60 GPa, in the PSO-p40-I calculations, the structure found in the 4^{th} generation is not the global minimum. As mentioned in the Chapter 1, crude *k* point meshes were used during the structural search. Therefore, geometry optimization must be repeated for candidate structures with dense *k* mesh. It was found that the energy of the structure in the 4^{th} generation is much higher than the prior calculation (as mentioned in Chapter 1, using the coarse *k* points during the structural search can cause wrong energy convergence) and the lowest enthalpy structure was found in the 41^{st} generation. Both PSO calculations (PSO-p40-I and PSO-p50-II) found the same $P4_12_12$ structure. On the other hand, the most stable structure found by the GA method is very similar but not exactly the same as the PSO structure. A summary of the lowest enthalpy structures of $XeCl_2$ at different pressures is shown in Table 4.1.

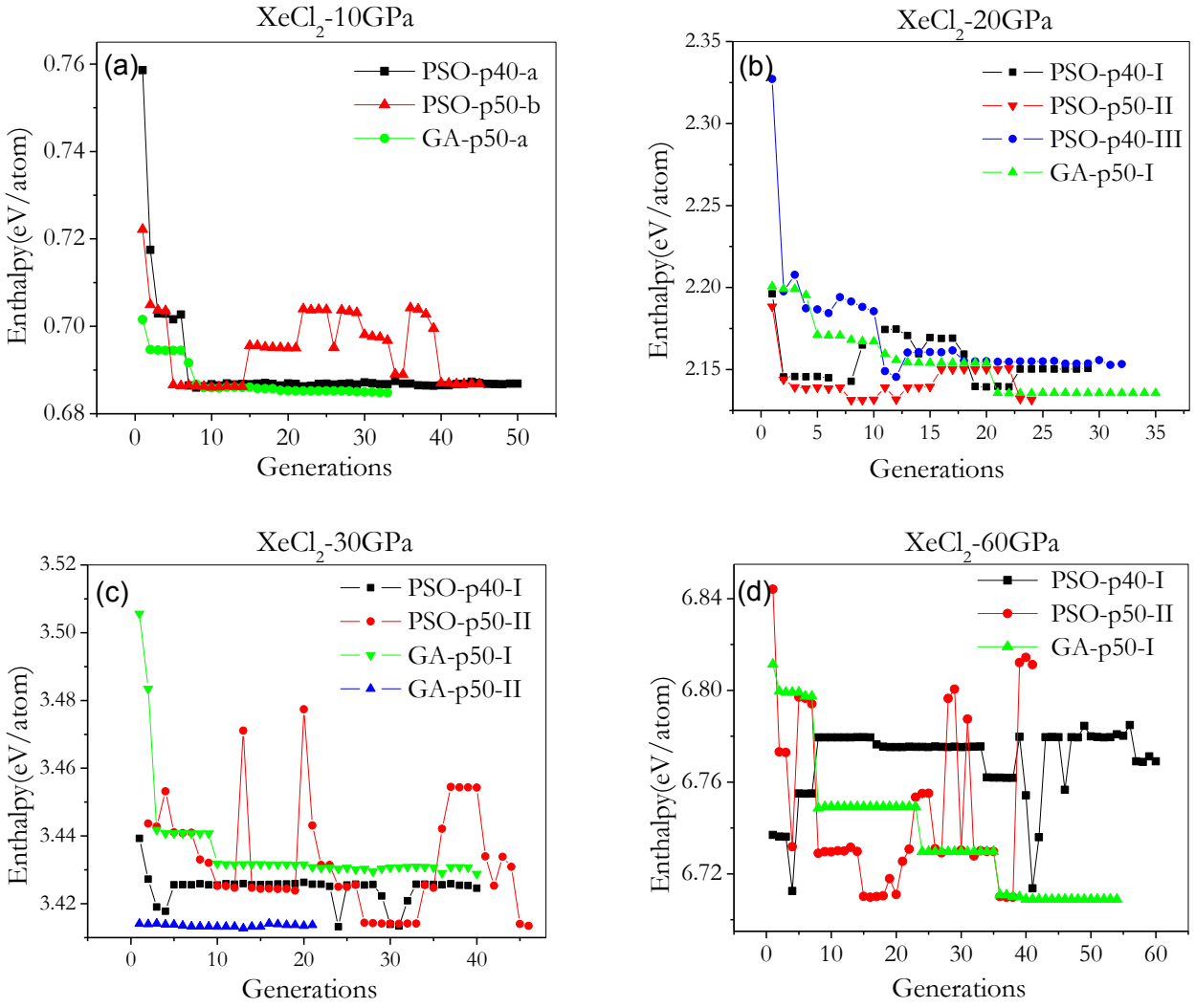

Figure 4.2 (a), (b), (c) and (d) represent the PSO and GA searches performed on $XeCl_2$ at 10, 20, 30 and 60 GPa.

The space groups of the predicted lowest enthalpy structures together with the pertinent information on the structural searches by PSO and GA methods are summarized in Table 4.1. Since the geometry optimizations in the structural searches were performed with relatively crude *k* meshes and small plane wave energy cutoffs, more calculations must be repeated for candidate structures using denser *k* meshes and higher cutoff energies. In these calculations, convergence to self-consistent iterations was reached when the total energy difference between cycles was less than 10^{-5} eV and the residual forces were less than 0.005 eV/Å. To compare relative stability of the candidate structures, we computed the equation of states in the pressure range from 10 to 80 GPa. Phonon calculations using density functional theory and the frozen phonon were performed to establish the structural stability, as shown in Table 4.1.

Table 4.1 Comparison of the lowest enthalpy structures of $XeCl_2$ (4 formula units) predicted with the GA and PSO methods in the pressure range from 10 to 60 GPa.

PSO	Population	40				50			
	Pressure (GPa)	10	20	30	60	10	20	30	60
	Total #Gen	50	29	40	60	46	29	46	41
	Structure	*Cmcm*	*Cmcm*	*Cmcm*	$P4_12_12$	*P*1	*Cmcm*	*Cmcm*	$P4_12_12$
	Found at #Gen	7	8	24	41	5	7	27	16
	Enthalpy (eV/atom)	0.6864	2.1317	3.4139	6.7082	0.6848	2.1317	3.4139	6.7082
GA	Population	50							
	Pressure (GPa)	10		20		30		60	
	Total #Gen	40		35		40		54	
	Structure	*P*1		$P2_1/m$		*C*2/*m*		$P2_12_12_1$	
	Found at #Gen	8		21		10		36	
	Enthalpy(eV/atom)	0.6845		2.1355		3.4288		6.7082	

We now analyze the effect of the population size (40 and 50) with the PSO method (Table 4.1). At 10 GPa, two different structures with the *Cmcm* and *P*1 space groups were obtained with populations of 40 and 50 structures, respectively. The energy of the *P*1 structure is slightly lower (0.002 eV/atom) than the *Cmcm* structure. However, at 20 and 30 GPa, both populations found the same *Cmcm* structures. At 60 GPa, the $P4_12_12$ structure was also found to be the most stable one from both populations. The GA method was performed at 10, 20, 30 and 60 GPa with a population of 50 structures. The *P*1 structure found at 10 GPa is the same as the *P*1 structure found by PSO. The GA failed to predict the lowest enthalpy structures predicted by PSO at 20 and 30 GPa but at 60 GPa the energy of the predicted $P2_12_12$ structure was almost identical to the $P4_12_12$ structure found by PSO. It indicates that both GA and PSO at 60 GPa might sample the same region of the potential energy landscape. The similarities of these two structures are explained in detail later.

The relative enthalpy as a function of pressure for several candidate structures obtained by PSO and GA are compared in Figure 4.3. Surprisingly, the $P2_1/m$ structure found at 20 GPa by GA is also the most stable at 10 GPa. The result shows that, contrary to claims of near-infallibility in structural search methods, both PSO and GA methods may miss the lowest enthalpy structure! The energy of the $P2_1/m$, $P1$ and *Cmcm* structures was nearly degenerated at 15 GPa. The *Cmcm* structure became the most stable up to 40 GPa. For convenience, the *Cmcm* structure was chosen to be the reference. Between ~40 and 60 GPa, three structures ($P4_12_12$, $P4_32_12$ and $P2_12_12_1$) had comparable energies. As indicated in the convex hull plot (Figure 4.1), the $P4_12_12$ structure resisted decomposition into Xe and molecular Cl_2 solids. Therefore this compound, in principle, can be synthesized above 50 GPa from Xe and Cl_2.

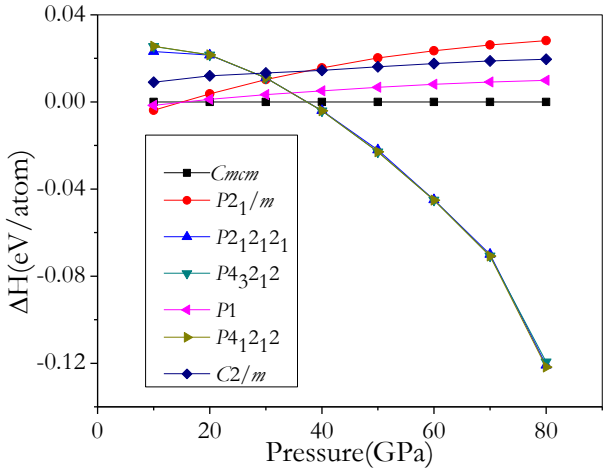

Figure 4.3 Relative enthalpies (ΔH) *vs* pressure for several $XeCl_2$ configurations, with respect to the *Cmcm* structure.

4.3.1 Structural analysis at 10 GPa

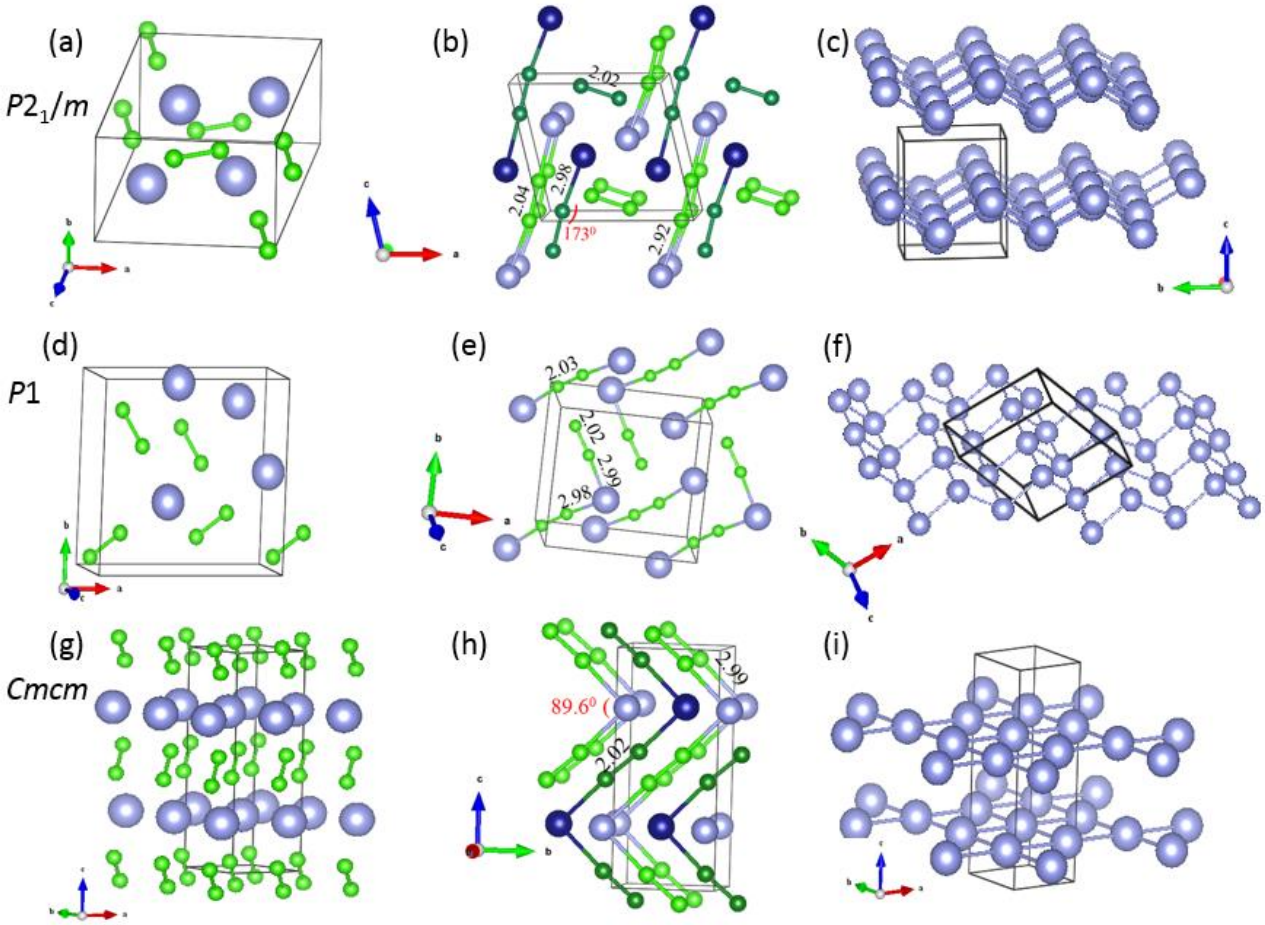

Figure 4.4 The lowest predicted enthalpy structures, $P2_1/m$ (a, b and c), $P1$ (d, e and f) and *Cmcm* (g, h and i) for solid $XeCl_2$ at 10 GPa. To distinguish layers in (b) and (h), Xe (blue) and Cl (green) atoms are shown with two different dark and light color tones.

We now examine the predicted crystal structures in detail. At 10 GPa, the three lowest energy structures ($P2_1/m$, $P1$ and *Cmcm*) found within an energy window of 3 meV/atom consist of molecular Cl_2 but different Xe sublattices. We will focus on the description of the prominent structural differences (Figure 4.4). The monoclinic $P2_1/m$ structure has 12 atoms in the unit cell (Figure 4.4a). In this structure, the Cl-Cl bond lengths alternate between 2.02 and 2.04 Å and are almost collinear between two Xe atoms (Figure 4.4b). The nearest Xe-Cl contacts are 2.92 and 2.98 Å. The Xe-Cl-Cl angle with the longer interatomic distance (2.98 Å) is 173˚ and with the shorter Xe-Cl-Cl (2.92 Å) is almost 180˚. Figure 4.4c shows that the Xe forms a puckered layer. The second lowest enthalpy $P1$ structure found by both GA and PSO (Figure 4.4d) has 12 atoms per unit cell. The gross structural features are similar to the $P2_1/m$ structure. The closest Xe-Cl

contacts are 2.98 and 2.99 Å. The Xe-Cl-Cl angles are in the range of 173.1°-175.6° (Figure 4.4e). The Xe sublattice also forms buckled layers. The third lowest enthalpy structure which was only found by PSO, has a base-centered orthorhombic structure with the *Cmcm* space group. Again, this structure has four formula units (12 atoms) per unit cell and was found to be the lowest enthalpy structure below 40 GPa. Unlike the other two structures, linear Cl-Cl-Xe units are arranged in a zigzag manner in the b-c plane. The molecular Cl_2 with 2.02 Å bond lengths connect to Xe atoms with 2.99 Å distances. The Cl-Xe-Cl angle is 89.6°. The Xe atoms form a 2D planar square network stacked along the *a* axis. The Xe sublattice, shown in Figure 4.4i, is in sharp contrast to the buckled Xe layers in the $P2_1/m$ and $P1$ structures.

The predicted structures in crystalline $XeCl_2$ are very different from the solid $XeFe_2$ where linear XeF_2 molecules having two equal Xe-F bond was predicted to be stable up to 100 GPa. Further compression only resulted in bending of the F-Xe-F molecule [181]. In comparison, linear Cl-Xe-Cl units did not form in a pressure range from 10 to 40 GPa. This result highlights the structural diversity of high pressure Xe-halides.

4.3.2 Electronic and dynamical properties at 10 GPa

To characterize the Xe-Cl interaction, electron localization functions (ELFs) were computed at 10 GPa. Only valance electrons were considered in the calculations [190], [191]. Usually, regions with ELF values close to 1 indicate a high probability of paired electrons such as lone pairs or covalent bonds. At an ELF value of ~0.5, the electrons behave as a uniform electron gas [14]. The contour plots of the ELFs in the $P2_1/m$, $P1$ and *Cmcm* structures at 10 GPa are compared in Figure 4.5. All the plots share a common feature: very low ELF values were found between Xe atoms and Cl_2 molecules and no electron localization was found in the voids. High ELF regions are centered spherically around the Xe atoms due to the filled 5*s* and 5*p* electrons. Moderate ELF values of ~0.7, corresponding to covalent bonds, were only found between the Cl pairs. In addition, high ELF values corresponding to the Cl lone pairs were also observed.

The calculated Bader charges show a small charge (~0.1e) transfer from the Xe to Cl atoms. Thus, it is likely that partial ionic chemical bonds exist between Xe atoms and Cl_2 molecules. The amount of charge transfer remains relatively constant from 10 to 30 GPa. From this analysis, we can conclude that Cl_2 is molecular in nature and the interaction with Xe atoms is weakly ionic.

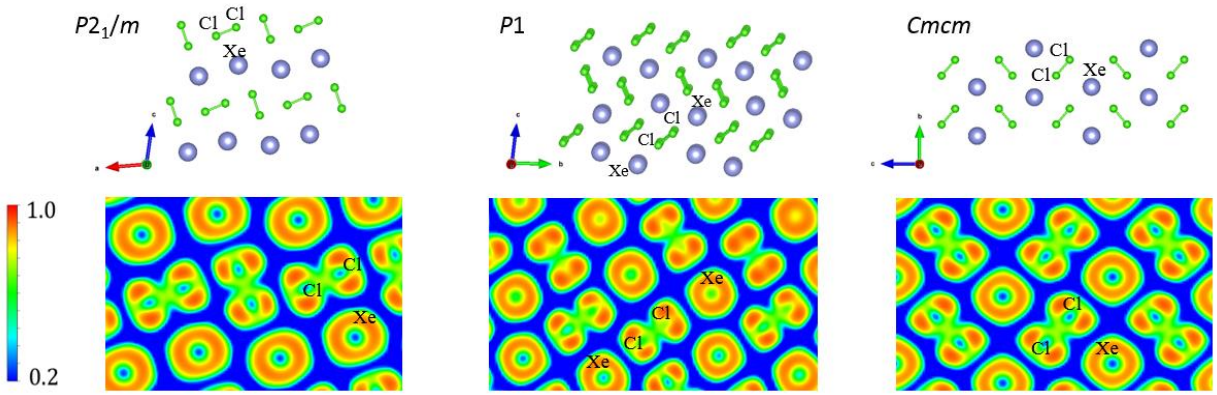

Figure 4.5 The ELF values for $P2_1/m$, $P1$ and *Cmcm* structures of $XeCl_2$ with cross sections of (010), (100) and (100) are shown at 10 GPa, respectively. The positions of Xe and Cl atoms are also shown for clarity.

We now examine the structural stability of the three candidates $P2_1/m$, $P1$ and *Cmcm* structures. Phonon band structures calculated by the supercell are shown in Figure 4.6. For comparison, linear response calculations (not shown) were also performed and the results were found to be almost identical. The phonon dispersion curves have no imaginary phonon frequency between 10 to 30 GPa, indicating that the three structures are dynamically stable.

The projected vibrational densities of states of the three structures at 10 GPa are compared with the solid Xe (fcc) and Cl_2 (*Cmca*) in Figure 4.7. The three nearly energetically degenerate structures exhibit similar features in their phonon densities of states. As expected, due to the heavier atomic mass, the low frequency modes (below 4 THz) are assigned to Xe vibrations. The vibrational bands between 13 and 14 THz are mainly derived from the Cl motions. The dominant vibrational bands of Xe atoms in the $XeCl_2$ compounds are slightly extended to higher frequencies than in the fcc Xe solid and are hybridized with the Cl bands. In the $P2_1/m$ and $P1$ structures (Figure 4.4), there are two distinctive Cl-Cl bond lengths and this resulted in two stretched bands at 12 and 14THz. In contrast, the Cl-Cl stretch in the *Cmcm* structure shows one vibrational band at 13.5 THz. The shift to a higher frequency is due to the shorter Cl-Cl bonds (~0.01 Å) as compare to the free Cl_2 molecule.

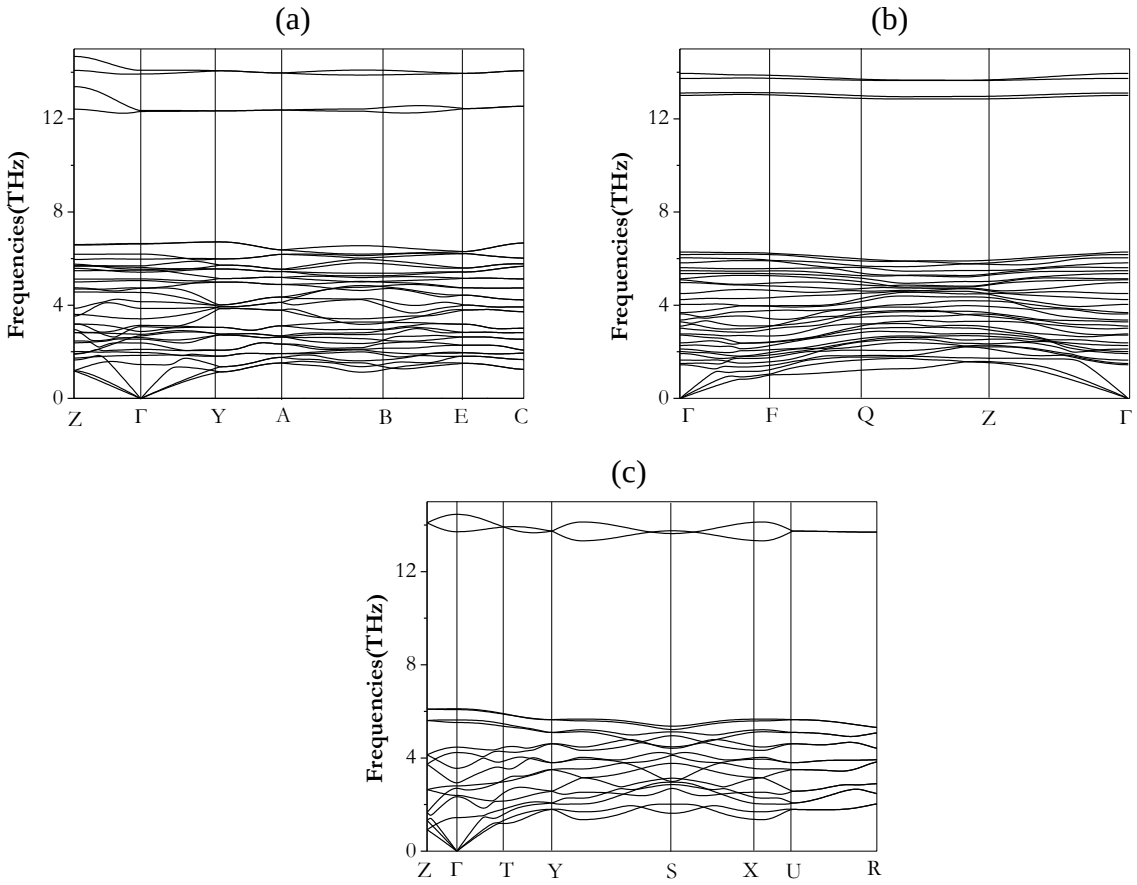

Figure 4.6 Phonon dispersion curves for $P2_1/m$ (a), $P1$ (b) and $Cmcm$ (c) of XCl_2 at 10 GPa.

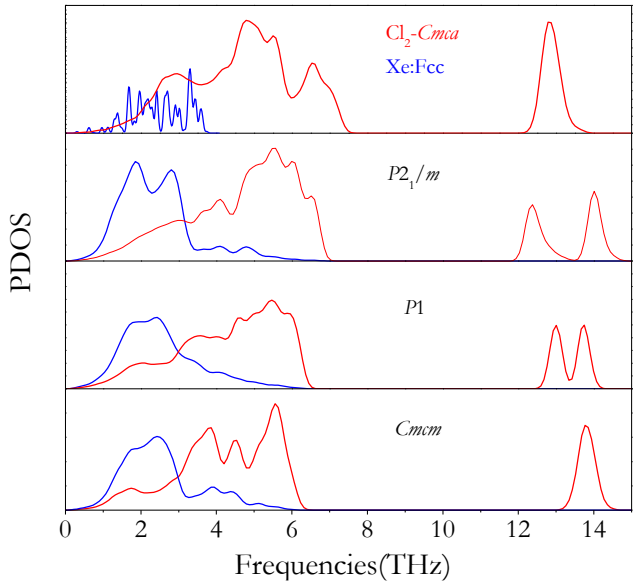

Figure 4.7 Comparison of phonon densities of states for molecular Cl_2 and Xe solids with $XeCl_2$ structures at 10 GPa.

4.3.3 Energy corrections beyond PBE functional

As the enthalpy differences between high pressure structures are typically around 5 meV/atom, dense *k* point sampling and energy convergence better than 0.01 meV/atom were required to reliably predict the relative stability. In addition, it was necessary to include the ZPE and vdW interactions. These effects were investigated and the results were reported below.

ZPE were calculated from the vibrational frequencies and the results are reported at 10 GPa in Table 4.2. Since Xe and Cl are heavy atoms, there is no surprise that ZPE did not affect the order of the stability. Another factor to be considered regarding the stability of the Xe-Cl_2 compounds is vdW interactions. Since the PBE functional used in the calculations is not able to describe this interaction [192], to this end, calculations were performed on the three candidate structures using the vdW-DF2 functional developed by the Langreth and Lundqvist [167]. The change in the functional has a significant effect. The difference in energy with and without the vdW interaction is more than 500 meV/atom. More significantly, the vdW functional calculations altered the order of the stability. The re-optimized *Cmcm* structure with the vdW functional becomes the most stable structure at 10 GPa. As described above, the major difference between the *Cmcm* and *P*1 and $P2_1/m$ structures is in the arrangement of the Xe atoms. Apparently, the planar square Xe network has a more dispersive interaction with the Cl_2 than the buckled layers observed in the $P2_1/m$ and *P*1 structures. The enthalpies of formation, however, do not change with ZPE and vdW interactions and remain positive with respect to solid Xe and Cl_2.

Table 4.2 Numerical values of the calculated lowest enthalpy structures with ZPE and vdW corrections.

Space Group	PBE (eV/atom)	PBE+ZPE (eV/atom)	PBE+vdW-DF2 (eV/atom)
$P2_1/m$	0.682606	0.712813	1.010094
*P*1	0.684546	0.713794	1.010773
Cmcm	0.685419	0.714667	1.009844

It should be noted that the vdW functional not only corrects the dispersive interaction but also properly accounts for the asymptotic behaviour of the exchange interaction at short distance. To further examine the effect of the vdW functional, calculations were extended to higher pressure on the $P2_1/m$ and *Cmcm* structures. The enthalpy differences relative to the $P2_1/m$ structure are shown in Figure 4.8a shows The energy difference increases slightly from 10 to 60 GPa for both the $P2_1/m$ and *Cmcm* structures. It is often misunderstood that the vdW functional only affects structures with weak intermolecular interactions rather than the PBE results. In fact, the vdW functional of Langreth *et al*., used in the present study, correctly accounts for the exchange interactions at both short and long distances. Therefore, the effect of exchange interaction becomes even more important at high pressure (shorter distances) than low pressure (longer distances). The results clearly show that the PBE functional overbinds the system at high pressure since the optimized volume of both the $P2_1/m$ and *Cmcm* structures obtained with the vdW functional are slightly larger at high compression.

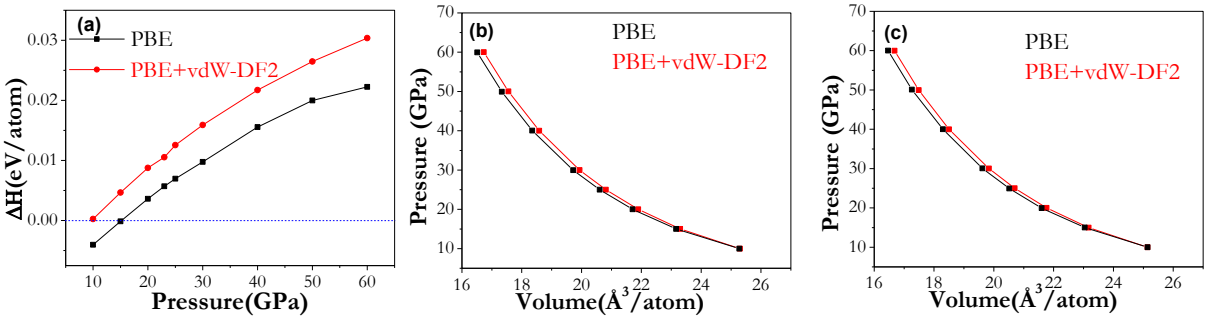

Figure 4.8 Comparison of calculated PBE and vdW-DF2 functionals for *Cmcm* and $P2_1/m$ structures of $XeCl_2$. (a) Relative enthalpy with respect to $P2_1/m$ structure. (b) and (c) the calculated equation of states of $P2_1/m$ and *Cmcm* structures, respectively.

4.3.4 Comparison with experiment

In the experimental study, formation of deep red crystalline phases was observed in the pressure range of 2-20 GPa [189]. Initially from a 50:50 mixture of Xe and Cl_2 at 14 GPa, the pressure dropped to 8 GPa when the sample was heated to 800 K. The drop in pressure hinted at the formation of a compound. The image shown in Figure 4.9b was taken when the sample was cooled from 440 K [189].

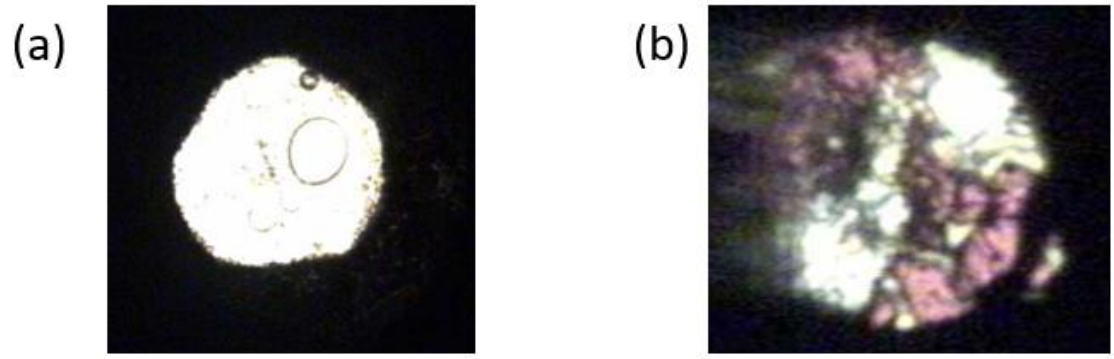

Figure 4.9 (a) The microscopic picture of Xe-Cl at ~ 0.1 MPa. The clear spherical regions were xenon-rich and (b) Xe-Cl at ~8 GPa. The crystals agglomerated as seen in the upper left on further cooling from 440 K [189]. The sample chamber is approximately 120 μm in diameter.

The experimental spectra acquired before thermal annealing at 14 GPa show a sharp peak near 520 cm^{-1}, which can be assigned to a Cl-Cl bond. After heating and reducing the pressure to 4.2 GPa, the sample remarkably separated into clear and red regions. In both the clear and red regions the strong Cl_2 peak had disappeared and a new band emerged at 390 cm^{-1} (Figure 4.10). In addition to this strong peak, a weaker band at 200 cm^{-1} was also observed. The peaks with energies higher than 600 cm^{-1} were attributed to overtones. The band at 401 cm^{-1} was tentatively assigned to Cl-Xe vibrations suggesting the formation of a xenon-chlorine compound.

To compare with experiment, the Raman spectra of the two lowest enthalpy structures ($P2_1/m$ and *Cmcm*) were computed (Figure 4.10). The Raman intensities were calculated from derivatives of the macroscopic dielectric tensor with respect to the normal mode coordinate [193]. Since the $P2_1/m$ and $P1$ structures are almost identical, we only show the result of the $P2_1/m$ and *Cmcm* structures. Figure 4.10 shows that for the $P2_1/m$ structure, the calculated Raman spectra reproduced the observed band around 440 cm^{-1}. In addition, the predicted peak centred around 116 cm^{-1} is slightly lower than the experimentally observed peak (~200 cm^{-1}). When the pressure was increased to 20 GPa, the intensity of the peak at 116 cm^{-1} was decreased and the peak shifted to higher energy (~250 cm^{-1}), while the strong peak shifted to lower energy (~400 cm^{-1}). For the *Cmcm* structure, the strong peak (470 cm^{-1}) slightly changed up to 20 GPa but the first peak, which was very weak, became stronger and emerged into the higher frequency region (~236 cm^{-1} at 30 GPa). Although the calculated and experimental spectra show some similarities, particularly the

appearance of a new Xe-Cl stretch vibration, the details, however, do not match. Therefore, the xenon chlorine complex observed with experiment is not one of the predicted structures.

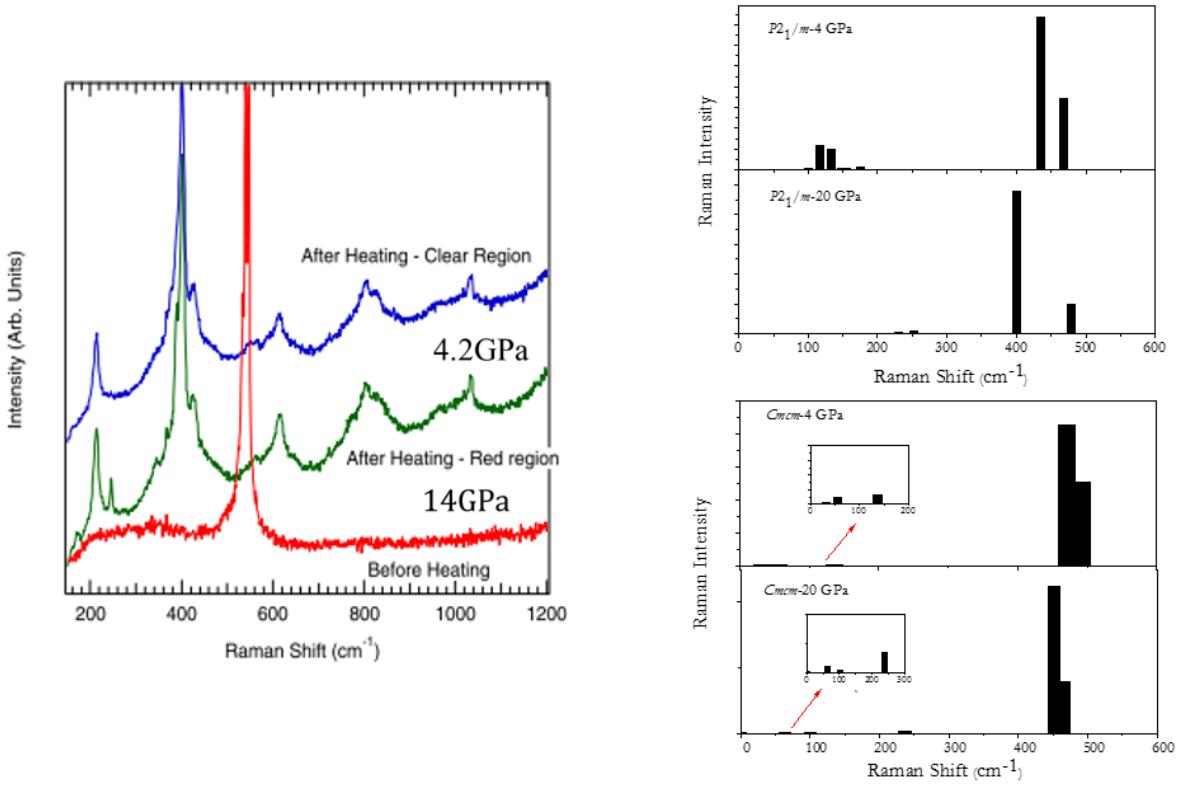

Figure 4.10 Comparison of Raman spectra of our calculated $P2_1/m$ and *Cmcm* structures of $XeCl_2$ at 4 and 20 GPa with the experimental result of that at 4 GPa [189].

In an attempt to characterize the crystal structure of the Xe-Cl compound found with Raman study, energy dispersive x-ray diffraction measurements were performed at two detector angles. Figure 4.11 shows only the results collected at 10 degrees [189]. In our calculations, the Bragg equation, $\lambda = 2d \sin\theta$, was used to determine energy ($E = {}^{hc}/_{\lambda}$). The presence of Xe is confirmed by fluorescence peaks at 30 and 34 keV. All the diffraction lines can also be indexed to the *Cmca* structure of Cl_2 and no additional diffraction lines due to the mixed alloy of Xe and Cl atoms are observed. Therefore, the x-ray results contradict the Raman measurement showing no formation of Xe-Cl_2 complex at 4 GPa. We computed the energy dispersive x-ray diffraction patterns for the $P2_1/m$ and *Cmcm* structures. Figure 4.11 shows the positions of the peaks of the calculated patterns are not consistent with the experimental measurements.

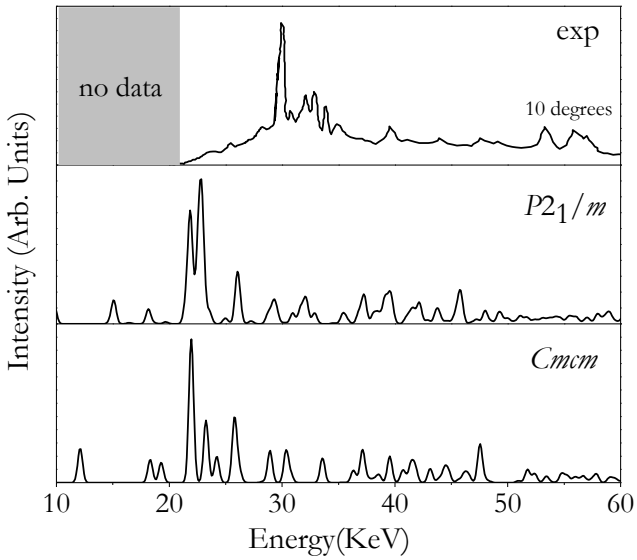

Figure 4.11 Comparison of the measured X-ray diffraction pattern of the Xe-Cl_2 sample [189] with $P2_1/m$ and *Cmcm* structures at 4 GPa.

4.3.5 Electronic structures at 15 GPa

The band structures of the $XeCl_2$, calculated at 15 GPa, are shown in Figure 4.12. The PBE results show that both the $P2_1/m$ and *Cmcm* are insulators with indirect band gaps of 1.75 and 2.15eV, respectively. Calculations with the TB-mbjLDA functional which correct self-interaction, also produced similar results. It is known that the PBE functional often underestimates the band gap and thus the real energy gap may be much larger. To provide an accurate description of the band structure, quasi-particle energy corrections were calculated using the GW approximation. In the DFT perturbation approach, self-energy corrections are added to the Khon-Sham eigenvalues at selected *k* points. In the calculation of the self-energy matrix, the number of unoccupied bands was increased to at least twice the number of occupied bands. The band structure was then constructed from the interpolation of the corrected GW eigenvalues at each *k* point using the Wannier function technique [194]. The GW corrected band structures are compared to the PBE results for the $P2_1/m$ and *Cmcm* structures in Figure 4.12. The calculated band gaps have increased to 4.06 and 4.31eV for $P2_1/m$ and *Cmcm,* respectively. The predicted large band gaps show the crystalline structures should be transparent.

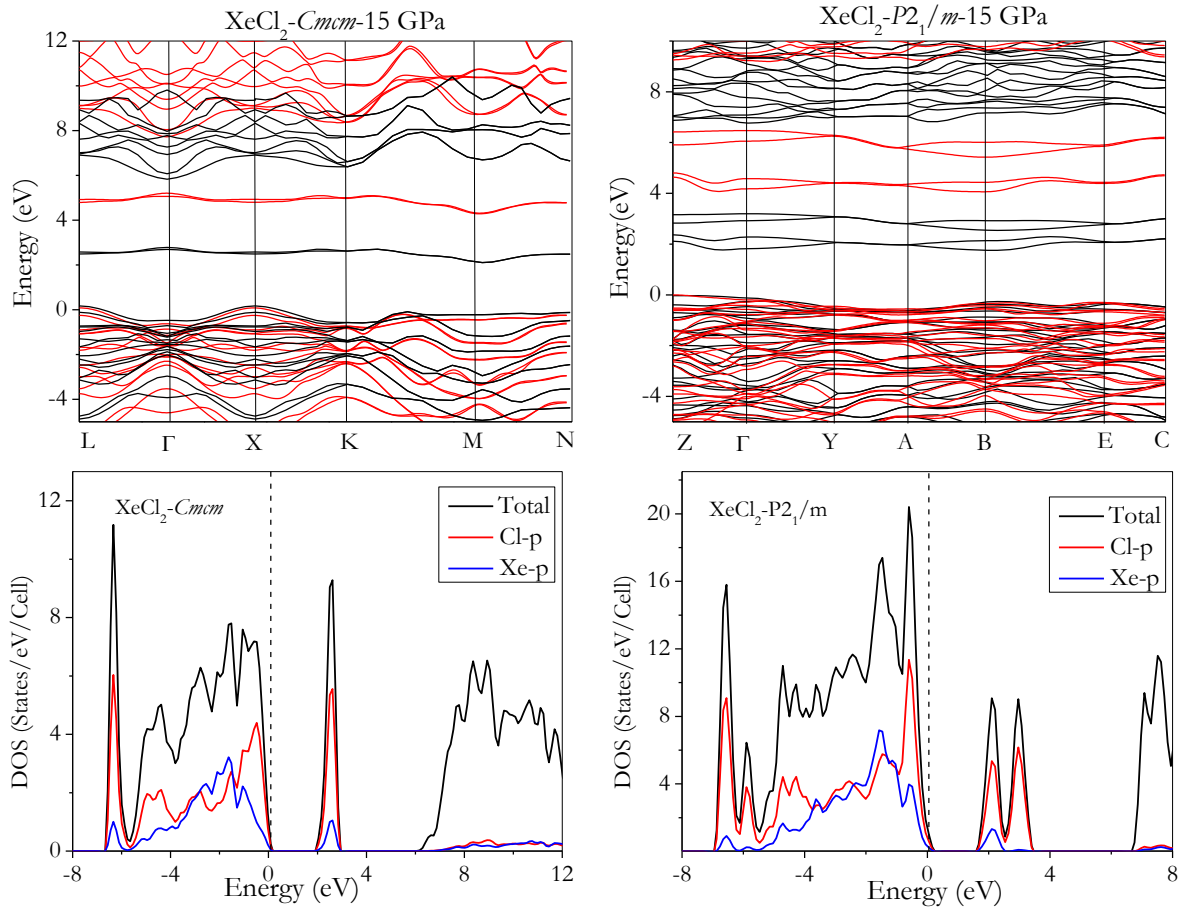

Figure 4.12 Band structures (top) and partial electronic DOSs (bottom) of the *Cmcm* and $P2_1/m$ structures of $XeCl_2$ are shown at 15 GPa. The black and red solid lines in band structure plots show results of PBE and GW corrections.

The projected densities of states of the *Cmcm* and $P2_1/m$ structures, calculated using the PBE functional (Figure 4.12), show the Cl 3*p* orbitals dominate the Fermi level. The *s* orbitals are not shown due to their small contribution near the Fermi level. For $XeCl_2$, at 15 GPa, each Cl atom shares one electron with another Cl atom to form a σ bond. The corresponding unoccupied antibonding Cl_2 orbitals are located at higher energies but close to the Fermi level.

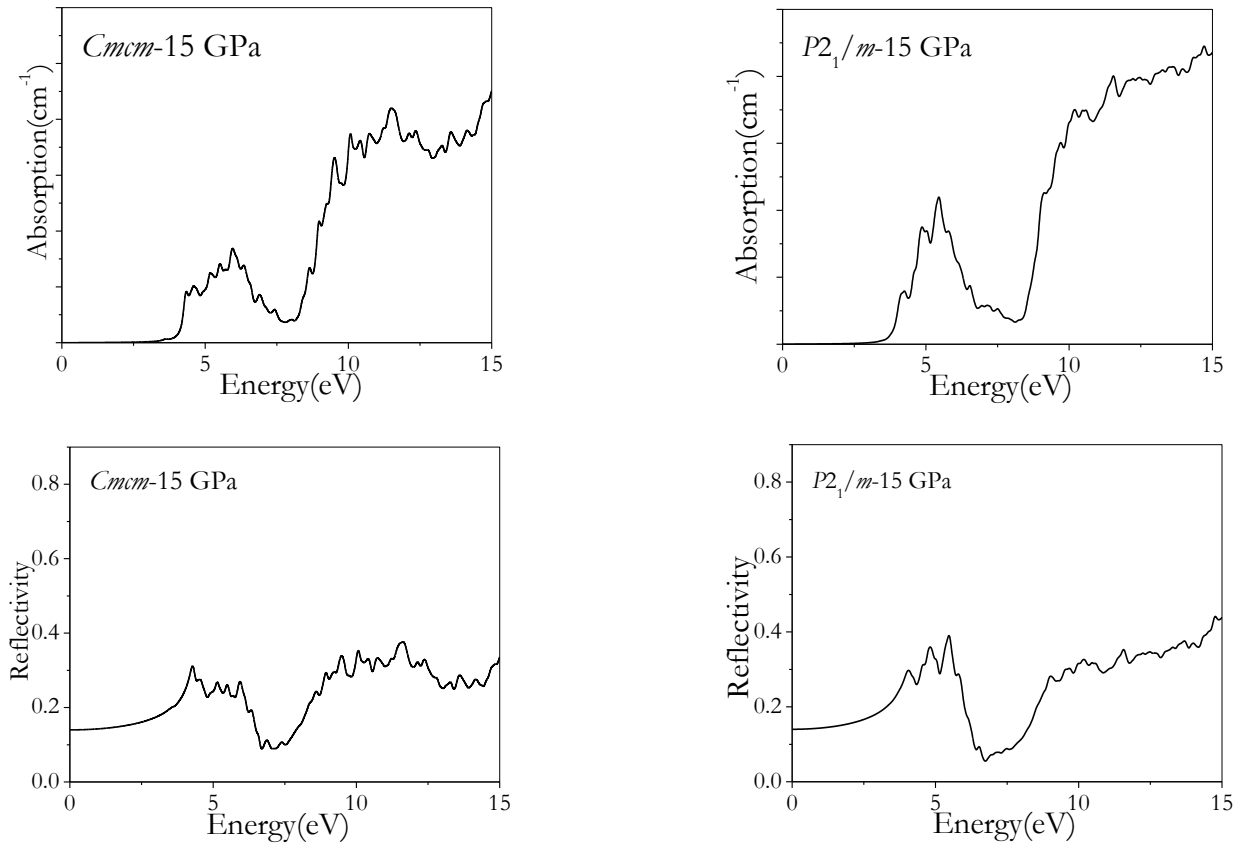

Figure 4.13 Absorption and reflectivity of *Cmcm* and $P2_1/m$ structures of $XeCl_2$ at 15 GPa are shown on the top, middle and bottom, respectively. The black and red solid lines in band structure plots show results of PBE and GW corrections.

The absorption and reflectivity spectra were then calculated by the BSE method using the GW corrected wave functions shown in Figure 4.13. The results of BSE spectra calculations show that a band gap of ~4eV for both structures is in agreement with the GW band structures. Moreover, reflectivities of these compounds are very low as expected for insulators.

4.3.6 Structural analysis at 60 GPa

Now we return to discussion on the stable structures found at higher pressure. As indicated in the convex hull plot (Figure 4.1), at 60 GPa, $XeCl_2$ with the $P4_12_12$ structure was stable against decomposition into solid Xe and Cl_2. In addition, the structural prediction calculations performed at 60 GPa also found two similar structures that are energetically competitive to the $P4_12_12$ phase. The difference of energies is within 0.1 meV/atom. Energies of the $P4_32_12$ and $P4_12_12$ structures are slightly less than an orthorhombic $P2_12_12_1$ phase. We will first describe the most stable one ($P4_12_12$) shown in Figure 4.14. From the EOS, this structure is found to be stable in the pressure

range from 37 to 60 GPa. The $P4_12_12$ structure is very different from the lower pressures structure and has four formula units per unit cell. Each Cl_2 unit is surrounded by 9 Xe atoms connected from 2.93-3.14 Å. Since a nominal Xe-Cl bond at ambient pressure is between 2.31-2.85 Å [195], the Xe..Cl separation of ~3 Å suggests a weak interaction. Locally, the Xe atoms are surrounded by 12 Cl atoms. This seemingly complex coordination can be explained easily from the consideration of the Cl and Xe sublattices. Figure 4.14c illustrates the Cl sublattice is composed of a triangle-like network of Cl atoms. The shortest Cl-Cl bond is 2.04 Å and Cl neighbours are located with < 2.64 Å distances. Most interestingly, the Xe atoms form a fcc sublattice (Figure 4.14b). Although the Xe..Xe distances are all equal (3.15 Å), the Xe-Xe-Xe angles are distorted from the ideal tetrahedral value and vary from 105-111°. Therefore the $XeCl_2$ structure can be simply described as a cubic fcc Xe lattice with Cl_2 situated in the octahedral sites. Bader charge analysis show about 0.2e as transferred from Xe to Cl atoms.

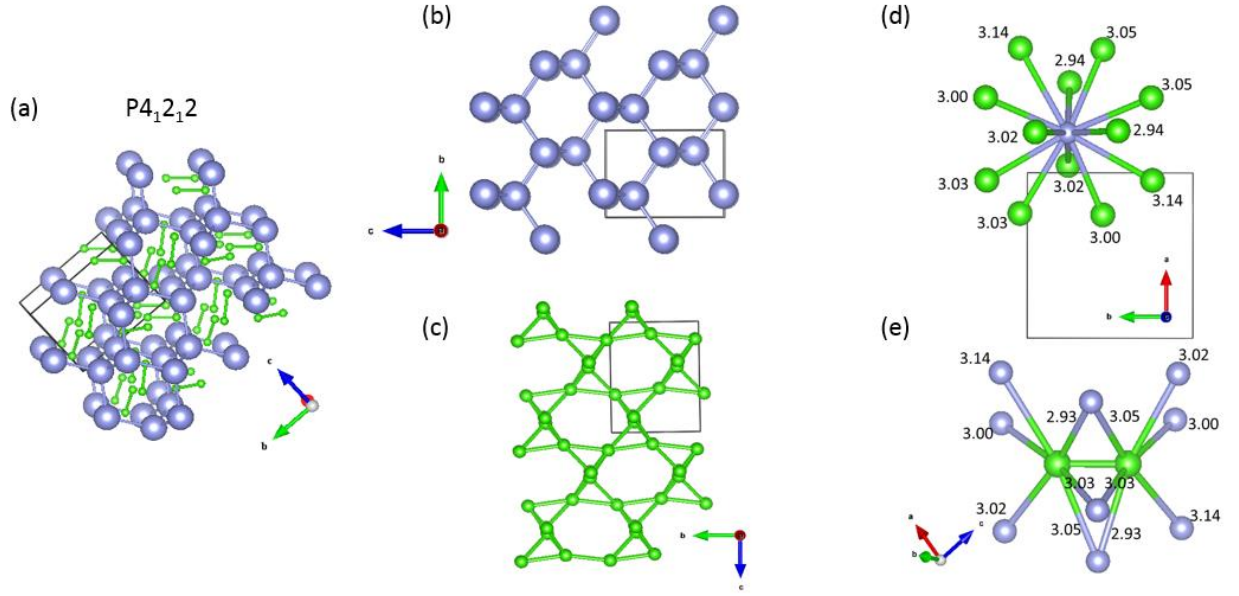

Figure 4.14 (a) the lowest predicted enthalpy structure, $P4_12_12$, for solid $XeCl_2$ at 60 GPa. (b) and (c) present the sublattices of Xe and Cl, respectively. (d) and (e) show the coordination of Xe and Cl_2.

The second lowest enthalpy candidate found at 60 GPa is the $P4_32_12$ structure and its energy is only 0.0002eV/atom higher than $P4_12_12$. The structural features of $P4_32_12$ are similar to $P4_12_12$. Here, we only show the coordination around Xe and Cl atoms in Figure 4.15.

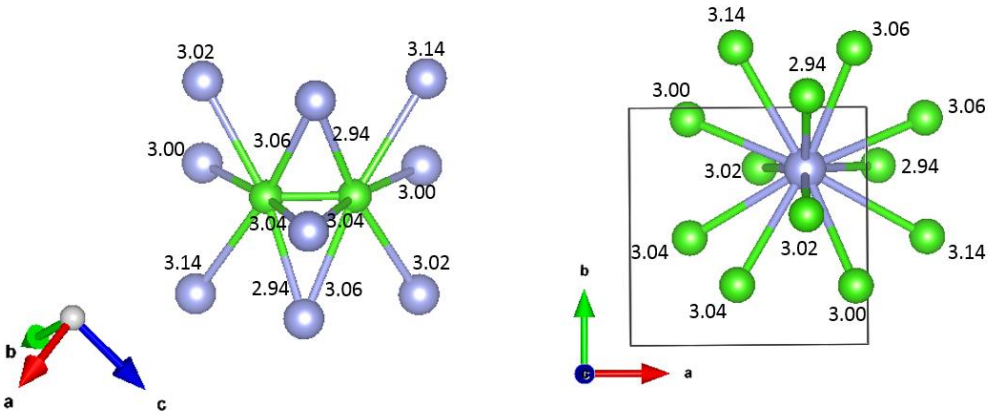

Figure 4.15 The coordination of Cl_2 and Xe for the $P4_32_12$ structure of solid $XeCl_2$ at 60 GPa.

The local structure of Xe in Figure 4.15 shows 6 unequal Xe-Cl contacts < 3.14 Å while each Cl_2 unit is surrounded by 9 Xe atoms separated from 2.94-3.14 Å. Similar to the $P4_12_12$ structure, the Xe..Xe distances are all equal (3.15 Å), but the Xe-Xe-Xe angles have a small variation from 108-111°.

In the third low enthalpy $P2_12_12$ structure, shown in Figure 4.16, the Xe is surrounded by 6 unequal Xe-Cl contacts < 3.15 Å. The number of coordinates at the Cl atoms, however, is the same as the $P4_32_12$ and $P4_12_12$. The fcc-like sublattice of Xe was also formed but with two unequal distances (3.14 and 3.17 Å) and the Xe-Xe-Xe angles are in a range of 108-111°. Once again, the Cl sublattice forms a triangle-shape bonding network with Cl-Cl contacts between 2.05-2.61 Å.

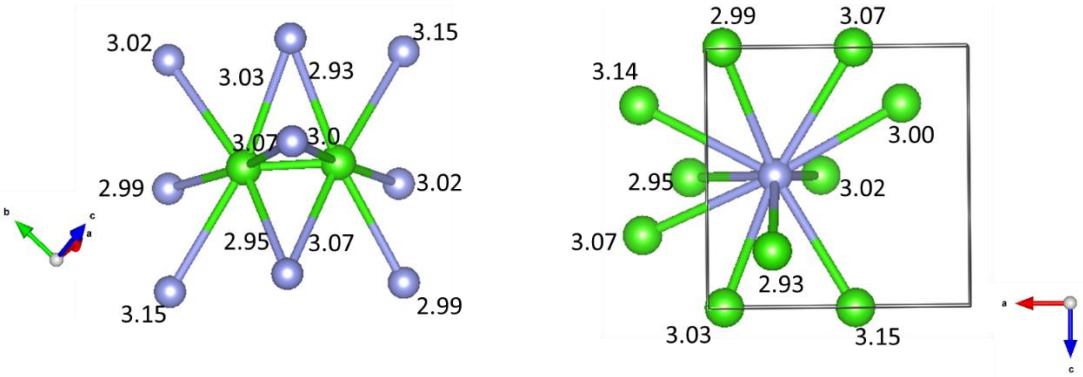

Figure 4.16 The coordination of Cl_2 and Xe for the $P2_12_12_1$ structure of solid $XeCl_2$ at 60 GPa.

4.3.7 Dynamical stability at 60 GPa

Frozen phonon calculations were performed to evaluate the stability of the $P4_12_12$, $P4_32_12$ and $P2_12_12_1$ structures (Figure 4.17). At 60 GPa, no imaginary frequency was found in the three structures. The projected vibrational densities of states of Cl and Xe atoms are also presented in Figure 4.17. In contrast to the low pressure structures at 10 GPa discussed above, mixing of Xe and Cl atomic motions is evident. In particular, the Cl-Cl stretch bands between 4 and 6 THz have broadened and hybridized with Xe vibrations. This observation suggests stronger Xe..Cl interactions than at low pressure. In view of the similarities in the crystal structures and very small energy differences in the predicted structures, they are just small variants of each other. The existence of stable but distinct structures reflects on the complexity of the multi-minimum energy landscape.

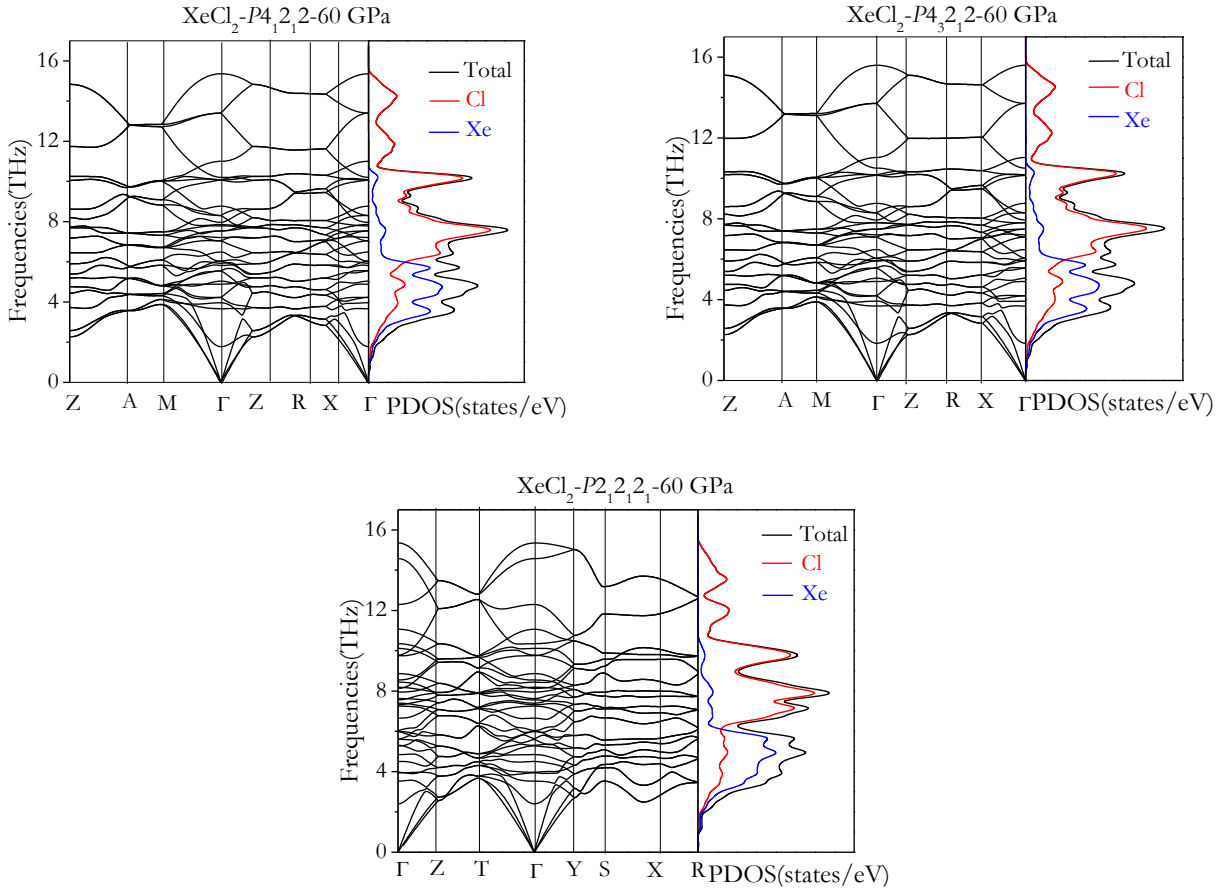

Figure 4.17 Phonon dispersion curves for $P4_12_12$, $P4_32_12$, and $P2_12_12_1$ structures of $XeCl_2$ at 60 GPa.

We have also investigated the effect of vdW interaction on the $P4_32_12$ structure and the result is compared with the PBE functional in Figure 4.18. In addition, we have also performed all electrons calculations to gauge the validity of the PAW potential at high pressure. The full potential and PAW results are indistinguishable below 30 GPa and they only deviated slightly at 60 GPa. This observation reaffirms the reliability of the PAW potentials at the pressure range studied. Once again, the vdW functional predicted a larger volume at high pressure. The "standard" parameterization of the PAW potential may not be accurate enough for studies at higher pressures. The same result was already observed in the calculations of the lower pressure structures.

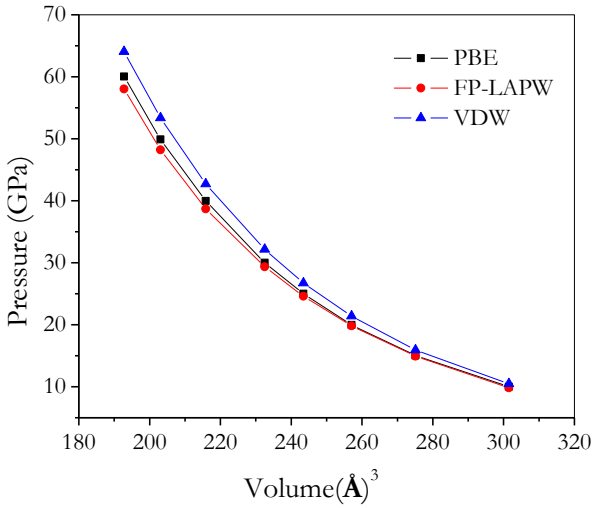

Figure 4.18 Three calculated equations of state of the $P4_32_12$ structure for $XeCl_2$ compound.

4.3.8 Raman spectra and electronic structures at 60 GPa

The calculated Raman spectra for the $P4_12_12$ and $P2_12_12_1$ structures at 60 GPa are shown in Figure 4.19. The two Raman spectra are very similar with a strong band predicted at 350 cm^{-1} and vibrations with lower interactions at around 200 cm^{-1}.

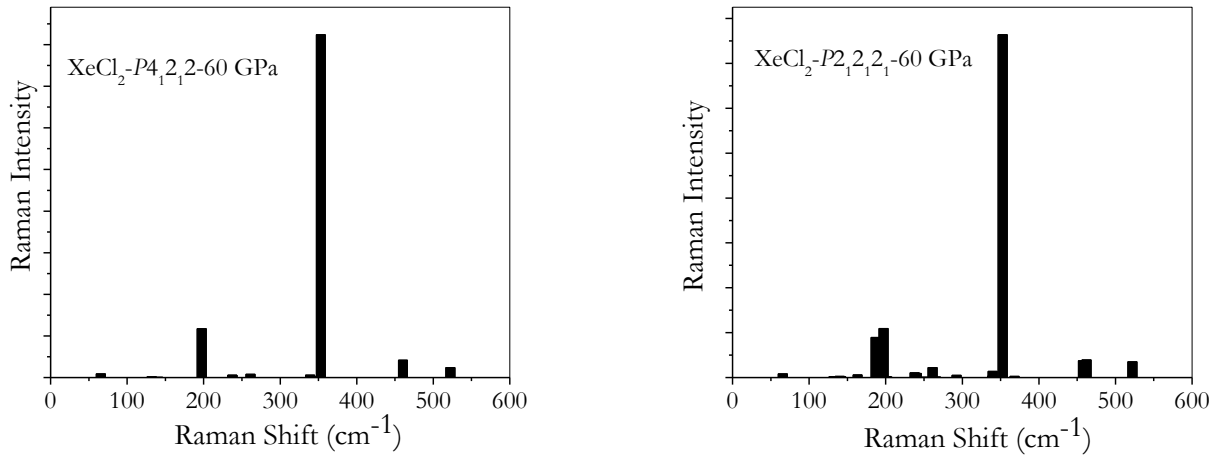

Figure 4.19 The calculated Raman spectra for the $P4_12_12$ and $P2_12_12_1$ structures of $XeCl_2$ at 60 GPa.

The band structures calculated using the PBE functional and GW corrections for the $P4_12_12$ and $P2_12_12_1$ structures at 60 GPa are shown in Figure 4.20. Details of the third low enthalpy structure ($P4_32_12$) are given in APPENDIX A. The GW band gaps are 1.92 and 1.66eV for $P4_12_12$ and $P2_12_12_1$, respectively. Both are larger than the corresponding PBE values of 0.85 and 0.69 eV, respectively. At this pressure, $XeCl_2$ is a semiconductor, which differs from high-pressure XeF_2 phases. The metallization of the XeF_2 phase was found at < 70 GPa [180]. $XeCl_2$ at this pressure still has a fairly large band gap and the color of the compound would be blue-green. The projected DOSs indicate that the *p* orbitals of Xe and Cl are strongly hybridized at the Fermi level.

The optical spectra and reflectivity, shown in Figure 4.21, were calculated using the BSE method. The reflectivity is slightly higher when compared to $XeCl_2$ at 15 GPa (Figure 4.13) due to much smaller energy gaps of the crystal structures at 60 GPa.

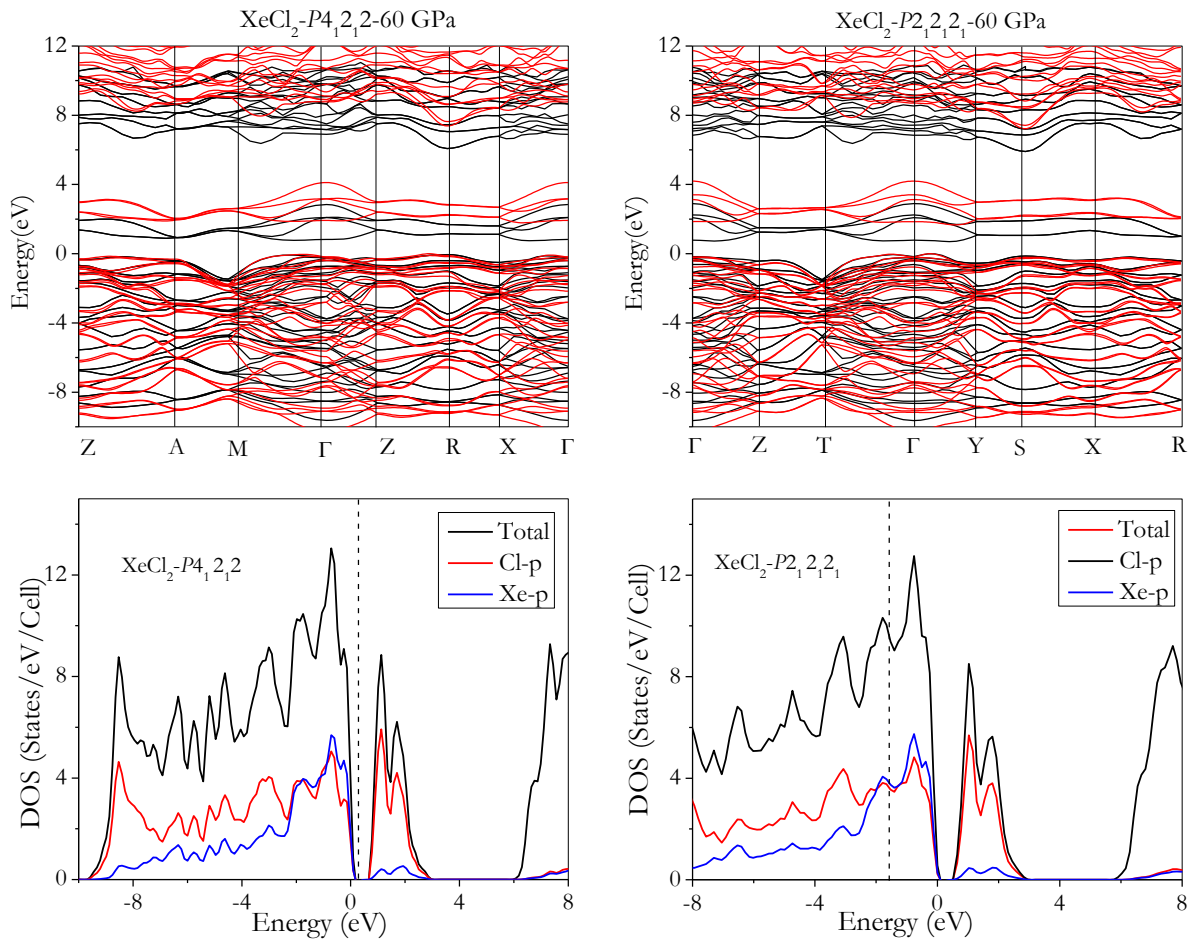

Figure 4.20 At 60 GPa, band structures (top) and partial electronic DOSs (bottom) of the $P4_12_12$ and $P2_12_12_1$ structures of $XeCl_2$ are shown. The black and red solid lines in band structure plots show results of PBE and GW corrections.

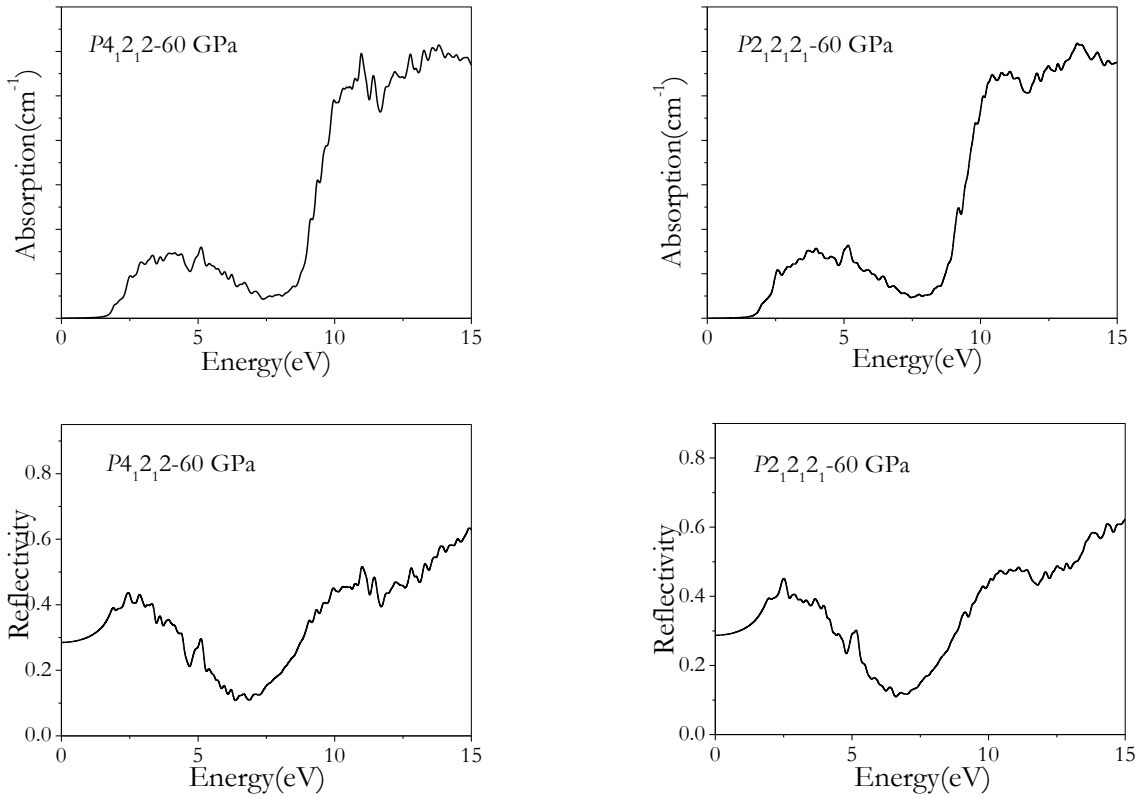

Figure 4.21 At 60 GPa, absorption and reflectivity of $P4_12_12$ (left) and $P2_12_12_1$(right) structures of $XeCl_2$.

4.4 Predicted high pressure structures of XeCl

We now discuss the results of the high pressure structures of XeCl. Information relevant to the structural search with the GA and PSO methods are summarized in Table 4.3. Once again, PSO and GA methods predicted different stable structures. Based on enthalpy calculations, only the *Cmcm* and *Cmc*2_1 structures found by PSO are thermodynamically stable at 60 GPa. At this pressure, the energy difference between these two structures is less than 2 meV/atom.

The GA method did not predict the lowest enthalpy structures at the desired pressures. At 20 GPa, the energy of the $P2_1/m$ structure found by GA is 0.005 eV/atom higher than the $C2/m$ structure found by PSO. Interestingly, the $P2_1/m$ structure was also found at 40 GPa by PSO with a population of 40 but it is not the lowest enthalpy structure. In the GA search, energies of the two different $P1$ structures found at 40 and 60 GPa are about 0.02 eV/atom higher than stable structures. Therefore, the $P1$ structures found by GA will not be examined further. In addition, the dynamical stabilities of all structures in Table 4.3 were determined from phonon calculations (APPENDIX A) and no imaginary frequencies were found at the pressures studied.

Table 4.3 Comparison of the lowest enthalpy structures of 8 formula units of XeCl, predicted with GA and PSO methods in pressure ranges of 20 to 60 GPa.

PSO	Population	40	50		
	Pressure (Gpa)	40	20	40	60
	Total #Gen	26	37	47	40
	Structure	$P2_1/m$	$C2/m$	$Cmc2_1$	$Cmcm$
	Found at #Gen	7	13	23	8
	Enthalpy (eV/atom)	5.5494	2.819	5.5329	7.8854
GA	Population	50			
	Pressure (GPa)	20	40		60
	Total # Gen	40	40		40
	Structure	$P2_1/m$	$P1$		$P1$
	Found at #Gen	14	25		14
	Enthalpy (eV/atom)	2.8245	5.5569		7.9367

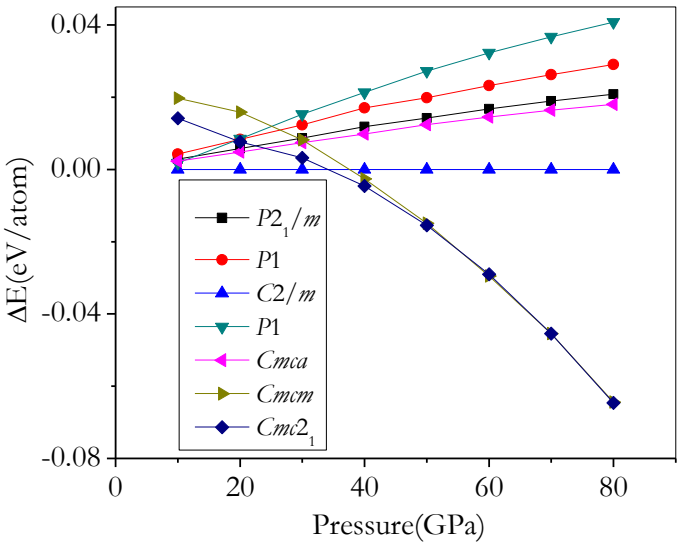

Figure 4.22 Relative enthalpy *vs.* pressure plot of the predicted structures of XeCl relative to the *C*2/*m* structure.

4.4.1 Structural analysis at 10 GPa

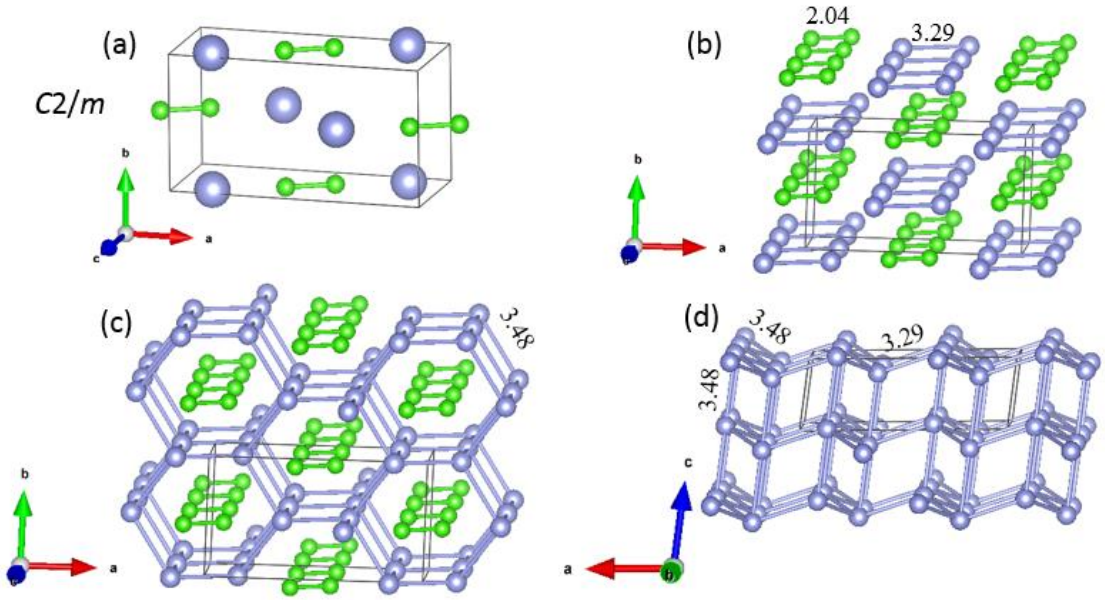

Figure 4.23 (a) The lowest enthalpy *C*2/*m* structures of solid XeCl at 10 GPa. This structure is shown along the *c* axis with (b) shorter and (c) longer cutoff of Xe..Xe atomic bonding distance and (d) is the sublattice of Xe.

We will describe the structural features of the three low enthalpy structures found by both GA and PSO methods at 10 GPa. The most stable structure in the pressure range 10-34 GPa predicted by PSO is a *C*-centred monoclinic *C*2/*m* with four formula units per unit cell (Figure 4.23a). The *C*2/*m* structure in Figure 4.23b shows the dimer Xe atoms connected with 3.29 Å Xe..Xe distances. After increasing the cutoff of the Xe..Xe contact to < 3.5 Å (Figure 4.23c), the occurrence rippled layers of Xe atoms with six members becomes apparent. The Cl_2 molecules are clearly seen arranged along the c direction through the Xe channels. Viewing down the layers in Figure 4.23d, the buckling of the Xe atoms in a chair form along the *c* axis is clear.

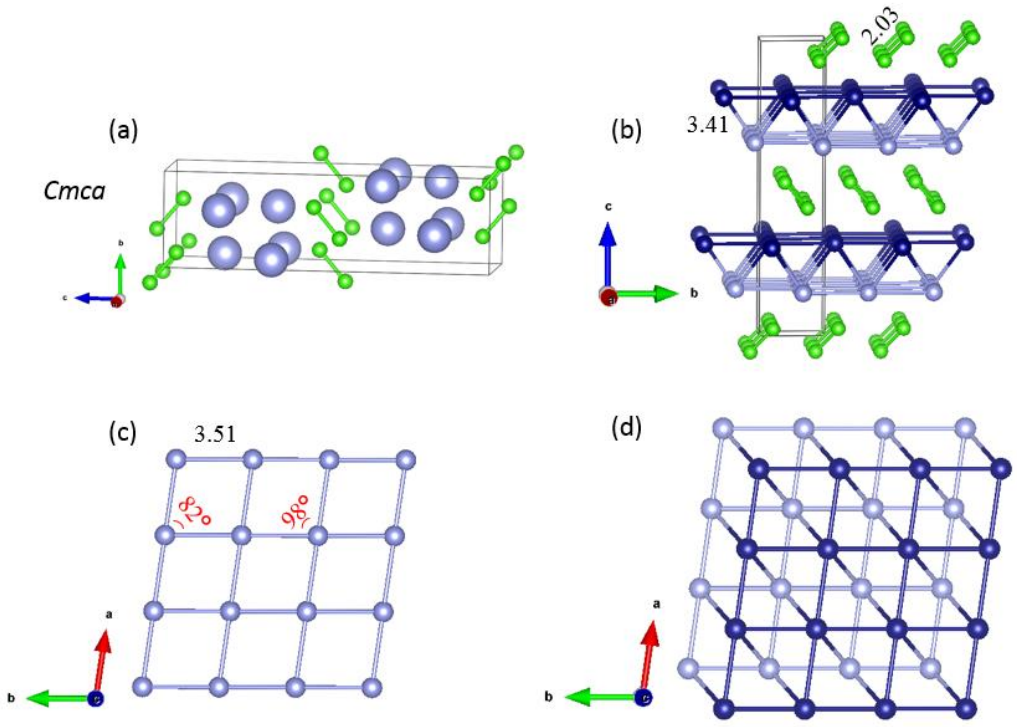

Figure 4.24 (a) The second lowest enthalpy *Cmca* structures of solid XeCl at 10 GPa. To preserve clarity, deep and light blue colors are used to illustrate the Xe atoms in the two planes. (b) shows the structure along *a* axis. (c) and (d) illustrate the Xe layers.

The next lowest enthalpy *Cmca* structure (found by PSO) has 16 atoms in the unit cell (Figure 4.24a). The Cl_2 molecules are arranged in a plane parallel to each other in Figure 4.24b. The Xe atoms are arranged to form layers and connected together at 3.41 Å distance. The bottom layer in Figure 4.24c forms a rhombus network with Xe-Xe-Xe angles of 82° and 98° and Xe..Xe contacts of 3.51 Å distance. The structure of the top layer is identical to the bottom layer. These two layers in Figure 4.24d are linked in the *c* direction but the top layer is shifted to the center of the rhombus network of the bottom layer.

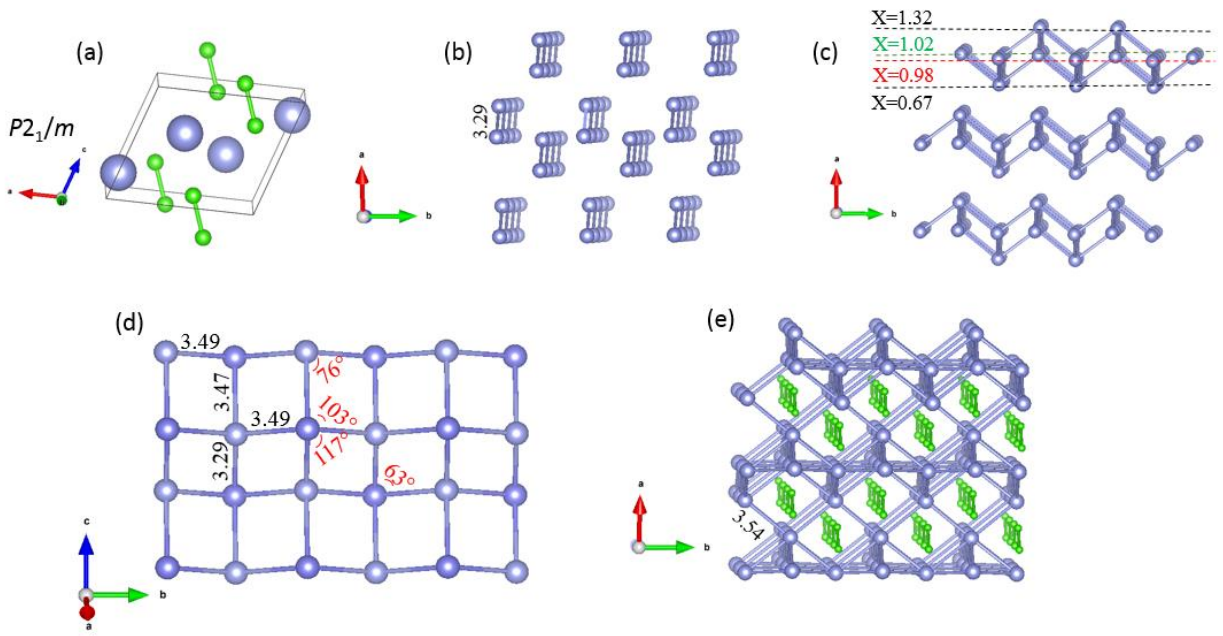

Figure 4.25 (a) The third lowest enthalpy $P2_1/m$ structures of solid XeCl at 10 GPa. (b), (c) and (d) show sublattices of Xe with different bond cutoffs. (e) shows Cl_2 molecules are located along Xe channels.

The third lowest energy structure with the $P2_1/m$ symmetry consists of 8 atoms per unit cell. The 3.29 Å distance connects two Xe atoms parallel to each other in the *a*-*b* plane but if the bond cutoff increases to < 3.3 Å other contacts appear, as shown in Figure 4.25c. the Xe atoms in puckered layer can be classified into four groups. In the first and fourth group all Xe atoms lie on the *b*-*c* plane with x=0.67 and x=1.32, respectively. In the second and third groups the Xe layers are similar and lie on the x=0.98 and x=1.02 planes. Increasing the cutoff to < 3.55 Å reveals new contacts between Xe atoms. A perspective view normal to the *a* axis in Figure 4.25d, shows corrugated Xe layers forming unequal parallelograms. Once again, long Xe..Xe contacts in Figure 4.25e form channels where Cl_2 molecules are running through the *c* axis.

To summarize, analysis of XeCl structures at 10 GPa shows that the Xe atoms tend to arrange into layers to interact with Cl_2 molecules. As discussed above, the $C2/m$ structure is energetically most favourable where Cl_2 molecules run along the *c* direction through the Xe channels. In comparison, in the *Cmca* structure, Cl_2 molecules are arranged along the *a* axis between the 2D Xe layers. Interestingly, a similar arrangement of the Xe 2D layers between Cl_2 molecules (the *Cmcm* structure in Figure 4.4g) was also found energetically favorable in $XeCl_2$ at 10 GPa.

Eventually, in the $P2_1/m$ structure, the puckered layers of Xe with Cl_2 aligned through the *c* axis have higher energy.

4.4.2 Energy corrections and electronic properties

The three structures are dynamically stable as no imaginary modes were found in the phonon calculations. In this case, inclusion of the vdW interaction did not change the energy sequence predicted by the PBE functional. In the PBE calculations in Table 4.4, the enthalpy difference for the *C*2/*m*, *Cmca* and $P2_1/m$ structures is less than 3 meV/atom at 10 GPa. Even though the vdW functional uniformly increased the energy by about 0.4 eV/atom, it did not change the energetic order. The *C*2/*m* structure remains the most stable structure in the pressure range from 10-34 GPa.

Table 4.4 Calculated lowest enthalpy structures with vdW corrections for XeCl compound at 10 GPa.

Space group	PBE (eV/atom)	PBE+vdW-DF2 (eV/atom)
*C*2/*m*	1.216801	1.630152
Cmca	1.219087	1.6315583
$P2_1/m$	1.219696	1.6332095

We have calculated the ELFs for the three lowest enthalpy structures at 10 GPa. Figure 4.26 shows high ELF contours are found at the region of the lone pairs and at the Xe atoms. Moderate ELF values (~0.7) are found between two Cl atoms showing the existence of a covalent bond. There is no evidence of any interaction between Xe and Cl atoms. Bader charge analysis [196] indicates an electronic charge being transferred from Xe to Cl atoms and, similar to $XeCl_2$, this value is about (~0.1e) for the three structures at 10 GPa. Once again, it is indicative that Xe and Cl atoms are slightly ionic at 10 GPa.

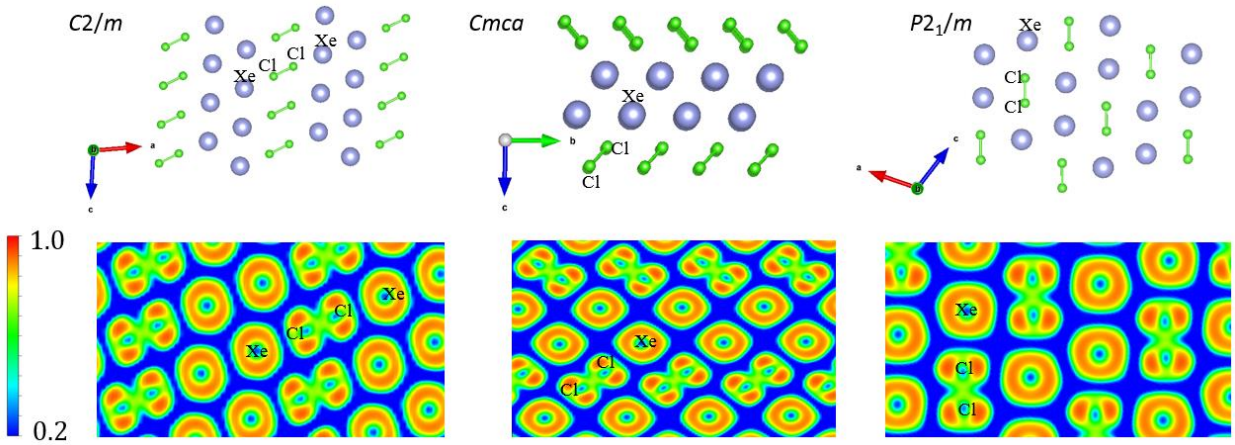

Figure 4.26 At 10 GPa, the ELF values for the *C*2/*m*, *Cmca* and *P*2$_1$/*m* structures of XeCl with cross sections of (010), (100) and (010), respectively. The positions of Xe and Cl atoms are also shown for clarity.

4.4.3 Comparison with experiment

Raman spectra were calculated for *C*2/*m*, *Cmca* and *P*2$_1$/*m* structures at 4 and 20 GPa. Figure 4.27 shows the Raman spectra of the *C*2/*m* structure are very similar at two pressures where the low intensity peaks emerge around 160 cm^{-1} and a strong band is evident at 440 cm^{-1}. At 4GPa, the *Cmca* Raman spectra show very weak peaks around 150 cm^{-1} and the strong band at 480 cm^{-1}. At 20 GPa, a few weak peaks appear at low frequency and the vibration of the strong peak shifts to 462 cm^{-1}. The first peak of the *P*2$_1$/*m* structure remains weak at 160 cm^{-1} at both pressures but the main peak has shifted from 460 to 443 cm^{-1}. The shift to a lower frequency is unusual as it would have suggested a weakening of Xe-Cl interactions. Once again, the calculated Raman spectra do not reproduce all the features in the observed spectra.

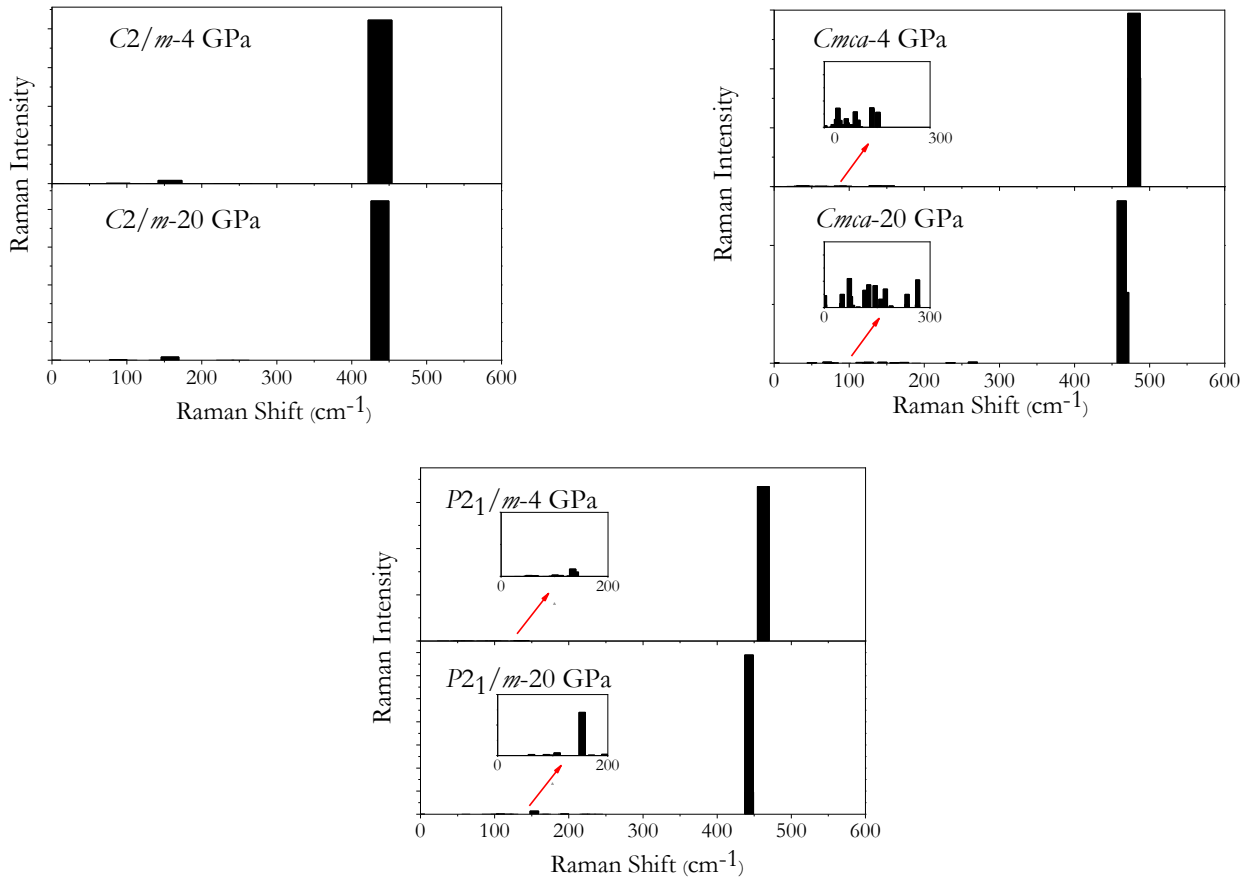

Figure 4.27 Comparison of Raman spectra of our calculated *C*2/*m*, *Cmca* and $P2_1/m$ structures of XeCl at 4 GPa with the experimental result of that at 4.2 GPa in Figure 4.10.

The calculated energy dispersive x-ray diffraction patterns of *C*2/*m*, *Cmca* and $P2_1/m$ structures were computed and compared with experiment at 4.2 GPa [189]. Figure 4.28 illustrates that once again, no agreement with experiment was observed.

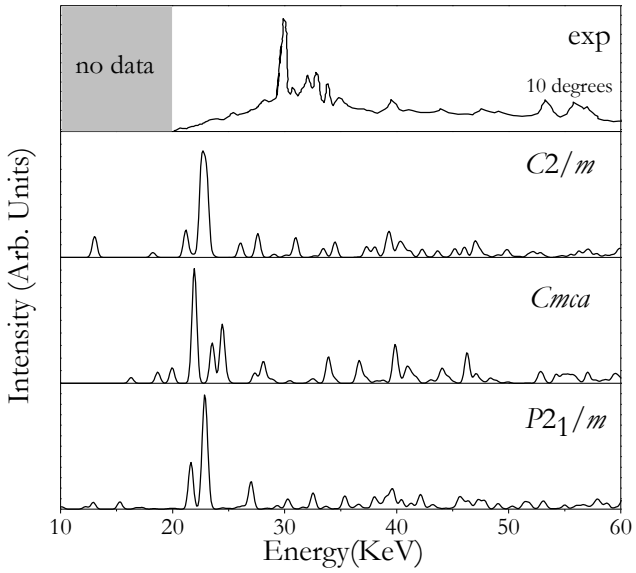

Figure 4.28 Comparison of the measured X-ray diffraction pattern of the Xe-Cl_2 sample [189] with *C*2/*m*, *Cmca* and $P2_1/m$ structures of XeCl at 4 GPa.

4.4.4 Electronic structure at 15 GPa

Since the electronic band structures of the predicted structures of $XeCl_2$ are shown at 15 GPa, we calculated the electronic properties of the *C*2/*m* structure at the same pressure using the PBE functional and GW corrections (Figure 4.29). An indirect gap separates the occupied band at Γ and *E* symmetry points of the conduction band. The PBE gap is 2.13 eV and increased to 4.17 eV after the GW corrections. The rather large band gap (> 4 eV) indicates that the compound should be transparent. The calculated partial DOS shows the *p* orbitals of Cl_2 contribute the most near the Fermi level. We also computed the optical absorption and reflectivity spectra using the BSE approximation. Once again at 15 GPa, reflectivity is weak due to the insulating property.

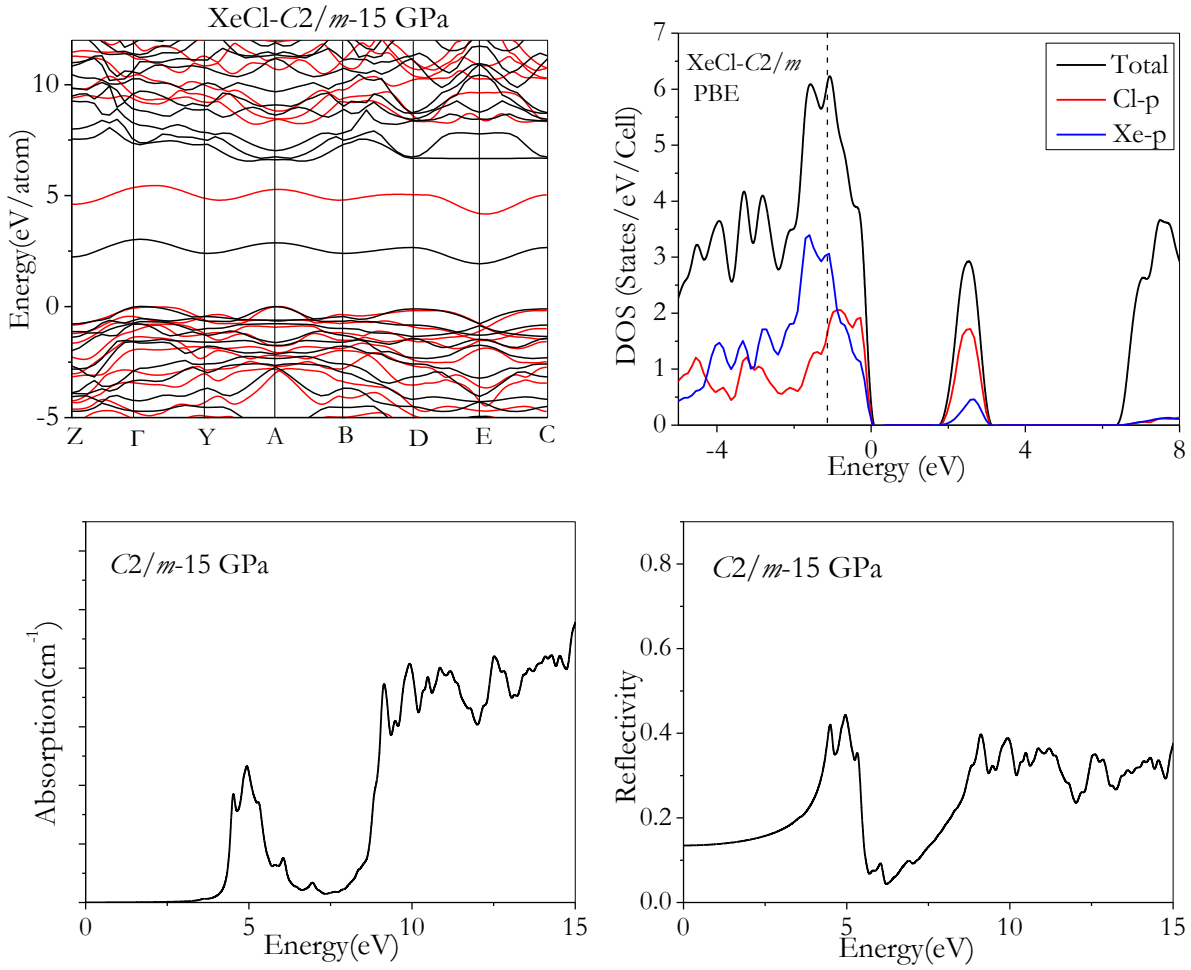

Figure 4.29 Band structures, partial electronic densities of states, absorption and reflectivity of the XeCl *C*2/*m* structure at 15 GPa.

4.4.5 Structural analysis at 40 and 60 GPa

Between 40 and 60 GPa, structure searches by the PSO method predicted the *Cmc*2_1 and *Cmcm* structures are the most stable, respectively. The *Cmc*2_1 orthorhombic structure consists of 8 formula units per unit cell. From EOS calculations, this structure has the lowest enthalpy among all the predicted structures in the pressure range 35-55 GPa. This structure at 40 GPa is illustrated in Figure 4.30. The Xe atoms located at the x=0.68 and at x=0.81 planes form buckled layers with Xe..Xe contacts < 3.32 Å. These connected atoms created the Xe channels as shown in Figure 4.30a. A perspective view down to the *a* axis in Figure 4.30b shows the corrugated Xe layers are constructed from a network of edge-shared parallelograms. The bond lengths of the Cl_2 in the channels alternate between 2.06 and 2.33Å. The Cl atoms form zigzag chains running

parallel to the *c* axis with a Cl-Cl-Cl angle of 75.7°(Figure 4.30c). When the Xe..Xe contacts were increased to 3.5 < Å, new linkage appeared between the Xe and a buckled hexagonal network of Xe atoms formed (top view of the *b*-*c* plane in Figure 4.30d).

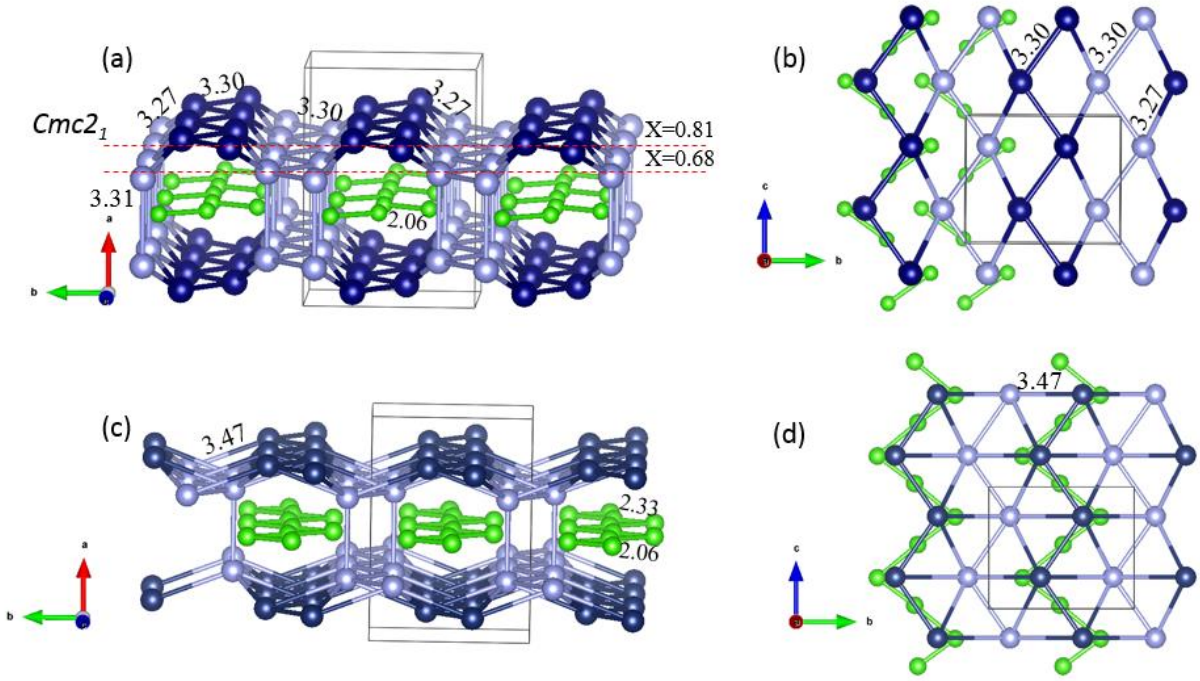

Figure 4.30 The *Cmc*2$_1$ structure for solid XeCl at 40 GPa. To preserve clarity, the Xe atoms are shown with deep and light blue colors. Different Cl and Xe bond cutoffs, (a) and (b) shorter and (c) and (d) longer, are shown.

The most stable structure predicted at 60 GPa has an orthorhombic structure with the *Cmcm* space group (Figure 4.31). This structure is related to the *Cmc*2$_1$ structure with 8 formulae per unit cell. The difference between the two structures is in the arrangement of the zigzag Cl chains. In the *Cmcm* structure, the Cl-Cl-Cl angle value is 73.1° and the Cl-Cl bond lengths are equal (2.17 Å). Two Xe atoms (light blue) from two buckled layers are connected with 3.2 Å distance. The features in the *Cmc*2$_1$ and *Cmcm* structures along the *a* axis are quite similar. Figure 4.31b shows the top view of the Xe and Cl networks. Clearly, the zigzag Cl-Cl chains follow the arrangement of Xe layers. This interesting configuration indicates that the interaction between the Xe and Cl layers may be important.

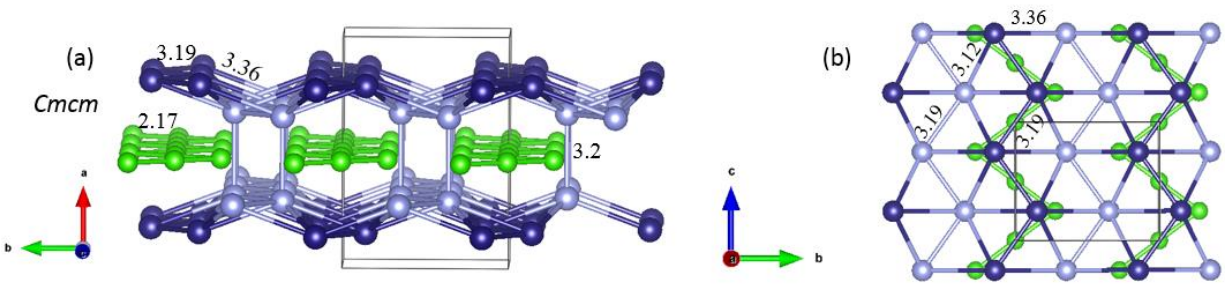

Figure 4.31 The *Cmcm* structure for solid XeCl at 60 GPa, shown in two perspectives.

4.4.6 Electronic properties at 40 and 60 GPa

The ELF contour maps for the *Cmc*2_1 and *Cmcm* structures respectively at 40 and 60 GPa in the (100) planes of the Cl layer are depicted in Figure 4.32a-b. At 40 GPa, due to the zigzag arrangement of Cl_2 molecules, ELF values are small between intermolecular Cl..Cl regions. (ELF values are about ~0.4 between longer Cl..Cl contacts). Indeed, higher ELF values are found between the shorter (intramolecular) Cl-Cl bonds. Therefore, at 40 GPa, there is little interaction between Cl_2 pairs and they are still molecular in character. At 60 GPa, the *Cmcm* structure becomes the most stable. ELF analysis shows an accumulation of electronic charge density located within the zigzag chain of the Cl atoms. The ELF values of ~0.6 between Cl-Cl pairs may indicate weak covalent bonds. In the (100) section of the Xe puckered layers (Figure 4.32c), highest ELF values are found in the region at the Xe atoms. No charge localization was found in the interstitial site of the Xe hexagonal networks. Bader analysis found that the charge transferred from the Xe to Cl atoms is about 0.2e at 60 GPa. We can conclude, similar to $XeCl_2$, that this amount of charge transfer shows ionic interaction between adjacent Xe and Cl layers.

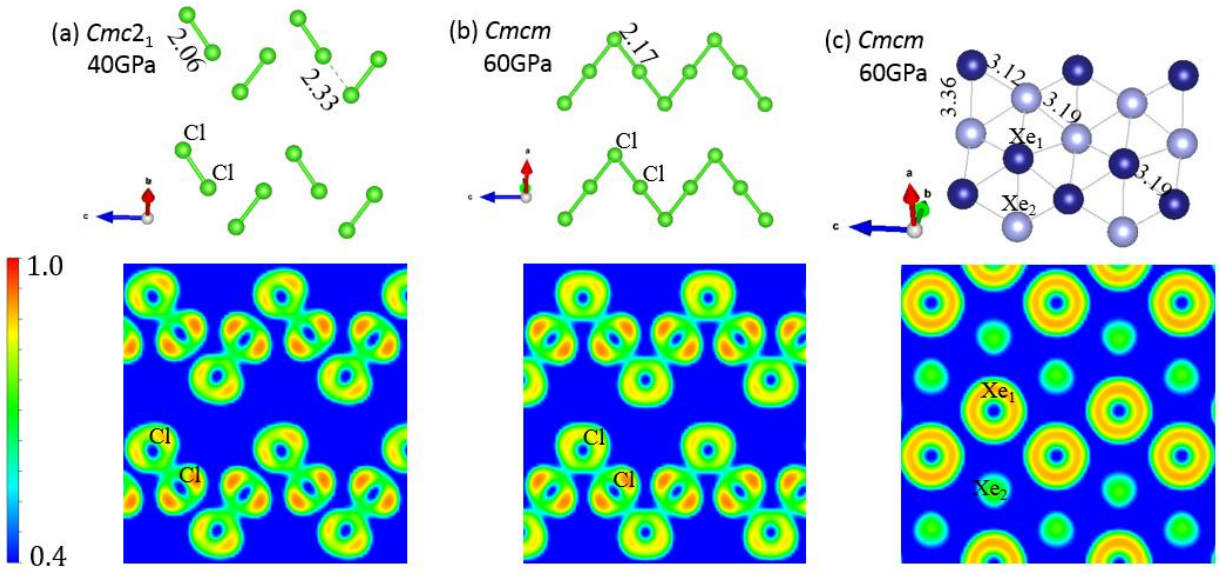

Figure 4.32 The ELF values for the (a) *Cmc*2$_1$ (b) and (c) *Cmcm* structures of XeCl with cross sections of (100). The ELF values were computed for the *Cmc*2$_1$ and *Cmcm* structures at 40 and 60 GPa, respectively. The positions of Xe (light and dark blue color) and Cl atoms are also shown for clarity.

4.4.7 Raman spectra and electronic structures at 40 and 60 GPa

The calculated Raman spectra for the *Cmc*2$_1$ and *Cmcm* structures at 40 and 60 GPa are shown in Figure 4.33.These calculated spectra are similar to the high pressure $XeCl_2$ structures (the *P*4$_1$2$_1$2 and *P*2$_1$2$_1$2 Raman spectra shown in Figure 4.19), with the lowest frequency vibrations found at 200 cm^{-1} and the strongest peak at ~350 cm^{-1}.

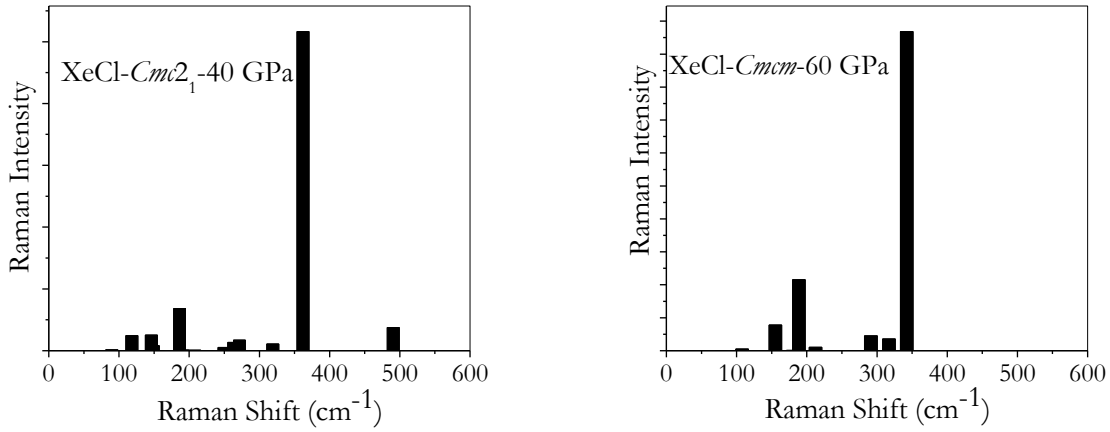

Figure 4.33 The calculated Raman spectra for *Cmc*2$_1$ and *Cmcm* structures of XeCl at 40 and 60 GPa, respectively.

Electronic band structures of *Cmc*2$_1$ *and Cmcm* were calculated using the PBE functional and GW corrections at 40 and 60 GPa, respectively. For the *Cmc*2$_1$ structure, the PBE and GW band gaps are 0.81 and 1.99 eV, respectively (Figure 4.34). At 60 GPa, in the *Cmcm* structure, the PBE gap is 0.3 eV and increases to 0.81 eV after GW corrections. In comparison to the electronic structures of the high pressure $XeCl_2$, the band gaps of the XeCl compounds are smaller. The larger Cl-Cl interactions in the Cl chains led to the substantial lowering of the band gaps. The calculated electronic density of states of both structures shows the DOS near the Fermi level are dominated by the Xe and Cl valence *p* orbitals. The substantially smaller band gap suggests XeCl may metallize at pressure higher than 60 GPa.

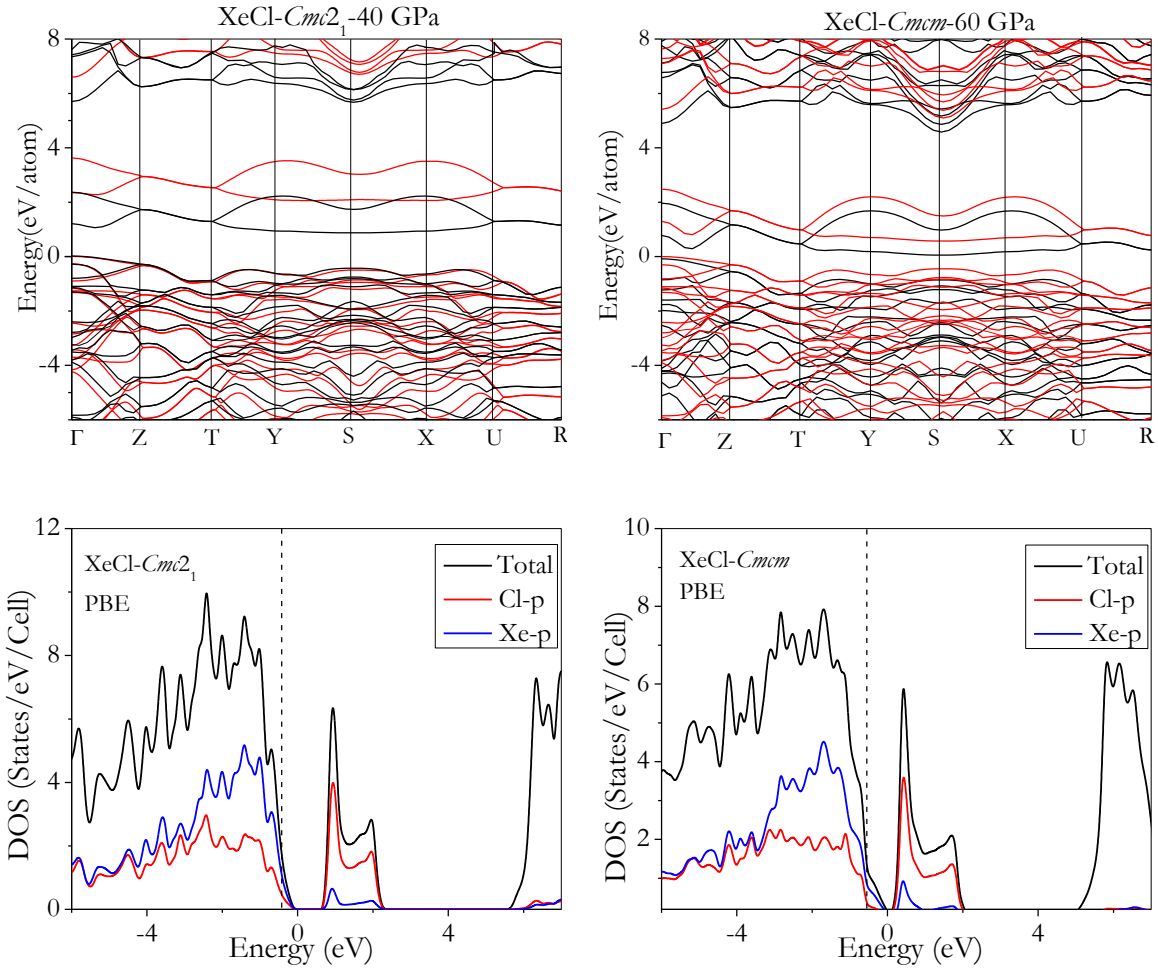

Figure 4.34 Band structures of $Cmc2_1$ and *Cmcm* structures of XeCl shown by black and red lines for PBE and GW corrections at 40 and 60 GPa, respectively. Total and partial DOSs of both structures are shown as well.

4.5 Predicted high pressure structures of $XeCl_4$

$XeCl_4$ is the last member of the $XeCl_n$ series studied. Structural searches were performed with both PSO and GA methods using populations consisting of 50 trial structures and four formula units of $XeCl_4$ (20 atoms). Results of the predicted lowest enthalpy structures are summarized in Table 4.5. In contrast to XeCl and $XeCl_2$, in the pressure range from 10 to 60 GPa, the formation enthalpies of the high pressure structures are highly positive. Therefore, all the predicted structures are not stable against dissociation into the elemental solids. Compared to the PSO results, the GA method failed to predict low enthalpy structures. The energies of the favorable predicted structures found by GA are at least 0.03 eV/atom higher than PSO structures. We have checked the stability of the predicted PSO structures and except for the *P*1 structure predicted at 20 GPa, the other

structures shown in Table 4.5 have imaginary modes, which means these structures are dynamically unstable. Details on the phonon band structures are given in the APPENDIX A.

Table 4.5 Comparison of the lowest enthalpy structures of 4 formula units of $XeCl_4$ predicted by GA and PSO methods in pressure range of 20 to 60 GPa.

PSO	Population	50		
	Pressure (GPa)	20	40	60
	Total #Gen	40	40	40
	Structure	$P1$	$P1$	$P\bar{6}2m$
	Found	9	17	30
	Enthalpy (eV/atom)	1.6116	3.8766	5.8232
GA	Population	50		
	Pressure (GPa)	20	40	60
	Total #Gen	40	40	40
	Structure	$P1$	$P1$	Pm
	Found	37	22	30
	Enthalpy(eV/atom)	1.6484	3.9257	5.8810

Although no stable structures were expected for $XeCl_4$ within the pressure range studied, an analysis the of low enthalpy structures is still of interest. At 60 GPa, the $P\bar{6}2m$ structure was predicted to have the lowest enthalpy. The existence of slabs of connected six-member Xe atoms is evident (Figure 4.35). Two types of Cl bondings are found: The first group, molecular Cl_2 with two lengths of 1.97 and 2.1Å, and the second group, a Cl chain with longer Cl..Cl contacts of 2.66 Å, are located along the Xe channels.

The second lowest enthalpy $P2_1/c$ structure is formed from 1D Xe chains and Cl_2 molecules. Higher enthalpy structures ($P1$ and $C2$) tend to arrange Xe in a planar form. Eventually, monoatomic Xe with Cl atoms arranged in a 1D chain found in the $C2/m$ structure has the highest

enthalpy (~0.1eV/atom higher than the $P\bar{6}2m$ structure). All the structures of $XeCl_4$ compounds are unstable and thus may not be synthesized in the pressure range from 10 to 60 GPa.

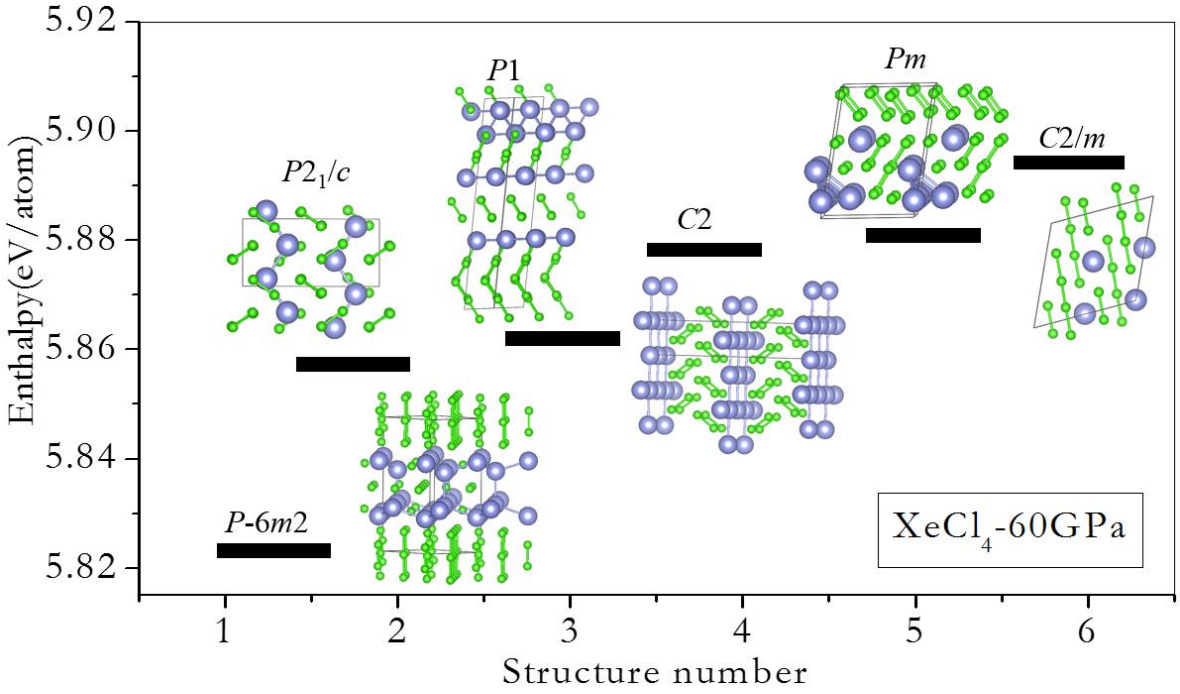

Figure 4.35 The lowest enthalpy predicted structures for solid $XeCl_4$ at 60 GPa.

4.6 Conclusions

In this study, we have examined possible high pressure structures of $XeCl_n$ (n=1, 2 and 4) below 60 GPa. We found that, quite often, the lowest enthalpy (global minimum) structures are missed by both PSO and GA methods. This observation is in contrary to claims of almost absolute reliability of the two structural search methods. For example, the low enthalpy $P2_1/m$ structure of the $XeCl_2$ compound was not predicted at 10 GPa. We should be caution that apart from the atomic species and the number of atoms in the model, both structural search methods have inherent parameters governing the convergence, such as the percentage of mutation *vs* heredity operations in GA and the relative weigh of the bias against local and global minimum is PSO. Only the recommended default values were used in this investigation. However, since randomly generated structures in the PSO search were constrained by 230 space groups, it was more efficient to find crystalline structures. Our comparisons indicate that the PSO method was more successful at predicting lower enthalpy $XeCl_n$ structures in the Cl-rich region. The calculated Raman spectra

and energy dispersive x-ray diffraction for XeCl and $XeCl_2$ structures are not consistent with experimental measurements [189]. At this point, the discrepancies between theory and experiment are not clear but, it is likely due to difficulties to the formation of Xe-rich Xe_nCl compounds. However, all predicted structures for XeCl and $XeCl_2$ turned out to be dynamically stable but thermodynamically unfavorable below 55 GPa. The stable compounds (XeCl and $XeCl_2$) found at 60 GPa, are semiconductors. In contrast to the XeCl and $XeCl_2$ compounds, in the pressure range from 10 to 60 GPa, the formation enthalpies are highly positive for $XeCl_4$. In addition, the predicted compounds are also not dynamically stable, which ensures the compound does not form below 60 GPa. In the next chapter, we will present the results on the possible of the formation of high pressure compounds for the two remaining Xe-halide (Br and I).

CHAPTER 5

Crystal structures and electronic properties of xenon bromide and iodide at high pressure

The primary motivation for the study of $XeBr_n$ and XeI_n (n=1, 2 and 4) compounds at high pressure is based on speculation since the size of Br and I atom are larger than Cl and more comparable to Xe, should be more polarizable and have a better chance in forming covalent bonds with Xe. Therefore, a systematic comparison of the evolution of the high pressure structures and chemical bonding in Xe-halides from Cl to Br and I at high pressure is worthy and is investigated in this chapter. The content of this chapter is divided into two major parts: the study of the high pressure structures of Xe-Br and Xe-I and the associated properties.

We first describe the structural transformation sequence of solid Br_2 under pressure. Similar to Cl_2, Br_2 is a diatomic molecular crystal at low pressure and has a base-centered orthorhombic *Cmca* structure. This structure is found to be stable by x-ray diffraction up to 70 GPa [197] A first-order phase transition associated with molecular dissociation was found to begin at 80 ± 5 GPa. Coexisting with the molecular phase, new diffraction peaks begun to emerge at 82 GPa that can be indexed to a body-centered orthorhombic structure with the *Immm* space group. The monatomic phase has a structure similar to that observed in solid iodine at 21 GPa [198]. However, the direct molecular → monoatomic phase transition was later challenged by a recent x-ray absorption spectroscopy experiment which presents evidence that an intermediate phase occurred at 84 GPa [199] This phase was suggested to have an incommensurate modulated structure. The monoatomic *Immm* phase was only observed at pressure above 115 GPa [199], [200].

Regarding the electrical property, studies have shown that bromine is a metal at high pressure [197],[201]. A hint of metallization was detected around 60 GPa where the surface of the sample begins to reflect light. Later, Shimizu *et al* reported direct measurements of the electrical resistance of solid bromine [202]. According to their measurements, molecular Br_2 metallized at *ca*. 80 GPa. In addition, the metallic phase is a superconductor with a critical temperature T_c of 1.5 K between 80 and 120 GPa [203]. This observation is supported by a theoretical calculation showing the monatomic phase is a superconductor with T_c of 1.46 K at 100 GPa [204]. In this chapter, we first report the theoretical investigation of the phase stabilities of stoichiometric $XeBr_n$

(n=1, 2 and 4) up to 60 GPa. Then, the electronic and vibrational properties of selected stable structures will be presented.

5.1 Thermodynamics stability of $XeBr_n$ (n=1, 2 and 4)

The enthalpies of formation were computed relative to solid fcc Xe and the *Cmca* structure of molecular Br_2 which is the stable phase below 60 GPa. Most of the predicted structures were found to have positive formation enthalpies (Figure 5.1). The exception is a $XeBr_2$ compound formed at 60 GPa. Detailed discussion on the crystal and electronic structures of XeBr, $XeBr_2$ and $XeBr_4$ is given below.

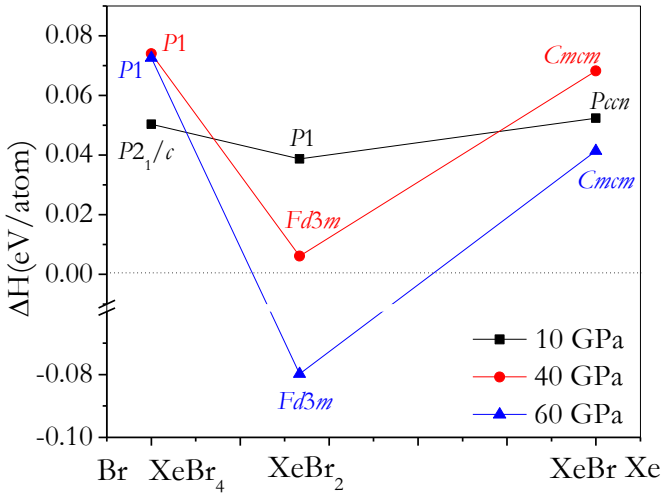

Figure 5.1 Predicted formation enthalpies of Xe–Br compounds below 60 GPa.

5.2 Predicted high pressure structures of XeBr

Similar to previous studies on $XeCl_n$, a structural search was terminated after a minimum energy structure was found and no new lower enthalpy structure appeared for at least 20 successive generations. We considered a model consisted of 8 formula units per unit cell with one population of 50 structures. The lowest enthalpy structures for XeBr found by PSO at 10, 40 and 60 GPa are summarized in Table 5.1. At 10 and 40 GPa, the $P2_1/c$ and *Cmcm* were found to be the lowest enthalpy structures, respectively. The *Cmcm* structure became the second lowest enthalpy structure at 60 GPa. At this pressure, the primitive cell of *Fmm*2 structure (32 atoms in the conventional cell) was found to have the lowest enthalpy.

Since the primitive cell of the *Cmcm* structure consists of $4XeBr_2$ formula units, we repeated the PSO search with the smaller primitive cell in order to affirm that the prediction procedure is robust. Surprisingly, during the structure search a *P*2 structure having higher enthalpy of formation found in the 9^{th} generation was trapped in a local minimum and no new stable structure was found. The observation suggests contrary to the perception that a global minimum structure should be easier to find in a smaller model with less degree of freedom, sometimes, as in this case, metastable structures can be trapped in local minima leading to erroneous results.

Table 5.1 The lowest enthalpy structures of XeBr with PSO method in pressure range of 10 to 60 GPa.

PSO	Population	50			
	Formula unit	4(XeBr)	8(XeBr)		
	Pressure (GPa)	60	10	40	60
	Total #Gen	39	40	36	31
	Structure	*P*2	$P2_1/c$	*Cmcm*	*Fmm*2
	Found at	9	26	16	8
	Enthalpy (eV/atom)	8.789223	1.49038	6.16024	8.69822

The formation enthalpies as a function of pressure for the predicted low energy candidate structures are compared in Figure 5.2. At 10 GPa, the $P2_1/c$ and *Cmcm* structures are energetically competitive with an energy difference less than 0.1 meV/atom. Their crystal structures are closely related with only small variations in the unit cell and atomic positions. However, these two structures are not the lowest enthalpy structures at 10 GPa! Instead, a *Pccn* structure, which is the second lowest enthalpy structure found by PSO search at 40 GPa, is found to be the most stable. From EOS calculations, at 10 GPa, the *Pccn* structure is ~0.003 eV/atom lower than $P2_1/c$ structure. Once again, the lowest enthalpy structure was missed in the PSO search! At 60 GPa, the *Fmm*2 structure was found to have the lowest enthalpy. Note that the energy of this structure decreased dramatically by increasing the pressure and eventually the formation enthalpy became negative above 70 GPa and was thermodynamically stable against the elemental components. The

Cmcm structure found at 40 GPa now becomes the second lowest enthalpy structure. The stabilities and characteristics of the *Pccn* and $P2_1/c$ structures at 10 GPa and *Cmcm* and *Fmm*2 structures at 60 GPa will be discussed in detail below.

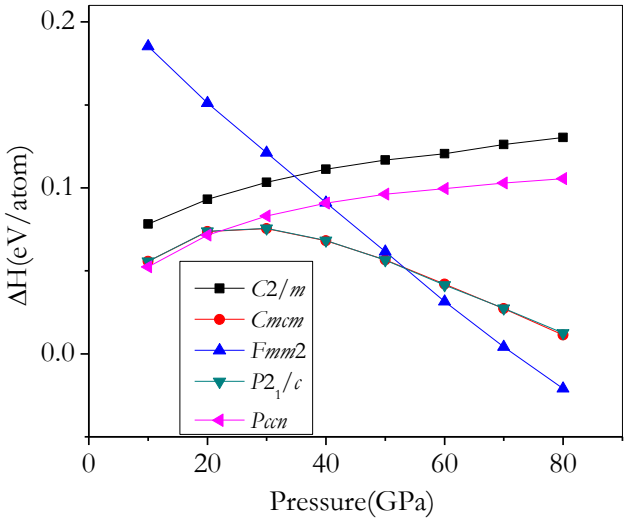

Figure 5.2 The formation per atom with respect to elemental Xe and molecular Br_2 for XeBr compounds.

5.2.1 Structural analysis at 10 GPa

The orthorhombic *Pccn* structure has 16 atoms (8XeBr) in the unit cell. The Br atoms form zigzag chains running parallel to the [1 1 0] and [$\bar{1}$ 1 0] directions with a Br-Br-Br angle of 88.7° (Figure 5.3b). The closest Br..Br atom contact is 2.51 Å. When viewed down the *a* axis, Xe also seems to form zigzag chains with Xe..Xe contacts < 3.6 Å (Figure 5.3c). However, in fact, a buckled square layer of Xe was observed when viewed along the *c* axis (Figure 5.3d). Two identical Xe layers depicted in Figure 5.3e show the top layer was displaced slightly in the *a* axis. When a longer Xe..Xe contact (~3.75 Å) was used, the two layers were linked and a triangle network of Xe appeared (Figure 5.3f).

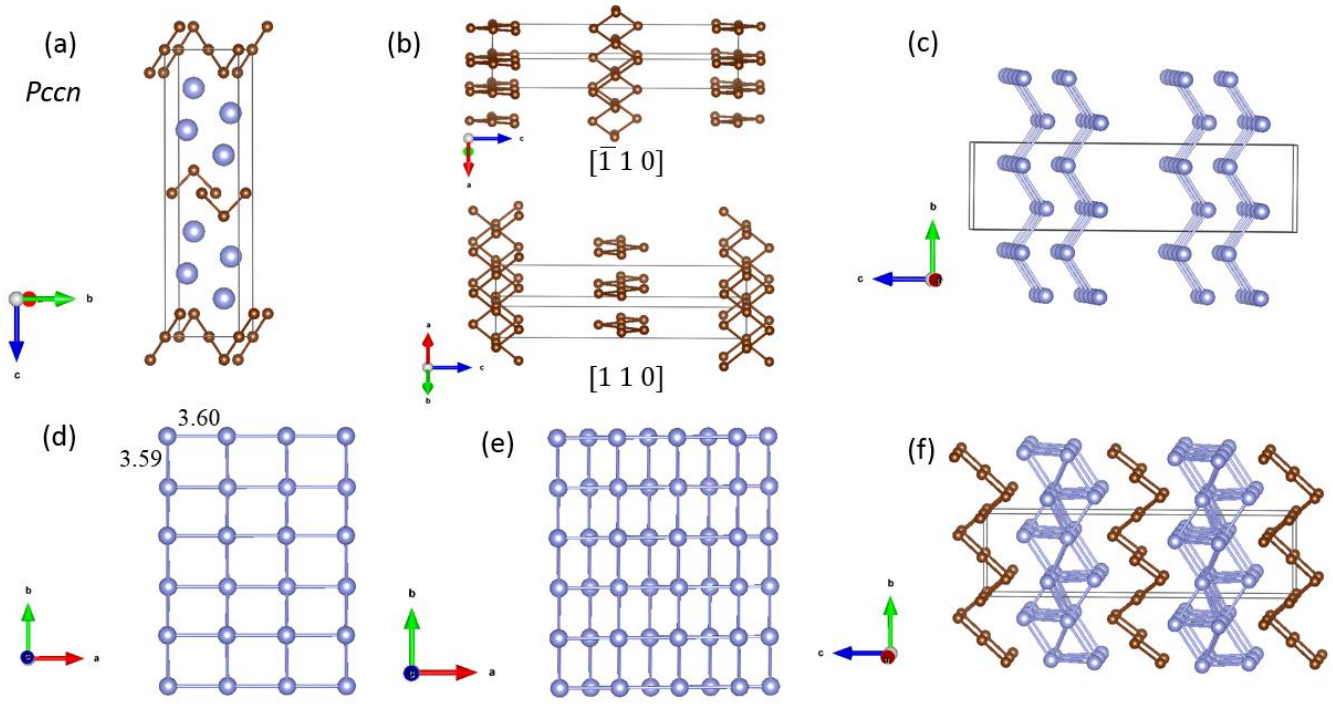

Figure 5.3 (a) the lowest predicted enthalpy *Pccn* structure of XeBr at 10 GPa. Br sublattice in two different directions is shown in (b). (c), (d) and (e) show sublattice of Xe with bond cutoff < 3.6 Å and (f) the *Pccn* structure with Xe bond cutoff < 3.75 Å.

The second lowest enthalpy $P2_1/c$ structure is composed of 8 formula units. This structure is similar to *Cmcm* XeCl at 60 GPa in Figure 4.31, which also formed from zigzag chains of Cl running along the channels created by the Xe (Figure 5.4b). The Br chains running parallel to the *b* axis have Br-Br-Br angles of 78.5°. The shortest Br..Br atoms contact is 2.49 Å and the Xe..Xe contacts alternate between 3.79 and 3.95 Å.

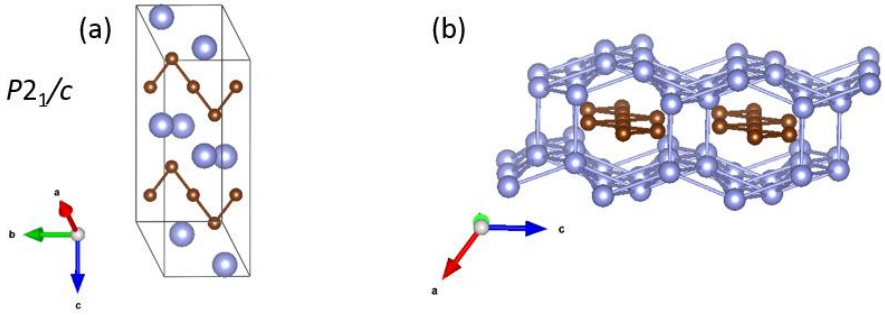

Figure 5.4 The second lowest predicted enthalpy $P2_1/c$ structure of XeBr at 10 GPa.

5.2.2 Electronic and dynamical properties

Even though the *Pccn* and $P2_1/c$ are not thermodynamically stable, we wish to examine the dynamical stability with phonon calculations using the supercell method. Frozen phonon calculations reveal a number of imaginary branches. More accurate calculations were then repeated with the linear response method with a dense *k* mesh at the *q* points where imaginary frequencies were found. Same results were obtained thus confirming the supercell results. We also employed the vdW functional in the frozen phonon calculations and obtained the same results. Therefore, the *Pccn* structure is not dynamically stable. Phonon calculations on the $P2_1/c$ structure also showed imaginary modes indicating that this structure is not dynamically stable.

The effect of vdW interaction for the *Pccn* structure is investigated in Figure 5.5. The predicted volumes are almost equal to the PBE result at 10 GPa. The calculated volumes only deviated slightly at higher pressures with the PBE having a smaller volume.

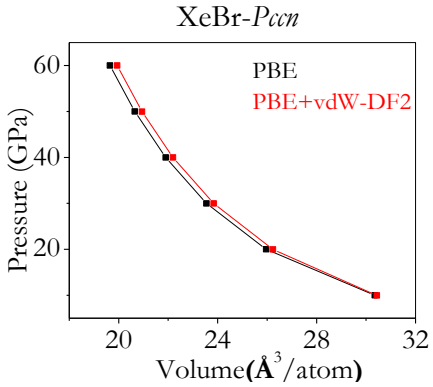

Figure 5.5 The calculated equation of state of *Pccn* structure of XeBr compound.

The ELF of the two lowest enthalpy structures at 10 GPa (*Pccn* and $P2_1/c$) were calculated. Small ELF values (< 0.5) between Br atoms in the zigzag chains indicate the absence of strong covalent bond (Figure 5.6). Bader analysis show very small charge transfer (< 0.1e) between Br and Xe atoms, suggesting a weak ionic interaction at 10 GPa.

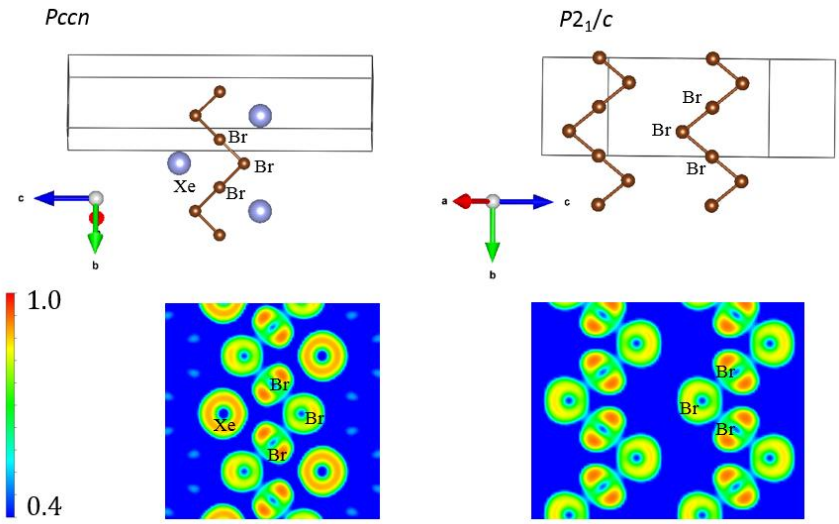

Figure 5.6 The ELF values of zigzag chains of Br atoms in the *Pccn* and $P2_1/c$ structures. For clarity, the positions of Xe and Br atoms were shown.

5.2.3 The *Fmm*2 structure at 60 GPa

The orthorhombic *Fmm*2 structure has 32 atoms per unit cell and is not thermodynamically stable at 60 GPa. To assist the description of the structure in Figure 5.7, the two types of Xe and Br atoms in the structure are highlighted in dark and light blue and red, respectively. Slabs consisting of three Xe layers are stacked along the *c* direction (Figure 5.7A) and hexagonal patterns of the layers are evident when viewed down the *c* axis. The Br sublattice is composed of two identical layers running parallel to *b* axis (Figure 5.7B). The top view of the Br atoms in the *a*-*b* plane is composed of a triangular pattern (brown atoms) with diatomic Br (red atoms).

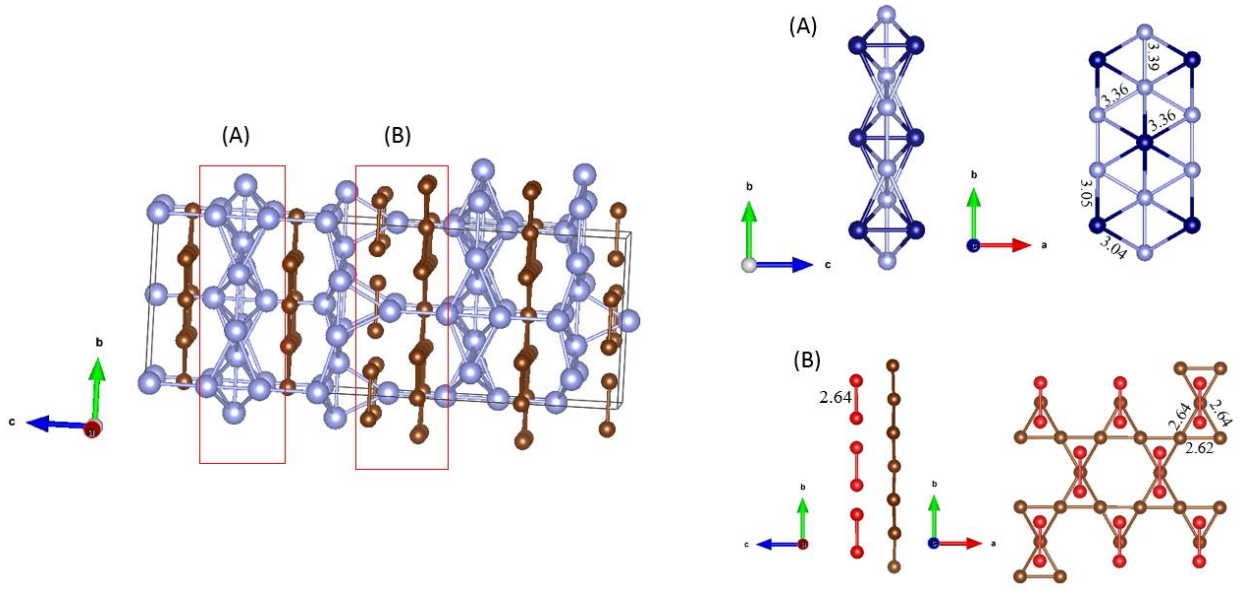

Figure 5.7 The *Fmm*2 structure of XeBr at 60 GPa. For clarity sublattice of Xe and Br atoms were shown with deep and light colors.

Phonon calculations indicate that the *Fmm*2 structure is not dynamically stable even though it is the predicted lowest enthalpy structure. It is likely that the 8 formula units used in the search may not be sufficient and bigger models are needed in order to obtain the most stable structure. The result points to a weakness of current computational limitation on the use of models with small number of atoms. This, however, is not an inherent problem with the methodology. Therefore, care must be exercised relating to the consequence on the size of the model. Convergence in the structure search is not always guaranteed unless models with bigger structural model and larger population are used.

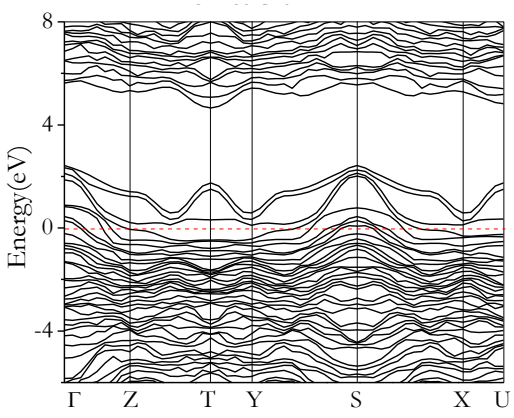

Figure 5.8 The band structure of the *Fmm*2 structure of XeBr at 60 GPa.

Despite the dynamical instability of the *Fmm*2 structure, a study of the electronic properties could be informative. The electronic band structures of *Fmm*2 computed using the PBE functional shown in Figure 5.8 inculcates the XeBr compound is metallic at 60 GPa.

5.2.4 The *Cmcm* structure at 60 GPa

At 60 GPa, the second lowest enthalpy *Cmcm* structure is consisted of 8 formula units per unit cell. The structural features are quite similar to the *Cmcm* structure of XeCl (Figure 4.31). Like the XeCl structure, the Br atoms form zigzag chains running parallel to the *c* axis with a smaller Br-Br-Br angle of 63.9°.The shortest Br..Br distances are all 2.48 Å with Xe..Xe contacts alternating between 3.1 and 3.49 Å. The Xe and Br layers viewed along the *a* axis (Figure 5.9) indicate that the Xe atoms form hexagonal puckered layers.

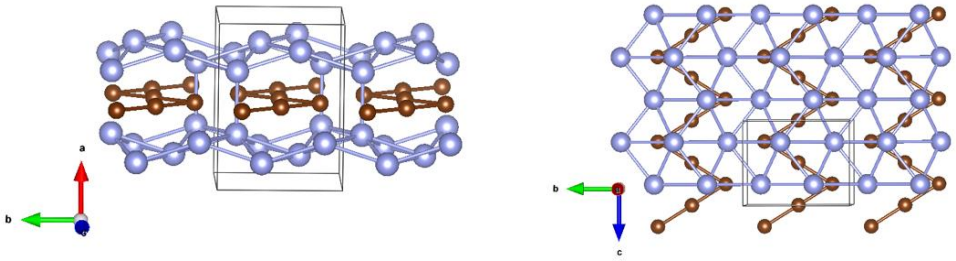

Figure 5.9 The *Cmcm* structures for solid XeBr at 60 GPa.

The ELF plotted in the (100) plane of the Br atom layer at 60 GPa are illustrated in Figure 5.10. ELF analysis shows an accumulation of electronic charge density located on the Br in the zigzag chains. The calculated ELF value of ~0.4 between the Br atoms again indicates that no covalent bond exists and the structure is a monoatomic phase. Bader analysis also found a small charge transfer from Xe to Br of about 0.1e at 60 GPa.

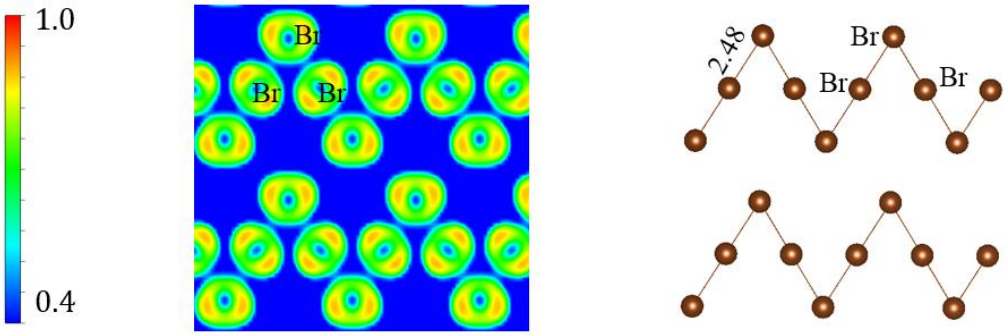

Figure 5.10 The ELF values for the *Cmcm* structure of XeBr with cross section of (100).

The phonon band structure of the *Cmcm* phase calculated at 60 GPa, is shown in Figure 5.11. The absence of imaginary vibration modes shows the structure is dynamically stable. The vibrational bands of Xe atoms are hybridized with the Br bands up to 9 THz while the higher frequencies Br vibrations extended to 11 THz. As expected, at 60 GPa, due to heavier atomic mass of Br rather than Cl, the highest vibrational bands are ~4 THz lower than Cl motions in XeCl but for the low frequency modes of Xe in XeCl and XeBr compounds, there is no significant change. The band structures and projected DOS calculated at 60 GPa are shown in Figure 5.11. The PBE result indicates that *Cmcm* is metallic. The Xe-*p* and Br-*p* states dominate the DOS near the Fermi level but the *s* and *d* electrons contributed from both atoms (not shown) are significant quite below and above Fermi level. Therefore, the electrical conductivity originates from the electrons of the overlapping *p* bands. Moreover, a distinctive flat band is observed near the Fermi level, for example, at the S point and midway of the T→ Y line. In addition a steep band was found to cross the Fermi level in the Γ→ Z direction. The co-existence of flat (heavy effective mass) and steep electronic bands (conducting) is a common feature in pressure-induced superconductors, and this scenario has been suggested as a favorable condition for enhancing electron pairing, essential for superconductivity [205].

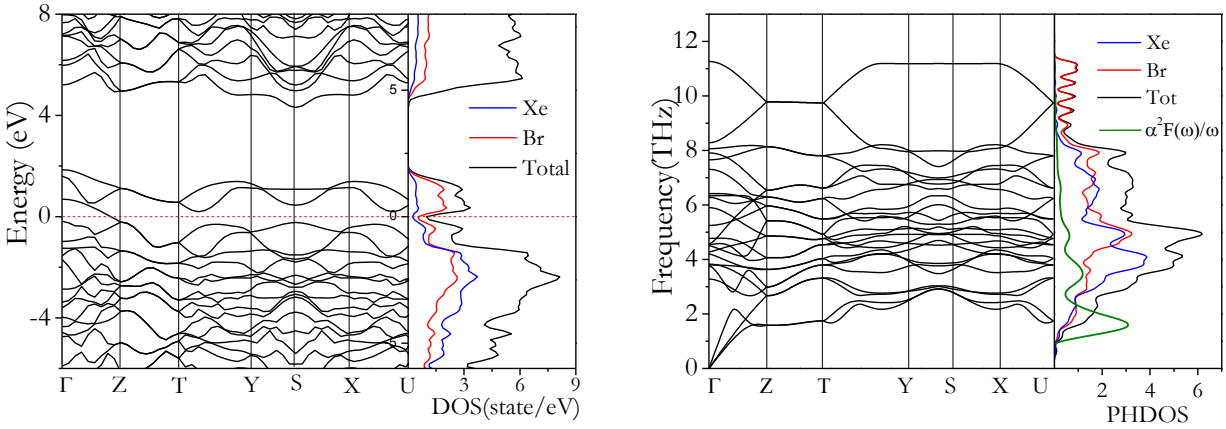

Figure 5.11 The band structures and phonon dispersion of the *Cmcm* structure of XeBr at 60 GPa.

To examine potential superconductivity, electron-phonon coupling calculations were performed. An electron-phonon coupling of λ=0.76, was calculated. Using the Allen-Dynes modified McMillan equation [169], which is applicable to weak electron phonon coupling (λ<1.5) with a nominal value of the Coulomb repulsive parameter μ* of 0.1,a T_c of ~6 K is predicted. This

is to be compared with the T_c =1.46 K calculated for monoatomic Br structure between 100 and 200 GPa [204] showing that XeBr is a better superconductor at lower pressure.

5.3 Predicted high pressure structures of $XeBr_2$

Results of the lowest enthalpy structures of $XeBr_2$ found by PSO at 10, 40 and 60 GPa are summarized in Table 5.2. At 10 GPa, a *P*1 structure was found to be the lowest enthalpy structure in the 6th generation. At 40 and 60 GPa, the same *Fd*3*m* phase was found to be the lowest enthalpy structure. Since the primitive cell of this structure is consisted of 2 formula units we again repeated the structural search with a model consisting of only 6 atoms per unit cell. In this case, the same *Fd*3*m* structure was found.

Table 5.2 The lowest enthalpy structures of $XeBr_2$ with PSO method in pressure ranges of 10 to 60 GPa.

PSO	Population	50			
	Formula unit	2($XeBr_2$)	4($XeBr_2$)		
	Pressure (GPa)	60	10	40	60
	Total #Gen	28	30	29	31
	Structure	*Fd*3*m*	*P*1	*Fd*3*m*	*Fd*3*m*
	Found at	1	6	1	12
	Enthalpy (eV/atom)	7.67056	1.0217	2.67006	7.67056

The formation enthalpies as a function of pressure for several candidate structures are compared in Figure 5.12. Once again, from the equation of state, the *Pnma* structure which was predicted to be the second lowest enthalpy in the structural search at 40 GPa, was found to be the lowest energy structure from 20 to 40 GPa. Again, the lowest enthalpy structure was missed at 20GPa. The *Fd*3*m* structure only becomes thermodynamically stable at pressures higher than 40 GPa. The stability and properties of the predicted structures are discussed below.

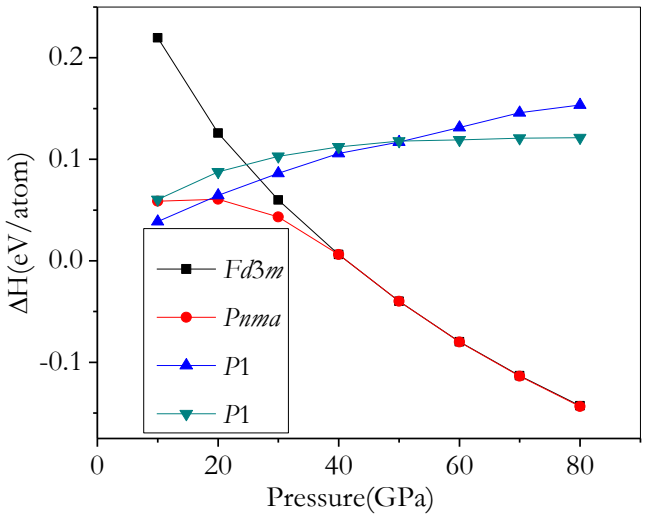

Figure 5.12 The relative enthalpies of formation per atom with respect to elemental Xe and molecular Br_2 for $XeBr_2$ compounds.

5.3.1 The *P*1 structure at 10 GPa

The *P*1 structure predicted at 10 GPa has 12 atoms in the unit cell. The Br atoms form twisted zigzag chains as shown in the perspective view in Figure 5.13b. In the chain, the Br..Br contacts alternate between 2.47 and 2.54 Å with Br-Br-Br angles of 90° and 117°. However, phonon calculations show this structure is not dynamically stable. We have studied the electronic structures and potential chemical bonding properties of this structure and we found no evidence to support the existence of strong covalent bond. Furthermore, all the low energy $XeBr_2$ compounds are insulators at 10 GPa.

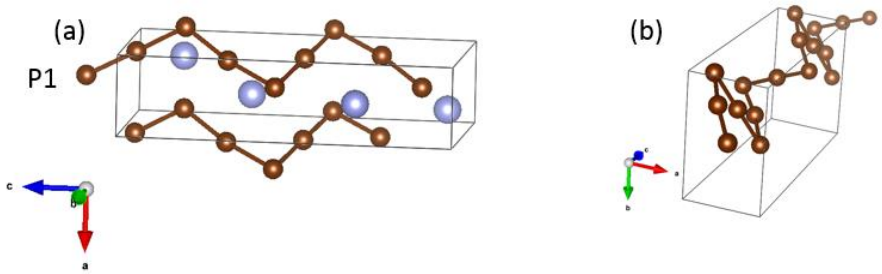

Figure 5.13 The lowest enthalpy *P*1 structure found at 10 GPa for $XeBr_2$ compound.

5.3.2 Comparison of the *Pnma* and *Fd*3*m* structures

The *Pnma* structure, the lowest enthalpy structure at 20 GPa, is consisted of 12 atoms per unit cell. From the calculation of the EOS, the *Pnma* structure transforms spontaneously to the *Fd*3*m* phase at 40 GPa. The similarities of the *Pnma* and *Fd*3*m* structures at 30 and 60 GPa are evident in Figure 5.14. The continuous structural changes suggest *Pnma* $\rightarrow$ *Fd*3*m* transformation with the fact that the *Pnma* structure was dynamically unstable at 30 GPa by phonon calculations and that the structural transformation is a second order transition.

(a) (b)

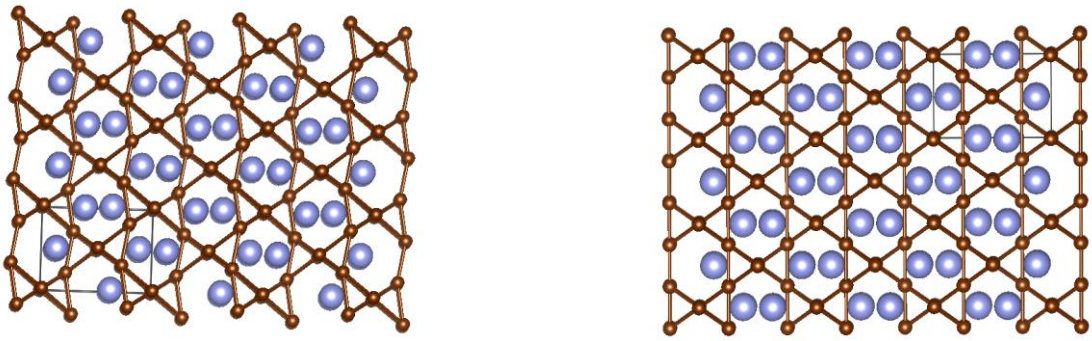

Figure 5.14 The top view along the [111] direction of the (a) *Pnma* and (b) *Fd*3*m* structures of $XeBr_2$ at 30 and 60 GPa, respectively.

5.3.3 The *Fd*3*m* structure at 60 GPa

At pressures higher than 40 GPa, the only thermodynamically stable structure found in the convex hull plot is the *Fd*3*m* phase. The fcc structure is consisted of 24 atoms per unit cell. The *Fd*3*m* phase and the local environment around Xe and Br are shown in Figure 5.15. The Xe atoms are surrounded by 12 Br atoms with Xe..Br contacts of 3.11 and 3.12 Å (Figure 5.15b). The Xe arrangement is similar to the stable $XeCl_2$ which forms an fcc sublattice at 60 GPa (Figure 5.15c). All the Xe..Xe distances are equal (3.26 Å) with Xe-Xe-Xe angles of 109.5° which is just the ideal tetrahedral angle. To describe the Br network, Br atoms in different crystallographic sites are represented with different colors as shown in Figure 5.15d and e. The Br atoms are tetrahedrally coordinated. In the middle layer, the slab of Br atoms forms 6-member planar rings connected to a triangle Br atoms from each side. All Br..Br contacts are equal to 2.66 Å.

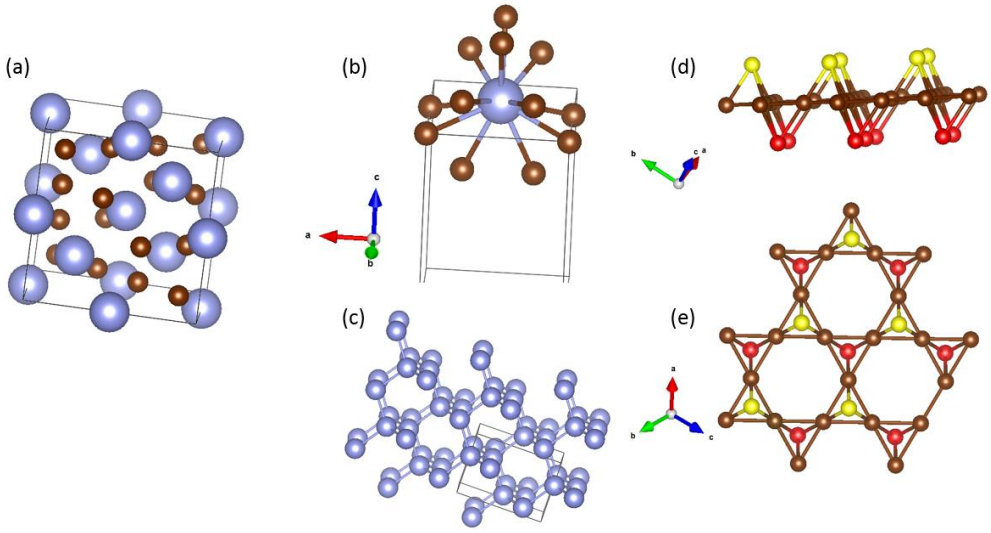

Figure 5.15 The *Fd*3*m* structure for $XeBr_2$ compound at 60 GPa.

Again, ELF calculations reveal that there is no evidence of Br-Br covalent bond. High ELF regions are only found around the Br atoms reflecting the atomic nature at 60 GPa (Figure 5.16).

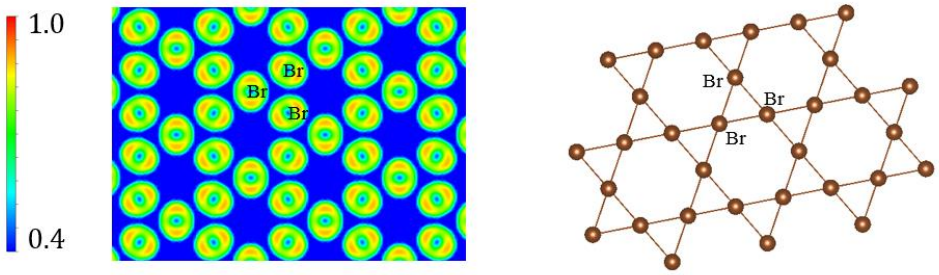

Figure 5.16 The ELF values of Br network in the *Fd*3*m* structure of $XeBr_2$ at 60 GPa.

The phonon dispersion curves of the *Fd*3*m* structure show no imaginary phonon frequency suggesting the structure is dynamically stable at 60 GPa (Figure 5.17). The projected vibrational densities of states show the flat bands slightly above 4 THz are dominated by Br vibrations. At 4.36 THz, the phonon modes at the Γ point can be assigned to the rotation of Br atoms. Higher frequency modes (~12 THz) are mainly derived from Br stretch motions. The band structures calculated with the PBE functional indicates that the $XeBr_2$ is metallic at 60 GPa. Once again, similar to *Cmcm* XeBr, the band structure shows features of coexistence curve and flat bands. Additionally, electron-phonon coupling calculations predicted λ=0.43. Using a μ^* of 0.1, a superconducting critical temperature of the *Fd*3*m* phase is estimated to be ~1.4 K at 60 GPa.

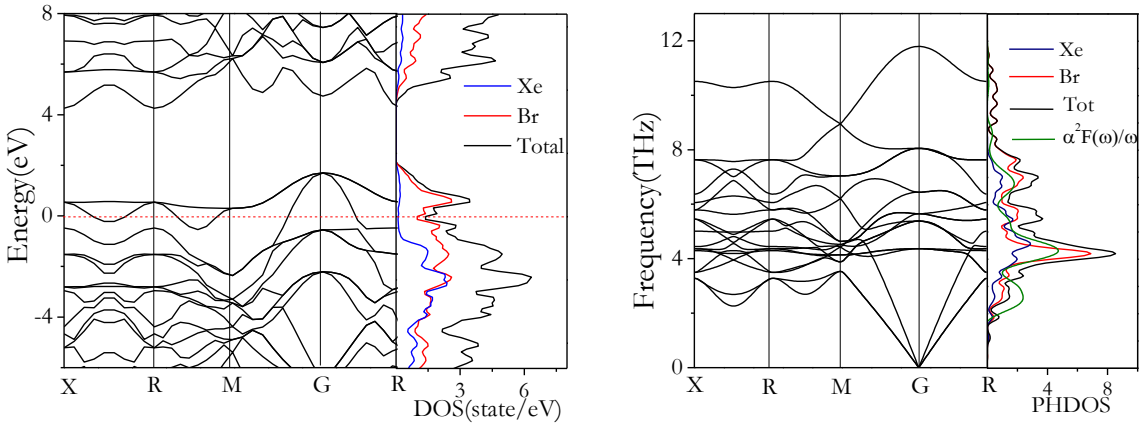

Figure 5.17 The band structures and phonon dispersion of the *Fd*3*m* structure of $XeBr_2$ at 60 GPa.

5.4 Predicted high pressure structures of $XeBr_4$

A summary on the technical details of search procedure for the predicted lowest enthalpy structures of $XeBr_4$ found by PSO at 10, 40 and 60 GPa is shown in Table 5.3. Due to highly positive formation enthalpies of all the predicted structures, since none of the structures is likely to exist, the PSO search was terminated at 30th generations.

Table 5.3 The lowest enthalpy structures of $XeBr_4$ with PSO method in pressure ranges of 10 to 60 GPa.

PSO	Population	50		
	Formula unit	4($XeBr_4$)		
	Pressure (GPa)	10	40	60
	Total #Gen	31	30	30
	Structure	$P2_1/c$	$P1$	$P1$
	Found at	2	1	16
	Enthalpy (eV/atom)	0.62178	4.72822	7.01736

The formation enthalpies of several structures with respect to solid Xe and Br were computed and are compared in Figure 5.18. Similar to predicted $XeCl_4$ structures, in the pressure range from 10 to 60 GPa, the formation enthalpies are highly positive showing $XeBr_4$ possibly cannot be

synthesized. For this reason, we simply summarize the structures and enthalpies in Figure 5.19. The lowest enthalpy *P*1 structure is consisted of Br zigzag chains. The higher enthalpy structures also tend to form similar zigzag chains. The *P*1 structure with a linear arrangement of Br atoms has the highest enthalpy.

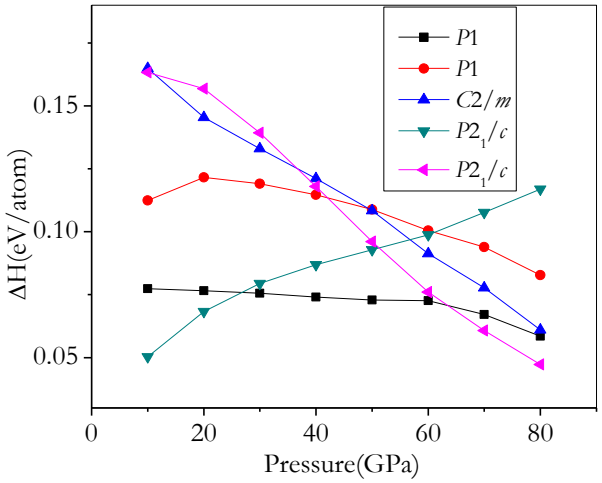

Figure 5.18 The relative enthalpies of formation per atom with respect to elemental Xe and molecular Br_2 for $XeBr_4$ compounds.

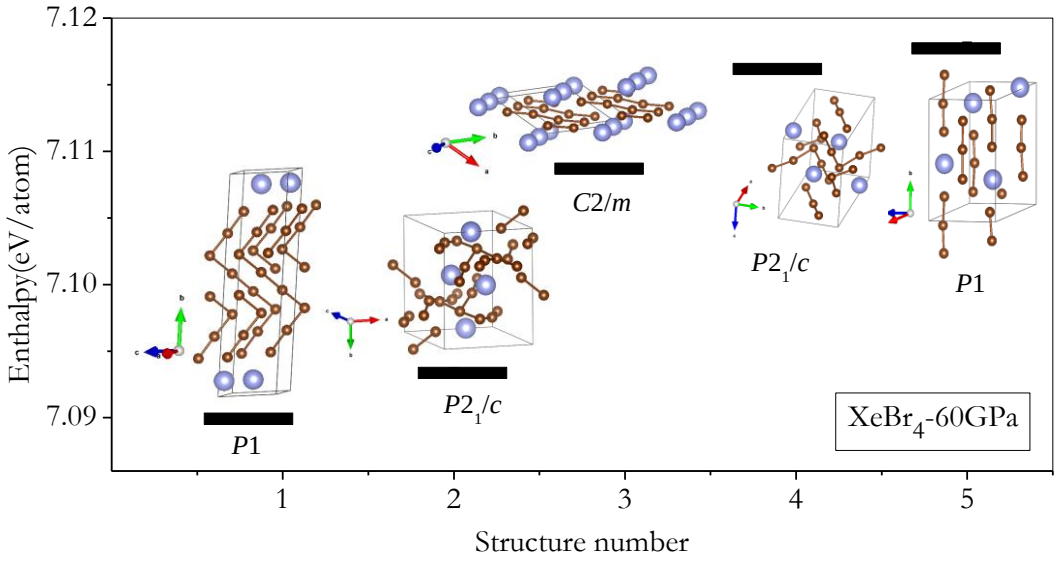

Figure 5.19 The group of the lowest predicted enthalpy structures for solid $XeBr_4$ at 60 GPa.

5.5 Predicted structures of XeI_n (n=1, 2 and 4)

Iodine, the fourth halogen in group VII was discovered in 1811 by the French chemist Curtois during the process of manufacturing potassium nitrate to make gunpowder for the French Revolution. Iodine is a nutrient mineral which easily reacts with organic compounds and is needed for human diet. Moreover, due to the low toxicity, iodine-based compounds are used in x-ray medical imaging. In spite of the electronegativity of this element being less than that of chlorine and bromine, the chemical properties of I_2 are generally similar to the lighter halogens. In the periodic table iodine is situated next to Xe atom therefore, it is probable that the two atoms may react and form compounds under pressure. As will be shown below, the contrary was predicted.

In comparison to the stability of solid diatomic molecular Cl_2 up to 142 GPa [188], iodine undergoes several phase transitions below 55 GPa. At low pressure, iodine forms a diatomic molecular crystal (body-centred orthorhombic) with the *Cmca* space group (phase I) [198]. The crystal structure of the monoatomic phase having an *Immm* space group was found at 21 GPa (phase II)[198]. Metallization of iodine was found to occur before the dissociation into a monoatomic solid at about 16 GPa [200]. On further compression, phase III with *I*4/*mmm* was observed at about 43 GPa and eventually phase IV with the *Fm*3*m* space group became stable from 55 to 276 GPa. A recent study has also identified a novel incommensurate phase (phase V) between 12.5-23.5 GPa prior to the pressure-induced molecular dissociation [206]. In the calculations of the enthalpies, we have used the *Cmca* phase of I_2 and fcc phase of Xe atoms in the pressure range studied. As shown in Figure 5.20 all the predicted low enthalpy structures have positive formation with respect to solid Xe and I.

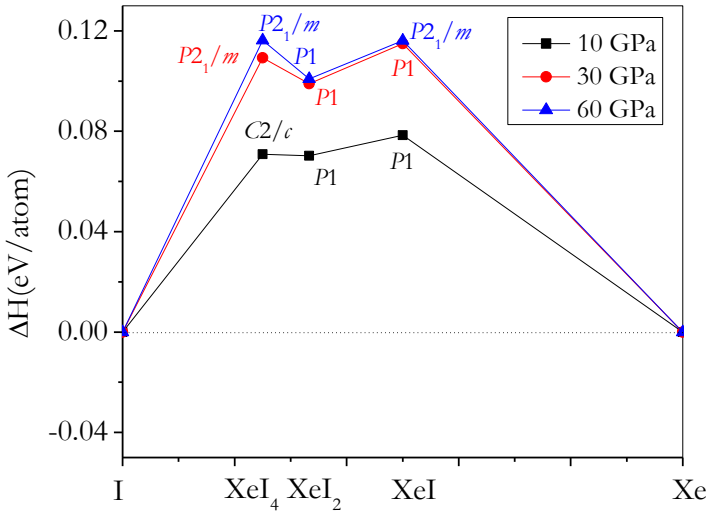

Figure 5.20 The convex hull plots of Xe–I systems at 10, 30 and 60 GPa.

5.5.1 Predicted high pressure structures of XeI

Results of the lowest enthalpy structures for XeI found by PSO and GA methods at 10, 30 and 60 GPa are summarized in Table 5.4 At 10 GPa, two *P*1 structures predicted by both methods are very similar with the energy difference less than 0.0001 eV/atom. The zigzag I sublattice is observed in both structures (Figure 5.21). EOS calculations found the *P*1 structures predicted at 10 GPa are not the lowest enthalpy at 10 GPa. Instead, a *P*1 but with a different structure predicted by PSO at 30 GPa was found to have the lowest energy at 10 GPa. Once again, both PSO and GA failed to find the lowest enthalpy structure at 10 GPa. Moreover, GA and PSO did not find the same structures at 30 and 60 GPa. Although the GA method did not find the lowest enthalpy structure at 30 GPa, it predicted the lowest enthalpy $P2_1/m$ structure at 60 GPa.

Table 5.4 Comparison of the lowest enthalpy structures of 8 formula units of XeI with GA and PSO methods in pressure ranges of 10 to 60 GPa.

PSO	Population	50		
	Pressure (GPa)	10	30	60
	Total #Gen	26	25	25
	Structure	*P*1	*P*1	*C*2/*m*
	Found	21	21	5
	Enthalpy (eV/atom)	1.8190	5.4431	9.8440
GA	Population	50		
	Pressure (GPa)	10	30	60
	Total #Gen	23	21	25
	Structure	*P*1	*P*1	$P2_1/m$
	Found	8	9	13
	Enthalpy(eV/atom)	1.8190	5.4642	9.8089

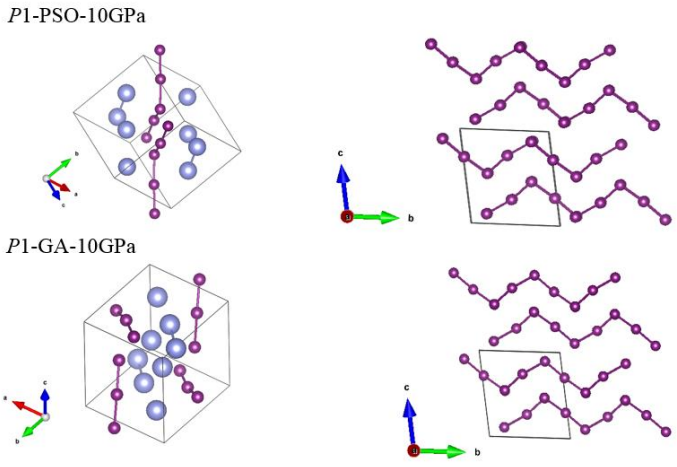

Figure 5.21 The lowest predicted enthalpy structures for solid XeI at 10 GPa.

The calculated formation enthalpies (Figure 5.22) indicate that all the predicted structures of XeI below 60 GPa are not thermodynamically stable. More significantly, the absolute values of

formation enthalpies are highly positive ranging from 0.08 to 0.26 eV/atom. Therefore, it is unlikely that XeI compounds can be synthesized in this pressure range.

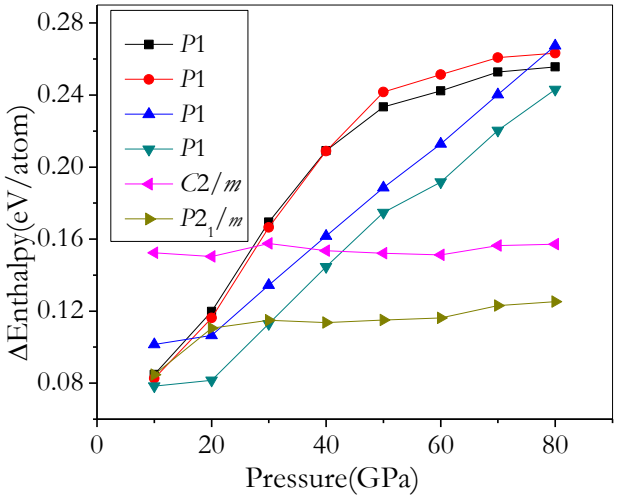

Figure 5.22 The relative enthalpies of formation per atom with respect to elemental Xe and molecular I_2 for XeI compounds.

A few low enthalpy structures of XeI within an energy window of ~0.14 eV/atom found at 60 GPa are shown in Figure 5.23. Distinctive Xe and I regions are observed in these structures. The lowest enthalpy $P2_1/m$ and $C2/m$ structures have a 2D hexagonal closed pack of Xe and I atoms. The high enthalpy structures are mainly consisted of separated sublattice of I and Xe networks.

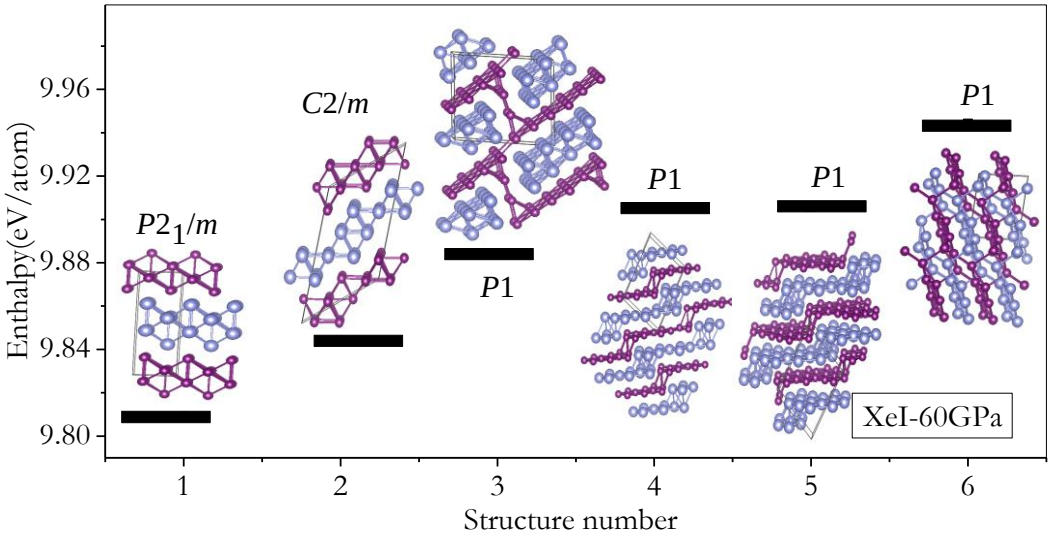

Figure 5.23 The group of the lowest predicted enthalpy structures for solid XeI at 60 GPa.

5.5.2 Predicted high pressure structures of XeI_2

We have explored low enthalpy structures at 10, 30 and 60 GPa using PSO and GA methods and the results are summarized in Table 5.5. PSO searches with population size of 40 and 50 did not find similar low energy structures at the desired pressures. Moreover, the structures found by GA search at 10, 30 and 60 GPa are also different from the PSO search.

Table 5.5 Comparison of the lowest enthalpy structures of 4 formula units of XeI_2 with GA and PSO methods in pressure ranges of 10 to 60 GPa.

PSO	Population	40			50		
	Pressure (GPa)	10	30	60	10	30	60
	Total #Gen	42	40	30	46	45	35
	Structure	*Cmmm*	*Fd*3*m*	*C*2/*m*	*P*1	*P*1	*Cm*
	Found	15	20	30	26	26	10
	Enthalpy (eV/atom)	1.4677	4.9971	9.2327	1.4553	4.9755	9.2473
GA	Population	50					
	Pressure (GPa)	10		30		60	
	Total #Gen	41		50		40	
	Structure	*P*1		*P*1		*Cm*	
	Found	14		50		7	
	Enthalpy(eV/atom)	1.4690		4.9746		9.2317	

The formation enthalpies on selected structures plotted as a function of the pressure are compared in Figure 5.24. It can be seen that all the predicted structures are not stable towards the dissociation into the elemental solids. Interestingly, two low enthalpy structures in the pressure range from 10 to 80 GPa (black and red lines: the first *P*1 structure (Figure 5.24#1) found by PSO at 10 GPa and the second *P*1 structure (Figure 5.24#2) found by GA at 30 GPa) share very similar structural motifs. The calculated phonon dispersion curves of the two *P*1 structures (Figure 5.25) show no imaginary phonon frequencies at 60 GPa.

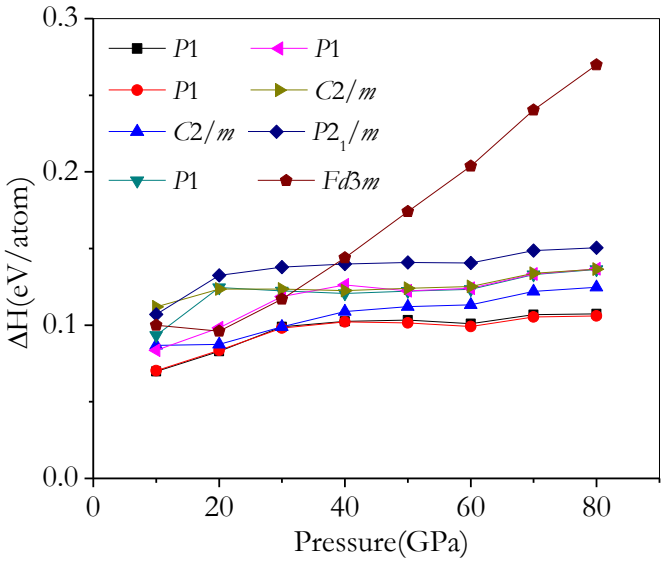

Figure 5.24 The relative enthalpies of formation per atom with respect to elemental Xe and molecular I_2 for XeI_2 compounds.

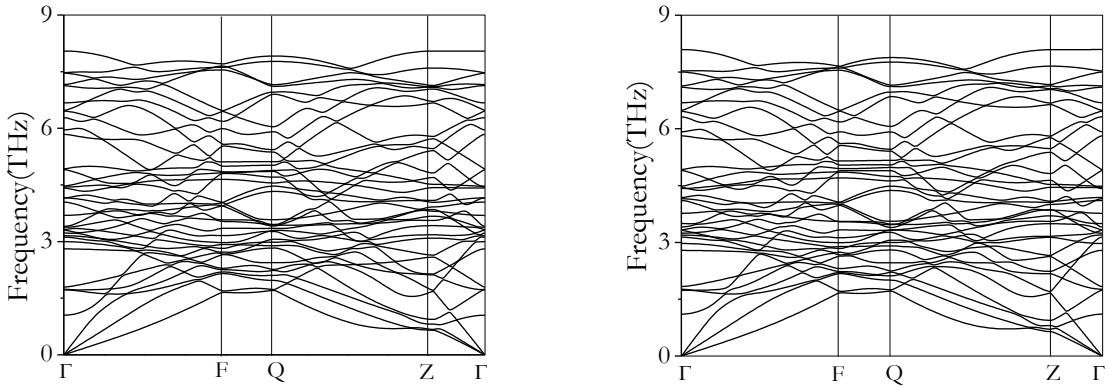

Figure 5.25 Phonon dispersion curves for the *P*1 structure of XeI_2 found by, (left) PSO and (right) GA at 60 GPa.

The structures of several low enthalpy structures XeI_2 were shown in Figure 5.26. Once again, we found that these structures are characterized by segregated Xe and I regions. The two lowest energy *P*1 structures are composed of 2D hexagonal closed pack sublattices of both Xe and I atoms. The higher enthalpy structures are mostly consisted of hexagonal packing of I and Xe and eventually the $P2_1/m$ structure is composed of hexagonal-like I and zigzag Xe chains. For the highest enthalpy structure (*Fd*3*m*), all Xe atoms are tetrahedrally bonded with I atoms situated in the interstitial sites of Xe sublattice. Note that the enthalpy of *Fd*3*m* structure is much higher than other dissociated phases suggesting that XeI_2 should separate into Xe and I rich sides.

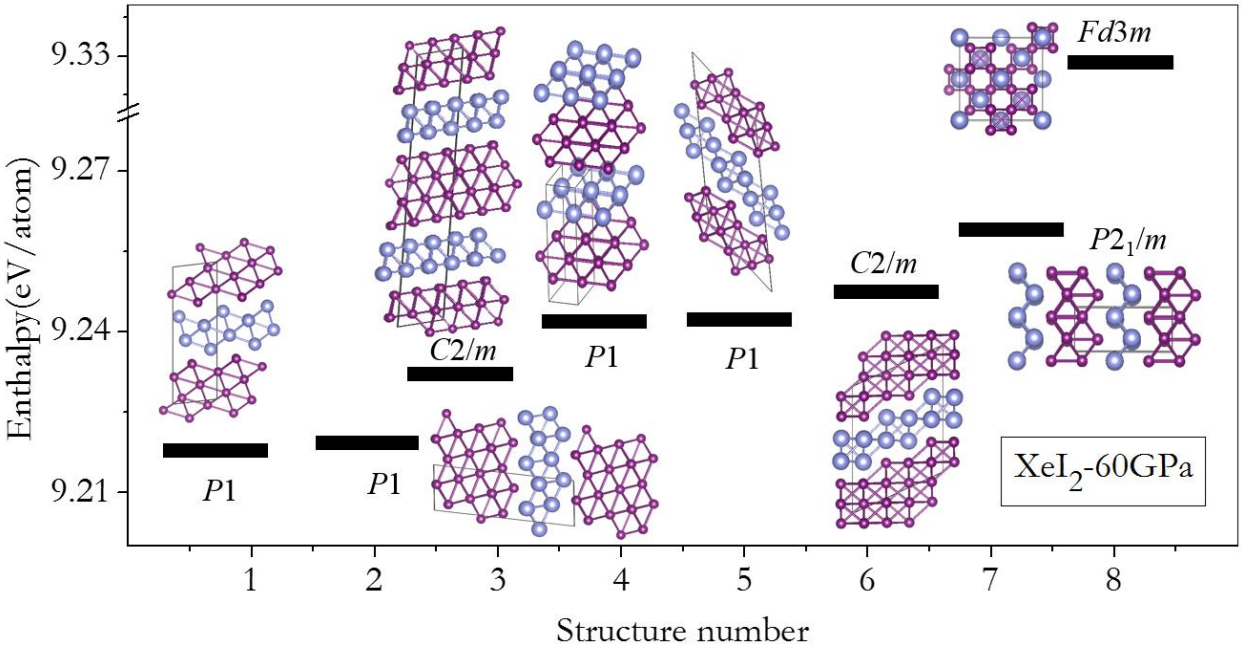

Figure 5.26 The group of the lowest predicted enthalpy structures for solid XeI_2 at 60 GPa.

5.5.3 Predicted high pressure structures of XeI_4

Structural searches were also performed for XeI_4 using PSO and GA methods. Details on the search and the candidate structures are given in Table 5.6. In this case, both methods found the same lowest enthalpy structure (*C*2/*c*) at 10 GPa. The difference of energies between candidate structures at 30 and 60 GPa are less than 10 meV/atom. Thus, we re-optimized the predicted structures to higher precision and report the results in Table 5.6.

Table 5.6 Comparison of the lowest enthalpy structures of 4 formula units of XeI_4 with GA and PSO methods in pressure ranges of 10 to 60 GPa.

PSO	Population	40		50		
	Pressure (GPa)	30	60	10	30	60
	Total #Gen	32	40	25	25	26
	Structure	*C*2/*m*	*Cm*	*C*2/*c*	*Pm*	*P*1
	Found	22	7	11	10	9
	Enthalpy (eV/atom)	4.6338	8.7811	1.1855	4.6290	8.7828
GA	Population	50				
	Pressure (GPa)	10		30	60	
	Total #Gen	26		25	26	
	Structure	*C*2/*c*		*P*2$_1$/*m*	*P*1	
	Found	10		9	8	
	Enthalpy(eV/atom)	1.1855		4.6229	8.7737	

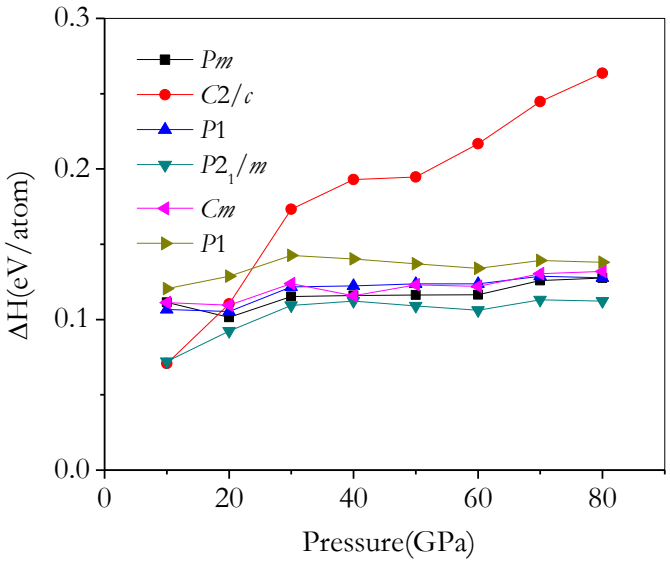

Figure 5.27 The relative enthalpies of formation per atom with respect to elemental Xe and molecular I_2 for XeI_4 compounds.

Formation enthalpy calculations (Figure 5.27) predicted two low enthalpy structures, *C*2/*c* structure at 10 GPa and $P2_1/m$ structure at 60 GPa. Both have highly positive values of formation enthalpies in a range of 0.07-0.26eV/atom. On thermodynamic reason, XeI_4 compounds are not expected to exist below 80 GPa. Several low enthalpy structures predicted at 60 GPa were shown in Figure 5.28. The lowest enthalpy structure ($P2_1/m$) shows segregated Xe and I regions. The next higher enthalpy structures (*Pm*, *Cm* and two *P*1) are consisted of hexagonal network of I while Xe atoms arrange into I channels. Finally, the *Immm* structure with linear chain of Xe atoms has the highest enthalpy. We can conclude that the XeI_4 has phase segregated into rich in I and Xe rich regions and high activation energy is needed to force these two elements to react.

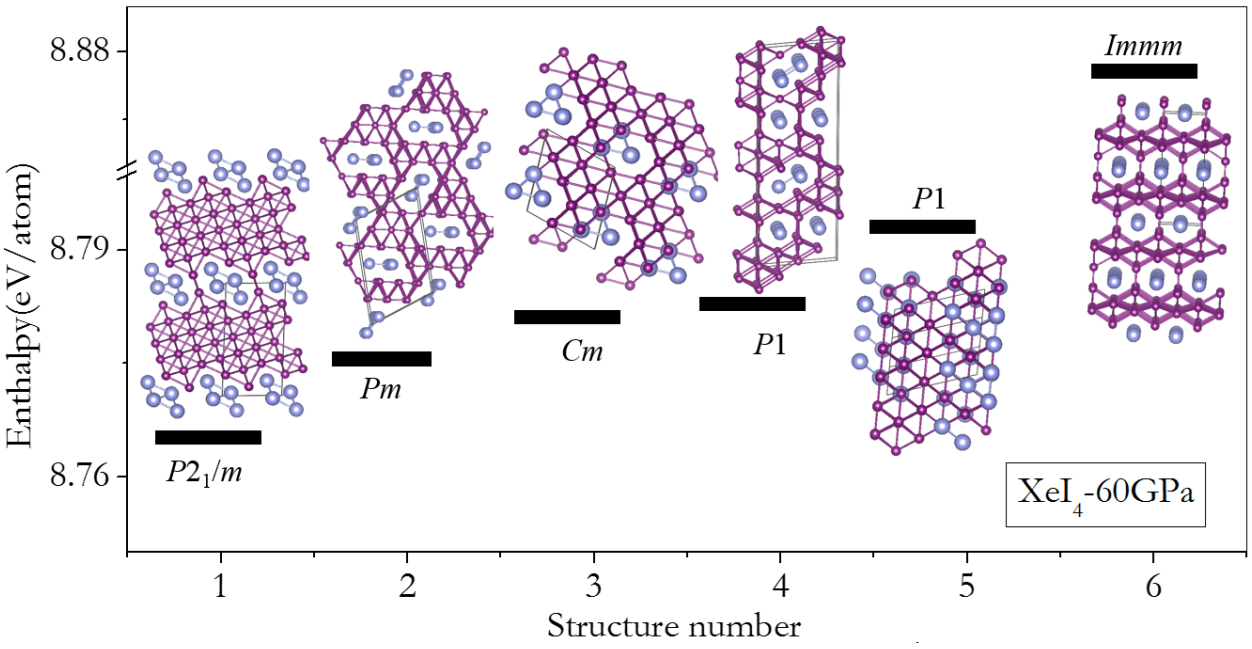

Figure 5.28 The group of the lowest predicted enthalpy structures for solid XeI_4 at 60 GPa.

5.6 Conclusions

We have performed a less exhaustive investigation on possible high pressure structures of $XeBr_n$ and XeI_n (n=1,2 and 4) to complete the Xe-haldies series. Since the reliability of pseudopotentals used in this study have been tested below 60 GPa and that the experimental synthesis was performed at low pressures, we focused on the crystal structures and properties of Xe-halides below 60 GPa. From the theoretical studies, we can first compare the structural features and properties of XeH_n (n=2, H:halides). It has been reported in a recent theoretical study that the molecular structure of XeF_2 with *I*4/*mmm* symmetry, remains the most stable one, up to 105 GPa

[181]. This molecular solid is consisted of linear F-Xe-F molecule with two equal Xe-F bond lengths. Above 105 GPa, a *Pnma* structure was found with bent F-Xe-F and unequal Xe-F distances. In this structure, if the Xe-F contact cutoff is set to < 2.8 Å, 11 F atoms are found in the first coordination sphere of the Xe. Further compression up to 200 GPa, resulted in the dissociation of XeF_2 into an ionic solid. ELF analysis indicated that ionicity of one of the Xe..F bonds of the *Pnma* structure increases with pressure and eventually leads to self-dissociation into Xe-F and F atoms at 200 GPa. In comparison, we found $XeCl_2$ is not thermodynamically stable below 55 GPa. However, we did not find linear Cl-Xe-Cl molecule in the calculations. Instead, below 40 GPa, molecular Cl_2 and Xe atoms is energetically favorable. At 60 GPa, $XeCl_2$ is stable with the Xe surrounded by 12 Xe-Cl contacts < 3.15 Å. For $XeBr_2$, a stable structure forms above 40 GPa. The lowest enthalpy *P*1 structure of $XeBr_2$ at 10 GPa contains twisted zigzag chains of Br atoms and monoatomic Xe. At 60 GPa, the *Fd*3*m* structure is thermodynamically stable. Similar to $XeCl_2$, Xe is connected to 12 Br atoms within a distance of < 3.12 Å. For XeI_2, the formation enthalpy is highly positive indicating this compound is not stable at the high pressure. The lowest enthalpy *P*1 structure which is dynamically stable, is consisted of hexagonal packing of I and Xe atoms. For other stoicheometries of XeH_n (n=1 and 4), except XeCl at 60 GPa, the formation enthalpies of Xe-Br and Xe-I compounds are positive.

In addition, a theoretical study has reported that metallization of XeF_2 should occur at 60 GPa [181]. In comparison, up to 60 GPa all the predicted $XeCl_2$ compounds are semiconductors. In comparison, one of the $XeBr_2$ compounds is found to be a superconductive metal at this pressure. The present theoretical study suggests that even though no thermodynamic Xe-I compounds can be formed, the lowest enthalpy structure at 60 GPa is a metal.

CHAPTER 6

Summary and conclusion

The two primary goals of this thesis were (i) accurate determination of the electronic structure of AlH_3 and EuO at high pressure, and (ii) evaluation and search for possible high pressure polymorphs of binary systems (CS_2 and Xe-halides) using state-of-the-art first principles algorithms. In Chapter 1, the methodologies used in the thesis research, including the background on density functional theory, various types of practical functionals and their improvements and two structural search methods were introduced. In Chapter 2, these methods were applied to investigate the properties of potentially superconductive AlH_3 and to the study on the structural phase transformation and insulator to metal transition of compressed EuO. In Chapter 3, we investigate in detail the possible existence of metallic crystalline structures of recently discovered metallic phase of CS_2 up to 100 GPa. A detailed comparison of the performances of two structure search methods, *viz.* PSO and GA was made on the Xe-Cl system in Chapter 4. Finally, the same structure prediction techniques were applied to the study of Xe-Br and Xe-I binary systems. In this chapter, the major results and achievements are briefly summarized and perspectives future works are presented.

The first objective of the research was to apply recently developed functionals to calculate the band structure of AlH_3 at about 100 GPa in order to explain the discrepancy between experiment and previously predicted superconducting behavior of this compound. For this purpose ground state wave functions computed from PBE and HSE functionals were improved using increasing levels of electron correlation treatment using the GW method. Electronic band structures of AlH_3 obtained from the commonly used PBE and recently proposed self-interaction corrected TB-mBJLDA functionals at selected pressures were compared in detail. It was found, contrary to the PBE prediction, the nesting of two pieces of Fermi surfaces which was attributed to the superconducting behavior got removed in the more advanced calculations. This observation leads us to conclude that high pressure AlH_3 is a poor metal or even a low band gap semiconductor and not a superconductor. The result is consistent with experiment which indeed failed to detect superconductivity at high pressure. The second objective of Chapter 2 was to describe electronic structure and the equation of state of EuO with localized 3*d* or 4*f* electrons which is a prototypical system for the study of highly correlated phenomena. From experiments, EuO is known to exhibit an anomalous isostructural transition (B1→B'1) at 35 GPa. We applied several functionals

including mbjLDA, PBE0 and PBE+U to describe this system. It was found that none of the functionals were able to reproduce the isostructural phase transition. However, PBE+U model correctly predicted the semiconductor to metal transition with a very small volume change near 12 GPa. Although the mBJLDA+U method also predicted an indirect band gap at ambient conditions, it failed to reproduce the metallic phase of B1 and B2 structures at higher pressure. Finally, we calculated the *s*-electron density near the nucleus which is directly related to the Mössbauer isomer shift. Around ~30 GPa, a discontinuity related to the B1 to B1' isostructural transition was predicted in agreement with experiments. In summary, in this chapter, we found that no mean-field approximation (*i.e.* PBE+U or mBJLDA) can consistently reproduce all the experimental observations. We speculated that a single determinant wave function is not accurate to describe rapid changes of the electron density of localized electrons under pressure. EuO as a highly correlated system with half-filled 4*f* shell should be treated with rigorous quantum mechanics. That goal can be achieved by quantum Monte Carlo calculations using multi-determinant wave fucntions in order to describe the mixed valence states of EuO correctly.

In Chapter 3, we focused on the effect of pressure on the structure and properties of molecular CS_2 solid using the PSO and GA structure prediction methods. The study was restricted to one stoichiometry with C:S ratio of 1:2, *i.e*. CS_2. To complement the structural prediction calculations, we also compressed the solid molecular CS_2 phase to high pressure with constant-pressure MD at 300 K. The structural search found that molecular CS_2 is metastable at low pressure. At high pressure (> 20 GPa) the carbon and sulfur tend to segregate. This may indicate the possibility of the formation of other C_xS (x>1) species. In agreement with experiment, both MD and static total energy calculations show that the molecular CS_2 is not stable at pressure above 20 GPa and transformed into a polymeric phase. Both GA and PSO methods found a crystalline $P2_1/m$ structure which has the lowest enthalpy from 60 to 100 GPa. Although the structure search revealed carbon or sulfide rich regions, it did not imply that CS_2 will phase separate into the elements. This is confirmed by experiment in which the x-ray diffraction patterns did not reveal the presence of the elements. The $P2_1/m$ structure is novel as it is constructed from C-C layers sandwiched between two adjacent S layers and linked in the third dimension by C-S bonds. This feature of the structure is similar to the observation made in the MD calculation in which CS_2 was also separated into layers of sulfur and carbon. We found that the crystalline phase was metallic and superconductive. The origin of the superconductivity is due to electron-phonon couplings in

the S layers. The existence of closed pack S atom layers is a feature common to the high pressure structures of CS_2 and similar to the superconducting phase of solid sulfur. As mentioned above, a full characterization of highly compressed CS_2 and the origin of the superconducting phase require further study of variable stoichiometries (C_xS_x) that will require substantially larger effort. The present study was the first step towards this goal.

In Chapters 4 and 5, we explored the low enthalpy crystal structures of XeH_n (H=Cl, Br and I) with (n=1,2 and 4) up to 60 GPa using the GA and PSO techniques. From the theoretical results, we found only XeCl, $XeCl_2$ and $XeBr_2$ are thermodynamically stable at 60 GPa. There is no theoretical evidence to support the formation of thermodynamically stable Xe-I compound at this pressure. In fact, for Xe-I, the predicted lowest enthalpy structures are formed from segregated regions of I and Xe atoms. We proposed a possible explanation for the formation of Xe-halides at high pressure. Since fluorine has the highest electronegativity and smallest atomic radius among halogens, the stability of Xe-F compounds that has been established from low pressure to 200 GPa from both theoretical and experimental studies, is mainly due to ionic interaction. Linear XeF_2 molecule is found to be stable below 100 GPa. At higher pressures the linear F-Xe-F bent with unequal Xe-F distances. A metallic phase of Xe-F was observed at 67 GPa. On the other hand, compared to F, Cl atom has a smaller electronegativity and the Xe-Cl compounds are only stabilized at pressures > 55 GPa. We found no evidence on the formation of covalent Xe-Cl bonds up to 60 GPa. No thermodynamically stable Xe-Cl compounds were found. However, it is likely that partial ionic interactions of Xe and Cl atoms help to stabilize the high pressure structures. In the hope that the theoretical results will be useful to guide experiments, we computed accurate band structures using GW approximation and predicted the, Raman, optical and reflectivity spectra using the BSE method. The results indicate that all Xe-Cl compounds are semiconductors at 60 GPa. The only thermodynamically stable structure found in Xe-Br compounds is $XeBr_2$ at pressures higher than 40 GPa. There is no evidence of Xe-Br and Br-Br covalent bonds in ELF calculations indicating that both Br and Xe are atomic in nature at 60 GPa. In contrast to Xe-F and Xe-Cl compounds, $XeBr_2$ was found to be a metal and superconductor with a critical temperature of 1.4 K at 60 GPa. Finally, although the chemical properties of I are similar to the lighter halogens, Xe-I compounds do not form below 60 GPa. Both elements separate into solid Xe and I rich sides. In the present study, we only focused on stoichiometric XeH_n (n=1,2 and 4) and the stoichiometry was not optimized. We cannot rule out the possibility that stoichiometric Xe_nH may form stable

structures. Substantial larger effort is needed to investigate Xe-rich halogen compounds. A major finding of these two chapters is that that both PSO and GA methods must be used with care. We often found different structures predicted by the two methods. Hence, we cannot conclude that one method is better than the other. However, it must be realized that the recommended default settings for both methods were used in this study. Hence, we aim to further explore the efficiency of the structural search methods by adjusting the default settings.

APPENDIX A

Supplementary data for Chapter 4

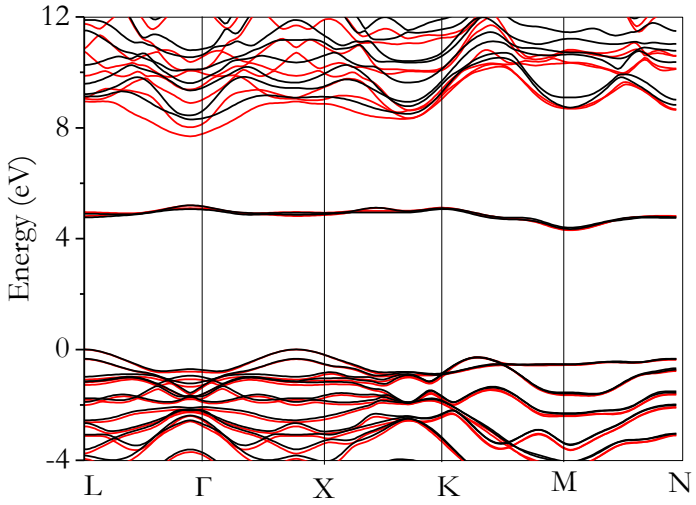

Figure A.1 Electronic band structure of the *Cmcm* structure of $XeCl_2$ at 15 GPa using two different pseudopotentials (black and red lines including valence electron configuration of s^2p^6 and $d^{10}s^2p^6$, respectively.

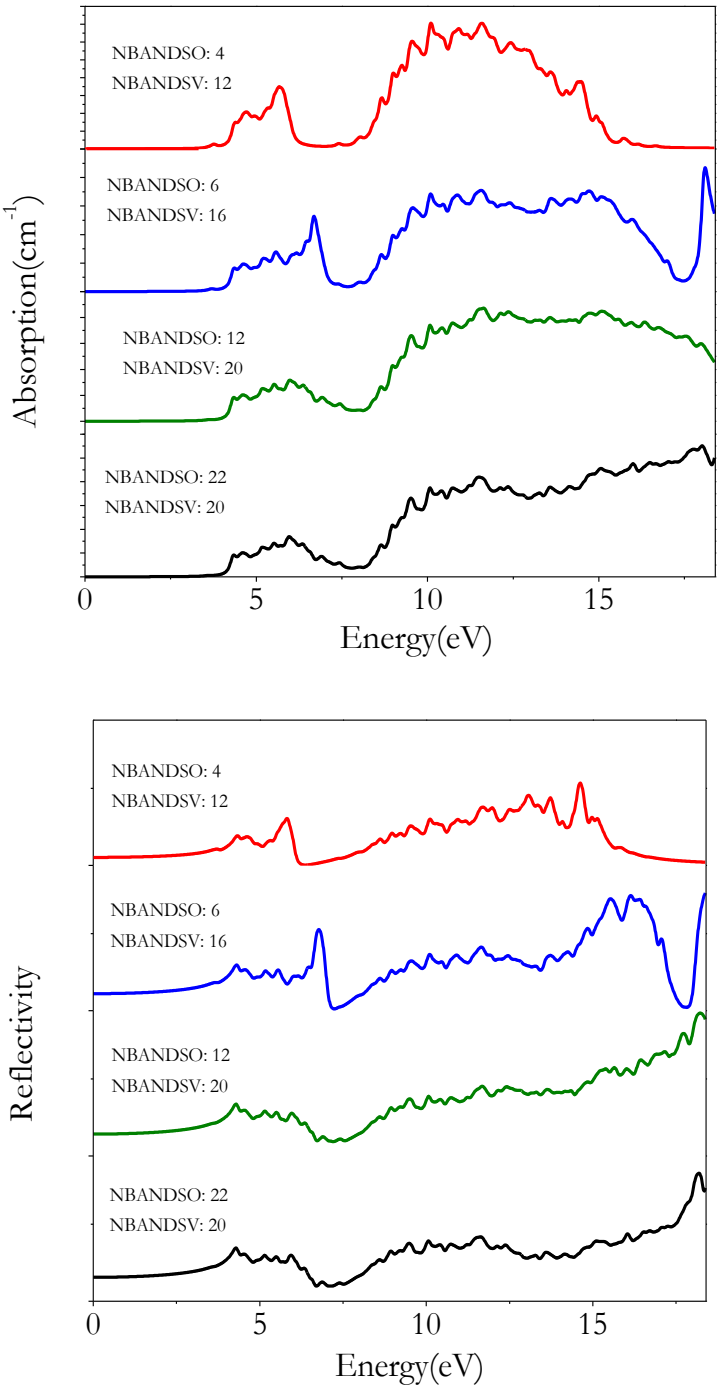

Figure A.2 Optical properties of *Cmcm* structure of $XeCl_2$ at 15 GPa with convergence test of BSE calculations using different number of valence (O) and conducting (V) bands.

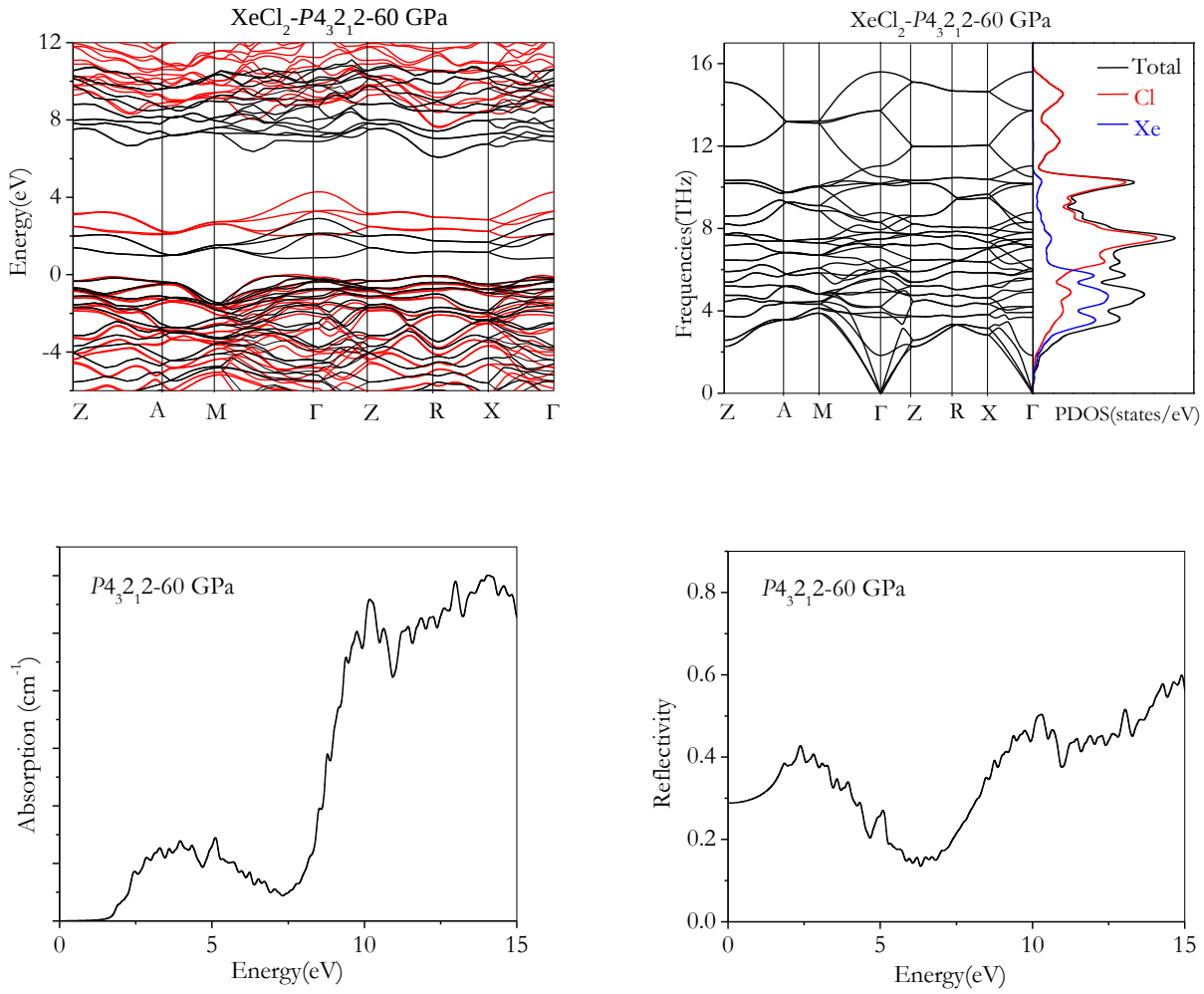

Figure A.3 Band structures, phonon dispersion, absorption and reflectivity of the $XeCl_2$ $P4_32_12$ structure at 60 GPa.

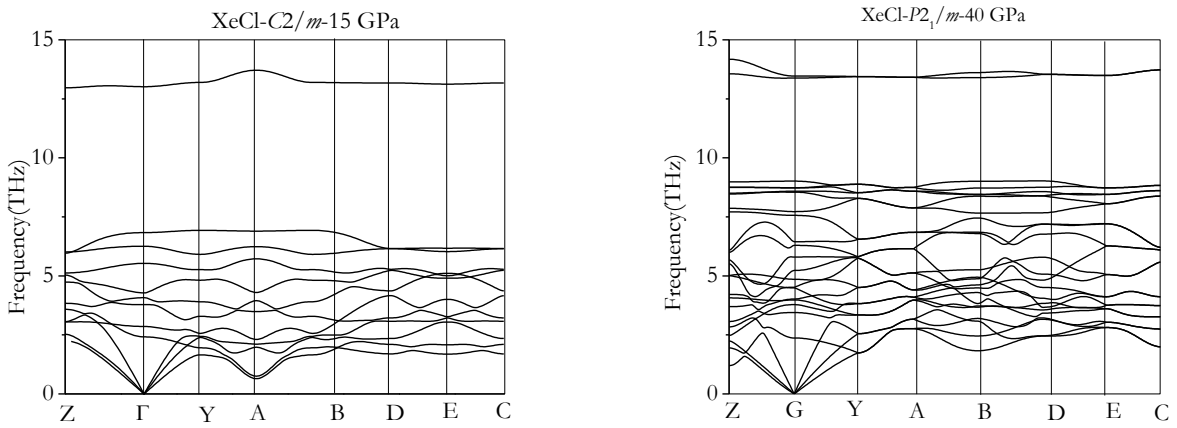

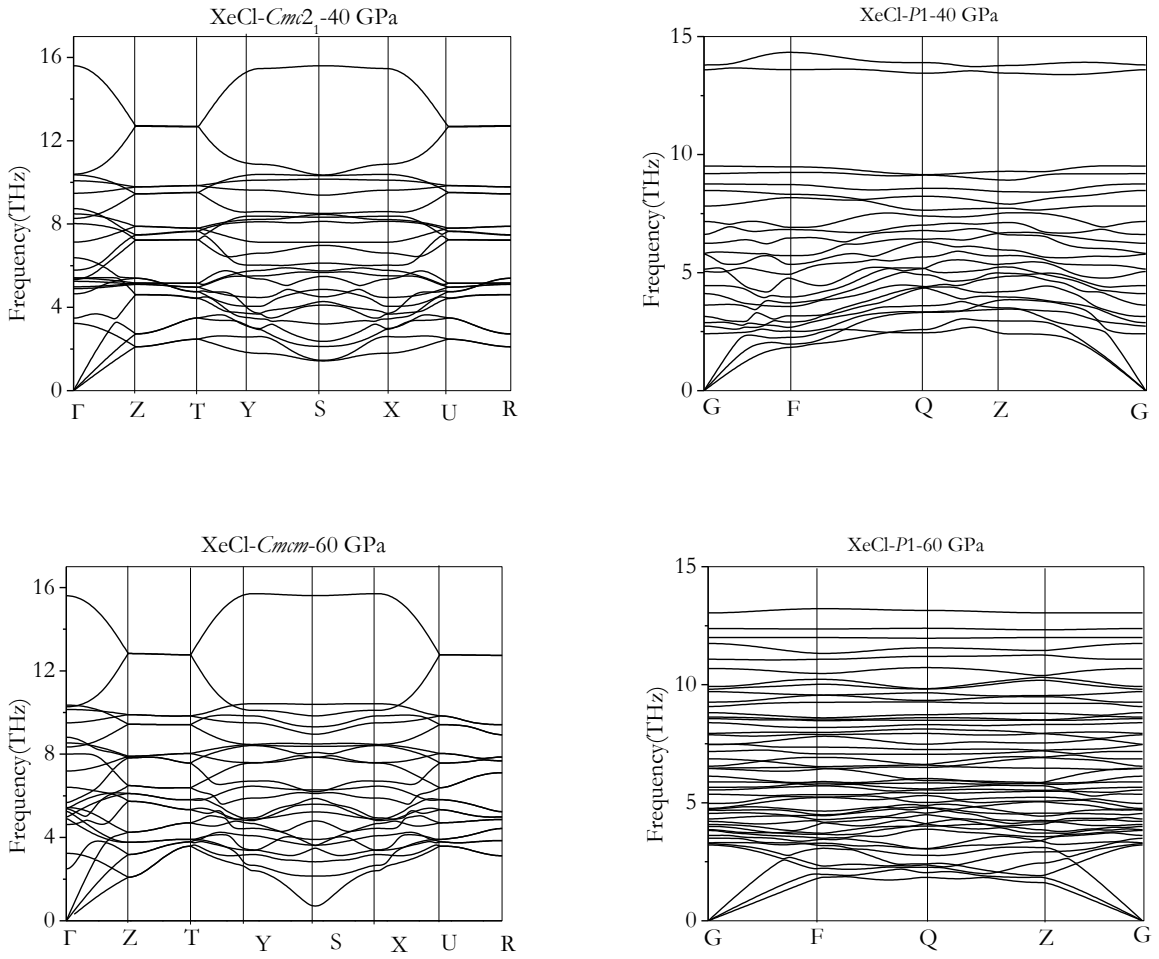

Figure A.4 Phonon dispersions of predicted XeCl structures in Table 4.3.

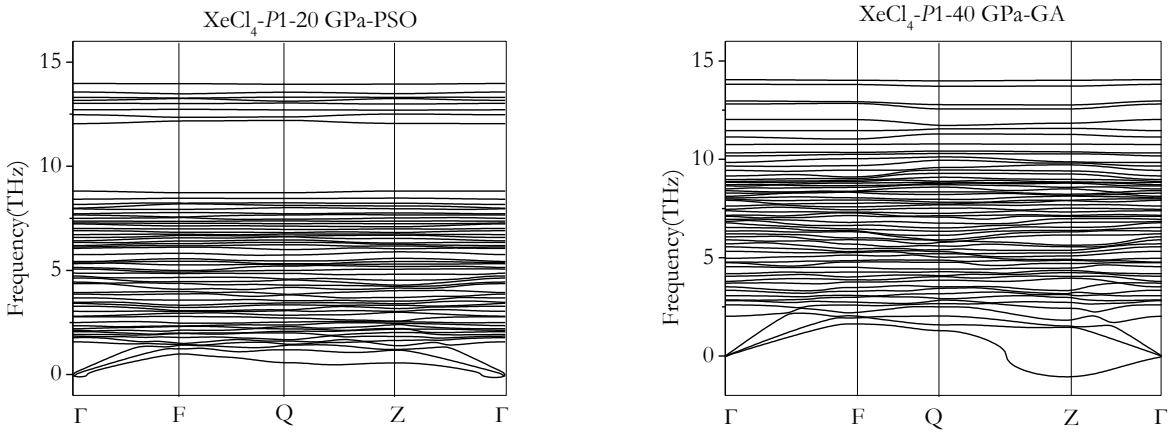

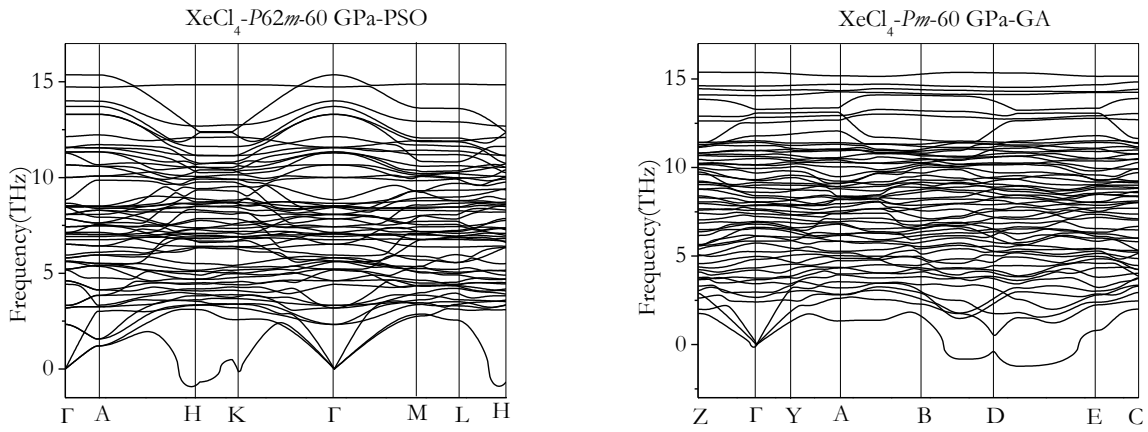

Figure A.5 Phonon dispersions of predicted $XeCl_4$ structures in Table 4.4.

LIST OF REFERENCES

[1] P. Hohenberg and W. Kohn, "Inhomogeneous electron gas," *Phys. Rev. B*, vol. 136, p. B864, 1964.

[2] W. Kohn and L. J. Sham, "Self-consistent equations including exchange and correlation effects," *Phys. Rev.*, vol. 140, p. A1133, 1965.

[3] I. Gilbert, "Hohenberg-Kohn theorem for nonlocal external potentials," *Phys. Rev. B*, vol. 1, p. 2112, 1975.

[4] H. Rietveld, "A profile refinement method for nuclear and magnetic structures," *J. Appl. Crystallogr.*, vol. 2, pp. 65–71, 1969.

[5] M. B. and J. R. Oppenheimer, "Zur Quantentheorie der Molekeln," *Ann. Phys*, vol. 84, p. 457, 1927.

[6] V. Fock, "Näherungsmethode zur Lösung des quantenmechanischen Mehrkörperproblems," *Zeitschrift fur Phys.*, vol. 61, pp. 126–148, 1930.

[7] J. C. Slater, "The theory of complex spectra," *Phys. Rev.*, vol. 34, pp. 1293–1322, 1929.

[8] L. H. Thomas, "The calculation of atomic fields," *Proc. Cambridge Phil. Roy. Soc*, vol. 23, p. 542, 1927.

[9] E. Fermi, "Un metodo statistico per la determinazione di alcune priorietà dell'atome," *Rend. Accad. Naz. Lincei*, vol. 6, pp. 602–607, 1927.

[10] D. M. and B. J. A. Ceperley, "Ground State of the Electron Gas by a Stochastic Method," *Phys. Rev. Lett.*, vol. 45, pp. 566–569, 1980.

[11] A. D. Becke, "Density-functional exchange-energy approximation with correct asymptotic behavior," *Phys. Rev. A*, vol. 38, pp. 3098–3100, 1988.

[12] C. Lee, W. Yang, and R. G. Parr, "Development of the Colle-Salvetti correlation-energy formula into a functional of the electron density.," *Phys. Rev. B*, vol. 37, pp. 785–789, 1988.

[13] J. P. Perdew et al., "Atoms, molecules, solids, and surfaces: Applications of the generalized gradient approximation for exchange and correlation," *Phys. Rev. B*, vol. 46, pp. 6671–6687, 1992.

[14] J. P. Perdew, K. Burke, and M. Ernzerhof, "Generalized Gradient Approximation Made Simple," *Phys. Rev. Lett.*, vol. 77, pp. 3865–3868, 1996.

[15] J. C. Slater, “Quamtum Theory of Molecules and Solids,” vol. 4. New York: McGraw-Hill, 1974.

[16] E. H. Lieb and S. Oxford, “Improved Lower Bound on the Indirect Coulomb Energy,” in *Int. J. Quantum Chem*, vol. 19, New Jersey, 1981, pp. 427–439.

[17] S. K. Ghosh and R. G. Parr, “Phase-space approach to the exchange-energy functional of density-functional theory,” *Phys. Rev. A*, vol. 34, pp. 785–791, 1986.

[18] A. D. Becke and M. R. Roussel, “Exchange holes in inhomogeneous systems: A coordinate-space model,” *Phys. Rev. A*, vol. 39, pp. 3761–3767, 1989.

[19] V. I. Anisimov and O. Gunnarsson, “Density-functional calculation of effective Coulomb interactions in metals,” *Phys. Rev. B*, vol. 43, pp. 7570–7574, 1991.

[20] I. V. Solovyev and P. H. Dederichs, “Ab initio calculations of Coulomb U parameters for transition-metal impurities,” *Phys. Rev. B*, vol. 49, pp. 6736–6740, 1994.

[21] M. Cococcioni and S. de Gironcoli, “Linear response approach to the calculation of the effective interaction parameters in the LDA+U method,” *Phys. Rev. B*, vol. 71, pp. 035105–16, 2005.

[22] F. Zhou et al., “First-principles prediction of redox potentials in transition-metal compounds with LDA + U,” *Phys. Rev. B*, vol. 70, pp. 235121–8, 2004.

[23] F. Tran et al., “Hybrid exchange-correlation energy functionals for strongly correlated electrons: Applications to transition-metal monoxides,” *Phys. Rev. B*, vol. 74, pp. 15108–10, 2006.

[24] M. Ernzerhof and G. E. Scuseria, “Assessment of the Perdew-Burke-Ernzerhof exchange-correlation functional,” *J. Chem. Phys.*, vol. 110, pp. 5029–5036, 1999.

[25] C. Adamo and V. Barone, “Toward reliable density functional methods without adjustable parameters: The PBE0 model,” *J. Chem. Phys.*, vol. 110, pp. 6158–6170, 1999.

[26] J. Paier et al., “Screened hybrid density functionals applied to solids,” *J. Chem. Phys.*, vol. 124, pp. 154709–13, 2006.

[27] M. Marsman et al., “Hybrid functionals applied to extended systems.,” *J. Phys. Condens. Matter*, vol. 20, pp. 064201–9, 2008.

[28] F. Tran, P. Blaha, and K. Schwarz, “Band gap calculations with Becke–Johnson exchange potential,” *J. Phys. Condens. Matter*, vol. 19, pp. 196208–8, 2007.

[29] F. Tran and P. Blaha, “Accurate band gaps of semiconductors and insulators with a semilocal exchange-correlation potential,” *Phys. Rev. Lett.*, vol. 102, pp. 226401–4, 2009.

[30] G. Madsen et al., “Efficient linearization of the augmented plane-wave method,” *Phys. Rev. B*, vol. 64, pp. 195134–9, 2001.

[31] P. Blaha and G. Madsen, *WIEN2k*, vol. 2. 2014.

[32] John P. Perdew and Yue Wang, “Accurate and simple analytic representation of the electron-gas correlation energy,” *Phys. Rev. B*, vol. 45, pp. 13244–13249, 1992.

[33] W. E. Pickett, “Pseudopotential methods in condensed matter applications.,” *Comput. Phys. Reports*, vol. 9, pp. 115–197, 1989.

[34] P. E. Blöchl, “Projector augmented-wave method,” *Phys. Rev. B*, vol. 50, pp. 17953–17979, 1994.

[35] C. J. Pickard, “Ab Initio Electron Energy Loss Spectroscopy,” Cambridge, 1997.

[36] G. and J. H. Kresse, “Ab initio molecular dynamics for liquid metals,” *Phys. Rev. B*, vol. 47, pp. 558–561, 1993.

[37] G. and D. J. Kresse, “From ultrasoft pseudopotentials to the projector augmented- wave method,” *Phys. Rev. B*, vol. 59, pp. 1758–1775, 1999.

[38] P. B. K. Schwarz, “Quantum mechanical computations at atomic sclae for material science,” in *Fifth world congress on computational mechanics*, 2002.

[39] M. C. Payne et al., “Iterative minimization techniques for ab initio total-energy calculations: molecular dynamics and conjugate gradients,” *Rev. Mod. Phys.*, vol. 64, pp. 1045–1097, 1992.

[40] S. B. J. Grotendorst and D. Marx, “The pseudopotential plane wave approach,” in *NIC Series: John von Neumann Institute for Computing*, 2006, pp. 71–83.

[41] L. J. W. Aulbur and J. Wilkins, “Quasiparticle Calculations in Solids,” *Solid State Phys.*, vol. 54, p. 1, 2000.

[42] L. Hedin, “New Method for Calculating the One-Particle Green’s Function with Application to the Electron-Gas Problem,” *Phys. Rev.*, vol. 139, pp. A796–823, 1965.

[43] R. W. Godby and M. Schluter, “Accurate Exchange-Correlation Potential for Silicon and Its Discontinuity on Addition of an Electron,” *Phys. Rev. Lett.*, vol. 56, pp. 2415–2418, 1986.

[44] Mark S. Hybertsen and Steven G. Louie, “First-principles theory of quasiparticles: calculation of band gaps in semiconductors and insulators,” *Phys. Rev. Lett.*, vol. 55, pp. 1418–1421, 1985.

[45] M. Shishkin, M. Marsman, and G. Kresse, "Accurate quasiparticle spectra from self-consistent GW calculations with vertex corrections," *Phys. Rev. Lett.*, vol. 99, pp. 246403–4, 2007.

[46] F. Fuchs et al., "Quasiparticle band structure based on a generalized Kohn-Sham scheme," *Phys. Rev. B*, vol. 76, pp. 115109–8, 2007.

[47] M. Shishkin and G. Kresse, "Implementation and performance of the frequency-dependent GW method within the PAW framework," *Phys. Rev. B*, vol. 74, pp. 035101–13, 2006.

[48] M. Shishkin and G. Kresse, "Self-consistent GW calculations for semiconductors and insulators," *Phys. Rev. B*, vol. 75, pp. 235102–9, 2007.

[49] N. Marzari et al., "Maximally localized Wannier functions: Theory and applications," *Rev. Mod. Phys.*, vol. 84, pp. 1419–1475, 2012.

[50] N. Marzari and D. Vanderbilt, "Maximally localized generalized Wannier functions for composite energy bands," *Phys. Rev. B*, vol. 56, pp. 12847–12865, 1997.

[51] I. Souza, N. Marzari, and D. Vanderbilt, "Maximally localized Wannier functions for entangled energy bands," *Phys. Rev. B*, vol. 65, pp. 035109–13, 2001.

[52] A. Mostofi et al., "wannier90: A tool for obtaining maximally-localised Wannier functions," *Comput. Phys. Commun.*, vol. 178, pp. 685–699, 2008.

[53] E. E. Salpeter and H. A. Bethe, "A relativistic equation for bound-state problems," *Phys. Rev.*, vol. 84, pp. 1232–1242, 1951.

[54] W. Hanke and L. J. Sham, "Many-particle effects in the optical spectrum of a semiconductor," *Phys. Rev. B*, vol. 21, pp. 4656–4673, 1980.

[55] G. Onida et al., "Ab initio calculations of the quasiparticle and absorption spectra of clusters: The sodium tetramer," *Phys. Rev. Lett.*, vol. 75, pp. 818–821, 1995.

[56] S. Albrecht, G. Onida, and L. Reining, "Ab initio calculation of the quasiparticle spectrum and excitonic effects in Li_2O," *Phys. Rev. B*, vol. 55, pp. 10278–10281, 1997.

[57] G. Onida, L. Reining, and A. Rubio, "Electronic excitations: Density-functional versus many-body Green's-function approaches," *Rev. Mod. Phys.*, vol. 74, pp. 601–659, 2002.

[58] M. J. Van Setten et al., "Optical response of the sodium alanate system: GW0-BSE calculations and thin film measurements," *Phys. Rev. B*, vol. 83, pp. 035422–6, 2011.

[59] M. Rohlfing and S. Louie, "Excitonic Effects and the Optical Absorption Spectrum of Hydrogenated Si Clusters," *Phys. Rev. Lett.*, vol. 80, pp. 3320–3323, 1998.

[60] J. Paier, M. Marsman, and G. Kresse, “Dielectric properties and excitons for extended systems from hybrid functionals,” *Phys. Rev. B*, vol. 78, pp. 121201–4, 2008.

[61] L. E. Ramos et al., “Optical spectra of Si nanocrystallites: Bethe-Salpeter approach versus time-dependent density-functional theory,” *Phys. Rev. B*, vol. 78, pp. 195423–9, 2008.

[62] R. Bader and M. Stephens, “Spatial localization of the electronic pair and number distributions in molecules,” *J. Am. Chem. Soc.*, vol. 97, pp. 7391–7399, 1975.

[63] A. D. Becke and K. E. Edgecombe, “A simple measure of electron localization in atomic and molecular systems,” *J. Chem. Phys.*, vol. 92, pp. 5397–5403, 1990.

[64] K. Parlinski, Z. Li, and Y. Kawazoe, “First-principles determination of the soft mode in cubic ZrO_2,” *Phys. Rev. Lett.*, vol. 78, pp. 4063–4066, 1997.

[65] R. P. Feynman, “Forces in molecules,” *Phys. Rev.*, vol. 56, pp. 340–343, 1939.

[66] von H. Hellmann, “Einführung in die Quantenchemie,” p. 350, 1939.

[67] S. Baroni, P. Giannozzi, and A. Testa, “Green’s-function approach to linear response in solids,” *Phys. Rev. Lett.*, vol. 58, pp. 1861–1864, 1987.

[68] P. Pavone and S. Baroni, “Ab initio calculation of phonon dispersions in semiconductors,” *Phys. Rev. B*, vol. 43, pp. 7231–7242, 1991.

[69] R. Martoňák et al., “Simulation of structural phase transitions by metadynamics,” *Zeitschrift für Krist.*, vol. 220, pp. 489–498, 2005.

[70] R. Martoňák, A. Laio, and M. Parrinello, “Predicting crystal structures: the Parrinello-Rahman method revisited,” *Phys. Rev. Lett.*, vol. 90, pp. 075503–4, 2003.

[71] S. Goedecker, “Minima hopping: An efficient search method for the global minimum of the potential energy surface of complex molecular systems,” *J. Chem. Phys.*, vol. 120, pp. 9911–9917, 2004.

[72] J. Pannetier et al., “Prediction of crystal structures from crystal chemistry rules by simulated annealing,” *Nature*, vol. 346, pp. 343–345, 1990.

[73] J. C. Schön and M. Jansen, “First step towards planning of syntheses in solid state chemistry: determination of promising structure candidates by global optimization,” *Angew. Chemie Int. Ed. English*, vol. 35, pp. 1286–1304, 1996.

[74] J. Kennedy and R. C. Eberhart, “A discrete binary version of the particle swarm algorithm,” in *IEEE International Conference on Computational Cybernetics and Simulation*, 1997, vol. 5, pp. 4104–4108.

[75] C. J. Pickard and R. J. Needs, “Ab initio random structure searching.,” *J. Phys. Condens. Matter*, vol. 23, pp. 053201–23, 2011.

[76] T. S. Bush, C. R. Catlow, and P. D. Battle, “Evolutionary programming techniques for predicting inorganic crystal structures,” *J. Mater. Chem.*, vol. 5, pp. 1269–1272, 1995.

[77] S. Woodley et al., “The prediction of inorganic crystal structures using a genetic algorithm and energy minimisation,” *Phys. Chem. Chem. Phys.*, vol. 1, pp. 2535–2542, 1999.

[78] C. J. Pickard and R. Needs, “High-Pressure Phases of Silane,” *Phys. Rev. Lett.*, vol. 97, pp. 045504–4, 2006.

[79] C. J. Pickard and R. J. Needs, “Highly compressed ammonia forms an ionic crystal.,” *Nat. Mater.*, vol. 7, pp. 775–779, 2008.

[80] C. J. Pickard and R. J. Needs, “Dense low-coordination phases of lithium,” *Phys. Rev. Lett.*, vol. 102, pp. 100–103, 2009.

[81] Y. Ma et al., “Transparent dense sodium.,” *Nature*, vol. 458, pp. 182–186, 2009.

[82] Y. Ma et al., “Novel high pressure structures of polymeric nitrogen,” *Phys. Rev. Lett.*, vol. 102, pp. 100–103, 2009.

[83] Q. Li et al., “Superhard Monoclinic Polymorph of Carbon,” *Phys. Rev. Lett.*, vol. 102, pp. 175506–4, 2009.

[84] M. Amsler and S. Goedecker, “Crystal structure prediction using the minima hopping method,” *J. Chem. Phys.*, vol. 133, pp. 224104–8, 2010.

[85] D. J. Wales and J. P. K. Doye, “Global optimization by basin-hopping and the lowest energy structures of Lennard-Jones clusters containing up to 110 atoms,” *J. Phys. Chem. A*, vol. 101, pp. 5111–5116, 1997.

[86] R. C. Eberhart and J. Kennedy, “A new optimizer using particle swarm theory,” in *Proceedings of the sixth international symposium on micro machine and human science*, 1995, vol. 1, pp. 39–43.

[87] Y. Wang et al., “CALYPSO: A method for crystal structure prediction,” *Comput. Phys. Commun.*, vol. 183, pp. 2063–2070, 2012.

[88] Y. Wang et al., “Crystal structure prediction via particle-swarm optimization,” *Phys. Rev. B*, vol. 82, pp. 094116–8, 2010.

[89] Y. Wang et al., “An effective structure prediction method for layered materials based on 2D particle swarm optimization algorithm.,” *J. Chem. Phys.*, vol. 137, pp. 224108–6, 2012.

[90] E. Zurek and D. C. Lonie, “XtalOpt: An Open-source Evolutionary Algorithm for Crystal Structure Prediction,” *Comput. Phys. Commun*, vol. 182, pp. 372–387, 2011.

[91] E. Zurek and D. C. Lonie, “New Version Announcement: XtalOpt Version r7: An Open-Source Evolutionary Algorithm for Crystal Structure Prediction.,” *Comput. Phys. Commun*, vol. 182, 2011.

[92] A. R. Oganov, M. Valle, and A. O. Lyakhov, “How Evolutionary Crystal Structure PredictionWorks,” *Acc. Chem. Res*, vol. 44, pp. 227–237, 2011.

[93] C. W. Glass, A. R. Oganov, and N. Hansen, “USPEX—Evolutionary Crystal Structure Prediction,” *Comp. Phys. Comm*, vol. 175, pp. 713–720, 2006.

[94] Y. Yao, J. Tse, and K. Tanaka, “Metastable high-pressure single-bonded phases of nitrogen predicted via genetic algorithm,” *Phys. Rev. B*, vol. 77, pp. 052103–4, 2008.

[95] D. Deaven and K. Ho, “Molecular geometry optimization with a genetic algorithm,” *Phys. Rev. Lett.*, vol. 75, pp. 288–291, 1995.

[96] A. R. Oganov and C. W. Glass, “Crystal structure prediction using ab initio evolutionary techniques: principles and applications.,” *J. Chem. Phys.*, vol. 124, pp. 244704–15, 2006.

[97] G. Trimarchi and A. Zunger, “Global space-group optimization problem: Finding the stablest crystal structure without constraints,” *Phys. Rev. B*, vol. 75, pp. 104113–8, 2007.

[98] N. L. Abraham and M. I. J. Probert, “A periodic genetic algorithm with real-space representation for crystal structure and polymorph prediction,” *Phys. Rev. B*, vol. 73, pp. 224104–6, 2006.

[99] C. J. Pickard and R. Needs, “Metallization of aluminum hydride at high pressures: A first-principles study,” *Phys. Rev. B*, vol. 76, pp. 144114–5, 2007.

[100] I. Goncharenko et al., “Pressure-Induced Hydrogen-Dominant Metallic State in Aluminum Hydride,” *Phys. Rev. Lett.*, vol. 100, pp. 045504–4, 2008.

[101] H. Shi et al., “Electron band structure of the high pressure cubic phase of AlH_3,” *J. Phys. Conf. Ser.*, vol. 377, pp. 012093–8, 2012.

[102] N. W. Ashcroft, “Hydrogen dominant metallic alloys: High temperature superconductors?,” *Phys. Rev. Lett.*, vol. 92, pp. 187002–4, 2004.

[103] M. I. Eremets et al., “Superconductivity in hydrogen dominant materials: silane.,” *Science*, vol. 319, pp. 1506–1509, 2008.

[104] T. A. Strobel et al., “High-pressure study of silane to 150 GPa,” *Phys. Rev. B*, vol. 83, pp. 144102–14, 2011.

[105] M. Hanfland et al., “High-pressure synthesis, amorphization, and decomposition of silane,” *Phys. Rev. Lett.*, vol. 106, pp. 095503–4, 2011.

[106] O. Degtyareva et al., “Formation of transition metal hydrides at high pressures,” *Solid State Commun.*, vol. 149, pp. 1583–1586, 2009.

[107] J. S. Tse, Y. Yao, and K. Tanaka, “Novel superconductivity in metallic SnH_4 under high pressure,” *Phys. Rev. Lett.*, vol. 98, pp. 117004–4, 2007.

[108] X. Jin et al., “Superconducting high-pressure phases of disilane.,” *Proc. Natl. Acad. Sci. U. S. A.*, vol. 107, pp. 9969–9973, 2010.

[109] K. Burke, J. P. Perdew, and M. Ernzerhof, “Why semilocal functionals work: Accuracy of the on-top pair density and importance of system averaging,” *J. Chem. Phys.*, vol. 109, pp. 3760–3771, 1998.

[110] S. Baroni et al., “Phonons and related crystal properties from density-functional perturbation theory,” *Rev. Mod. Phys.*, vol. 73, pp. 515–562, 2001.

[111] I. G. Gurtubay, B. Rousseau, and A. Bergara, “Undamped low-energy plasmon in AlH_3 at high pressure,” *Phys. Rev. B*, vol. 82, pp. 085113–5, 2010.

[112] B. Rousseau and A. Bergara, “Giant anharmonicity suppresses superconductivity in AlH_3 under pressure,” *Phys. Rev. B*, vol. 82, pp. 104504–9, 2010.

[113] J. W. Garland, K. H. Bennemann, and F. M. Mueller, “Effect of lattice disorder on the superconducting transition temperature,” *Phys. Rev. Lett.*, vol. 21, pp. 1315–1319, 1968.

[114] A. D. Becke and E. R. Johnson, “A simple effective potential for exchange,” *J. Chem. Phys.*, vol. 124, pp. 221101–4, 2006.

[115] J. Heyd, G. E. Scuseria, and M. Ernzerhof, “Hybrid functionals based on a screened Coulomb potential,” *J. Chem. Phys.*, vol. 118, pp. 8207–8215, 2003.

[116] H. Search et al., “The GW method,” *Reports Prog. Phys.*, vol. 61, pp. 237–312, 1998.

[117] D. J. Singh, “Electronic structure calculations with the Tran-Blaha modified Becke-Johnson density functional,” *Phys. Rev. B*, vol. 82, pp. 205102–10, 2010.

[118] Y. Ma, Y. Wang, and A. Oganov, “Absence of superconductivity in the high-pressure polymorph of MgB_2,” *Phys. Rev. B*, vol. 79, pp. 054101–5, 2009.

[119] H. J. Monkhorst and J. D. Pack, “Special points for Brillouin-zone integrations,” *Phys. Rev. B*, vol. 16, pp. 1748–1749, 1977.

[120] Y. Ma, A. R. Oganov, and C. W. Glass, "Structure of the metallic ξ-phase of oxygen and isosymmetric nature of the ε-ξ Phase transition: Ab initio simulations," *Phys. Rev. B*, vol. 76, pp. 064101–5, 2007.

[121] D. Y. Kim et al., "Structurally induced insulator-metal transition in solid oxygen: A quasiparticle investigation," *Phys. Rev. B*, vol. 77, pp. 092104–4, 2008.

[122] J. S. Tse et al., "Electronic structure of ε-oxygen at high pressure: GW calculations," *Phys. Rev. B*, vol. 78, pp. 132101–3, 2008.

[123] J. Laflamme Janssen et al., "Electron-phonon coupling in C_{60} using hybrid functionals," *Phys. Rev. B*, vol. 81, pp. 073106–4, 2010.

[124] M. Grundmann, *The Physics of semiconductors: an introduction including devices and nanophysics*. New York: Springer, 2006.

[125] A. Schmehl et al., "Epitaxial integration of the highly spin-polarized ferromagnetic semiconductor EuO with silicon and GaN.," *Nat. Mater.*, vol. 6, pp. 882–887, 2007.

[126] S. J. Cho, "Spin-polarized energy bands in Eu chalcogenides by the augmented-plane-wave method," *Phys. Rev. B*, vol. 1, pp. 4589–4603, 1970.

[127] A. Mauger and C. Godart, "The magnetic, optical, and transport properties of representatives of a class of magnetic semiconductors: The europium chalcogenides," *Phys. Rep.*, vol. 141, pp. 51–176, 1986.

[128] R. J. Husband et al., "Europium-IV : An incommensurately modulated crystal structure in the lanthanides," *Phys. Rev. Lett.*, vol. 109, pp. 095503–4, 2012.

[129] W. Bi et al., "Synchrotron x-ray spectroscopy studies of valence and magnetic state in europium metal to extreme pressures," *Phys. Rev. B*, vol. 85, pp. 205134–12, 2012.

[130] H. Wang, C. Schuster, and U. Schwingenschlögl, "First principles description of the insulator-metal transition in europium monoxide," *Chem. Phys. Lett.*, vol. 524, pp. 68–72, 2012.

[131] N. J. C. Ingle and I. S. Elfimov, "Influence of epitaxial strain on the ferromagnetic semiconductor EuO: First-principles calculations," *Phys. Rev. B*, vol. 77, pp. 121202–4, 2008.

[132] S. Q. Shi et al., "Electronic structure and magnetism of EuX (X = O, S, Se and Te): A first-principles investigation," *EPL*, vol. 83, pp. 69001–5, 2008.

[133] J. N. Farrell and R. D. Taylor, "Coexistence of intermediate valence and antiferromagnetic ordering in europium metal," vol. 42, pp. 2478–2481, 1979.

[134] A. Jayaraman, "Pressure-Induced Electronic Collapse and Semiconductor-to-Metal Transition in EuO," *Phys. Rev. Lett.*, vol. 29, pp. 1674–1676, 1972.

[135] N. M. Souza-Neto et al., "Reentrant valence transition in EuO at high pressures: Beyond the bond-valence model," *Phys. Rev. Lett.*, vol. 109, pp. 026403–4, 2012.

[136] S. Heathman et al., "High pressure behaviour of TmTe and EuO," *J. Alloys Compd.*, vol. 230, pp. 89–93, 1995.

[137] M. M. Abd-Elmeguid and R. D. Taylor, "Onset of valence and magnetic instabilities in the ferromagnetic semiconductor EuO at high pressures," *Phys. Rev. B*, vol. 42, pp. 1048–1051, 1990.

[138] E. G. Ponyatovskii and V. G. Tissen, "Bahavior of the Curie temperature of EuO at pressures up to 20 GPa," *JETP Lett.*, vol. 46, p. 287, 1987.

[139] H. G. Zimmer et al., "Insulator-metal transition and valence instability in EuO near 130 kbar," *Phys. Rev. B*, vol. 29, pp. 2350–2352, 1984.

[140] V. Eyert and W. Nolting, "Influence of valence instabilities on the Curie-temperature of ferromagnetic 4f-systems," *Solid State Commun.*, vol. 60, pp. 905–911, 1986.

[141] E. R. Bauminger et al., "Charge fluctuations in Europium in metallic $EuCu_2Si_2$," *Phys. Rev. Lett.*, vol. 30, pp. 1053–1056, 1973.

[142] J. Röhler and G. Kaindl, "Influence of pressure on the inhomogeneous mixed-valent state in Eu_3S_4," *Solid State Commun.*, vol. 37, pp. 737–739, 1981.

[143] F. Birch, "Finite elastic strain of cubic crystals," *Phys. Rev.*, vol. 71, pp. 809–824, 1947.

[144] F. D. Murnaghan, "Finite deformations of an elastic solid," *Am. J. Math*, vol. 49, pp. 235–260, 1937.

[145] M. Filatov, "First principles calculation of Mössbauer isomer shift," *Coord. Chem. Rev.*, vol. 253, pp. 594–605, 2009.

[146] T. C. Gibb and N. N. Greenwood, "Mössbauer Spectroscopy." Chapman and Hall, London, 1971.

[147] F. E. Wagner and G. K. Shenoy, *Mössbauer isomer shifts*. North-Holland, Amsterdam, 1978.

[148] N. Zarifi, H. Liu, and J. S. Tse, "Structures of the metallic and superconducting high pressure phases of solid CS_2," *Sci. Rep.*, vol. 5, pp. 10458–8, 2015.

[149] J. Sun et al., "Persistence and eventual demise of oxygen molecules at terapascal pressures," *Phys. Rev. Lett.*, vol. 108, pp. 045503–4, 2012.

[150] J. B. Neaton and N. W. Ashcroft, "Low-energy linear structures in dense oxygen: implications for the epsilon phase.," *Phys. Rev. Lett.*, vol. 88, pp. 205503–4, 2002.

[151] Y. Ma et al., "Novel high pressure structures of polymeric nitrogen," *Phys. Rev. Lett.*, vol. 102, pp. 065501–4, 2009.

[152] M. I. Eremets et al., "Single-bonded cubic form of nitrogen," *Nat. Mater.*, vol. 3, pp. 558–563, 2004.

[153] C. J. Pickard and R. J. Needs, "High-pressure phases of nitrogen," *Phys. Rev. Lett.*, vol. 102, pp. 125702–4, 2009.

[154] M. J. Lipp et al., "High-energy-density extended CO solid.," *Nat. Mater.*, vol. 4, pp. 211–215, 2005.

[155] J. Sun et al., "Controlling the bonding and band gaps of solid carbon monoxide with pressure," *Phys. Rev. Lett.*, vol. 106, pp. 145502–4, 2011.

[156] W. J. Evans et al., "Pressure-induced polymerization of carbon monoxide: Disproportionation and synthesis of an energetic lactonic polymer," *Chem. Mater.*, vol. 18, pp. 2520–2531, 2006.

[157] V. Iota et al., "Six-fold coordinated carbon dioxide VI.," *Nat. Mater.*, vol. 6, pp. 34–38, 2007.

[158] J. Sun et al., "High-pressure polymeric phases of carbon dioxide.," *Proc. Natl. Acad. Sci. U. S. A.*, vol. 106, pp. 6077–6081, 2009.

[159] A. Sengupta et al., "Polymerization of carbon dioxide: A chemistry view of molecular-to-nonmolecular phase transitions," *J. Phys. Chem. C*, vol. 116, pp. 2061–2067, 2012.

[160] C. Lu, M. Miao, and Y. Ma, "Structural evolution of carbon dioxide under high pressure.," *J. Am. Chem. Soc.*, vol. 135, pp. 14167–71, Sep. 2013.

[161] E. G. Butcher et al., "Formation and properties of the black form of carbon disulphide," *Nature*, vol. 199, pp. 756–758, 1963.

[162] G. Dolling, B. M. Powell, and B. H. Torrie, "The lattice modes of CS_2, and neutron scattering selection rules," *Can. J. Phys.*, vol. 59, pp. 122–129, 1981.

[163] S. F. Agnew, R. E. Mischke, and B. I. Swanson, "Pressure- and temperature-induced chemistry of carbon disulfide," *J. Phys. Chem.*, vol. 92, pp. 4201–4204, 1988.

[164] R. P. Dias et al., “Insulator-metal transition of highly compressed carbon disulfide,” *Phys. Rev. B*, vol. 84, pp. 144104–6, 2011.

[165] R. P. Dias et al., “Superconductivity in highly disordered dense carbon disulfide.,” *Proc. Natl. Acad. Sci. U. S. A.*, vol. 110, pp. 11720–4, 2013.

[166] L. Chaput et al., “Phonon-phonon interactions in transition metals,” *Phys. Rev. B*, vol. 84, pp. 094302–6, 2011.

[167] K. Lee et al., “Higher-accuracy van der Waals density functional,” *Phys. Rev. B*, vol. 82, pp. 081101–4, 2010.

[168] C.-S. Yoo, “Physical and chemical transformations of highly compressed carbon dioxide at bond energies.,” *Phys. Chem. Chem. Phys.*, vol. 15, pp. 7949–66, 2013.

[169] P. B. Allen and R. C. Dynes, “Transition temperature of strong-coupled superconductors reanalyzed,” *Phys. Rev. B*, vol. 12, pp. 905–922, 1975.

[170] P. B. Allen, “Neutron spectroscopy of superconductors,” *Phys. Rev. B*, vol. 6, pp. 2577–2579, 1972.

[171] V. V Struzhkin et al., “Superconductivity at 10 – 17 K in compressed sulphur,” *Nature*, vol. 390, pp. 382–384, 1997.

[172] C. Hejny et al., “Incommensurate sulfur above 100 GPa,” *Phys. Rev. B*, vol. 71, pp. 7–10, 2005.

[173] A. P. Drozdov, M. I. Eremets, and I. A. Troyan, “Conventional superconductivity at 190 K at high pressures,” 2014.

[174] W. Kossel, “Molecule formation as a question of atomic structure,” *Ann. Phys*, vol. 49, pp. 229–362, 1916.

[175] G. N. Lewis, “The atom and the molecule,” *J. Am. Chem. Soc*, vol. 38, pp. 762–785, 1916.

[176] N. Bartlett, “Xenon hexafluoroplatinate Xe^{+} $[PtF^{6}]^{-}$,” *Proc. Chem. Soc.*, vol. 218, 1963.

[177] D. Nishio-Hamane et al., “No reactions observed in Xe-Fe system even at Earth core pressures,” *Geophys. Res. Lett.*, vol. 37, pp. 35–38, 2010.

[178] K. K. M. Lee and G. Steinle-Neumann, “High-pressure alloying of iron and xenon: ‘Missing’ Xe in the Earth’s core?,” *J. Geophys. Res. Solid Earth*, vol. 111, pp. B02202–7, 2006.

[179] L. Zhu et al., “Reactions of xenon with iron and nickel are predicted in the Earth’s inner core.,” *Nat. Chem.*, vol. 6, pp. 644–8, Jul. 2014.

[180] M. Kim, M. Debessai, and C. S. Yoo, "Two- and three-dimensional extended solids and metallization of compressed XeF_2.," *Nat. Chem.*, vol. 2, pp. 784–8, 2010.

[181] D. Kurzydłowski et al., "Freezing in resonance structures for better packing: XeF_2 becomes $(XeF^+)(F^-)$ at large compression.," *Inorg. Chem.*, vol. 50, pp. 3832–3840, 2011.

[182] M. S. Somayazulu, "Novel Xenon Chemistry with a diamond anvil cell," in *HPCAT workshop*, 2012.

[183] X. Gonze, "Dynamical matrices, Born effective charges, dielectric permittivity tensors, and interatomic force constants from density-functional perturbation theory," *Phys. Rev. B*, vol. 55, pp. 10355–10368, 1997.

[184] A. Togo, F. Oba, and I. Tanaka, "First-principles calculations of the ferroelastic transition between rutile-type and $CaCl_2$-type SiO_2 at high pressures," *Phys. Rev. B*, vol. 78, pp. 134106–9, 2008.

[185] P. Giannozzi et al., "QUANTUM ESPRESSO: a modular and open-source software project for quantum simulations of materials.," *J. Phys. Condens. Matter*, vol. 21, pp. 395502–19, 2009.

[186] A. N. Zisman, I. V. Aleksandrov, and S. M. Stishov, "X-ray study of equations of state of solid xenon and cesium iodide at pressures up to 55 GPa," *Phys. Rev. B*, vol. 32, pp. 484–487, 1985.

[187] D. Schiferl, R. L. Mills, and L. E. Trimmer, "X-ray study of xenon to 23 GPa," *Solid State Commun.*, vol. 46, pp. 783–785, 1983.

[188] P. Li, G. Gao, and Y. Ma, "Modulated structure and molecular dissociation of solid chlorine at high pressures," *J. Chem. Phys.*, vol. 137, pp. 064502–6, 2012.

[189] M. Somayazulu et al., "High Pressure-High Temperature Reactions in Xenon-Chlorine System," *Mater. Res. Soc. Symp. Proc*, vol. 987, 2007.

[190] B. Silvi and A. Savin, "Classification of chemical bonds based on topological analysis of electron localization functions," *Nature*, vol. 371. pp. 683–686, 1994.

[191] A. Savin et al., "Electron localization in solid-state structures of the elements: the diamond structure," *Chem., Int. Ed. Engl*, vol. 31, pp. 187–188, 1992.

[192] F. J. Ribeiro et al., "Structural and electronic properties of carbon in hybrid diamond-graphite structures," *Phys. Rev. B*, vol. 72, pp. 214109–6, 2005.

[193] D. Porezag and M. Pederson, "Infrared intensities and Raman-scattering activities within density-functional theory," *Phys. Rev. B*, vol. 54, pp. 7830–7836, 1996.

[194] X. Wang et al., “Ab initio calculation of the anomalous Hall conductivity by Wannier interpolation,” *Phys. Rev. B*, vol. 74, pp. 195118–15, 2006.

[195] W. Grochala, “Atypical compounds of gases, which have been called ‘noble,’” *Chem. Soc. Rev.*, vol. 36, pp. 1632–55, 2007.

[196] W. Tang, E. Sanville, and G. Henkelman, “A grid-based Bader analysis algorithm without lattice bias.,” *J. Phys. Condens. Matter*, vol. 21, pp. 084204–7, 2009.

[197] Y. Fujii et al., “Evidence for molecular dissociation in bromine near 80 GPa,” *Phys. Rev. Lett.*, vol. 63, pp. 536–539, 1989.

[198] K. Takemura and S. Minomura, “Observation of molecular dissociation of iodine at high pressure by x-Ray diffraction,” *Phys. Rev. Lett.*, vol. 45, pp. 1881–1884, 1980.

[199] A. San-Miguel et al., “New phase transition of solid bromine under high pressure,” *Phys. Rev. Lett.*, vol. 99, pp. 015501–4, 2007.

[200] T. Kume et al., “High pressure raman study of bromine and iodine: soft phonon in the incommensurate phase,” *Phys. Rev. Lett.*, vol. 94, pp. 065506–4, 2005.

[201] H. Search et al., “First-principles studies of solid halogens under pressure : scaling rules for properties among I_2, Br_2 and Cl_2,” *J. Phys. Condens. Matter*, vol. 14, pp. 10441–10444, 2002.

[202] Shimizu K, Amaya K, and Endo S, “Proc. XVth AIRAPT Int. Conf. (Warsaw) (Singapore: World Scientific),” 1995, p. 498.

[203] K. Amaya et al., “Observation of pressure-induced superconductivity in the megabar region,” *J. Phys. Condens. Matter*, vol. 10, pp. 11179–11190, 1998.

[204] D. Duan et al., “The crystal structure and superconducting properties of monatomic bromine.,” *J. Phys. Condens. Matter*, vol. 22, pp. 015702–6, 2010.

[205] A. Simon, “Superconductivity and Chemistry,” *Angew. Chemie Int. Ed. English*, vol. 36, no. 17, pp. 1788–1806, 1997.

[206] T. Kenichi et al., “Modulated structure of solid iodine during its molecular dissociation under high pressure.,” *Nature*, vol. 423, pp. 971–974, 2003.